

Synthesis and Characterisation of new Tetrathiafulvalene-  
Oligofluorene derivatives for Moisture Indicators

PhD Thesis

Katrina Scanlan

Professor Peter J. Skabara Group

Pure and Applied Chemistry

University of Strathclyde, Glasgow

2020

This thesis is the result of the author's original research. It has been composed by the author and has not been previously submitted for examination which has led to the award of a degree.

The copyright of this thesis belongs to the author under the terms of the United Kingdom Copyright Acts as qualified by University of Strathclyde Regulation 3.50. Due acknowledgement must always be made of the use of any material contained in, or derived from, this thesis.

Signed:

Date:

## Acknowledgement

I would like to thank Engineering and Physical Sciences Research Council (EP/M506643/1) for funding my research. Additionally, I would like to thank Professor Peter J. Skabara for affording me the opportunity to begin and finish this research, it's helped me grow as an individual and as a professional. I would also like to thank collaborators at the University of Glasgow for their input with regards to photophysical studies.

I would like to expand an enormous thank you to Dr. Oleksandr Kanibolotskyy for his supervision and support over these four years; ensuring I made the most from my research and always providing a positive work environment. Additionally, I would like to extend a huge thanks to Dr. Neil Findlay, Dr. Joseph Cameron and Dr. Rupert Taylor for encouraging me to be the best that I can be. All the post-doctoral researchers and student's in the Skabara group are fantastic individuals and it's been a pleasure to know them.

I would like to thank the technical staff at Strathclyde University, including Kate Reid, Craig Irving, Pat Keating, Gavin Bain and Alexander Clunie for assistance in TGA measurements, NMR, SPS maintenance and elemental analysis. Furthermore, I would like to thank Dr. Christine Davidson, Dr. Edward Cussen and Isabel Scott for encouraging me to keep moving forward even when life threw me curveballs.

To my family, thanks for your support throughout these years. A special thanks to my fiancé and best friend, thank you for everything! Thank you for taking our son out for long walks multiple times a day so I could finish this thesis. Lastly, to my little boy,

Marko, thanks for giving me inspiration in all areas of my life. It's a pleasure to be your mother.

## Abstract

The term ‘smart materials’ refers to a category of materials that are able to dynamically respond to external stimuli through a change in physical and/or chemical properties. The versatility afforded by organic materials makes them attractive candidates in the development of new sensing materials. An in-depth understanding of the structure-property relationships that drive a sensing material is a necessity in understanding device operation and reliably predicting their performance.

Chapter 1 provides an overview of organic stimuli responsive materials and the types of physical properties that can induce a response in such materials. Chapter 1 further introduces the operating principles of sensors and their applications.

Chapter 2 provides an introduction to the development of the novel hexylated oligofluorene-thiophene systems wherein versatile 1,3-dithiole-2-one moiety is incorporated into the centre of the oligofluorene systems. The chapter follows a synthetic strategy used as a way to increase the dimensionality of oligofluorene systems and discusses the influence of the synthetic strategy *vis-à-vis* yield and reproducibility of the systems. Chapter 2 further looks at the impact of the core unit on the photophysical behaviour of the oligofluorene spores and discusses the changes in the thermal and electronic properties of the new oligofluorene-thiophene systems as a consequence of the core unit.

Chapter 3 discusses the development of new star-shaped oligofluorene-thiophene systems wherein redox-active dithiophene-tetrathiafulvalene is used as a core unit, providing an increase in dimensionality to a plurality of hexylated oligofluorene spores. The synthesis and properties of the oligofluorene systems are discussed. The photophysical behaviour, thermal and electronic properties of the new systems are

investigated. Furthermore the core system displayed upon oxidation interesting features as fluorescence moisture indicator and are further investigated wherein the proof of concept is visible to the naked eye.

The experimental procedures of chapters 2-3 are presented in chapter 4.

## Abbreviations

°C	degrees celsius
2D	two-dimensional
3D	three-dimensional
A	absorbance
a.u.	arbitrary units
ACQ	aggregation-caused quenching
BEDT-TTF	bis(ethylenedithio)tetrathiafulvalene
BGBC	bottom-gate bottom-contact
BGTC	bottom-gate top-contact
BLA	bond length alternation
b.p.	boiling point
c	concentration
CHDV	1,4-cyclohexyldimethanol divinyl ether
cm	centimetre
CT	charge transfer
CV	cyclic voltammetry
D	doublet
D-A	donor-acceptor
dd	doublet of doublets
DCM	dichloromethane
DMF	dimethylformamide
DPV	differential pulse voltammetry
DSC	differential scanning calorimetry
DT-TTF	2, 2'-bithieno[3,4-d]-1,3-dithiole

E	potential
EA	electron affinity
$E_B$	exciton binding energy
$e^-$	electron
$E_f$	fermi level
e.g.	<i>exempli gratia</i>
$E^\theta$	deviation from molecular planarity
$E^{1/2}$	half-wave potential
$E^{\delta r}$	bond length alternation
$E_g$	HOMO-LUMO energy gap
$E^{int}$	interchain electronic communication in the solid state
$E_{opt}$	optical gap
$E_{ox}$	oxidation potential
$E_g^{opt}$	optical HOMO-LUMO energy gaps
EQE	external quantum efficiency
$E_{red}$	reduction potential
$E^{Res}$	aromatic resonance energy
$E^{Sub}$	energy influence contributed to substituents
ETL	electron-transporting layers
eV	electron volts
F	Faraday's constant
Fc	ferrocene
$Fc^+$	ferrocenium
FF	fill factor
FRET	fluorescence resonance energy transfer

g	gram
h	hour
$h$	Plank's constant
HOMO	highest occupied molecular orbital
HTL	hole-transporting layers
I	current
IC	internal conversion
$I_0$	intensity of light before passing through sample
IP	ionisation potential
ISC	intersystem crossing
J	coupling constant
$J_{max}$	current density at the maximum of $J \times V$ in 4 th quadrant
$J_{sc}$	the current density through the device
K	Kelvin
l	path length of the light through sample
LCAO-MO	linear combination of atomic orbitals molecular orbital
LDA	lithium diisopropylamide
LMW	low molecular weight
LUMO	lowest occupied molecular orbital
M	molarity
MALDI-TOF	matrix-assisted laser desorption/ionization – time of flight
Me	methyl
mg	milligram
min	minute
mL	millilitre

mM	millimolar
mmol	millimole
m	multiplet
$M_w$	weight-average molecular mass
n	number of electrons
NIR	near infra-red
nm	nanometre
NMR	nuclear magnetic resonance
OLED	organic light-emitting diode
OFET	organic field-effect transistor
OPV	organic photovoltaic
OSC	organic semiconductor
PAG	photoacid generator
PAH	polycyclic aromatic hydrocarbon
PCE	power conversion efficiency
PDA	polydiacetylene
$P_{in}$	power input
PITN	polyisothianaphthene
PL	photoluminescence
PLQY	photoluminescence quantum yield
$P_{out}$	power output
PPE	poly( <i>p</i> -phenylene-ethynylene)
PPV	poly( <i>p</i> -phenylenevinylene)
P3HT	poly(3-hexylthiophene)
q	quartet

R	gas constant
rt	room temperature
s	second / singlet
s <sub>0</sub>	singlet ground state
s <sub>1</sub>	singlet excited state
SCE	saturated calomel electrode
SHE	standard hydrogen electrode
SWV	square-wave voltammetry
t	triplet
T	temperature
TBAF	tetra- <i>n</i> -butylammonium fluoride
TBAF <sub>6</sub>	tetra- <i>n</i> -butylammonium hexafluorophosphate
TCNQ	tetracyano- <i>p</i> -quinodimethane
T <sub>g</sub>	glass transition temperatures
TGA	thermogravimetric analysis
thieno-TTF	2-(1,3-dithiol-2-ylidene)thieno[3,4- <i>d</i> ][1,3]dithiole
TLC	thin-layer chromatography
TMS	trimethylsilyl
TNT	trinitrotoluene
TPE	tetraphenylethene
TTF	tetrathiafulvalene
UV	ultra-violet
V	voltage
Vis	visible
V <sub>max</sub>	maximum voltage

$V_{OC}$  open circuit voltage

## Greek

$\alpha$  1<sup>st</sup> position on heterocycle

$\beta$  2<sup>nd</sup> position on heterocycle

$\mu$  charge-carrier mobility

$\delta$  chemical shift

$\pi$  pi bonding orbital

$\pi^*$  pi anti-bonding orbital

$\sigma$  sigma bonding orbital

$\sigma^*$  sigma anti-bonding orbital

$\lambda$  wavelength

$\lambda_{max}$  absorption maximum

$\lambda_{ex}$  excitation wavelength

## Table of Contents

Acknowledgement.....	iii
Abstract.....	v
Abbreviations.....	vii
<b>1 Introduction .....</b>	<b>1</b>
1.1 Band Theory.....	2
1.2 The Role of sp <sup>2</sup> Hybridised Bonds.....	7
1.3 Organic Semiconductors.....	10
1.3.1 <i>The Role of Molecular Design</i> .....	12
1.4 Optical Processes of Organic Semiconductors .....	32
1.5 Organic Sensors .....	36
1.5.1 <i>Chemosensors</i> .....	39
1.5.2 <i>Overview of Existing Chemosensors</i> .....	44
1.6 Methods of Characterisation.....	53
1.6.1 <i>Ultra-Violet/Visible Absorption Spectroscopy</i> .....	53
1.6.2 <i>Electrochemical Analysis Cyclic Voltammetry</i> .....	56
<b>2 Synthesis, development and characterisation of novel hybrid tetrathiafulvalene-oligofluorene-thiophene systems .....</b>	<b>68</b>
2.1 Abstract.....	69
2.2 Introduction.....	70
2.3 Tetrathiafulvalene as a Redox-Switchable Core.....	71
2.3.1 <i>Thieno[3,4-d][1,3]-dithiole-2-one as a Building Block to Functional Materials</i> .....	74
2.3.2 <i>Extending <math>\pi</math>-Conjugation</i> .....	79
2.4 Synthetic Strategy .....	81

2.4.1	<i>Synthetic strategy 1: 1,3-dithiole-2-one as a starting material</i> .....	81
2.4.2	<i>Synthetic strategy 2: perbromo-2,2'-bithieno[3,4-d][1,3]dithiolylidene as a starting material</i> .....	85
2.5	Results and discussion.....	91
2.5.1	<i>Thermal properties</i> .....	91
2.5.2	<i>Electrochemical properties</i> .....	94
2.5.3	<i>Optical properties</i> .....	100
2.6	Conclusions and further work.....	109
<b>3</b>	<b>Application of hybrid star-shaped tetrathiafulvalene-oligofluorene-thiophene derivatives as a photoluminescence switch</b> .....	<b>111</b>
3.1	Abstract.....	112
3.2	Introduction.....	113
3.3	Experimental.....	115
3.3.1	<i>Adjusting the conformational flexibility of TTF-oligofluorene-thiophene systems</i> .....	115
3.3.2	<i>Perbromo-2,2'-bithieno[3,4,d][1,3]dithiolylidene oligofluorene-thiophene as a PL sensor</i> .....	121
3.4	Conclusions and further work.....	126
<b>4</b>	<b>Experimental</b> .....	<b>128</b>
<b>5</b>	<b>References</b> .....	<b>171</b>

## List of Figures

- Figure 1-1.** H<sub>2</sub> molecule represented as a linear combination of atomic orbitals.
- Figure 1-2.** Schematic showing the differences between a metal, a semiconductor and an insulator, wherein E<sub>g</sub> is the band gap and E<sub>f</sub> is the fermi level.
- Figure 1-3.** Schematic representation depicting the effects of doping on the band gap, wherein E<sub>g</sub> is the band gap.
- Figure 1-4.** Molecular orbital diagram of ethene.
- Figure 1-5.** Energy differences in the molecular orbitals of butadiene.
- Figure 1-6.** Chemical structures of well-known organic semiconductor systems.
- Figure 1-7.** Factors that influence the electronic behaviour in linear π-conjugated materials.
- Figure 1-8.** Comparison of the dihedral angles between phenyl units in biphenyl and fluorene.
- Figure 1-9.** The different orientations of P3HT on a substrate: (i) edge-on; (ii) end-on; (iii) face-on.
- Figure 1-10.** Commonly used core building blocks for introducing increased dimensionality to organic systems.
- Figure 1-11.** Typically used heterocyclic building blocks for organic semiconductor materials.

**Figure 1-12.** The numbering in thiophene systems and known thiophene derivatives: thiophene (1); 2,3-dihydrothiophene (2); 3-thienyl (3); 2,5-dihydrothiophenethiophene (4) and 2-thienyl (5).

**Figure 1-13.** Jablonski diagram illustrating electronic states and the transitions between them.

**Figure 1-14.** Schematic of the essential components of a sensing device.

**Figure 1-15.** Example classifications of sensors (outlined in red) and the measurable physical and chemical parameters (outlined in red).

**Figure 1-16.** Known molecules used in application as fluorescent probes.

**Figure 1-17.** Schematic of the gate and contact configuration of OFETs: (i) top-gate top-contact; (ii) top-gate bottom-contact; (iii) bottom-gate top-contact; (iv) bottom-gate bottom-contact, wherein S – source and D – drain.

**Figure 1-18.** Bilayer photovoltaic cell (left) and bulk heterojunction photovoltaic cell (right).

**Figure 1-19.** OLED device architectures: (i) including HTL and ETL layers; (ii) including hole blocking layer and electron-blocking layer.

**Figure 1-20.** OLED-based biological sensor.

**Figure 1-21.** Energy diagram with the possible electronic transitions in organic molecules and spectral region of observance.

**Figure 1-22.** Schematic diagram showing 2-beam UV-Vis Spectrometer.

**Figure 1-23.** A graph to show potential (E) as a function of time during a CV experiment.

**Figure 1-24.** Cyclic voltammogram for a reversible system where (a) represents the area of the peak characteristic of Butler-Volmer Kinetics and (b) is controlled by diffusion process.

**Figure 1-25.** Variation of applied potential with time in DPV resulting in staircase waveform; arrows indicate the position of current measurements used to take an average.

**Figure 1-26.** Example of an SWV voltammogram; arrows indicate the position of current measurements used to take an average.

**Figure 2-1.** Structures for new hybrid star-shaped TTF-oligofluorene-thiophene systems.

**Figure 2-2.** Structures for new oligofluorene-thiophene (HU-F1 and HU-F2) systems.

**Figure 2-3.** Fluorene with positions numbered.

**Figure 2-4.** Thermal gravimetric analysis (TGA) showing decomposition temperature ( $T_d$ , 5% mass loss) of compounds HU-F1-2 and TTF-(F1-F4)-X series.

**Figure 2-5.** DSC of compounds HU-F1-2 and TTF-F(1-4)-X series showing glass transition temperatures ( $T_g$ ).

**Figure 2-6.** Cyclic voltammetry of compounds HU-F1 and TTF-(F1-F4)-X in CH<sub>2</sub>Cl<sub>2</sub>.

**Figure 2-7.** Structure of star-shaped oligofluorene-truxene derivatives.

**Figure 2-8.** Normalised absorption and PL spectra of compounds HU-F1, HU-F2 and TTF-F<sub>n</sub>-X in dichloromethane.  $\lambda_{\text{ex}}$  (HU-F1) = 378 nm,  $\lambda_{\text{ex}}$  (HU-F2) = 399 nm,  $\lambda_{\text{ex}}$  (TTF-F1) = 372 nm,  $\lambda_{\text{ex}}$  (TTF-F1-TMS) = 384 nm,  $\lambda_{\text{ex}}$  (TTF-F2-TMS) = 392 nm,  $\lambda_{\text{ex}}$  (TTF-F3-TMS) = 396 nm,  $\lambda_{\text{ex}}$  (TTF-F4-TMS) = 378 nm. Concentrations for the emission spectra:  $1.3 \times 10^{-5}$  M (HU-F1);  $1.3 \times 10^{-7}$  M (HU-F2);  $1.0 \times 10^{-6}$  M (TTF-F1);  $3.1 \times 10^{-6}$  M (TTF-F1-TMS);  $1.0 \times 10^{-6}$  M (TTF-F2-TMS);  $1.0 \times 10^{-6}$  M (TTF-F3-TMS);  $1.0 \times 10^{-6}$  M (TTF-F4-TMS).

**Figure 2-9.** The spectra of compounds HU-(F1-F2) and TTF-(F1-F4)-X (extinction coefficient versus wavelength) in dichloromethane. The onsets and positions of peaks are marked.

**Figure 2-10.** PL spectra of compounds HU-F1-2 and TTF-(F1-F4)-X in dichloromethane at different concentrations ( $1 \cdot 10^{-5}$  -  $1 \cdot 10^{-7}$  M).  $\lambda_{\text{ex}}$  (12) = 378 nm,  $\lambda_{\text{ex}}$  (13) = 399 nm,  $\lambda_{\text{ex}}$  (TTF-F1) = 372 nm,  $\lambda_{\text{ex}}$  (TTF-F1-TMS) = 384 nm,  $\lambda_{\text{ex}}$  (TTF-F2-TMS) = 392 nm,  $\lambda_{\text{ex}}$  (TTF-F3-TMS) = 396 nm,  $\lambda_{\text{ex}}$  (TTF-F4-TMS) = 378 nm. The peak positions are marked.

**Figure 2-11.** Normalised absorption and PL spectra of compounds HU-F1, HU-F2 and TTF-F<sub>n</sub>-X in the solid state as films drop-cast from toluene at 3 mg ml<sup>-1</sup>.  $\lambda_{\text{ex}}$  (HU-F1) = 389 nm,  $\lambda_{\text{ex}}$  (HU-F2) = 395 nm,  $\lambda_{\text{ex}}$  (TTF-F1) = 373 nm,  $\lambda_{\text{ex}}$  (TTF-F1-TMS) = 377 nm,  $\lambda_{\text{ex}}$  (TTF-F2-TMS) = 367 nm,

$\lambda_{\text{ex}}$  (TTF-F3-TMS) = 389 nm,  $\lambda_{\text{ex}}$  (TTF-F4-TMS) = 370 nm. The onsets of the absorption are marked, as well as the absorption and emission peak positions.

**Figure 3-1.** Structures for new spiro oligofluorene-thiophene Spiro-Fn systems.

**Figure 3-2.** Photoluminescence spectra showing the enhancement in emission of doped TTF-F3-TMS in  $\text{CH}_2\text{Cl}_2$  ( $1.0 \times 10^{-6}$  M) in the presence of water. Dopant used was  $\text{NOPF}_6$  in  $\text{CH}_3\text{CN}$  (2 equiv.);  $\lambda_{\text{ex}} = 396$  nm.

**Figure 3-3.** Absorption spectra of TTF-F3-TMS ( $1 \cdot 10^{-6}$  M) before and after oxidation with  $\text{NOPF}_6$  followed by treatment with  $\text{N}_2\text{H}_4 \cdot \text{H}_2\text{O}$  (1 drop); (b) PL spectra of TTF-F3-TMS in neutral state, after oxidation with  $\text{NOPF}_6$  ( $t = 130$  min) and after additional treatment with  $\text{N}_2\text{H}_4 \cdot \text{H}_2\text{O}$  (1 drop).

**Figure 3-4.** Proposed rearrangement product of TTF-F3-TMS.

**Figure 3-5.** Components of the photoresist, comprising CHDV, PAG and TTF-F3-TMS.

**Figure 3-6.** Photographs of the cured films prepared from blends: CHDV with 0.1% of PAG (left); CHDV with 0.1% of TTF-F3-TMS and 0.1% of PAG before (middle) and after exposure to water (right).

**Figure 3-7.** Absorption/emission spectra of UV cured film drop cast from blends: CHDV with 0.1 % of PAG (a); CHDV with 0.1 % of TTF-F3-TMS and 0.1 % of PAG before (b) and after exposure to water (c).

## List of Schemes

- Scheme 1-1.** An approach to reducing the  $E_g$  through the system containing a fused aromatic ring when the polymer is in its quinoidal form, wherein (a) is poly(isothianaphthene) and (b) is PTB7.
- Scheme 1-2.** The influence of fused aromatic rings in promoting the quinoidal character in thiophene-based polymers.
- Scheme 1-3.** Constructing star-shaped systems through axial symmetry operations.
- Scheme 1-4.** TTF and its cation and dication species.
- Scheme 1-5.** The proposed catalytic cycle in the Suzuki coupling.
- Scheme 1-6.** The formation of boroxines from boronic acid via condensation.
- Scheme 1-7.** The proposed mechanism for the Stille cross-coupling.
- Scheme 1-8.** Doping of polyaniline through protonation.
- Scheme 2-1.** Formation of cation and dication state of TTF by removal of one or two electrons respectively.
- Scheme 2-2.** An example of synthetic routes to symmetrical TTF, wherein (i)  $PR_3$ ; (ii)  $M(CO)_n$ ; (iii)  $PR_3$ ; (iv)  $NR_3$ ; (v)  $Zn/Br_2$ .
- Scheme 2-3.** Formation of symmetrical tetrathiafulvalene derivative 2.28 through the bromination of thieno[3,4-d][1,3]-dithiole-2-one 2.1.

- Scheme 2-4.** The formation of 1,3-dithiole-2-one precursors in the formation of functionalised TTF-oligothiophenes: (i)  $\text{MnO}_2$ ,  $\text{CH}_2\text{Cl}_2$ ; (ii)  $\text{Hg}(\text{OAc})_2$  and (iii)  $\text{P}_2\text{S}_5$ .
- Scheme 2-5.** Retrosynthetic pathway showing the different synthetic routes for the formation of thieno[3,4-d][1,3]-dithiole-2-one 2.1 moiety.
- Scheme 2-6.** Formation of 1,3-dithiole-2-thione derivatives using aldehydes F1-CHO and F2-CHO via a two-fold lithium-halogen reaction.
- Scheme 2-7.** Formation of oligofluorene-aldehyde derivatives.
- Scheme 2-8.** Formation of diol intermediate during the formation of 1,3-dithiol-2-thione derivative.
- Scheme 2-9.** Synthesis of oligofluorene-thiophene derivatives (HU-F1 and HU-F2) tetrathiafulvalene-oligofluorene-thiophene derivatives (TTF-F1 and TTF-F2) using 1,3-dithiole-2-one derivatives.
- Scheme 2-10.** Formation of the TTF-oligofluorene-thiophene systems TTF-Fn-X.
- Scheme 2-11.** Preparation of 9,9-dihexyl-2,7-dibromofluorene 2.24.
- Scheme 2-12.** Preparation of oligofluorene arms ( $n = 1-4$ ) through the Suzuki coupling.
- Scheme 2-13.** Formation of starting material perbromo-2,2'-bithieno[3,4-d][1,3]dithiolylidene 2.3.

- Scheme 3-1.** Proposed scheme for using TTF as a molecular switch to enhance fluorescence.
- Scheme 3-2.** Proposed scheme for oxidation of TTF-F3-TMS.
- Scheme 3-3.** Previously reported proposed scheme for the rearrangement to form spiro systems from TTF.
- Scheme 3-4.** Cross-linking of the monomer CHDV by UV irradiation in the presence of a photoacid generator (PAG).

### List of Tables

- Table 2-1.** The yields obtained by compounds synthesised for use in the synthetic route for coupling oligofluorenes to VTC.
- Table 2-2.** The yields attained by compounds synthesised through coupling to perbromo-2,2'-bithieno[3,4-d][1,3]dithiolylidene.
- Table 2-3.** Thermal properties of compounds HU-Fn (n = 1-2) and TTF-Fn-X series.
- Table 2-4.** Electrochemical properties of compounds HU-Fn and TTF-Fn-X series, alongside the optical HOMO-LUMO energy gaps ( $E_g^{\text{opt}}$ ) extracted from the corresponding absorption spectra.
- Table 2-5.** UV-Vis absorption data for for HU-Fn and the TTF-Fn-X series in  $\text{CH}_2\text{Cl}_2$ .
- Table 2-6.** Photoluminescence (PL) data and quantum yields (PLQY) for HU-Fn and the TTF-Fn-X series in  $\text{CH}_2\text{Cl}_2$  solution and in the film.

**Table 3-1.** Spiro-Fn yields vis-à-vis the number of fluorene monomers.

**Table 3-2.** PLQY measurements of the cured blends.

## List of Equations

**Equation 1-1.** Contributions to the band gap,  $E_g$ , of polyaromatic linear conjugation systems.

**Equation 1-2.** Stern-Volmer equation.

**Equation 1-3.** Calculation of PCE.

**Equation 1-4.** Determination of the fill factor.

**Equation 1-5.** Energy difference between optical levels.

**Equation 1-6.** Beer Lambert Law.

**Equation 1-7.** Beer's law.

**Equation 1-8.** The relationship between the faradic current and oxidation and reduction processes

**Equation 1-9.** Relationship between free energy and concentration of oxidized and reduced species.

**Equation 1-10.** Gibbs free energy as a function of electrode potential.

**Equation 1-11.** Nernst equation.

- Equation 1-12.** The relationship between reaction rate and current density at electrode surface.
- Equation 1-13.** The rate of reduction.
- Equation 1-14.** The rate of oxidation.
- Equation 1-15.** The Arrhenius equation.
- Equation 1-16.** Partial current density for reduction.
- Equation 1-17.** Partial current density for oxidation.
- Equation 1-18.** Butler-Volmer equation.
- Equation 1-19.** Fick's first law.
- Equation 1-20.** Fick's second law
- Equation 1-21.** Equilibrium between ferrocene and ferrocenium.
- Equation 1-22.** Calculating the LUMO of the analyte.
- Equation 1-23.** Calculating the HOMO of the analyte.
- Equation 1-24.** Band gap calculation.

## 1 Introduction

The discovery of polymers once thought to be insulating materials exhibiting conductivity upon doping led to the advent of a new field of research and development. This new field spanning chemistry, physics, material science, engineering and technology resulted in Heeger, Macdiarmid and Shirakawa winning the Chemistry Nobel Prize in 2000 for their research.<sup>1,2</sup> Consequently, research over the last four decades has provided the electronics industry with lighter weight, flexible and cost-effective semiconductor materials.<sup>3,4,5</sup>

Organic semiconductors (OSCs) are  $\pi$ -conjugated materials that demonstrate varying physical characteristics based upon the interplay between their  $\pi$ -electronic structure and their geometrical structure.<sup>6</sup> Due to the chemical versatility of carbon and its moderate electronegativity, OSCs can provide tailored electronic, optical and mechanical properties.  $\pi$ -conjugated materials encompass molecular, oligomeric and polymeric materials and majority of the research concerning these materials has centered around semiconductor devices including organic light-emitting diode (OLED), organic photovoltaic (OPV) and organic field-effect transistors (OFETs). However,  $\pi$ -conjugated materials have also been proven to be effective in sensing applications due to the utilisation of their variation in electrical conductivity upon exposure to certain environments.<sup>7</sup> The mechanical properties of OSCs make them suitable materials for implantable electronics due to the intimate conformability provided with complex surfaces, such as tissues and organs.<sup>8</sup>

OSCs may have varying applications, however the physical characteristics desired often include that of reliable electronic properties and thermal stability. It is often desired that the  $\pi$ -conjugated material is chemically reproducible and can be synthesised in a reasonable number of steps and in a cost-effective manner. The remaining physical characteristics including thermal, optical and electronic properties are dependent on the application of the material. The design of  $\pi$ -conjugated materials is critical in achieving the desired physical characteristics.<sup>9</sup>

## 1.1 Band Theory

The electrical properties of a solid are determined by a solid's distribution of electrons. In the tight-binding approximation, electrons are considered to reside in molecular orbitals which are delocalised within a solid. The influence of electron distribution in solids can be explained by considering a one-dimensional solid consisting of a linear arrangement of atoms in which each atom contributes a 1s orbital to the formation of two molecular orbitals. The linear combination of atomic orbitals molecular orbital (LCAO-MO) theory refers to the overlapping of atomic orbitals and the construction of an electronic structure using the Aufbau principle, wherein electrons occupy molecular orbitals from the lowest energy to the highest.<sup>10</sup>

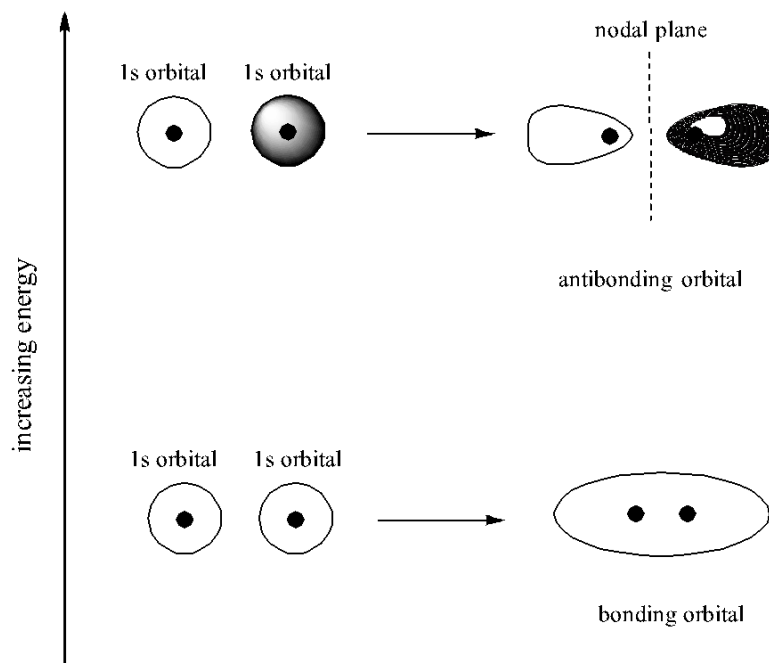


**Figure 1-1.** H<sub>2</sub> molecule represented as a linear combination of atomic orbitals.<sup>11</sup>

Two atoms each contribute a 1s orbital at a precise energy and overlap in two forms, in-phase and out-of-phase. The in-phase overlap of atomic orbitals leads to an increase in electron density between the two nuclei, resulting in a lower energy bonding molecular orbital (Figure 1-1). A destructive overlap between two atomic orbitals causes a decrease in the electron density between the nuclei of the two orbitals, leading to an anti-bonding molecular orbital, the anti-bonding molecular orbital thereof, being higher in energy relative to that of the bonding orbital, as a result of destabilisation. In the case of an additional third atom overlapping with its nearest neighbour and only partially with the next-nearest neighbour leads to the formation of three molecular orbitals: bonding, antibonding and the intermediate nonbonding orbital, all at individual energies. As the number of atoms,  $N$ , added to the solid increase, more molecular orbitals are formed resulting in a finite range of energies that are cumulatively referred to as a band. Where an overlap of both s- and p- atomic orbitals

occur, two bands are formed, referred to as an s-band and a p-band, respectively. The p-orbitals are in a higher energy than that of the s-orbitals thus, the p-band consequently exists in a higher energy than that of the s-band. The energy difference between that of the s-band and the p-band results in a band gap between the two bands. In the absence of a band gap between the s-band and p-band, both bands overlap.<sup>12</sup>

A solid is defined as a metallic conductor if its band is partially occupied at  $T=0$ . A metal where each atom  $N$  contributes one electron to the structure of the solid will have  $N$  electrons and  $N$  molecular orbitals. At  $T=0$ , only  $\frac{1}{2}N$  molecular orbitals are occupied, the highest occupied level thereof, is referred to as the Fermi level,  $E_f$ . Electrical conductivity occurs when an electron is excited into an unoccupied orbital where it becomes mobile. This leaves behind a positive charge in the electron's original position allowing a new electron to enter the vacant space. This continuous mechanism affords the movement of charge throughout the solid.

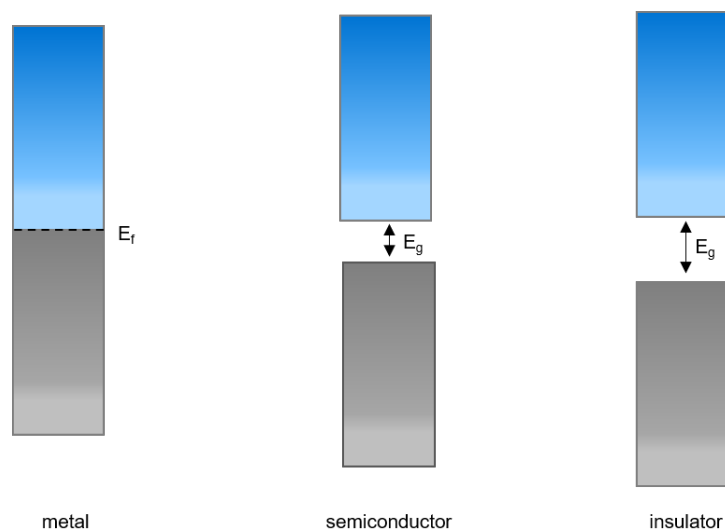


**Figure 1-2.** Schematic showing the differences between a metal, a semiconductor and an insulator, wherein  $E_g$  is the band gap and  $E_f$  is the Fermi level.

A semiconductor is a solid with a complete band at  $T=0$ . An atom,  $N$ , that contributes two electrons to its structure has  $2N$  electrons and  $N$  molecular orbitals. At  $T=0$ ,  $N$  orbitals are filled and there is a gap before the next band begins. In order for the solid to conduct, electrons must be excited from the occupied orbitals of the lower band into the unoccupied orbitals of the upper band. The lower band is known as the valence band and the upper band is referred to as the conduction band.<sup>13</sup>

The size of the energy barrier influences the number of electrons which can occupy the conduction band. The larger the band gap, the more thermal energy required to excite electrons. An insulator is a material in which the gap is too large to afford sufficient occupancy of the conduction band by electrons. In addition to the use of thermal energy in aiding electrons overcome the band gap, stimuli such as photons and electrical stimulation are effective.<sup>14</sup>

As shown in Figure 1-2, the band gap,  $E_g$ , refers to the difference between the top of the valence band and the bottom of the conduction band. In organic molecules, this is referred to as the highest occupied molecular orbital (HOMO) – lowest occupied molecular orbital (LUMO) gap. The band gap defines the difference in energies between the ionisation potential (IP) and the electron affinity (EA) of the material, where the IP corresponds to the HOMO and EA corresponds the LUMO. The band gap can be approximated experimentally using either electrochemical or optical methods.

The electronic structure and consequently, conductivity of OSC materials can be altered through doping (Figure 1-3), thereby allowing the carrier concentration and electrical conductivity of the material to be changed, depending on the desired application of the material. Doping via chemical or electrochemical means causes structural and energetic disorder and refers to the addition (reduction) or extraction (oxidation) of electrons.<sup>15</sup> Adding an electron to the LUMO of the host material creates free electrons and corresponds to n-type doping. In contrast, accepting an electron from the HOMO of the host material provides holes, corresponding to p-type doping. In chemical doping, molecular dopants including acids and bases are typically used over atomic dopants due to a decrease in diffusion.<sup>16-18</sup>

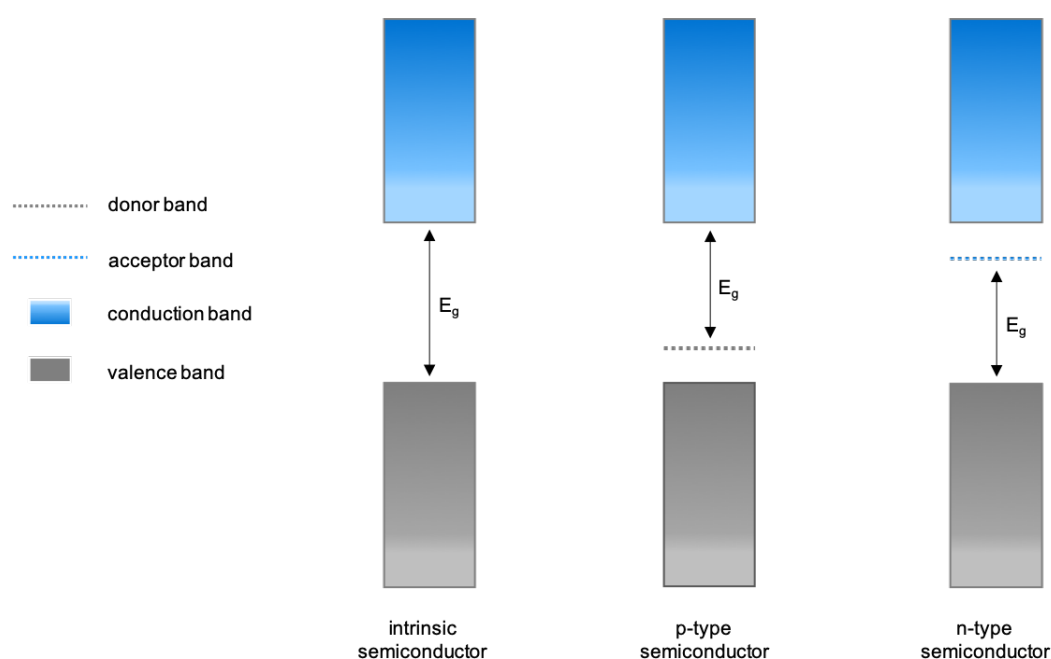


**Figure 1-3.** Schematic representation depicting the effects of doping on the band gap, wherein  $E_g$  is the band gap.

The optical gap,  $E_{opt}$ , refers to the energy required to excite an electron from its ground state to the first excited state wherein the electron-hole remain electrostatically bound. As a result, the values of the electrochemically determined band gap differ from that of the optically determined value, due to the exciton binding energy,  $E_B$ .<sup>19</sup>

## 1.2 The Role of $sp^2$ Hybridised Bonds

The chemical character of a molecule is defined by its electronic structure and its ability to rearrange to form new bonds. Atomic orbitals are capable of hybridising to form new geometries. The electronic structure of carbon (atomic number 6):  $1s^2 2s^2 2p^2$  suggests carbon can form only two bonds. However, due to hybridisation, the s and p atomic orbitals can combine to form  $sp$ ,  $sp^2$  or  $sp^3$  orbitals. The number of groups surrounding the carbon atom determines the number of atomic orbitals that will hybridise.<sup>20</sup>

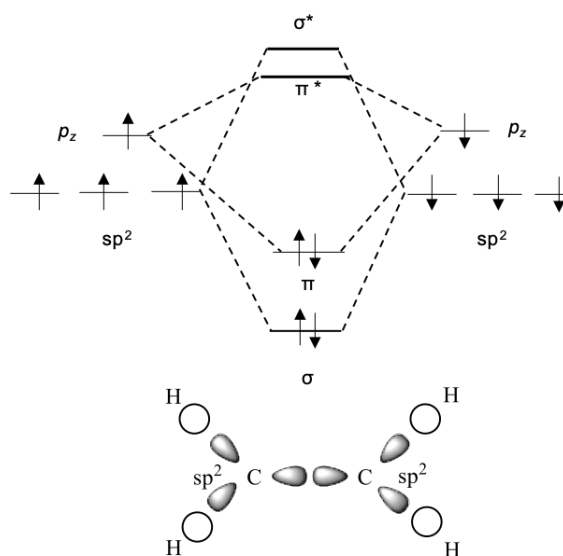


**Figure 1-4.** Molecular orbital diagram of ethene.

As shown in Figure 1-4, the carbon atoms in ethene are said to be  $sp^2$  hybridised, referring to the combination of three atomic orbitals: s,  $p_x$  and  $p_y$ . The remaining  $p_z$  orbital is not involved in the hybridisation process and is said to be unchanged. The  $p_x$  and  $p_y$  orbitals overlap with the 1s orbitals of hydrogen atoms, participating in C-H sigma bonding. The remaining hybridised orbital overlaps with the  $sp^2$  orbital on the adjacent carbon, also forming a sigma bond. The non-hybridised p orbital overlaps the  $p_z$  orbital on the adjacent carbon, forming a  $\pi$ -bond, that is perpendicular to the internuclear axis. The resultant in-phase and out-of-phase molecular orbitals produce the bonding (lower energy) and antibonding (higher energy) orbitals. In the ground state, lower energy molecular orbitals will be filled and higher energy molecular orbitals unfilled. The HOMO is the occupied orbital of highest energy and the LUMO is the lowest energy orbital which remains unoccupied. Transitions between these frontier states are essential in the absorption and creation of energy.<sup>11</sup>

Conjugation in molecules is a sequence of alternating single and double bonds. The conjugation present is indicative that the carbon atoms are  $sp^2$  hybridised.  $\pi$ -bonds in conjugated molecules are not localised as its structure suggests but distributed throughout the system; this is known as delocalisation.<sup>21</sup> The more conjugation a molecule has, the lower the HOMO-LUMO gap.

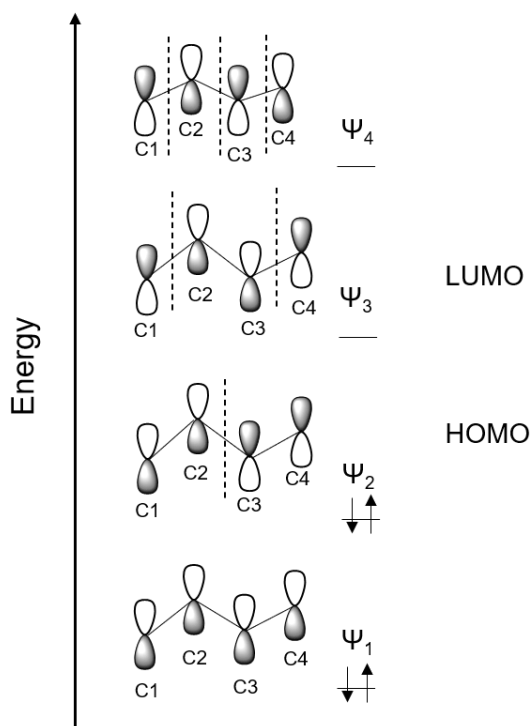


**Figure 1-5.** Energy differences in the molecular orbitals of butadiene.<sup>22</sup>

Butadiene has four electrons in its  $\pi$ -system. In the lowest energy,  $\Psi_1$ , all atomic orbitals are constructively interacting leading to delocalisation throughout the system. In  $\Psi_2$ , there is bonding present between pairs C1-C2 and C3-C4, but not between C2-C3 where a node is present, known as an antibonding interaction.  $\Psi_3$  shows two nodes present between C1-C2 and C3-C4, whereas,  $\Psi_4$  shows three nodes and no bonding interactions between any of the p orbitals. The HOMO is  $\Psi_2$  and the LUMO is  $\Psi_3$ .  $\Psi_4$  is the least stable interaction and the highest in energy (Figure 1-5).

In contrast, ethene has two electrons in its  $\pi$ -system and each of its molecular orbital can hold two electrons, i.e. two electrons in the bonding and two electrons in the antibonding molecular orbital, due to a lower degree of conjugation, ethene has a higher HOMO-LUMO gap.<sup>11</sup>

For a molecule to be aromatic, conjugation is required. Aromaticity affords a molecule increased stability due to the resonance delocalisation of  $\pi$ -electrons. Electron density is sparser due to the resonance delocalisation of  $\pi$ -electrons thereby providing less interelectronic repulsion and decreasing the overall energy of the molecule. Huckel's molecular orbital theory is employed to predict aromaticity and requires that the molecule in question is cyclic, planar, conjugated and possesses a system of  $4n + 2\pi$ -electrons, wherein  $n$  is an integer. In view of Huckel's rule, molecules or ions possessing 2, 6, 10, 14...  $\pi$ -electrons are said to be aromatic.<sup>23</sup>

### 1.3 Organic Semiconductors

OSCs combine the chemical versatility and intrinsic mechanical flexibility of carbon with the electronic properties of semiconductors. Silicon-based semiconducting materials have dominated in the field of semiconductors due to their high-levels of charge mobility. While the goal of OSCs is not to transcend the performance of silicon in device applications, it has broadened the capabilities of semiconducting materials.

Carbon-based semiconducting materials tend to be classified into polymer materials or low molecular weight materials (LMW), such as oligomer materials. LMW provide benefits due to their definite molecular weight, their monodisperse nature as a consequence of well-defined structures and their ability to self-assemble into ordered domains.<sup>24</sup> The electrochemical and optical properties of low-molecular weight molecules have been analysed in order to better understand the electronic properties of their corresponding polydisperse polymer systems, acting as models for understanding charge transport in  $\pi$ -conjugated materials.<sup>25, 26</sup>

While inorganic analogues possess covalent bonds, carbon-based semiconductors have weaker van der Waals interactions present between molecules. The van der Waals interactions provide OSC materials with flexibility and lower melting points, thereby allowing manipulation with minimal energy input.

Silicon's ordered structures include crystalline, polycrystalline, monocrystalline and amorphous forms. While crystalline silicon exhibits high charge mobility within device applications (ca.  $10^3 \text{ cm}^2 \text{ V}^{-1} \text{ s}^{-1}$ ), it requires high levels of purity in order to reach such mobilities.<sup>27</sup> Monocrystalline silicon refers to a continuous crystal of silicon and exhibits high mobility in device applications, however due to the degree of manufacturing required, it is an expensive material. Polycrystalline silicon refers to numerous crystallites of different sizes and orientations, however the numerous crystallites are often subject to two-dimensional defects in the crystal structure, which can inhibit charge-carrier mobility and hence negatively impact device performance. Amorphous silicon is economical to manufacture, however its mobility (ca.  $1 \text{ cm}^2 \text{ V}^{-1} \text{ s}^{-1}$ ) is substantially lower than that of crystalline and monocrystalline analogues.<sup>28</sup>

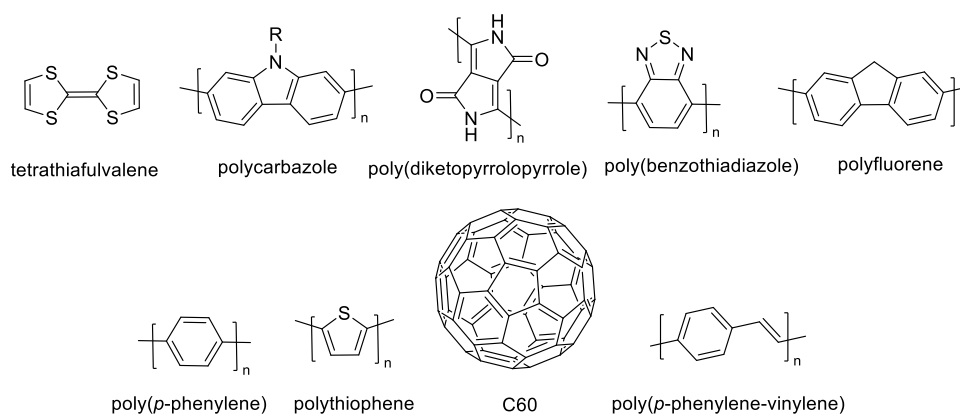


**Figure 1-6.** Chemical structures of well-known organic semiconductor systems.

Consequently, OSC materials such as those depicted in Figure 1-6 have emerged as practical alternatives, providing large-area application through solution-processing achieved through fabrication techniques such as spin-coating and affording lighter weight electronics with a lower cost of fabrication.<sup>29-32</sup>

### **1.3.1 The Role of Molecular Design**

The molecular design of OSC materials can allow control over the properties of the material, the migration of charge within the material and moreover, provide an overall insight into how the material will perform within a device.

Newly developed OSC materials often comprise systematic variations of aromatic conjugated units. The materials thereof are later isolated and investigated in order to probe the structure-property relationships of the newly designed system. In order to understand the design criteria necessary to control the properties of the material, comparative studies between the properties of the new material and that of previously published materials occur. This contributes to advancing electronic devices through an improved understanding of the capabilities of particular materials.

#### **1.3.1.1 Band Gap Engineering**

The electronic properties of a semiconducting material define its application. The frontier molecular orbitals of materials impact charge-carrier transport and the formation and diffusion of bound electron-hole pairs.<sup>33</sup> Therefore, it is imperative to know the characteristics required of the goal application at the early stages of the design process. For instance, if the goal application requires a high mobility of charge in order to attain even satisfactory performance, then the material should be designed

with consideration to favouring charge-carrier migration. It is known that charge-carriers migrate through the semiconducting material and their transport is subject to the effects of intermolecular separation and molecular order.<sup>6</sup> Consequently, factors such as steric interactions from alkyl chains that affect both the molecular arrangement and intermolecular distance need to be considered.<sup>34-37</sup> While alkyl chains provide solubility and lower the cost of the fabrication process, the orientation of the conjugated backbone can be undesirably influenced by the incorporation of alkyl chains to the backbone of molecules.<sup>38, 39</sup>

The frontier molecular orbital energies as well as their distribution along the  $\pi$ -conjugated chain influence a variety of factors for electronic devices, including intramolecular charge transport, intermolecular charge transport, light absorption, light emission, charge injection, charge extraction and charge trapping. Figure 1-7 shows known factors that influence the electronic behaviour in linear  $\pi$ -conjugated materials.<sup>40</sup>

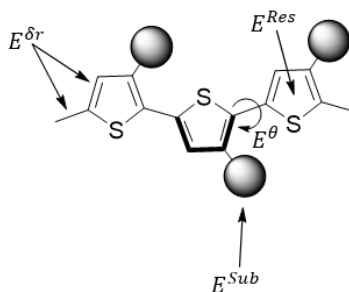


**Figure 1-7.** Factors that influence the electronic behaviour in linear  $\pi$ -conjugated materials.<sup>41</sup>

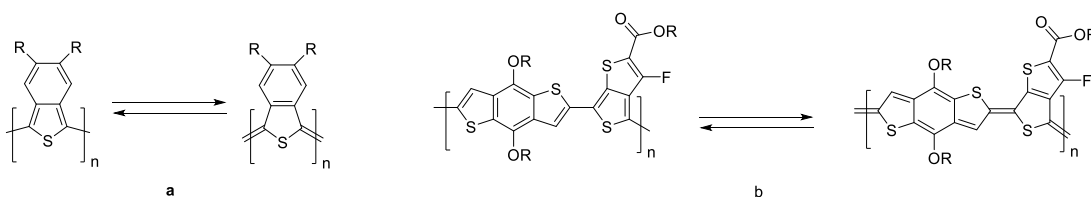
The band gap can be influenced through a plurality of energetic contributions, as shown in Equation 1-1, wherein  $E^{\delta r}$  is the bond length alternation;  $E^{\theta}$  corresponds to

the mean deviation from planarity;  $E^{Res}$  is the aromatic resonance energy;  $E^{Sub}$  refers to the influence of substituent groups, such as electron-donating or electron-withdrawing groups.  $E^{\delta r} + E^{\theta} + E^{Res} + E^{Sub}$  each correspond to intramolecular influences, whereas  $E^{int}$  refers to intermolecular influences. The band gap,  $E_g$ , is influenced by reducing the energetic contribution of one or more of these parameters.

$$E_g = E^{\delta r} + E^{\theta} + E^{Res} + E^{Sub} + E^{int}$$

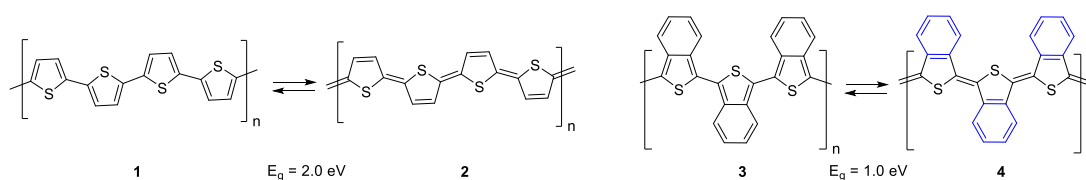
**Equation 1-1.** Contributions to the band gap,  $E_g$ , of polyaromatic linear conjugation systems.<sup>41</sup>

$E^{\delta r}$  – Bond length alternation (BLA) is defined as the average of the difference in the length of adjacent carbon-carbon bonds. Conjugated molecules have two competing resonance forms, one being aromatic and the other quinoidal. As an example, if all the bonds in polyacetylene were the ideally the same length, the band gap would be 0 eV thereby providing metallic conductivity. This is based on the assumption that each carbon bond is subject to the same chemical environment. However, in reality a localisation of single and double bonds occurs, known as Peierls distortion, thereby resulting in an increase of the band gap.<sup>42</sup> A manner in which to minimise the effect BLA has on the band gap is to use systems that have aromatic rings in their quinoidal form, thereby favouring delocalisation. As is shown in Scheme 1-1, both poly(isothianaphthene) and PTB7 comprise aromatic rings when in their quinoidal forms.



**Scheme 1-1.** An approach to reducing the  $E_g$  through the system containing a fused aromatic ring when the polymer is in its quinoidal form, wherein (a) is poly(isothianaphthene) and (b) is PTB7.<sup>43</sup>

$E^{Res}$  – The difference in energy between the quinoidal and aromatic forms is known as the resonance energy.  $\pi$ -Electrons have a tendency to confine to the aromatic rings rather than delocalise over the entire conjugated system. The degree of long-range delocalisation can be increased through reducing the aromaticity in the system and increasing the quinoidal character of the system.<sup>44</sup> As depicted in Scheme 1-2, polythiophene has aromatic character in **1**, however loses its aromatic character as a result of disruption from the quinoid form **2**. Polyisothianaphthene (PITN) **3**, **4** is formed through fusing a benzene ring to the thiophene units of polythiophene. In PITN, the quinoid resonance contributor is able to improve the electronic distribution in the molecule as a consequence of benzene having a higher aromatic resonance energy. This results in the decreased band gap of 1.1 eV for the PITN system *vis-à-vis* a band-gap of 2.0 eV for polythiophene.<sup>45, 46</sup>



**Scheme 1-2.** The influence of fused aromatic rings in promoting the quinoidal character in thiophene-based polymers.<sup>47</sup>

$E^\theta$  – Increasing the dihedral angle between adjacent orbitals interrupts the conjugation along the backbone of the molecule, thereby causing an increase in the band gap. An increase in the dihedral angle may occur along C-C single bonds as a result of steric hinderance, e.g. through  $sp^3$  hybridised heteroatoms or twisted

molecular structures.<sup>48</sup> A known approach in reducing the dihedral angle comprises the use of spacer groups that inhibit torsional twisting of the ring systems, alternatively fusing ring systems also inhibits torsional twisting. An example of the effects spacer groups have on reducing dihedral angles present in systems can be observed in the comparison of biphenyl and fluorene (Figure 1-8). Fluorene comprises two phenyl units that are forced into planarity by a methylene bridge. Comparatively, biphenyl comprises two phenyl units linked through a C-C bond. Both systems comprise similar moieties, yet the mode in which the biphenyl rings are connected causes a variation in the torsion angle present between the planes of the two biphenyl rings.<sup>49</sup>

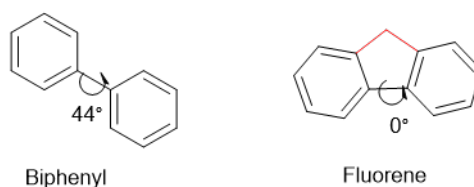


**Figure 1-8.** Comparison of the dihedral angles between phenyl units in biphenyl and fluorene.<sup>50</sup>

$E^{Sub}$  - The electronic properties of introduced substituents can influence the frontier orbitals of a  $\pi$ -conjugated system. The incorporation of electron-withdrawing substituents, e.g. fluorine or carbonyl groups can stabilise of the LUMO and reduce the reduction potential of the system. Comparatively, the introduction of electron-donating substituents results in donated electron density to the system, thereby increasing the energy-levels of the HOMO and decreasing the solid-state ionisation potential. This can be achieved either mesomerically, i.e. through lone-pair donation or inductively, i.e. through alkyl chains.<sup>41, 51</sup> Known electron-donating substituents include nitrogen, oxygen and sulfur. The position and quantity of substituents added to a system can directly affect the conformation of the  $\pi$ -conjugated system and

furthermore, decrease the solubility of the system. Consequently, the number of substituents added to a system and furthermore, the locations thereof, must be strategic.<sup>52</sup>

$E^{Int}$ - Intermolecular interactions comprise non-covalent heteroatom interactions, dipole-dipole forces, hydrogen bonding and  $\pi$ - $\pi$  stacking. In the condensed state, the degree of intermolecular interactions present can affect band-gap of a system. A presence of strong intermolecular interactions can contribute to an improved orbital overlap between adjacent molecules, formed through close-contacts and thereby can facilitate in stabilising the band-gap.<sup>53</sup>

The energy terms represent a fundamental correlation between chemical structure and the band-gap. Furthermore, the correlation between band-gap and device performance is known.<sup>54, 55</sup> In view of these facts, it is imperative to strategically design OSC materials with respect to the band-gap characteristics sought. As most of the aforementioned energy terms present their own drawbacks, it is reasonable to consider the synergistic effect of addressing the energy terms collectively, as opposed to addressing specific energy terms in isolation.

### **1.3.1.2 Controlling Structure-Transport Properties**

Controlling the orientation of anisotropic systems is important to the performance of the material within device application. This is due to the physical properties of OSC materials being influenced by the orientation of the  $\pi$ -conjugated backbone and the manner in which orientation of the  $\pi$ -conjugated backbone can influence charge-carrier mobility.  $\pi$ -Conjugated materials that demonstrate high charge-carrier mobilities are important to the development of efficient organic electronic devices.

While a variety of aspects govern the performance of OSC materials within electronic devices, molecular packing and long-range order are known to be a contributing factor.<sup>56, 57</sup>

As a consequence of intramolecular electronic coupling being larger than that of intermolecular electronic coupling, charge transport travels more effectively through the  $\pi$ -conjugated backbone of a material and the  $\pi$ - $\pi$  stacking direction via interchain electronic orbital overlap. Contributors to a decrease in intermolecular charge-carrier mobility include the presence of structural defects such as polydispersity and poor molecular packing, both of which can contribute to the trapping of charge-carriers, thereby limiting mobility.<sup>58</sup> While film fabrication techniques such as temperature annealing have been used to enhance molecular order in films, the molecular orientation of systems relative to the substrate can be a dominant factor in limiting charge-carrier mobility.<sup>59, 60</sup>

Poly(3-hexylthiophene) (P3HT) is known for its application in OPVs due to its high absorption coefficient in the visible region. The performance of P3HT in device is dependent on the way in which the material orientates relative to the substrate.<sup>61</sup> As shown in Figure 1-9, P3HT in the edge-on orientation, both the conjugated backbone and the  $\pi$ -stacking direction lays parallel to the surface of the substrate. Due to the architecture of field-effect transistors, the edge-on orientation is more favourable for optimal device performance due to in-plane charge transport. An edge-on orientation would negatively impact the efficiency of an OPV due to a limitation of the absorption of incident light and a lack of charge transport along the thickness of the photovoltaic cell.<sup>62</sup>

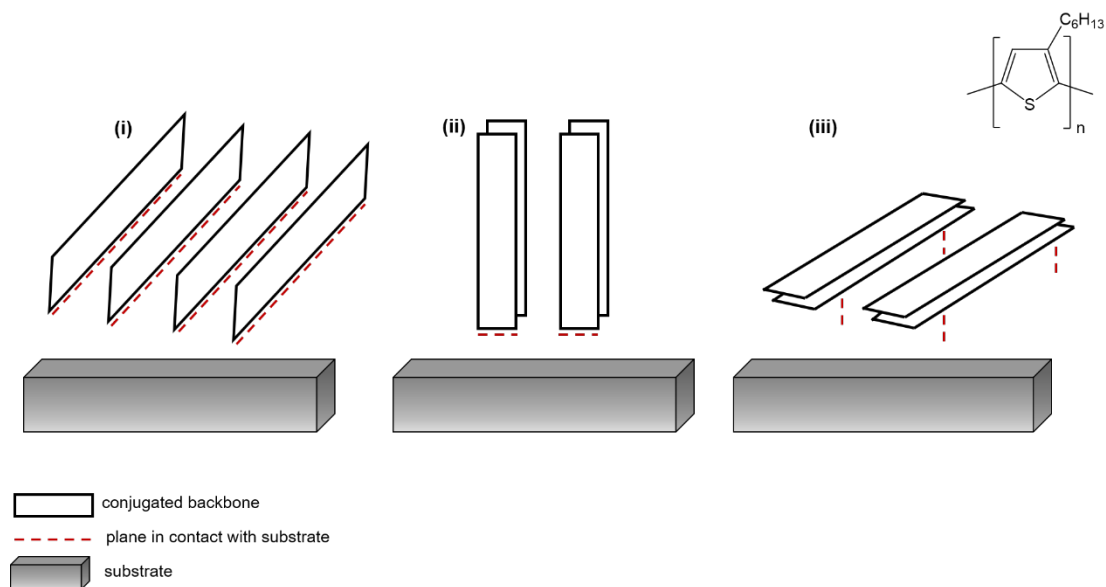


**Figure 1-9.** The different orientations of P3HT on a substrate: (i) edge-on; (ii) end-on; (iii) face-on.<sup>63</sup>

Both end-on orientations and face-on orientations are more applicable to device architectures such as photovoltaic cells and light-emitting diodes. In the end-on orientation, the conjugated backbone lies perpendicular to the surface of the substrate and the  $\pi$ -stacking direction occurs parallel to the substrate surface. The face-on orientation allows the conjugated backbone lays parallel to the surface of the substrate and the  $\pi$ -stacking direction occurs perpendicular to the substrate surface.<sup>64</sup>

The mobilities of charge-carriers are higher in single crystal materials than in polycrystalline materials, as has been shown by single crystal materials such as pentacene and rubrene when compared to their corresponding polycrystalline forms. The single crystal model implies the use of physical processes to increase the order in the backbone of the material, thereby allowing the properties of a material to resemble a single crystal.<sup>65</sup>

Due to the dependency of the device performance on the molecular organisation of their OSC materials, alternative solutions have been sought to control the organisation

of molecular system. One approach to achieving isotropic electronic properties in OSC systems is to develop organic semiconductors with increasing dimensionality.<sup>66</sup>

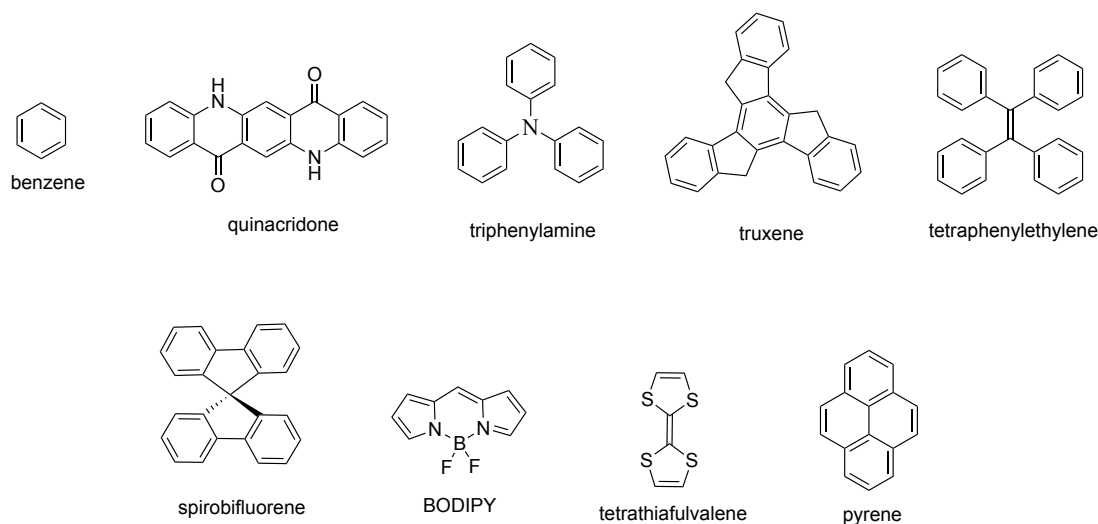


**Figure 1-10.** Commonly used core building blocks for introducing increased dimensionality to organic systems.

$\pi$ -Conjugated systems of 1D character demonstrate anisotropic properties due to conjugation extending along the backbone of the system and charge migrating within one dimension. Increasing the dimensions of molecular systems has been explored in order to easier control the self-organisation of molecules without influencing the device fabrication process. Known techniques for increasing the dimensionality of molecular systems, include utilising a central core (Figure 1-10) and extending the conjugation from the core through directly attaching multiple conjugated chains.

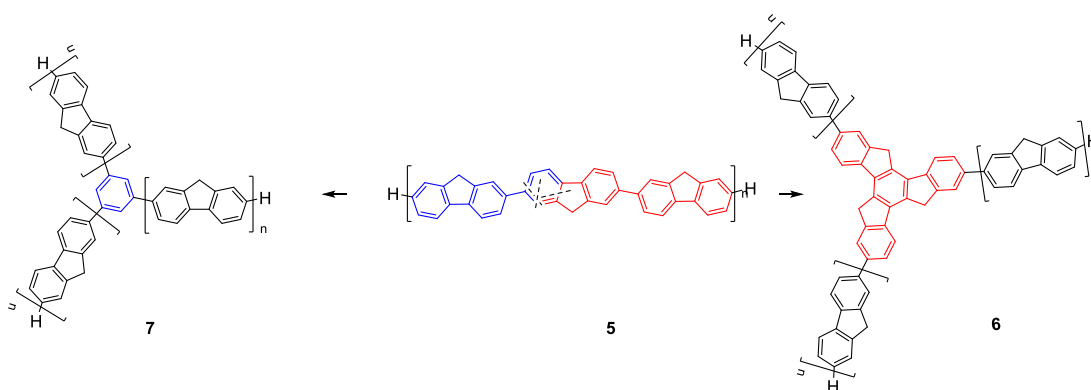
Planarity is desirable in the design of  $\pi$ -conjugated systems as it can contribute to an increase in  $\pi$ - $\pi$  overlap between adjacent molecules in the solid-state, thereby enhancing the mobility of charge carriers. Consequently, cores that provide dimensionality and a degree of planarity are preferred.<sup>67</sup>

OSC materials of 3D character do not provide the same degree of  $\pi$ - $\pi$  stacking interactions as systems with a decrease in dimensionality, however they are beneficial to increasing the degree of isotropic behaviour in systems. Three-dimensional systems constitute ‘Onsager crosses’ and hence enhanced solubility, proving advantageous in chemical purification and film deposition from solution. Furthermore, the Onsager crosses also provide a resistance to crystallinity *vis-à-vis* systems of a similar molecular weight with a linear configuration. A benefit of systems comprising Onsager crosses, is that fewer alkyl chains are required in order to achieve solubility, thereby decreasing the effective molecular weight.<sup>68</sup>

Known multi-dimensional architectures include star-shaped systems wherein each system comprises a central core directly attached to three or more conjugated spores, also termed ‘arms’. The core of the system can be defined by a single atom or multiple fused aromatic units. The cores of star-shaped systems typically introduce 2D or 3D character dependent on the degree of planarity afforded by the core.

The symmetry of star-shaped systems is defined by the core, wherein the system is a sub-group of the symmetry of the core. When a conjugated oligomer chain comprises a rotational symmetry operation with an order greater than two, i.e. wherein  $C_n$  is  $n \geq 3$ , applying this symmetry operation to the entire molecule results in the construction of the analogous star-shaped system. For instance, applying the  $C_3$  or  $C_6$  symmetry operation of oligo-*p*-phenylene to a benzene moiety in an oligo-*p*-phenylene chain results in a star-shaped system with three or six arms. In the instance that only part of the oligomer chain comprises a rotational symmetry operation, applying the symmetry operation generates a star-shaped system and additionally, a new core. Scheme 1-3

shows applying a C<sub>3</sub> symmetry operation to the oligofluorene (**5**), results in two systems, either with truxene (**6**) or with benzene (**7**). The resultant system being dependent on the aspect of the oligomer subjected to the symmetry operation. Rotational symmetry of a molecule with an order above 2, i.e. e.g. wherein C<sub>n</sub> is  $n \geq 3$  results in electronic changes, including degeneracy of HOMO and LUMO levels. The degeneracy of frontier molecular orbitals thereof, being exploitable in electronic materials application.



**Scheme 1-3.** Constructing star-shaped systems through axial symmetry operations.<sup>69</sup>

The term ‘spiro-concept’ refers to synthetically linking two or more  $\pi$ -conjugated systems through a common  $sp^3$  hybridised atom.<sup>70</sup> The two or more  $\pi$ -conjugated systems can be identical or unidentical, forming a perpendicular arrangement of two molecular halves. It has been reported that spiro-compounds when compared to their parent compounds comprising one half of the spiro compound, exhibit an increase in the glass transition temperature. The glass transition temperature,  $T_g$ , is a physical parameter that can be used to indicate the stability of a material. When an amorphous material is heated above the glass transition temperature, molecular motion increases

thereby providing a crystalline state, which is devoid of grain boundaries and easier to achieve than single crystal growth.<sup>71,72</sup>

In view of the above, the benefits of increasing the isotropic character of OSC systems are realised.

### **1.3.1.3 Chemical Building Blocks**

The synthesis of complex target molecules can require many synthetic transformations, thereby reducing the yield of the product and the efficiency of the overall synthetic strategy. Building blocks have been known to simplify the molecular construction of complex systems by allowing the incorporation of required functional groups building, the necessary oxidation states and the essential stereochemistry, thereby allowing target structure to be developed in a controlled manner. As a result, building blocks are of significance in accelerating the discovery of novel OSC materials.

An ideal building block is chemically versatile and caters to a large degree of structural variation. Building blocks have typically been used in customised iterative synthesis, wherein multiple building blocks are conjoined through a series of repeated chemical transformations. The customised iterative synthesis approach typically differs in the type of bond used to connect the multiple building blocks and the reactions used to form the connection, which is usually determined by the functional groups present. The customised iterative approach allows the functions of a simple building block to be changed or improved.<sup>73</sup>

Two approaches are often used in the customized iterative assembly approach, divergent and convergent. The convergent method comprises the separate synthesis of key moieties of a target system prior to conjoining the separate moieties to form the target system. The divergent method comprises developing several compounds using the same reaction, thereby creating a series of systems, before subjecting the series of systems to a new synthetic transformation in order to develop a different series of systems. A convergent strategy typically has a limited scope of targets, whereas a divergent approach often requires more synthetic steps.

Building blocks typically constitute small molecules because these low molecular weight systems tend to be highly structurally diverse. Building blocks comprising heteroatoms are typically used in OSC materials as a result of their ability to form ordered molecular arrangements. The use of heteroatoms such as sulfur have been known to result in intermolecular S $\cdots$ S interactions in the solid-state, thus forming contributing to closer molecular contact (Figure 1-11). It is suggested that the strong intermolecular interactions afforded by sulfur occur as a result of the element's large atomic radius. Furthermore, it is suggested that the high electron density present around sulfur results in an improved overlap between the HOMOs of adjacent molecules in the solid-state.<sup>74, 75</sup>

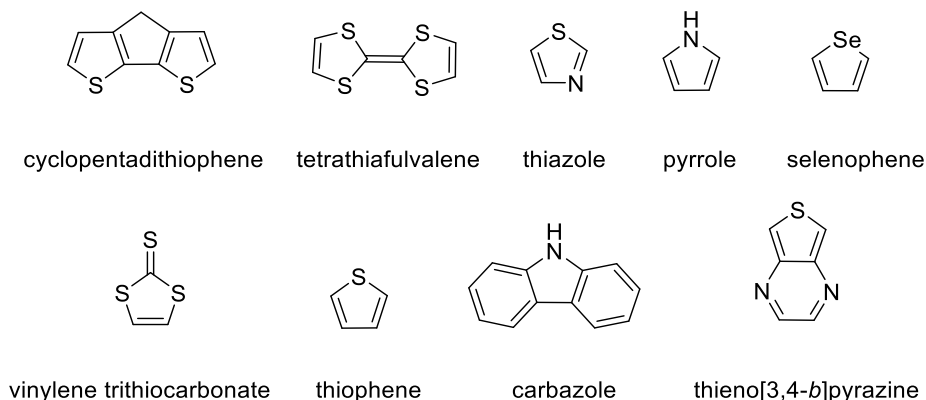


**Figure 1-11.** Typically used heterocyclic building blocks for organic semiconductor materials.

Thiophene-based oligomeric systems represent building blocks for numerous organic semiconducting materials.<sup>76-78</sup> The synthetic reproducibility of thiophene benefits the stability of thiophene-based materials within devices. Furthermore, due to their planar nature, they can form long-range ordering in the solid-state, contributing to efficient charge-carrier mobility.<sup>79</sup> High thermal stabilities for thiophene-based materials and low molecular weights make these moieties beneficial in device fabrication.<sup>80</sup> Thiophene is structurally versatile and can be modified in the sulfur position or more commonly, in the  $\alpha$ - and  $\beta$ - positions (Figure 1-12). Modification at the  $\alpha$ - positions is facile and can provide extension of the  $\pi$ -conjugated backbone and alkyl chains can be incorporated to provide solubility of the material at the  $\alpha$ - or  $\beta$ - positions.<sup>81</sup> The sulfur atom present in thiophene provides inherent polarizability that contributes to electron-donating properties. Furthermore, the sulfur atom allows a greater degree of intermolecular interactions thereby contributing to a desirable morphology for efficient charge transport.<sup>82</sup>

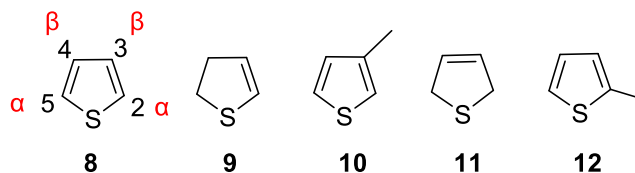


**Figure 1-12.** The numbering in thiophene systems and known thiophene derivatives: thiophene (**8**); 2,3-dihydrothiophene (**9**); 3-thienyl (**10**); 2,5-dihydrothiophene (**11**) and 2-thienyl (**12**).

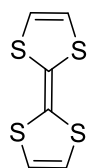
Aside from being used to form conjugated chains, thiophene derivatives can be used for core construction of multidimensional systems, wherein the thiophene derivatives provide a means to incorporating multiple conjugated spores along multiple planes.<sup>83</sup>

The use of building blocks can be complex, particularly when factoring in the reactivity of some structures versus site-specific functionalisation required for the assembly of the target system. In order to achieve site-specific functionalisation, protection groups are typically exploited thereby purposefully blocking a reactive site of the molecule and promoting a chemoselective transformation.<sup>84</sup> The ‘masking and deprotection’ strategy is used in iterative assembly methods to temporarily block a reactive site of the molecule for one chemical transformation, before removing the protection group before the consecutive reaction.<sup>85</sup> Contemplating synthetic approaches for the development of OSC materials require consideration of the choice of building block that constitute the  $\pi$ -backbone. It is important to consider how factors such as the planarity, molecular arrangement and length of the ultimate  $\pi$ -backbone may affect the morphology of the material with respect to structure-property relationships of the material within its ultimate application.

Tetrathiafulvalene (TTF) is a  $\pi$ -electron donor known for its role as a molecular building block in electroactive materials in a diverse range of applications.<sup>86</sup> Interest

in TTF chemistry increased after the discovery of charge transfer complexes, such as the donor–acceptor complex comprising TTF and tetracyano-*p*-quinodimethane (TCNQ) which demonstrated metallic conductivity.<sup>87</sup> Further interest in TTF has focused on mixed valence state materials.<sup>88</sup> Bis(ethylenedithio)tetrathiafulvalene (BEDT-TTF) based mixed valence states have demonstrated multi-dimensional stacking interactions as a consequence of S⋯S non-covalent bonding, affording a record transition temperature for ambient pressure TTF-based superconductors.<sup>89</sup>

Conjugation in a TTF derivatives can be extended through the 1,3-dithiole rings, providing the system increased dimensionality. Additionally, the sulfur-rich character of TTF derivatives contributes to increased intermolecular interactions in the solid-state, thereby aiding the system's ability to self-assemble. Further work that has surrounded the development of exploiting intermolecular interactions.<sup>90,91</sup>



**TTF**

**Scheme 1-4.** Structure of TTF.<sup>92</sup>

The preparation of TTF and its oxidation to form a radical cation has previously been reported.<sup>93</sup> TTF is non-aromatic with 14  $\pi$ -electron system that readily undergoes a one-electron oxidation to form the cationic species and readily undergoes a further one-electron oxidation to form the dication species. Both dithiolium rings possess aromatic character and results in a structure wherein delocalisation is interrupted between the two dithiolium rings (Scheme 1-4).<sup>94</sup> Each sequential oxidation is

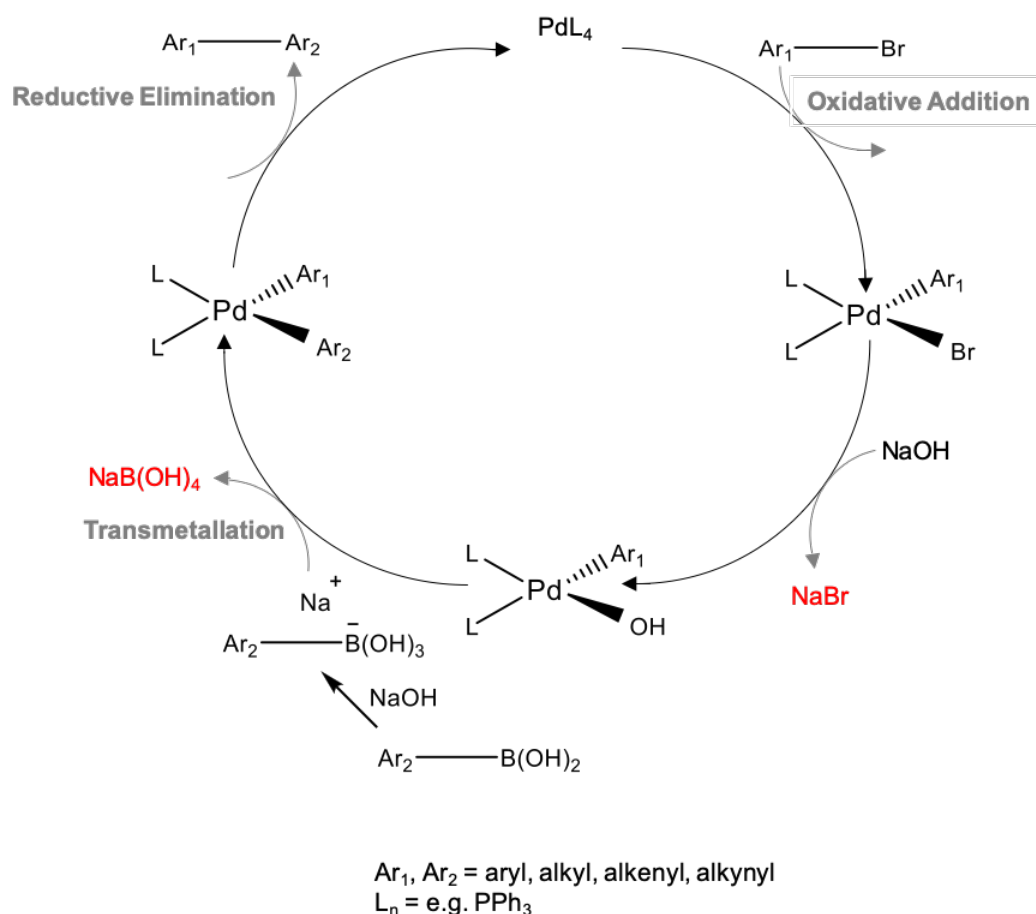
reversible, indicating stability of both the cationic and dicationic species and affords itself to applications where an electron-donating capacity is required.<sup>95</sup>

This increased stability concomitant with the formation of the oxidised species makes the TTF system a desirable electroactive unit. Neutral TTF molecules possess  $C_{2v}$  symmetry, however in the cation and dication states  $D_{2h}$  and  $D_2$  symmetry are formed, respectively. The radical cation state of TTF therefore has a planar structure encouraging intermolecular stacking interactions and facilitating charge transport within devices.<sup>96</sup>

Transition metal-catalysed reactions have emerged as important reactions in the synthesis of OSC materials, owing to their use in cross-coupling reactions where they aid in allowing complex molecular systems to be developed from readily available starting materials. In particular, palladium cross-catalysed reactions have proven effective in the creation of carbon-carbon (C-C) bonds between aryl groups, which is beneficial in linking aryl building blocks in order to develop  $\pi$ -conjugated backbones. The Suzuki-Miyaura coupling has been hailed for its reliability and mild reaction conditions of a less toxic nature, thereby providing an advantageous processing conditions in the development of new OSC materials.<sup>97</sup>

#### **1.3.1.4 Suzuki-Miyaura Coupling**

The awarding of the Nobel Prize in 2010 to Heck, Negishi and Suzuki highlight the essential nature of palladium catalysed cross-coupling reactions, particularly in last few decades.<sup>98-100</sup>

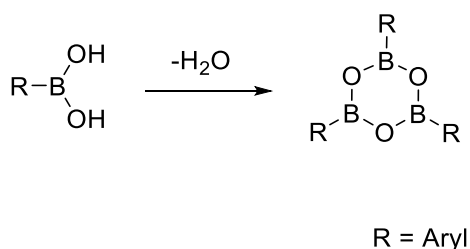


**Scheme 1-5.** The proposed catalytic cycle in the Suzuki coupling.<sup>101</sup>

The Suzuki reaction employs readily available substrates and tolerates a selection of functional groups. The boronic acids employed in the reaction are stable to heat and water, thereby proving reliable in the reaction. Owing to the tolerance for a variety of functional groups, numerous materials have been synthesised using palladium-catalysed cross-coupling reactions using organotins (Stille coupling)<sup>102</sup> or organoborons (Suzuki coupling).<sup>103</sup> Transition metals have typically been used as catalysts in cross-coupling mechanisms and have provided a diverse class of novel oligomeric and polymeric semiconducting materials. Most mechanisms for the transition metal catalysed reactions are not established yet, but serve as models for

working hypotheses based on electron count and oxidation states. The Suzuki coupling has its advantages in that the reagents used are less toxic and the boronic acids used are commercially available.<sup>104</sup>

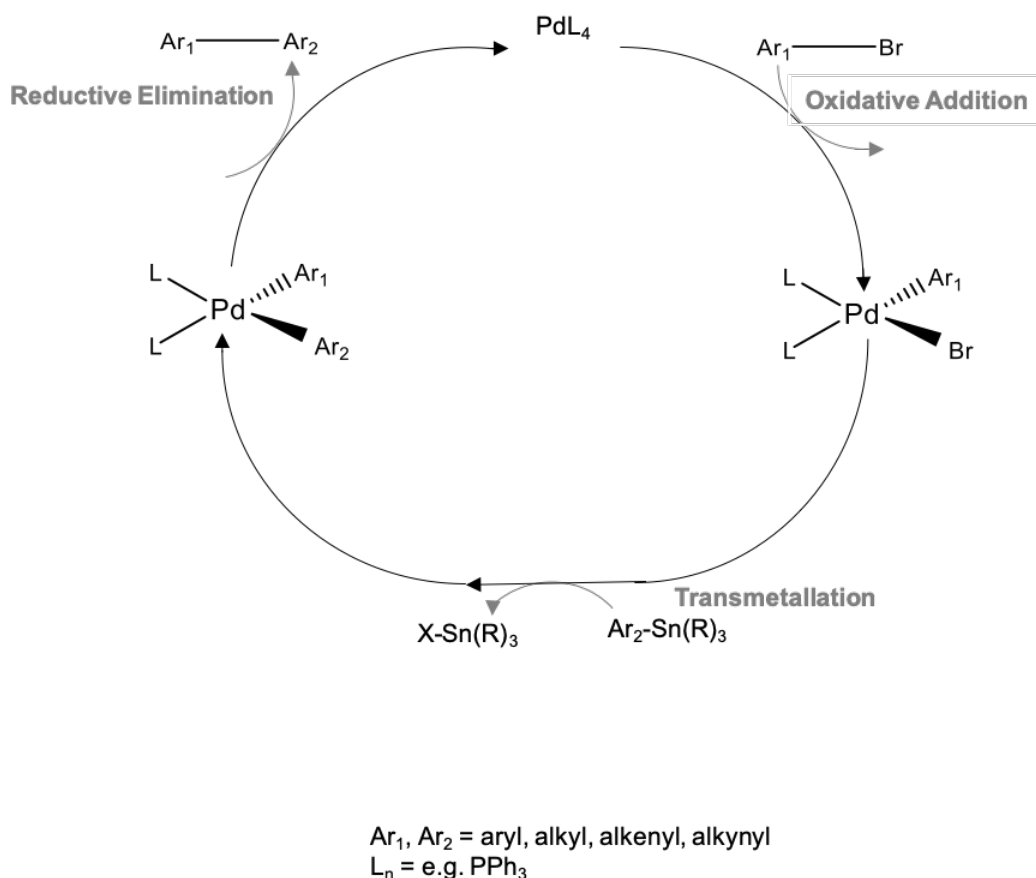
In Scheme 1-5, the proposed mechanism shows that the formation of C-C bonds occurs through the reaction of arylboronic acid with aryl halide in the presence of bases. The Suzuki coupling allows a diverse range of materials to be used including, alkyl, alkenyl and alkynyl halides.<sup>105-107</sup> The oxidative addition of Pd(0) occurs using the aryl halide and is considered to be the rate-determining step. The reactivity of aryl halides is generally improved when the halide is iodide or bromide, rather than chloride. A boronic ester rather than a boronic acid is permissible in the reaction, furthermore, boronic acids are known to interchangeably form boroxines upon dehydration (Scheme 1-6). It is proposed that the base activates the organoboron reagent and facilitates the movement of the organic group from the boron to the palladium.<sup>108, 109</sup>



**Scheme 1-6.** The formation of boroxines from boronic acid via condensation.<sup>110</sup>

In the strategy for preparing oligofluorenes using the Suzuki methodology, trimethylsilyl groups have previously been used to control regioselectivity and protect against polymerisation.<sup>111, 112</sup>

The Suzuki coupling is often compared to the Stille coupling, due to the similarities in synthetic transformation (Scheme 1-7). However, the Stille reaction has drawbacks related to the toxicity of organotin reagents and furthermore, the low polarity of tin compounds reduce their solubility in water.<sup>113</sup> Organotin reagents however, possess good functional group tolerance. In the Stille reaction, a palladium catalysed cross-coupling reaction occurs between aryl or alkenyl halides with aryl, alkenyl or alkynyl tin compounds.



**Scheme 1-7.** The proposed mechanism for the Stille cross-coupling.<sup>114</sup>

The Negishi coupling while also demonstrating similar transformations to the Suzuki coupling, has been reported to produce lower yields; is sensitive to the presence of oxygen and water.<sup>115, 116</sup> Furthermore, the substrate used has a lower tolerance for functional groups. The Negishi, Stille and Suzuki couplings are widely used in aryl and heteroaryl synthesis, however, in view of the low yields produced from the Negishi reaction, the Suzuki and Stille reactions are preferred in large scale synthesis.

#### 1.4 Optical Processes of Organic Semiconductors

In a molecular system, electrons can be optically excited resulting in an electronic transition from the valence band to the conduction band. The energy required to excite an electron from the valence band to the conduction band depends on the band gap of the material. For OSC materials, typically, the energy required to overcome the band gap lies in the ultraviolet-visible (UV-Vis) region. However, in low band gap materials, the transition may be overcome using light near infrared light (NIR) region.

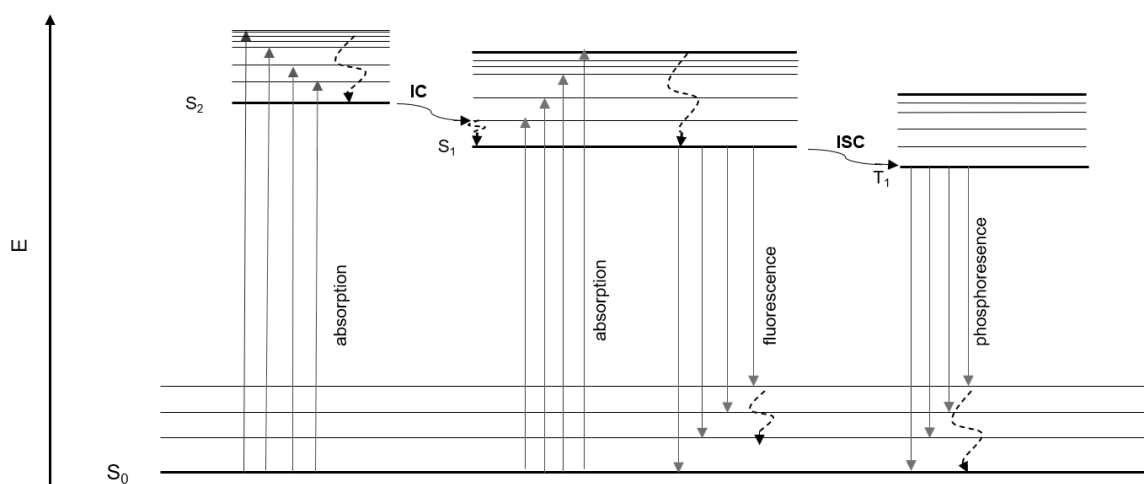


**Figure 1-13.** Jablonski diagram illustrating electronic states and the transitions between them.<sup>117</sup>

In optical excitation, an electron may be excited to a singlet state wherein one electron resides in the antibonding  $\pi^*$  orbital and another electron remains in the bonding  $\pi$  orbital, the electrons thereof being in anti-parallel spin relative to each other. Alternatively, a triplet state can occur upon excitation wherein one electron resides in the antibonding  $\pi^*$  orbital and the other electron remains in the bonding  $\pi$  orbital, both electrons thereof being in parallel spins relative to each other.<sup>118</sup> A molecule is said to be in its ground state when it is in the lowest electronic level, known as  $S_0$  (Figure 1-4).

As shown in Figure 1-13 the Jablonski diagram represents the electronic states of molecules and shows radiative and non-radiative processes that occur upon the absorption of photons, resulting in the formation of an excited state. At room temperature, a molecule will reside in the ground state and upon the absorption of photons (represented by vertical arrows orientated upwards) with a wavelength of energy equal to or in excess of the band gap, a molecule becomes excited and electrons are promoted to a vibrational level of an excited singlet state  $S_n$ , wherein  $n$  is an integer ( $n = 1, 2, 3 \dots$ ). The lifetime of the singlet excited states is in the order of  $10^{-15}$  seconds before the excited molecule collides with surrounding molecules leading to vibrational relaxation.

Vibrational relaxation (represented by the dashed-curly arrows in Figure 1-13) causes a loss of energy through the conversion of excitation energy to kinetic energy and results in the molecule returning to the lowest vibrational energy in its excited state. Both the processes of absorption and vibrational relaxation occur very fast and hence cannot be observed individually. When there is a sufficient energetic overlap between

electronic levels of different energies, vibrational relaxation can also occur between different electronic levels. The phenomenon of vibrational relaxation occurring between different electronic levels is known as internal conversion (IC) and most commonly occurs between higher energy singlet states, e.g.  $S_2$  or  $S_3$ . In higher energy electronic levels, the energies are closer spaced together and hence there is more likely to be sufficient energetic overlap.

Following the relaxation to the lowest vibrational state of the electronic energy level, the excited molecule can return to any of the vibrational levels of the electronic ground state without a change in multiplicity. This occurs through the radiative process of fluorescence (represented by vertical arrows orientated downwards in Figure 1-13). This process typically occurs slower than vibrational relaxation. The fluorescence process is as an allowed radiative process and the radiative energy released equates to that of the energy transition. Fluorescence can occur between various vibrational levels of the singlet ground and singlet excited states and hence, is observed over different wavelengths, leading to the observation of broadband absorption and broadband emission spectra. As the energy of fluorescence is lower than that of the absorption due to the loss of energy during the vibrational relaxation processes, fluorescence appears at longer wavelengths than absorption. The separation between the absorption band and the fluorescence band is typically known as Stokes shift.

An alternative process that can occur after the absorption of a photon involves a spin forbidden non-radiative transition between two states of different multiplicity, known as intersystem crossing (ISC). In ISC, electrons residing in the singlet excited state of the molecule undergo vibrational relaxation to the lowest vibrational energy of the

triplet excited state. A non-radiative transition to the ground state is spin-forbidden, however due to the ISC which has occurred, the triplet state is able to emit radiation weakly; this decay is known as phosphorescence. Due to the longer half-life of phosphorescence, emission occurs for longer periods of time than fluorescence ( $10^{-4}$  –  $10^{-1}$  s).<sup>119</sup> Decay through other processes including intermolecular collisions, formation of excimers or energy transfer to other molecules can also occur.<sup>120</sup>

The Frank-Condon principle describes the vibrational structure in the electronic spectrum of a molecule. The vertical electronic transitions observed in the Jablonski diagram are in accordance with the Franck-Condon principle that states that the process of excitation occurs without changes to the position of the nuclei or its surrounding environment. After excitation, the nuclei responds to a change in the force field as a result of the displacement of electron density, leading to a larger separation in internuclear distance. As the transitions are vertical, the extent of overlap between vibrational wavefunctions can be estimated using potential energy curves, allowing the intensity of vibrational transitions between both electronic states to be estimated.<sup>121</sup>

The macroscopic properties of OSC materials do not always correlate with the properties of isolated single molecules. This phenomenon occurs as a result of molecular packing in the solid-state. Luminophores may emit light in variety of physical forms including solid, gas and liquid. For practical applications, luminophores tend to be exploited in their solid-state for use in film. In the solid-state, luminophores tend to exhibit emission quenching, at least partially or completely, as a result of intermolecular  $\pi$ - $\pi$  stacking interactions; the phenomenon is known as aggregation-caused quenching (ACQ).<sup>122, 123</sup> The aggregation of molecules in the

solid-state causes excited states to decay through non-radiative paths, thereby causing a loss of emission. In order not to diminish the performance of luminescent materials in device, it is important to find an interplay between reducing the effects of ACQ without jeopardising the other useful properties of the luminophores.

The architecture of planar  $\pi$ -conjugated systems which are known to facilitate  $\pi$ - $\pi$  stacking and benefit properties such as charge transport, can be detrimental to optical properties of emissive materials. Strategies use to inhibit the aggregation caused quenching effect comprise decreasing the crystalline character of materials through introducing amorphous regions in the system, incorporating long alkyl chains in order to alter the arrangement of the conjugated backbone and inhibiting triplet formation.<sup>124,</sup>

125

Controlling the structural arrangement of molecules in the solid-state is imperative to ensuring the same physical properties observed for isolated molecules are observed for molecules in the bulk.

## 1.5 Organic Sensors

In the last two decades, sensors based on organic devices have emerged.<sup>126</sup> The primary purpose of sensing technology was to acquire an improved understanding of surrounding environments and relay the acquired data accordingly. In the last two decades, there has been a demand for more environmental monitoring in particular, related to the toxicity of gases and food quality monitoring.<sup>127</sup> However, the detection and identification of external stimuli is useful even in a variety of technological areas and day-to-day life, for instance as gas sensors within the home.<sup>128</sup> Sensors based on

$\pi$ -conjugated systems can have tailored selectivity, incorporate flexibility into the device and be fabricated at lower cost.

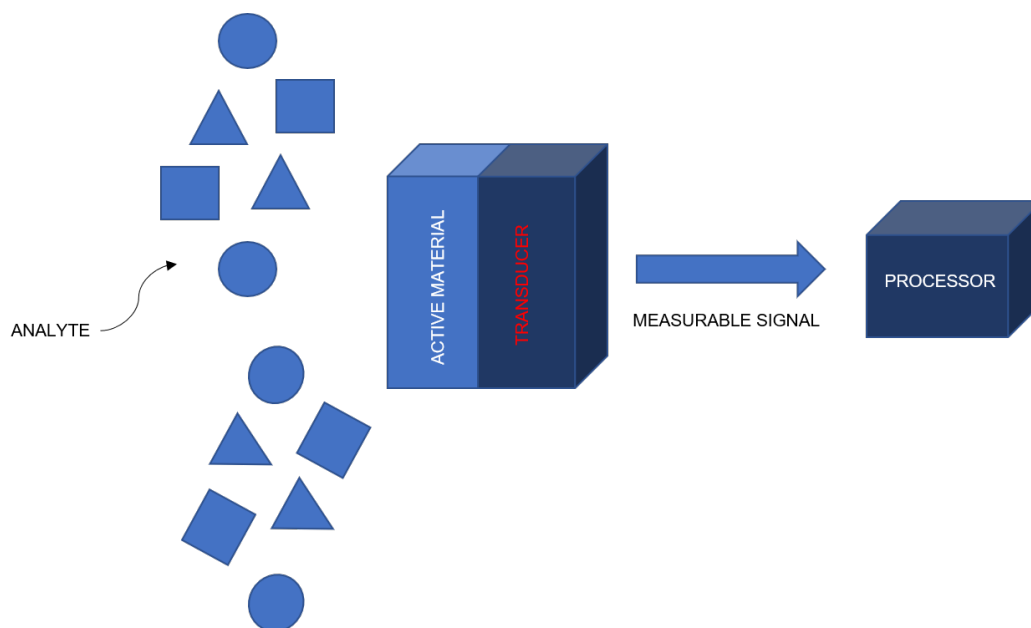


**Figure 1-14.** Schematic of the essential components of a sensing device.

The fundamental principle of a sensor is a device that responds to external stimulus. The external stimulus can be any one of a variety of physical and chemical parameters.<sup>129</sup> A sensor device typically consists of two main components: (i) a chemical recognition phase also referred to as the sensing material and (ii) a physical transducer element (Figure 1-14). In OSC sensors, the active material is typically a  $\pi$ -conjugated material that is exposed to the analyte. The transducer exists to detect the changes in the physical properties of the  $\pi$ -conjugated material as a result of exposure to the analyte and transform the detected changes into a measurable parameter for processing by a system. A processor connected to the transducer typically amplifies and outputs the data for analysis.<sup>130</sup> The signal from a sensor is commonly electronic in nature and involves current change, voltage change or impedance/conductance

change. In view of the sensing application, the molecular structures of the chemosensors can be chemically modified to improve sensitivity, response-time and stability.<sup>131, 132</sup>

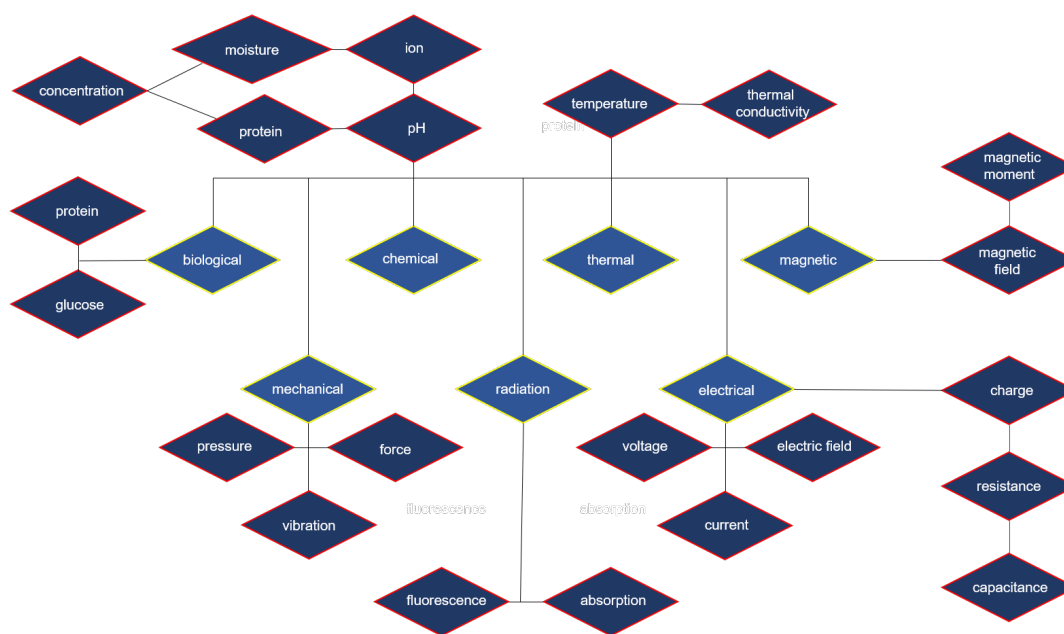


**Figure 1-15.** Example classifications of sensors and the measurable physical and chemical parameters.

The classification of sensors is particularly complex due to the broad scope of conversion principles, sensing applications, output signal types and the active materials involved in the sensing technology (Figure 1-15). Sensing devices are commonly classified according to the detection principle, *i.e.* the physical, chemical or biological parameters upon which the sensor operates, *i.e.* the parameter that changes upon exposure to the analyte. For instance, a  $\pi$ -conjugated material that undergoes a change in current upon exposure to an analyte is commonly categorised as an electrochemical sensor. Similarly, a  $\pi$ -conjugated material that undergoes a change related to absorption or emission characteristics when exposed to an analyte

may be categorised as an optical sensor. Moreover, chemical sensors can be further categorised based on the material type employed in the sensing system, *i.e.* small molecular system or polymeric system.<sup>133</sup>

### **1.5.1 Chemosensors**

A chemosensor may be defined as a device that transforms chemical information of a quantitative or qualitative nature into an analytically useful signal, thereby undergoing a specific chemical change that is measurable upon interacting with an analyte. The ideal chemical sensor has the characteristics of being inexpensive, selective, sensitive, stable, reversible and additionally exhibit short response times. In designing a sensor with a target application, the sensing material must be designed with respect to the application and exhibit specificity to the target analyte. A sensor that has a low degree of specificity may interact with other environmental factors such as temperature, humidity, shock and vibration, thereby affecting the intended performance of the sensor. The electronic structure of the sensing material can be tailored through the incorporation of certain functional groups, thereby altering the energy levels of the frontier orbitals and altering the sensing material's response to the analyte interaction.<sup>134</sup>

#### **1.5.1.1 Optical Sensors**

Optical sensors are used in a variety of technological areas and have proven reliable in detection and identification of analytes due to their selectivity capabilities and immunity to electromagnetic interference. Furthermore, analytical data from optical

instrumentation is easily derivable from spectra, making the investigations of analytes simpler in comparison to other sensing devices.

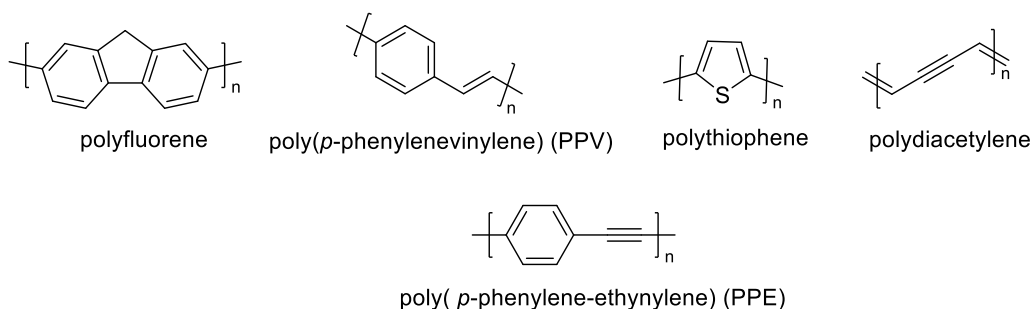


**Figure 1-16.** Known molecules used in application as fluorescent probes.

Optical sensors refer to a subclass of chemical sensor wherein electromagnetic radiation generates a measurable signal in the transducer.<sup>135</sup> Upon detecting the analyte, the sensing material provides an optical signal corresponding to the magnitude of the detected parameter. The optical detection principles are diverse and comprise any one of absorbance, luminescence and reflectance. Luminescence has proven to provide higher specificity and sensitivity to analytes and hence, is deemed a useful detection principle.<sup>136-138</sup> Luminescent sensing materials comprise a luminophore, which refers to a functional group responsible for the exhibited emission properties of the system. Luminophores are classified according to their excited state characteristics; a fluorophore is a term used to describe a molecule that decays from the singlet excited state, thereby decaying through a fluorescent radiative pathway. Figure 1-16 shows known fluorophores used as fluorescent probes. Certain measurements of luminescence are more reliable than others, as for instance emission intensity can be subject to the influences of fluctuation in the light source, detector sensitivity and/or film layer thickness of the sensing material.<sup>139</sup>

An optical sensor may fall under one of two categories: (i) direct sensing; or (ii) indicator-mediated sensing.<sup>140</sup> In direct optical sensors, the analyte is detected through an intrinsic property of the material itself. In indicator-mediated sensing, the optical response of an intermediate agent is used to monitor the analyte. For instance, an analyte-sensitive dye molecule may be used. The intermediate agent can be present in or on a  $\pi$ -conjugated system. Colorimetric sensing applies indicators that undergo changes in colour upon being exposed to the analyte.<sup>141</sup>

### 1.5.1.2 Fluorescence Quenching

Sensing materials comprising donor moieties may be subject to fluorescence resonance energy transfer (FRET) upon exposure to an acceptor analyte in the photoinduced state. The influence of the FRET phenomenon is known to influence the fluorescence intensity of the donor moiety. FRET refers to a non-radiative phenomenon wherein energy is transferred from a donor molecule to an acceptor molecule. The donor molecule absorbs the photons and is in its excited state before subsequently transferring that energy to the acceptor molecule. This resonance phenomenon is distance dependent and occurs without molecular collision. As a result of the energy transfer, the donor molecule exhibits a reduction in fluorescence intensity and excited state lifetime. The acceptor molecule exhibits an increase in fluorescence intensity.<sup>142</sup>

A variety of optical sensors are known that are based on the interaction of a fluorescent materials with analytes that quench fluorescence.<sup>143, 144</sup> Fluorescent quenching is measured quantitatively using the Stern-Volmer equation (Equation 1-2), wherein  $F_0$  is

the measured fluorescence without quencher present and  $F_{[Q]}$  is the measured fluorescence with quencher present,  $K_{SV}$  is the Stern Volmer constant and  $[Q]$  is the concentration of the quencher. The Stern Volmer equation does not account for the concentration of fluorophore present, thus suggesting that the measured fluorescence quenching is independent of the concentration of the fluorophore.

$$\frac{F_0}{F_{[Q]}} = 1 + K_{SV} [Q]$$

**Equation 1-2.** Stern-Volmer equation.<sup>145</sup>

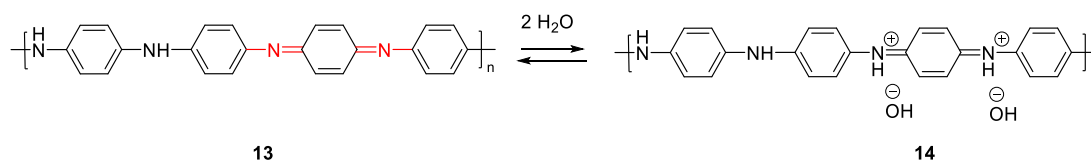
Fluorescence quenching can occur as a result of intramolecular charge transfer from the excited state of the molecule to the analyte, such as is seen with electron-rich polydiacetylene (PDA) in the presence of trinitrotoluene (TNT). The quenching that occurs is attributed to the formation of a charge-transfer complex with between TNT and PDA system.<sup>146</sup>

### 1.5.1.3 Humidity Sensors

$\pi$ -Conjugated materials can be doped through redox reactions involving an electron transfer from or to the analyte, or these systems can be doped electrochemically. The doping leads to a change in electrical resistance of the conjugated material and this principle can be exploited for sensing applications.

Humidity sensors can be applied in a diverse range of applications including but not limited to, the automobile industry with respect to window defoggers, pharmaceutical processing and food monitoring. Depending on the field of application, the humidity sensor requires different operating conditions. Humidity measurements define the

amount of moisture in a gas, e.g. air. Water's ability to protonate C-N double bonds is known and can be exploited for sensing purposes.<sup>147</sup>



**Scheme 1-8.** Doping of polyaniline through protonation.<sup>148</sup>

The altering of the electronic properties of  $\pi$ -conjugated systems through doping is known. In doping mechanisms, the number of electrons associated with the system is altered through partial oxidation or reduction. The increase in conductivity exhibited by polyaniline upon doping wherein the number of electrons remains unchanged is a well-known example of the different mechanisms of doping. The reversible reaction of the emeraldine base form of polyaniline with water as a Brønsted acid results in the protonation of the imine nitrogens within the polymer system. The protonation of the imine nitrogens resulted in a change in bulk properties of the system, e.g. solubility and morphology, but additionally a change was exhibited in the electronic properties of the system, evidenced by optical, magnetic and dielectric properties. Furthermore, the conductivity of the system increased by almost 8 orders of magnitude. As shown in Scheme 1-8, the lone pairs present on the nitrogen atoms of the polyaniline base **13** are protonated by water and an intrachain electron hopping mechanism occurs, forming the polyaniline salt **14**.<sup>149</sup>

## 1.5.2 Overview of Existing Chemosensors

### 1.5.2.1 OFET-based Sensors

An OFET is a multi-layered structure that can be exploited as a multiparametric sensor. A large quantity of information can be extracted from their characterisation, including mobility, threshold voltage and contact resistance. Due to the quantity of information that can be extracted from the characterisation of an OFET, a combination of variables can be investigated in order to characterise a response to an analyte. OFET-based sensors have proven useful in the detection of ions for environmental conservation and medicinal chemistry.<sup>150, 151</sup>

The OFET is an electronic device used to control current in a device and the first organic version of the device was developed in 1986 by Tsumura *et al.* using polythiophene.<sup>152</sup> OFETs are suitable transducers in that they may detect parameters such as a change in conductivity within the OSC layer or capacitive changes in the gate, thereby having the capability to detect external stimulus. Furthermore, the electrical response to particular analytes can be amplified within the transistor, without need for an additional device.

The components of the device include a gate terminal, source terminal and drain terminal; an organic semiconductor and insulating layer. The operating principle of an OFET comprises the injection of charge at the source electrode and migration of the charge through the semiconducting material. The conducting channel is located near the interface between both the semiconductor and the insulating layer. By application of different voltages to the source and drain electrodes, a source-drain current is generated in the conducting channel. The insulating material known as the

gate dielectric acts to control leakage of current within the device thus reducing the power required for the device to operate. The material typically used in the insulating layer is silicon dioxide.

Figure 1-17 shows a schematic of the four possible configurations of the OFET, wherein each configuration depends on the position of the electrodes in the device: bottom-gate top-contact, BGTC; bottom-gate bottom-contact, BGBC; top-gate top-contact and top-gate bottom-contact. Both bottom-gate top contact and bottom-gate bottom-contact are the most widely configured OFETS. BGBC has better contact with the semiconductor material and the source/drain electrodes, while BGTC is an easier configuration for deposition of the semiconductor material.<sup>153</sup>

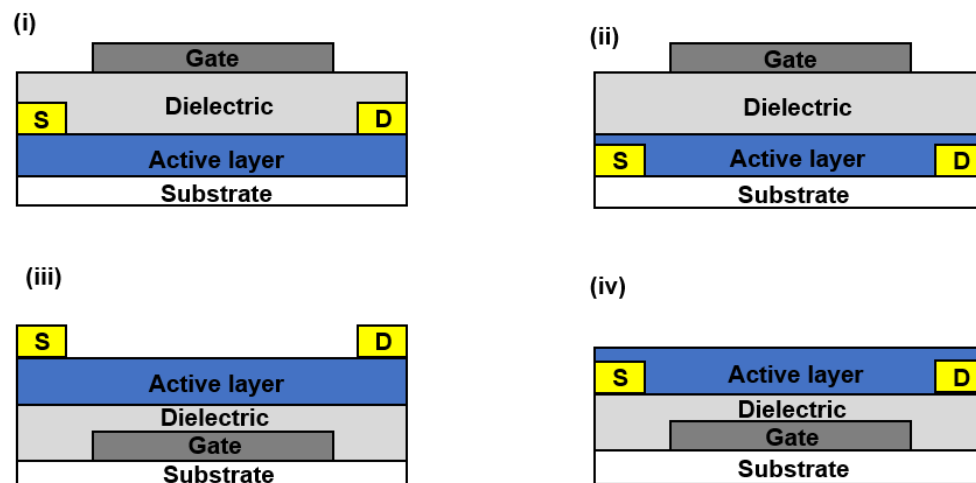


**Figure 1-17.** Schematic of the gate and contact configuration of OFETs: (i) top-gate top-contact; (ii) top-gate bottom-contact; (iii) bottom-gate top-contact; (iv) bottom-gate bottom-contact, wherein S – source and D – drain.<sup>154</sup>

OFETs usually operate in the accumulation mode. For p-channel OFETs this entails holes (majority charge-carrier) being injected into the semiconductor from the source

electrode and accumulated in the channel. In n-channel OFETs, electrons are injected from the source electrode into the conducting channel. P-channel devices operate with a gate voltage,  $V_g < 0$ ; n-channel devices operate with a  $V_g > 0$ . Defects in the device cause charge-carriers to become trapped at the semiconductor-insulator interface and are difficult to overcome, thus only when the gate voltage is above a certain threshold,  $V_{T_s}$ , can the channel operate as being in the ‘on’ state.<sup>155</sup>

When there is zero potential at the gate, charge carriers fail to accumulate in the conducting channel and the device is said to be in the ‘off’ state. OFET performance can be largely improved by ensuring sufficient field-effect mobility within the semiconductor material.<sup>156</sup> This can be achieved by ensuring rigidity and planarity in the design of the material, optimising  $\pi$ - $\pi$  stacking. The way in which material orientates upon the substrate is critical to device performance, particularly if the material is linear. Charge transport must occur in the direction parallel to the substrate to achieve good device performance. Defects present in the material also hinder charge transport but can be avoided by minimising the number of steps used in synthesis and ensuring purity in products.<sup>157</sup>

The monodispersity afforded by oligomer materials make them attractive as a semiconducting materials due to their ease of reproducibility.<sup>158</sup> Oligomer materials tend to have high crystallinity enabling efficient molecular packing through  $\pi$ - $\pi$  interactions.<sup>159</sup> High performing devices have been based upon low-molecular weight molecules, for instance pentacene which has shown high performance particularly in organic field-effect transistors, OFETs. The high performance of semiconducting

materials such as pentacene are attributed to its unidimensional character which provides anisotropic charge transport through the material.<sup>160, 161</sup>

### **1.5.2.2 OPV-based Sensors**

An emerging technology is fabric-based wearable devices.<sup>162</sup> The integration of electronic devices into everyday life is becoming common due the demand for portable devices. Electronic textiles refer to electronics incorporated into textiles, the level of incorporation being dependent on the fabric construction. In particular, there is a demand for flexible solar cells that can be attached to a fabric substrate. The reason for this demand is the continuous requirement to charge electronics whilst on the move.

Photovoltaic textiles are capable of generating energy upon exposure to solar irradiation. As a result, a photovoltaic cell is a sensor due to the analyte essentially being solar photons which cause the voltage generation which is measurable. Combined with the mechanical properties of OSC materials, such as the flexibility provided, photovoltaic textiles have the ability to be used in applications such as jackets and backpacks to power portable electronics.<sup>163</sup>

OPV operate by absorption of photons that result in the formation of excitons. Due to a concentration gradient, excitons migrate into the donor-acceptor (D-A) interface and subsequently dissociate into holes and electrons. The electrons drifts towards the cathode and the holes towards the anode. Charge is collected at the electrodes leading to the generation of electrical energy.<sup>164</sup>

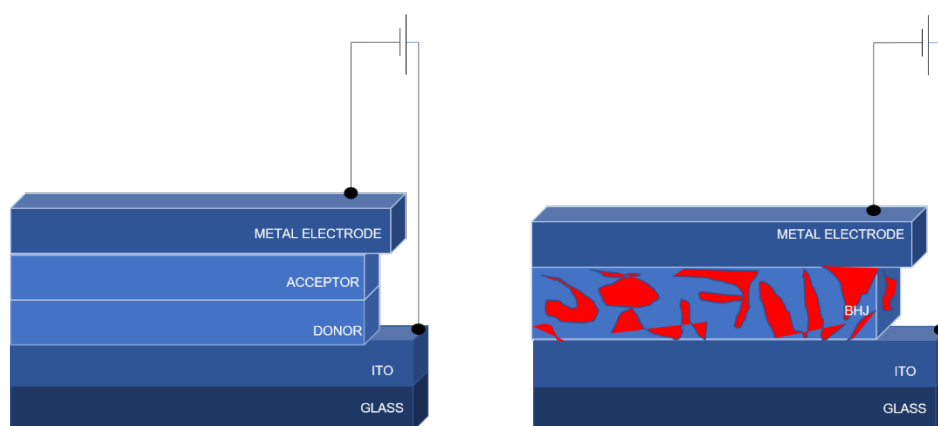


**Figure 1-18.** Bilayer photovoltaic cell (*left*) and bulk heterojunction photovoltaic cell (*right*).

Figure 1-18 shows a schematic of the bilayer configuration wherein the donor layer and acceptor layer are two separate layers (depicted on the left-hand side, Figure 1-18). Both layers have different ionisation potentials and electron affinities, resulting in electrostatic forces at the interface that aids the separation of excitons. This configuration has its disadvantages as the interface between the donor layer and acceptor layer can decrease efficiency exciton dissociation, thereby decreasing the generation of free charge-carriers. As also depicted in Figure 1-18, a bulk heterojunction configuration, the active layer is a mixture of both donor-acceptor components, increasing the interfacial area (depicted on the right-hand side, Figure 1-18). Increased interfacial area theoretically results in a higher chance of exciton dissociation.<sup>165</sup>

A low optical band gap is a requisite for a broad absorption spectrum. This can be achieved by extending conjugation in the  $\pi$ -conjugated system, thereby promoting easier excitation into the LUMO. The donor system should be able to stabilise a positive charge, which can be achieved by the incorporation of electron donating

groups. Similarly, the acceptor molecule should be capable of stabilising the negative charge and is achievable through incorporation of electron-withdrawing groups.<sup>166</sup>

The earliest bulk crystalline solar cell exhibited a power conversion efficiency (PCE) of 20%.<sup>167</sup> The overall efficiency of solar cells is defined in terms of current-voltage characteristics. The power conversion efficiency,  $\eta$ , is defined as the ratio of power output,  $P_{out}$ , to the power input,  $P_{in}$  taken as a percentage; wherein the  $P_{out}$  is dependent on the product of short-circuit current density,  $J_{sc}$ ; open circuit voltage,  $V_{oc}$ , and fill factor,  $FF$  (Equation 1-3):<sup>168</sup>

$$\eta = \frac{P_{out}}{P_{in}} = \frac{FF \times V_{oc} \times J_{sc}}{P_{in}}$$

**Equation 1-3.** Calculation of PCE.<sup>168</sup>

$$FF = \frac{V_{max}J_{max}}{V_{oc}J_{sc}}$$

**Equation 1-4.** Determination of the fill factor.<sup>169</sup>

The  $V_{oc}$  refers to the voltage from the device, when it is under illumination with no current passing. The  $J_{sc}$  refers to the current density through the device when no external bias is applied.  $FF$  is defined as the realistically achieved performance ( $J_{max}V_{max}$ ) over the ideally achievable performance ( $V_{oc}J_{sc}$ ), as shown in Equation 1-4. The parameters  $J_{max}V_{max}$  correspond to a bias applied with the corresponding current density that results in the maximum power generated from the device.<sup>170</sup>

### 1.5.2.3 OLED-based Sensors

OLED technology enjoys great commercial success in display markets.<sup>171</sup> The abundant luminophores capable of producing blue to red light ensure that OLED technology continues to advance, producing new and fascinating luminescent materials. A drawback of OLED materials for display devices is their sensitivity to ambient conditions, including water and oxygen. OLED sensitivity to oxygen and water, leads to premature device degradation as a result of instability. However, this drawback can be exploited in sensing technology, particularly in gas sensors wherein the analyte is oxygen.<sup>172</sup>

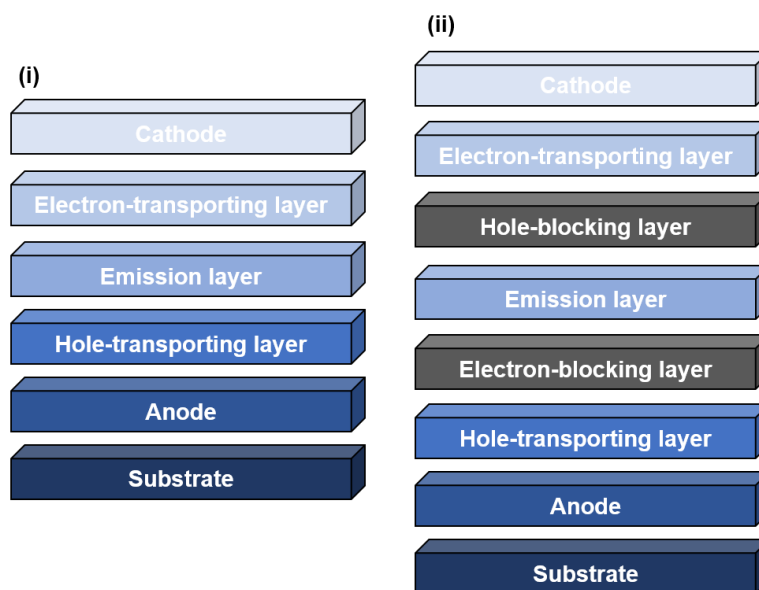


**Figure 1-19.** OLED device architectures: (i) including HTL and ETL layers; (ii) including hole blocking layer and electron-blocking layer.<sup>173</sup>

An organic light-emitting diode emits light in response to an applied potential. The general architecture of an OLED device comprises a substrate, one or several organic layers placed between two electrodes, one of which is transparent. The device operates by applying a voltage that injects electrons from a metal cathode with a low work

function, into the LUMO of the small molecule or conjugated polymer. Holes are injected from a bilayer anode (usually indium tin oxide) into the HOMO of the semiconductor material. Both these electrons and holes migrate towards each other under the applied electric field and recombine, forming an exciton. The formation of the exciton leads to the population of excited states in the semiconductor material. The excited state of a molecule can relax either via energy transfer to a second molecule or through radiative relaxation on return to the ground state, thereby releasing a photon of light.<sup>174</sup>

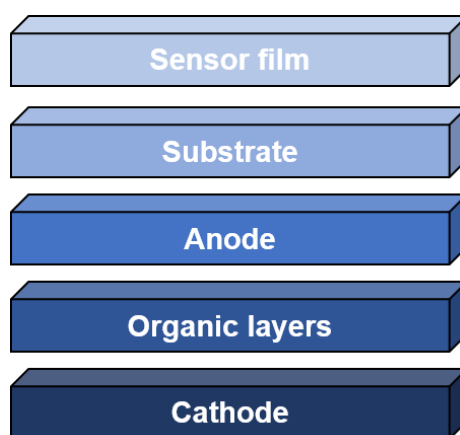


**Figure 1-20.** OLED-based biological sensor.

As shown in Figure 1-19, additional layers in an OLED device are often used in order to promote charge recombination or improve charge-carrier injection. Hole-transporting layers (HTL) and electron-transporting layers (ETL) are generally used and placed between their corresponding electrodes. The function of each layer is to facilitate either the injection of holes from the anode or electrons from the cathode. The hole-transporting and electron-transporting layers are chosen based on their energy barriers for charge injection into the emissive layer. A low energy barrier is desired as it corresponds to a smaller voltage required to induce charge injection in the device.<sup>175</sup> Further layers such as hole blocking layers or electron blocking layers can

be incorporated in order to confine species to the emissive layer, thereby improving emission.<sup>176</sup> For comparison, the basic structure of a fluorescence-based biological sensor is shown (Figure 1-20).<sup>177</sup>

In Figure 1-20., a DC current passed between the anode and the cathode excites the charge within the organic layers, thereby causing electroluminescence. The luminescence passes through the glass substrate and interacts with the sensor surface. The analyte is adsorbed on the sensor surface and the photoluminescence light interacts with the analyte molecules and changes the luminescence intensity. As a result of the change in intensity, the quantity of analyte present on the surface of the sensor film can be derived.

External quantum efficiency (EQE) refers to the ratio of photons that are emitted externally relative to the number of electrons or holes injected into the device; the efficiency is given as a percentage. The higher the EQE, the better the material's performance. Further desirable properties of the emissive material include oxidative stability and high colour purity, all of which can be optimised by chemical modifications to the material. Efficient  $\pi$ - $\pi$  stacking can lead to the quenching of luminescence and therefore, a balance between charge-carrier mobility and luminescence is critical to device performance.<sup>178</sup>

## 1.6 Methods of Characterisation

### 1.6.1 Ultra-Violet/Visible Absorption Spectroscopy

UV-Vis spectroscopy (or spectrophotometry) is a quantitative technique wherein organic molecules absorb light of a defined energy resulting in electronic optical transitions (Figure 1-21). The energy transition levels are inherently defined by the wavelength of light required for an electronic transition. These transitions are classified according to the bonding and non-bonding molecular orbitals,  $n$ ,  $\sigma$ , or  $\pi$ , involved (anti-bonding is denoted by superscript asterisk):

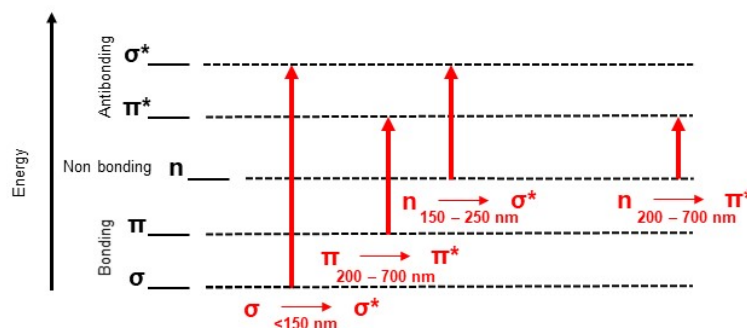


**Figure 1-21.** Energy diagram with the possible electronic transitions in organic molecules and spectral region of observance.<sup>179</sup>

The energy difference between these levels is described by Equation 1-5:

$$\Delta E = h\nu = \frac{hc}{\lambda}$$

**Equation 1-5.** Energy difference between optical levels.<sup>180</sup>

Where  $h$  is Planck's constant ( $6.63 \times 10^{-34} \text{ J s}$ ),  $\nu$  is the frequency of the incident light (expressed in  $\text{s}^{-1}$ ),  $c$  is the speed of light ( $3 \times 10^8 \text{ m s}^{-1}$ ), and  $\lambda$  is the wavelength

of the incident light (expressed in m). The UV region falls in the range between 190-380 nm, the Vis region fall between 380-750 nm. Electronic transitions observed from non-conjugated systems, such as  $\sigma/n \rightarrow \sigma^*$  are generally not seen in UV-Vis spectra due to their higher energy difference. On the other hand, electronic transitions from orbitals  $n/\pi \rightarrow \pi^*$  occur in the spectral region of 200 – 700 nm and are often observed in the UV-Vis spectrum.<sup>181</sup>

A UV-Vis spectrophotometer has an incidence beam split into two light beam paths, one irradiates the working sample and the other light beam irradiates the reference sample simultaneously (Figure 1-22). The Light beam interacts with the working sample and is partially absorbed at characteristic wavelength corresponding to possible electronic transitions as mentioned above. The reference measurement takes the absorbance by a material holder, in this case a cuvette, into account.

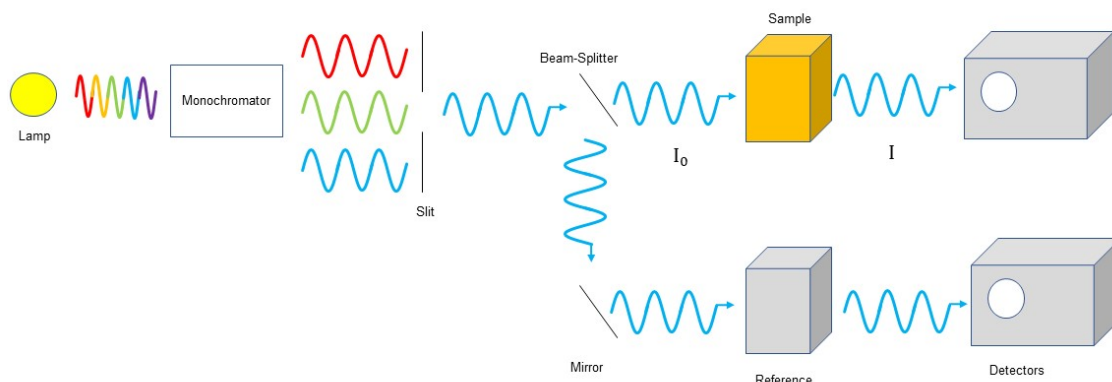


**Figure 1-22.** Schematic diagram showing 2-beam UV-Vis Spectrometer.

The Beer-Lambert law (Equation 1-6) states that the transmittance ( $T$ ), *i.e.* the light ( $I_0$ ) before passing through the sample over the incident intensity ( $I$ ), is dependent on the path length of the light through the sample ( $l$ ), the absorption cross section ( $\sigma$ ) of

the sample's transition, and the difference in the population of the initial state ( $N_1$ ) and final state ( $N_2$ ):

$$T = \frac{I}{I_0} = \exp(-\sigma(N_1 - N_2)l)$$

**Equation 1-6.** Beer Lambert Law.<sup>182</sup>

This is often written in a form referred to as *Beer's law* (Equation 1-7): the absorption of light is proportional to the number of absorbing molecules:

$$A = \epsilon cl = -\log\left(\frac{I}{I_0}\right)$$

**Equation 1-7.** Beer's law.

wherein  $A$ , is the absorbance (unitless value),  $\epsilon$  is the molar absorptivity coefficient of the material (expressed in  $\text{mol L}^{-1} \text{cm}^{-1}$ ),  $c$  is the concentration of the solution (expressed in  $\text{mol L}^{-1}$ ), and  $l$  is the path length of the light through the sample (expressed in cm). The molar absorptivity coefficient is dependent on whether a transition is spin-allowed or spin-forbidden, wherein allowed transitions lead to much more intense absorptions and therefore higher values of  $\epsilon$  than forbidden transitions.

The results of the UV-Vis-measurement are displayed in an absorption spectrum wherein the intensity of absorbance is plotted against its recorded wavelength.<sup>183</sup> These spectra obtained for organic molecules are generally broad with distinctive maximum absorbance intensity at a given wavelength ( $\lambda_{\text{max}}$ ). The presence of vibrational and rotational energy levels results in the distribution of the absorbed energies and consequent broadening of peaks. The UV-Vis-measurement is relatively

straightforward, and the data obtained is highly reproducible from lab to lab despite differences in lamp sources, spectrometers, experimental configuration, etc.

### 1.6.2 Electrochemical Analysis Cyclic Voltammetry

Electrochemistry associates the flow of electrons to chemical changes. A redox reaction corresponds to the transfer of at least one electron from one species to another one and by doing so changing the oxidation state of those species. A redox reaction comprises two processes, oxidation, wherein a molecule loses an electron and reduction, wherein a molecule gains an electron.<sup>184</sup> A redox reaction wherein  $n$  corresponds to the number of electrons:



By applying an external potential to an electrochemical cell, containing redox active chemicals (also known as analytes) and electrolytes, mechanistic and kinetic information can be obtained. The oxidation and reduction processes are displayed as the observed current, *i.e.* Faradaic current in Equation 1-8, wherein  $i$  = current,  $n$  = number of electrons,  $A$  = electrode area,  $F$  = Faraday constant and  $j$  = flux:<sup>185</sup>

$$i = nAFj$$

**Equation 1-8.** The relationship between the faradic current and oxidation and reduction processes

When an electrode potential is established, which translates as an electrical potential difference between the electrode surface and the electrolyte, it becomes interesting to

discuss in terms of energy levels, and so entering the area of electrochemical thermodynamics.<sup>186</sup> Equation 1-9 describes the relationship between the free energy  $\Delta G$  ( $\text{kJ mol}^{-1}$ ) and the concentration of oxidized  $[O]$  ( $\text{mol l}^{-1}$ ) and reduced  $[R]$  ( $\text{mol l}^{-1}$ ) species, where  $\Delta G^0$  is the standard Gibbs free energy,  $R$  is the gas constant ( $8.314 \text{ J mol}^{-1} \text{ K}^{-1}$ ),  $T$  is temperature (K):

$$\Delta G = \Delta G^0 + RT \ln \frac{[O]}{[R]}$$

**Equation 1-9.** Relationship between free energy and concentration of oxidised and reduced species.

As shown in equation 1-10, the Gibbs free energy can also be expressed as a function of electrode potential (V), where  $n$  is the number of electrons involved and  $F$  is Faraday's constant ( $96485 \text{ C mol}^{-1}$ ):

$$\Delta G = -nFE$$

**Equation 1-10.** Gibbs free energy as a function of electrode potential.

Any reactions can theoretically become spontaneous using electrochemistry if a high enough potential is applied which means  $\Delta G < 0$ .

One of the most important equations regarding the relation between electrochemical properties and thermodynamic properties, is the Nernst equation (equation 1-11).<sup>187</sup> This equation can be found by substituting Equation 1-9 into Equation 1-10 and rearranging to give Equation 1-11 where  $E^0$  is the standard redox potential:

$$E = E^0 + \frac{RT}{nF} \ln \frac{[O]}{[R]}$$

**Equation 1-11.** Nernst equation

The Nernst equation provides a powerful way to predict how a system will respond to a change of concentration of species in solution or a change in the electrode potential. Transfer kinetics play a key role in electrochemical process as an electrode process is limited by how many and how fast electrons can transfer at the electrode surface. This rate determining step is controlled by any of the following five processes, mass transfer to the electrode surface, adsorption, electron transfer, desorption or mass transfer back into the bulk. This translates for limitations in electrochemical systems: (1) a limitation due to mass transport where slow transport of species limits the current or (2) an electron-transfer limited system because of limited reaction kinetics.<sup>188</sup> The reaction rate,  $v$ , at the electrode surface can be related to the current density,  $i$ , which in turn is a useful description parameter for the activation barrier (that charge transfer must overcome), as shown in Equation 1-12:

$$i = nFv$$

**Equation 1-12.** The relationship between reaction rate and current density at electrode surface.

When considering a reversible redox reaction, the rate of reduction and oxidation are described by Equations 1-13 and 1-14, respectively, where  $k$  is the rate constant:

$$v_{red} = k_{red}[O] = -\frac{i_{red}}{nF}$$

**Equation 1-13.** The rate of reduction

$$v_{ox} = k_{ox}[R] = -\frac{i_{ox}}{nF}$$

**Equation 1-14.** The rate of oxidation.

When the reaction is in equilibrium  $i_{red} = i_{ox} = i_0$ .

The Arrhenius equation provides the relationship between the rate constant,  $k$ , and activation energy,  $E_A$  where  $A$  is a constant, as shown in Equation 1-15:

$$k_{(ox\ or\ red)} = A \exp \frac{-E_{A(ox\ or\ red)}}{RT}$$

**Equation 1-15.** The Arrhenius equation.<sup>189</sup>

From these Equation 1-12, 1-13, 1-14 and 1-15 the dependence between rate constant, potential and current density can be established. Equations 1-13 and 1-14 can be rewritten into partial current densities of the reduction and oxidation, Equations 1-16 and 1-17, respectively where  $\alpha$  is the transfer coefficient:

$$i_{red} = i_0 \exp \frac{(1-\alpha)nF(E-E^0)}{RT}$$

**Equation 1-16.** Partial current density for reduction.

$$i_{ox} = i_0 \exp \frac{-\alpha nF(E-E^0)}{RT}$$

**Equation 1-17.** Partial current density for oxidation.

In order to exceed the activation energy an overpotential,  $\eta = E - E^0$ , must be applied upon the system. Implementing this overpotential equation into the aforementioned Equations 1-16 and 1-17 results in the Butler-Volmer equation:

$$i = i_0 \left( \exp \frac{(1-\alpha)nF\eta}{RT} - \exp \frac{-\alpha nF\eta}{RT} \right)$$

**Equation 1-18.** Butler-Volmer equation<sup>190</sup>

From this equation, it can be determined that for large deviations from the equilibrium potential, that is, large  $\eta$  values, the partial currents approach the net current. Therefore, for large positive  $\eta$  values,  $i_{ox}$  tends towards  $i$ , and  $i_{red}$  tends towards  $i$  for large negative  $\eta$  values.

In electrochemistry Fick's second law is of great importance as electrochemical experiments focus more on changes in concentration as a function of time.<sup>191</sup> In Fick's second law (Equation 1-20) the principles of the first law, diffusional flux: rate of diffusion depends on the specific concentration gradient at any given point (see Equation 1-19), was combined with concentration changes within a certain area, where  $j$  is flux,  $D$  is diffusion coefficient,  $[O]$  is the concentration of species and  $x$  is the distance from the electrode surface:

$$j_{ox} = -D_{ox} \frac{\delta[O]}{\delta x}$$

**Equation 1-19.** Fick's first law.

$$\frac{\delta[ox]}{\delta t} = D_{ox} \frac{\delta^2[O]}{\delta x^2}$$

**Equation 1-20.** Fick's second law

The amount of oxidized or reduced species changes with the applied potential and the scan rate, resulting in a concentration gradient probing the diffusion process. Convection and migration also play a role in mass transport occurrences, albeit a smaller one.

Voltammetry techniques, *i.e.* applying a controlled potential (or current) to the cell while recording the resulting flow current (or potential), can be divided in two categories, potential sweep techniques such as cyclic voltammetry (CV) and the step or pulse techniques (e.g. chronoamperometry). In the former techniques the current response of an analyte is recorded while the electrode potential is changed linearly with time from one potential to another. In CV experiments a potential  $E_1$  is applied to the working electrode (at which redox processes do not occur). The potential is then increased to a value at which electron transfer occurs rapidly,  $E_2$ , and finally returns to the original potential  $E_1$ . When the applied voltage is plotted against time a triangular profile will be observed (Figure 1-23).<sup>192</sup>

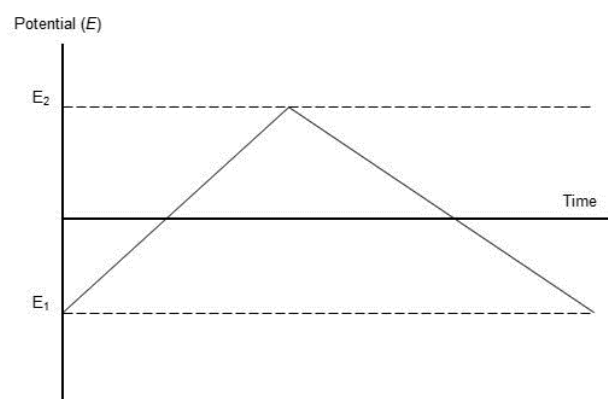


**Figure 1-23.** A graph to show potential,  $E$ , as a function of Time during a CV experiment.

Distinctive shapes in cyclic voltammograms contain a lot of information. When the potential is ramped up oxidation will start to occur at the electrode surface which in turn will initiate an increase in current. Upon increasing the potential, the current will remain to increase exponentially until a maximum is reached, *i.e.* the peak current,  $i_p$ . Once this peak is reached, there is no longer an excess of material at the surface and the peak current is solely dependent on diffusion characteristics. A similar shape in reverse for the reduction process is observed (Figure 1-24).

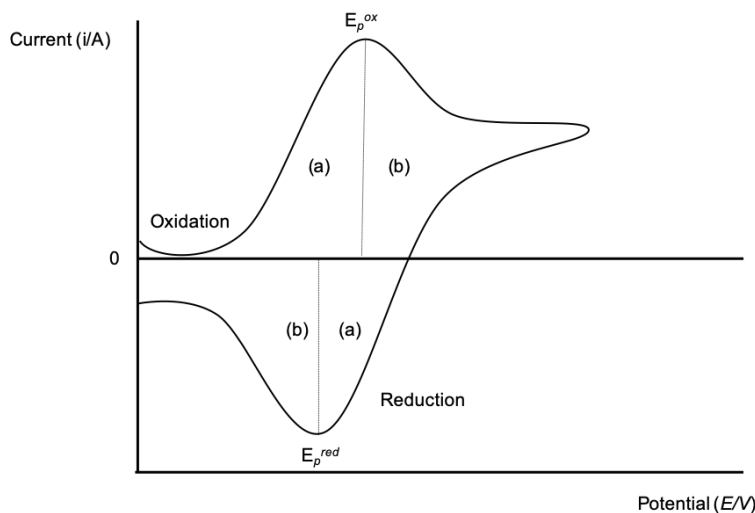
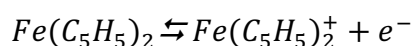


**Figure 1-24.** Cyclic voltammogram for a reversible system where (a) represents the area of the peak characteristic of Butler-Volmer Kinetics and (b) is controlled by diffusion process.

There are various electrode setups that can be used within an electrochemical cell, however, the most common used is the 3-electrode setup; the working electrode, the reference electrode and the counter electrode. The potential of the working electrode is controlled by a potentiostat functioning as feedback amplifier. The redox reaction occurs at the surface of the working electrode and the current travels between the working and counter electrode. The working electrode exists in various geometries and materials, usually consistent of inert metals (gold, silver or platinum), inert (glassy or pyrolytic) carbon or a mercury drop. The counter electrode consists of an inert metal (*e.g.* gold or platinum) and has a large surface area to lower the current density. The single function of the counter electrode is to carry the current flowing through the cell. At its surface no processes of interest occur. Lastly, the reference electrode, commonly used are the standard hydrogen electrode (SHE), the saturated calomel electrode (SCE) and the Ag/AgCl electrode, measures the potential of the working electrode relative to the reference electrode (as a voltammetry analyses measure potential differences).

Therefore, it should have a stable potential, ideally non-polarisable. When working in a non-aqueous solvent, pseudo-reference electrodes can be used. They consist of a simple metal wire such as platinum or silver, having good non-oxidative properties, they are directly immersed in the sample solution, having a low impedance and are easy to use. It is important to note that the reference potential is unknown and is dependent on the composition of the sample solution.

The ferrocene/ferrocenium ( $\text{Fc}/\text{Fc}^+$ ) redox couple is one of the most common internal standards (recommended by IUPAC) due to its solubility in non-aqueous solvents, robustness and well-understood kinetics.<sup>193</sup> Ferrocene is reversibly oxidized to form ferrocenium (Equation 1-21):



**Equation 1-21.** Equilibrium between ferrocene and ferrocenium.

By calibrating the results to the  $\text{Fc}/\text{Fc}^+$  redox couple, the HOMO and LUMO levels of the analyte can be calculated by subtracting the onset of the first oxidation and first reduction processes from the HOMO of ferrocene (Equation 1-22). In the literature, there is little consensus about the correct vacuum energy level of  $\text{Fc}/\text{Fc}^+$  redox couple (values between -4.4 and -5.4 eV have been reported)<sup>194</sup>, however many research groups opted to use to widely-accepted value of -4.8 eV. The estimations are done with the empirical relations:

$$E_{HOMO} = \left[ \left( E_{red} - E_{\frac{1}{2(ferrocene)}} \right) + 4.8 \right] eV$$

**Equation 1-22.** Calculating the LUMO of the analyte.

$$E_{LUMO} = \left[ \left( E_{ox} - E_{\frac{1}{2(ferrocene)}} \right) + 4.8 \right] eV$$

**Equation 1-23.** Calculating the HOMO of the analyte.

And subsequently the band gap energy,  $E_g$ , can be calculated using Equation 1-24:

$$E_g = E_{LUMO} - E_{HOMO}$$

**Equation 1-24.** Band gap calculation.

Besides CV differential pulse voltammetry (DPV) is the main electrochemical technique used where the potential is varied as a function of time.<sup>195</sup> DPV as contrary to CV optimizes the ratio of Faradaic current to the capacitive charging current, and in doing so increases the electrochemical sensitivity. In this technique the current is sampled over a series of potential pulses in a staircase manner (Figure 1-25):

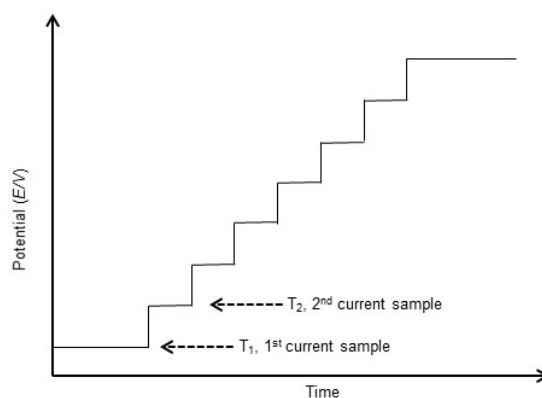


**Figure 1-25.** Variation of applied potential with time in DPV resulting in staircase waveform; arrows indicate the position of current measurements used to take an average.

In DPV the change in potential with each pulse can range from 10 – 100 mV with a timeframe of 5 – 100 ms between each change in potential. For each pulse two current samples,  $T_1$  and  $T_2$ , are taken. The first of which is recorded at the end of each potential change just before the next one so that the contribution to the current signal from the capacitive charging current is minimized.

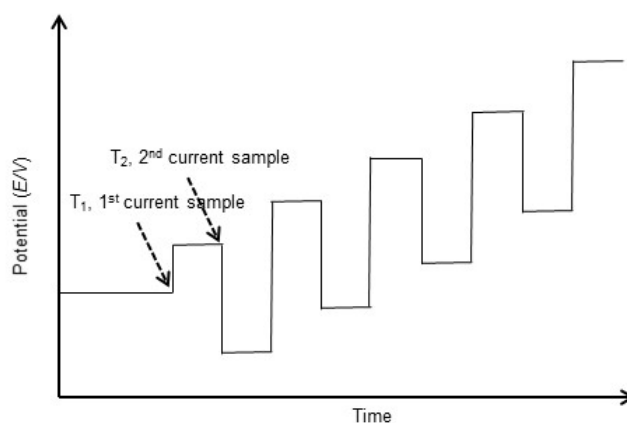


**Figure 1-26.** Example of an SWV voltammogram; arrows indicate the position of current measurements used to take an average.

Another technique to simplify convoluted voltammograms is square-wave voltammetry (SWV).<sup>196</sup> In SWV a symmetrical square wave (as shown in Figure 1-26), superimposed on a base staircase potential, is applied to the working electrode. During each square-wave cycle the current is sampled twice, once at the end of forward pulse,  $T_1$ , and another at the end of the reverse pulse,  $T_2$ . Similar to DPV the electrochemical sensitivity is greatly increased due to the larger net current than either forward or reverse components. Also scan time and very low detection limits can be attained.

**2 Synthesis, development and characterisation of novel  
hybrid tetrathiafulvalene-oligofluorene-thiophene  
systems**

## 2.1 Abstract

This chapter investigates synthetic strategies to developing a series of new star-shaped oligofluorene-thiophene-tetrathiafulvalene systems. The series incorporates well-defined oligofluorene arms, leading to precise energy levels in the electronic structure of the systems. Electronic communication is extended through the oligofluorene arms via a thiophene unit which is fused to the peripherals of chemically versatile TTF (DT-TTF). As demonstrated, the methods of synthesis and purification allow obtaining the systems with a high degree of batch-to-batch reproducibility of the final material properties.

This chapter further demonstrates through a gradual increase in conjugation through use of one to four oligofluorene units that the HOMO of the oligofluorene units can be brought closer to the vacuum level. The 1,3-dithiole-2-one building block has been demonstrated as suitable for construction of a TTF core and also suitable for the development of independent redox-active oligofluorene dithiole-2-one systems, referred to in this chapter as half-units.

In the interest of decreasing anisotropy and improving the film forming properties of the material in the solid-state, the systems are developed with a multidimensional architecture in view, thereby resisting crystallinity. The proposed lack of efficient  $\pi$ - $\pi$  stacking, indicates charge transport will be moderate allowing for a suitable charge-mobility/luminescence balance appropriate for potential application in OPVs, with an  $E_g$  that can be beneficial to the open-circuit voltage ( $V_{oc}$ ).

Some results described herein have already been published as:

Tetrathiafulvalene-oligofluorene star-shaped systems: new semiconductor materials for fluorescent moisture indicators, K. Scanlan, A. L. Kanibolotsky, B. Breig, G. J. Hedley and P. J. Skabara, *Journal of Materials Chemistry C*, 2019, **7**, 6582-6591.

## 2.2 Introduction

There is a large scope of existing functional materials in the field of flexible electronics and there are even more materials yet to be discovered. It is important for the advancement in the field that new functional materials are discovered that meet a growing demand. In order to achieve this, it is important to build upon the knowledge uncovered thus far and to be unafraid of trying something new. The earlier chapter has provided information on the theory of molecular design and discusses the intimate link between material design on a molecular level and device performance.

The aim of the project was to exploit chemically versatile tetrathiafulvalene (TTF) due to a number of factors: (i) TTF's symmetry in the neutral form and its changing symmetry upon oxidation; (ii) TTF's reliable redox properties; (iii) TTF's chemical versatility allowing it to be exploited as a chemical building block and (iv) TTF's propensity to provide multidimensional systems. The effects of using molecular building blocks that are planar in character are known. As previously discussed, it is known that a higher degree of molecular ordering facilitates intermolecular charge-carrier transport in the solid-state. Furthermore, it was previously discussed that increasing the dimensionality of a system encourages a resistance to crystallinity, thereby favouring amorphous character in the solid-state. It has been described that for

properties related to emission, amorphous character is desirable for enhancing emission.

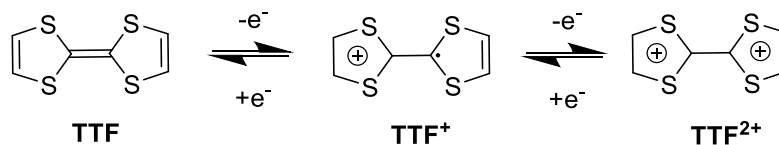
In view of this, it was an aim to develop a series of well-defined multidimensional systems that incorporated versatile TTF coupled to oligofluorene spores, that are known for their properties as blue-light emitters with high photoluminescence quantum yields. It was proposed that the system would have behaved as a molecular switch to the oligofluorene spores, decreasing fluorescence in its neutral form and enhancing in its oxidised form. The incorporation of alkyl substituents into the fluorene C-9 positions makes these systems perfect for attaining molecular solubility. More particularly, the use of hexyl chains in the C-9 positions act to inhibit efficient  $\pi$ - $\pi$  stacking due to orientating orthogonally to the plane of the conjugated system.

In order to increase the system's propensity to fluoresce, encouraging intramolecular electronic communication between the oligofluorene spores was implemented. In preparing new OSC materials, it is important that the synthetic procedure is optimised and somewhat facile. For instance, numerous OSC materials require multistep synthesis and hence may result in an overall lower yield at the end, hence it is beneficial that the steps are capable of being repeated.

### **2.3 Tetrathiafulvalene as a Redox-Switchable Core**

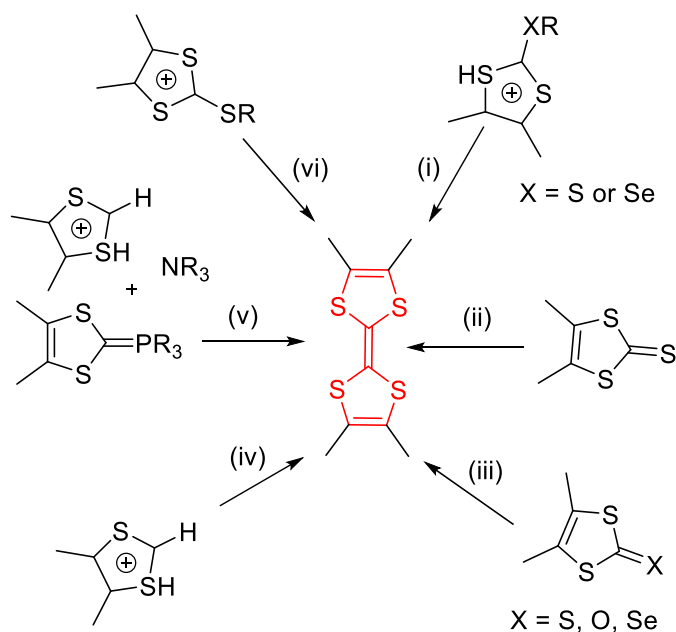
TTF has played a key role in the development of functional materials and has been widely applied as a molecular redox switch, due to its reversible and stable redox properties.<sup>197</sup> The nature of TTF to form ordered stacks in the solid-state often result in anisotropic behaviour due to charge-transport occurring in one dimension, however,

neutral TTF and TTF in its cation,  $\text{TTF}^+$ , and dication,  $\text{TTF}^{2+}$ , states each possess different symmetry, thereby affording the possibility to alter the planar characteristics of the system (Scheme 2-1).

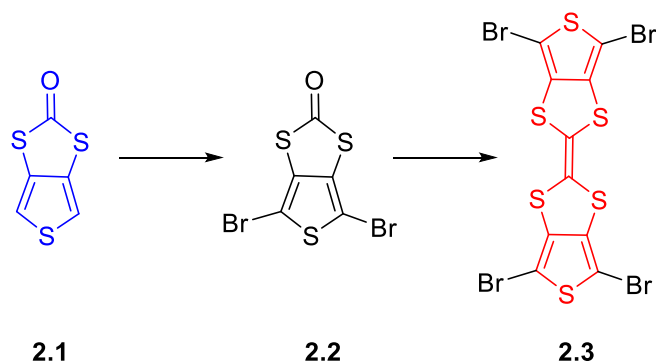


**Scheme 2-1.** Formation of cation and dication state of TTF by removal of one or two electrons respectively.

TTF derivatives tend to be constructed through one of two approaches. The first approach is that TTF is constructed using functionalised precursors as is seen in Scheme 2-2. The second approach is that the TTF is used as a starting material and directly functionalised.

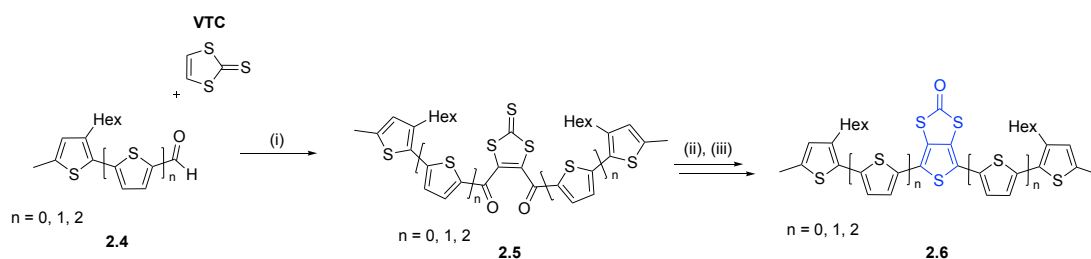


**Scheme 2-2.** An example of synthetic routes to symmetrical TTF, wherein (i)  $\text{PR}_3$ ; (ii)  $\text{M}(\text{CO})_n$ ; (iii)  $\text{PR}_3$ ; (iv)  $\text{NR}_3$ ; (v)  $\text{Zn}/\text{Br}_2$ .



**Scheme 2-3.** Formation of symmetrical tetrathiafulvalene derivative **2.3** through the bromination of thieno[3,4-d][1,3]-dithiole-2-one **2.1**.<sup>198</sup>

The formation of symmetrical TTF has previously been achieved through bromination of thieno[3,4-d][1,3]-dithiol-2-one (scheme 2-3). The 1,3-dithiole-2-one building block has also been used in the formation of cruciform systems with spiro-centres<sup>199</sup> and in the formation of asymmetrical TTF derivatives.<sup>200</sup>



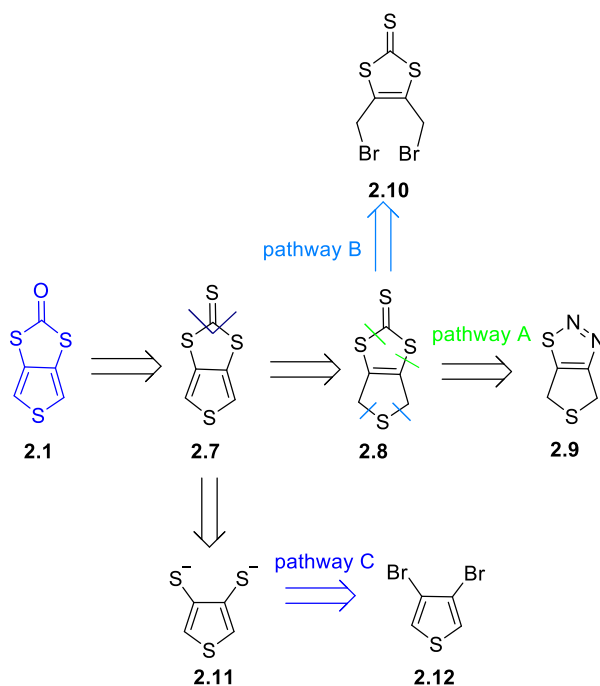
**Scheme 2-4.** The formation of 1,3-dithiole-2-one precursors in the formation of functionalised TTF-oligothiophenes: (i)  $\text{MnO}_2$ ,  $\text{CH}_2\text{Cl}_2$ ; (ii)  $\text{Hg}(\text{OAc})_2$  and (iii)  $\text{P}_2\text{S}_5$ .<sup>201</sup>

The novel series of multi-dimensional end-capped oligothiophenes as shown in Scheme 2-4 have been previously developed, the series thereof comprising methyl-capped ter-, quinque- and septithiophene chains to which a 1,3-dithiole-2-one moiety was fused onto the central thiophene unit **2.5**. Hexyl chains were incorporated into the

3-position of the terminal thiophenes to enhance solubility, these systems were developed with the view of application in OFETs and OPVs. On removal of the carbonyl-protecting group, the 1,3-dithiole-2-one moiety acted as a dinucleophilic synthon, allowing for structural variation of the core. Structural variation afforded by the dinucleophilic synthon allowed for the development of novel thiophene-based systems incorporating redox-active centres TTF and a spiro-germanium core. X-ray diffraction analysis of the developed spirocyclic germanium complex showed the material exhibited aggregation and multi-dimensional  $\pi$ - $\pi$  stacking. High extinction coefficients were observed as well as lower electrochemical HOMO-LUMO gaps vis-à-vis oligothiophenes.<sup>201</sup>

### **2.3.1 Thieno[3,4-*d*][1,3]-dithiole-2-one as a Building Block to Functional Materials**

The thieno[3,4-*d*][1,3]-dithiol-2-one (1,3-dithiole-2-one) moiety **2.1** has been a key building block in the synthesis of various electroactive materials for organic electronics and is available through a variety of synthetic routes (Scheme 2.5).



**Scheme 2-5.** Retrosynthetic pathway showing the different synthetic routes for the formation of thieno[3,4-d][1,3]-dithiole-2-one **2.1** moiety.<sup>202</sup>

The 1,3-dithiole-2-one unit **2.1** can be used to introduce increased dimensionality to organic systems, allowing for multi-dimensional intermolecular interactions to occur in the solid-phase. The sulfur content present in this building block can be exploited to improve film morphology through encouraging short intermolecular sulfur-sulfur interactions.<sup>202, 203</sup> The building block has previously proven synthetically versatile and can be used for incorporating the 2-(1,3-dithiol-2-ylidene)thieno[3,4-d][1,3]dithiole (thieno-TTF) unit into oligomeric or polymeric systems allowing for different components of the system to contribute to the properties of the material.<sup>200,</sup>

201

Chemically versatile 1,3-dithiole-2-one **2.1** may be synthesised from a variety of starting materials. As shown in scheme 2-4, the 1,3-dithiole-2-one moiety may be synthesised through starting material 3,4-dibromothiophene **2.12**, as shown in pathway

C. The removal of bromine from 3,4-dibromothiophene **2.12** provides the formation of a dinucleophilic synthon **2.11** which has been previously used in the construction of cruciform systems with electron rich spiro-centres. The dinucleophilic synthon **2.11** can be used to form the thione derivative, 1,3-dithiole-2-thione **2.7** which can then undergo a facile transchalcogenation reaction using mercury (II) acetate to form the 1,3-dithiole-2-one moiety **2.1**. The thione derivative **2.7** can be synthesised using starting materials that comprise either one of the cyclic rings present in 4,6-dihydrothieno[3,4-d][1,3]dithiole-2-thione **2.8**. For instance, a cyclisation of 4,5-bis(bromomethyl)-1,3-dithiole-2-thione **2.10** can be used to create the dihydrothieno 1,3-dithiole-2-thione derivative **2.8** (pathway B). Moreover, the 1,3-dithiole-2-thione derivative may be obtained from 4,6-dihydrothieno[3,4-d][1,2,3]thiadiazole **2.9** (pathway A).

As a result of the chemical versatility afforded by the 1,3-dithiole-2-one moiety and the capability of the building block to form multidimensional systems while incorporating extended  $\pi$ -conjugated chains, the building block seemed an ideal precursor to the construct the novel series of star-shaped TTF-thiophene-oligofluorene systems **TTF-F $n$ -X** (Figure 2-1).

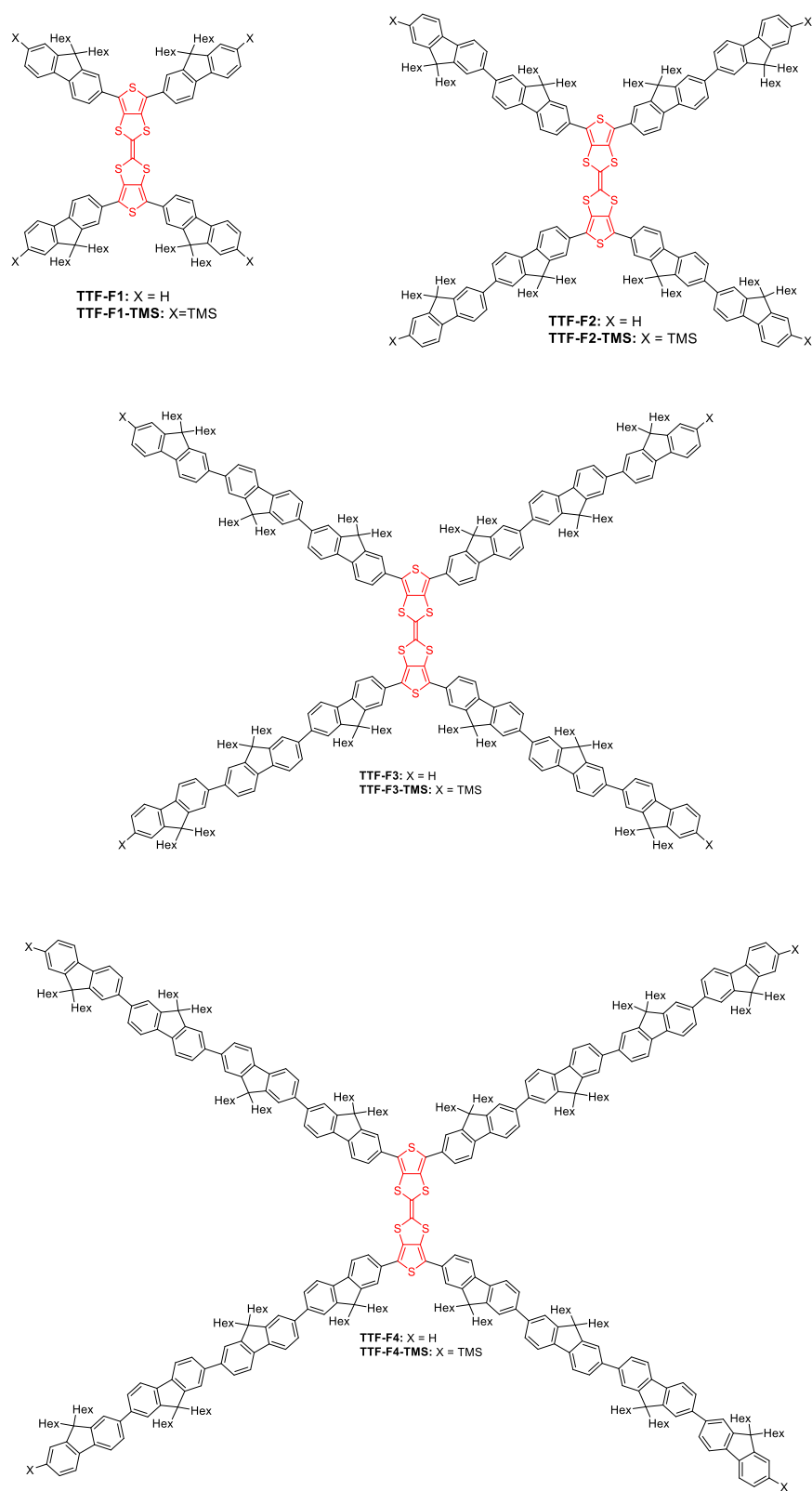


**Figure 2-1.** Structures for new hybrid star-shaped TTF-oligofluorene-thiophene systems.

Two synthetic strategies were employed in the synthesis of these electroactive systems. The first synthetic strategy employs the use of the 1,3-dithiole-2-one **2.1** building block to achieve the **TTF-Fn-X** systems and also affords novel electroactive oligofluorene-thiophene (**HU-F1** and **HU-F2**) intermediates (Figure 2-2), which have been investigated in order to understand the influence the 1,3-dithiole-2-one moiety has on the oligofluorene spores vis-à-vis the tetrathiafulvalene core. The second synthetic strategy employs the use of perbromo-2,2'-bithieno[3,4-*d*][1,3]dithiolyldiene **2.3** as a starting material (scheme 2-3).

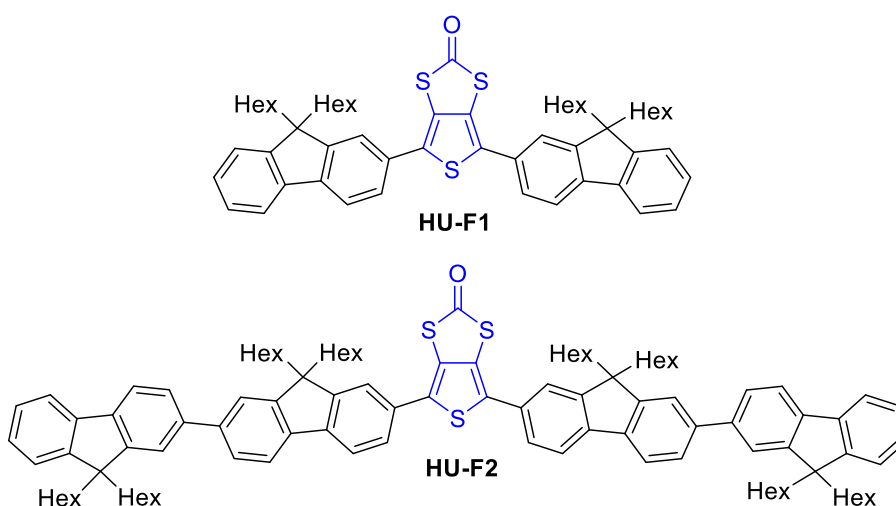


**Figure 2-2.** Structures for new oligofluorene-thiophene (**HU-F1** and **HU-F2**) systems.

The intermediate oligofluorene-thiophene systems (**HU-F1** and **HU-F2**) provide further insight into the physical properties of the unique hybrid TTF-thiophene-oligofluorene systems. Each system **HU-F1**, **HU-F2**, **TTF-Fn-X** incorporates  $\pi$ -conjugated fluorene monomers which are known for their electroluminescent properties.<sup>204, 205</sup> The monodispersity afforded by oligomers is attractive as they provide a well-defined structure and contribute to high purity materials to be prepared.

### 2.3.2 Extending $\pi$ -Conjugation

Fluorene belongs to the class of polycyclic aromatic hydrocarbons. The synthesis of fluorene can be achieved efficiently through a facile approach comprising starting materials 2-iodobiphenyl and  $\text{CH}_2\text{Br}_2$ .<sup>206</sup> Fluorene consists of two biphenyl rings linked by a mutual  $\text{sp}^3$  carbon, resulting in a five-membered ring stacked between the two benzene rings.<sup>207</sup>

Fluorene is unique in that it has properties related to cyclopentadienes as well as benzenes. The methylene bridge promotes the planarity of the phenyl rings, contributing to  $\pi$ - $\pi$  stacking interactions and promoting efficient charge transport through the fluorene-based material.<sup>208</sup> The known emissive properties of polymeric fluorene-based systems have made these materials popular as a building block for semiconducting materials. The reported quantum yields of these materials transcend 50% in solution and within the solid-state.<sup>208</sup> Similarly, well-defined oligofluorene systems have been reported to undergo a  $\pi$ - $\pi^*$  transition in the UV region and emit blue light. As the conjugation length increases, the band gap simultaneously decreases, resulting in a bathochromic shift in absorption and fluorescence.<sup>209, 210</sup>

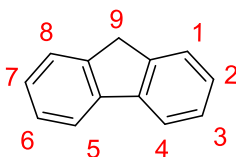


**Figure 2-3.** Fluorene with positions numbered.

As shown in Figure 2-3, the  $\text{sp}^3$  carbon is located at the C9 position and the hydrogen atoms attached to that position are high in acidity and hence, the incorporation of solubilising moieties such as alkyl chains can readily be achieved by treatment of a

strong base and alkyl halide. Deprotonation of the C9 position results in an aromatic fluorenyl anion that is resonance stabilised.<sup>211,212</sup>

The conjugation of fluorene systems can be increased through the C2 and C7 positions, providing extended delocalisation. Polyfluorene systems have been previously synthesised previously using the Suzuki polycondensation reaction. Due to the C9 position being excluded from conjugation of the phenyl rings and relatively isolated from the 2- and 7- positions, the influence of alkyl chains on the optical properties of the polyfluorene systems are minimal. The morphology of oligofluorenes are impacted by the degree of conjugation present and furthermore, by the length of the alkyl chains incorporated.<sup>213</sup> Shorter alkyl chains tend to form crystalline materials, whereas longer chains, e.g. pentyl chains tend to result in an amorphous glassy form.<sup>214</sup>

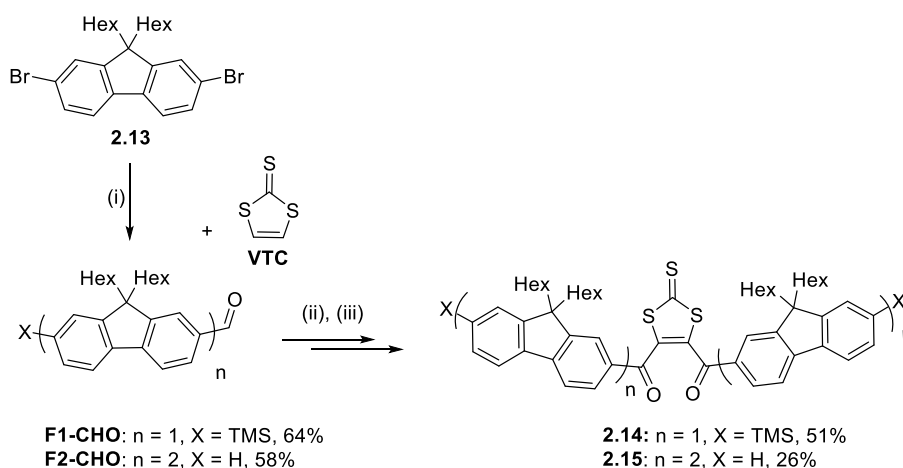
As a result of the versatility and the reliable PL previously exhibited by polyfluorenes combined with their ability to resist  $\pi$ - $\pi$  stacking by virtue of their hexyl chains which orientate perpendicular to the plane of conjugation, oligofluorene moieties were chosen for the development of the PL molecular switches. Oligofluorenes were of preference rather than polyfluorene in order to gauge a better understanding of the structure-property relationships and furthermore, to encourage batch-to-batch reproducibility. Additionally, unsubstituted fluorene is a commercially readily available starting material, making it an ideal compound for large-scale synthesis.

## 2.4 Synthetic Strategy

Two synthetic strategies were employed in the synthesis of TTF-oligofluorene-thiophene **TTF-F<sub>n</sub>-X** systems, both thereof employing a convergent synthesis. These methods differ in that the first strategy (strategy 1) involves the synthesis of the 1,3-dithiole-2-one moiety from vinylene trithiocarbonate (VTC); whereas, the second strategy (strategy 2) uses perbromo-2-2'-bithieno[3,4-*d*][1,3]dithiolydene as a starting material. The latter method has proven itself to be a more efficient strategy and comprises fewer synthetic steps and higher yields.

### 2.4.1 Synthetic strategy 1: 1,3-dithiole-2-one as a starting material

The first convergent synthetic approach employed VTC and was based on a previous procedure.

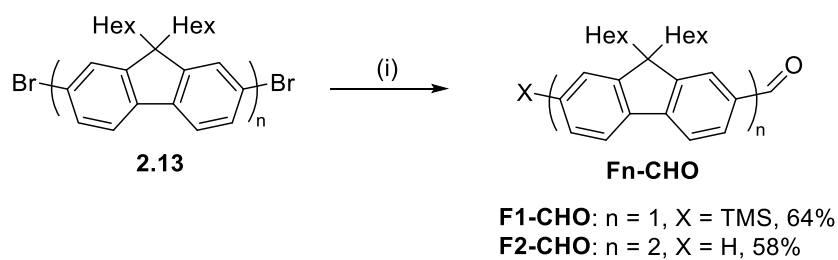


Reaction and conditions: (i) [ $n = 1$ ]  $n\text{-BuLi}$ ,  $\text{TMSCl}$ ,  $n\text{-BuLi}$ ,  $\text{DMF}$ ,  $-78^\circ\text{C}$ , [ $n = 2$ ]  $n\text{-BuLi}$ ,  $\text{DMF}$ ; (ii)

$\text{LDA}$ ,  $\text{THF}$ ,  $\text{THF}$ ,  $-55^\circ\text{C}$ ; (iii)  $\text{MnO}_2$ ,  $\text{CH}_2\text{Cl}_2$ ,  $rt$ , 1 min.

**Scheme 2-6.** Formation of 1,3-dithiole-2-thione derivatives using aldehydes **F1-CHO** and **F2-CHO** via a two-fold lithium-halogen reaction.

VTC was used as the starting material for the preparation of compound **2.14** and **2.15**. The synthesis was performed using two consecutive reaction sequences that consisted of lithiation of the VTC core followed by electrophilic attack by the respective corresponding aldehydes **F1-CHO** and **F2-CHO** (scheme 2-6). Fluoren-2-carboxaldehyde derivatives **F1-CHO** and **F2-CHO** were synthesised as starting materials prior to the coupling reaction (Scheme 2-7). The method for these novel monofluorene- and bifluorene- aldehydes were based upon a similar procedure used in the development of hybrid tetrathiafulvalene-oligothiophene systems.<sup>78</sup>



*Reaction and conditions: (i)  $n\text{-BuLi}$ ,  $\text{SiMe}_3\text{Cl}$ ,  $n\text{-BuLi}$ ,  $\text{DMF}$ ,  $-78^\circ\text{C}$ .*

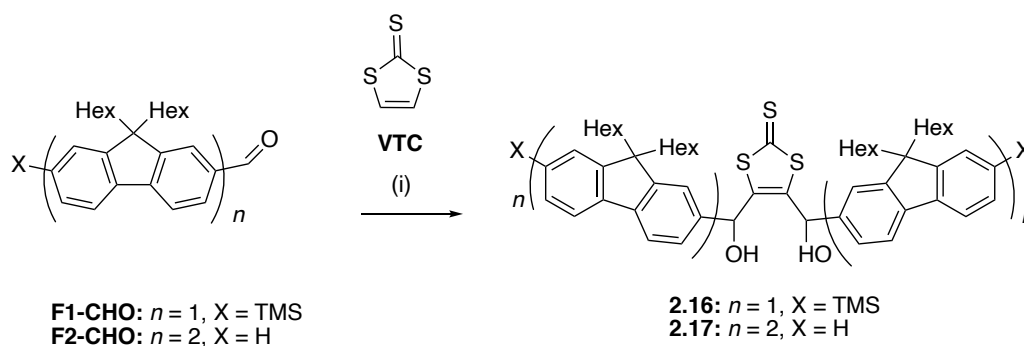
**Scheme 2-7.** Formation of oligofluorene-aldehyde derivatives.

The monofluorene aldehyde **F1-CHO** and the bifluorene aldehyde **F2-CHO** were achieved in two sequential lithium-halogen exchange reactions using *n*-butyllithium reagent. The lithium organic intermediates formed were reacted first with trimethylsilyl chloride and subsequently with dimethylformamide (DMF).

The trimethylsilyl substituent was used as a protective group to prevent possible by-processes related to the Li-Br exchange in the subsequent reaction of the aldehyde with Li-organic reagents. Compound **F1-CHO** was isolated using chromatography with a

hexane: dichloromethane gradient elution affording the system in 64% yield and **F2-CHO** was isolated similarly and in a 58% yield.

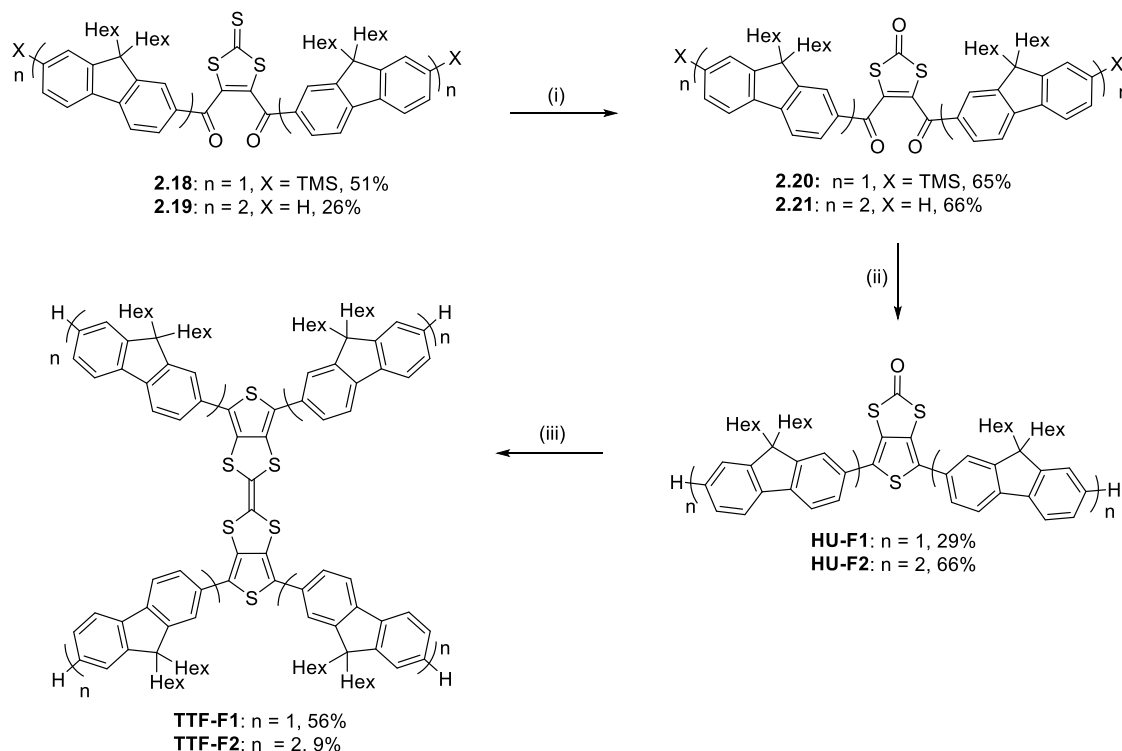
Lithiation was achieved through the use of strong base, lithium diisopropylamide, (LDA). The reaction resulted in the formation of an unstable diol intermediate (Scheme 2-8) and as a consequence, the reaction was immediately oxidised using manganese dioxide. Compound **2.16** was isolated on silica gel using a toluene: hexane solvent system, affording amorphous solid in 51% yield. Compound **2.17** was isolated similarly using a hexane: toluene gradient solvent system, affording an amorphous solid in 26% yield.



*Reaction and conditions: (i) LDA, THF, THF, -55°C.*

**Scheme 2-8.** Formation of diol intermediate during the formation of 1,3-dithiole-2-thione derivative.

Compounds **2.20** and **2.21** were synthesised through a transchalcogenation reaction that transformed the 1,3-dithiole-2-thione units of compounds **2.18** and **2.19** to the corresponding oxo-derivative using mercury (II) acetate based on a procedure used for the development of hybrid tetrathiafulvalene-oligothiophene systems.<sup>78</sup> As shown in Scheme 2.6 reaction was conducted at room temperature, overnight affording **2.20** and **2.21** as desilylated amorphous solid in 65% and 66% yield, respectively.



*Reaction and conditions:* (i)  $\text{Hg}(\text{OAc})_2$ ,  $\text{CH}_2\text{Cl}_2/\text{CH}_3\text{COOH}$  (3:1 v/v), rt, overnight; (ii)  $\text{P}_2\text{S}_5$ ,

$\text{NaHCO}_3$ , 1,4-dioxane,  $90^\circ\text{C}$ ; (iii)  $\text{P}(\text{OEt})_3$ ,  $125^\circ\text{C}$ .

**Scheme 2-9.** Synthesis of oligofluorene-thiophene derivatives (**HU-F1** and **HU-F2**)

tetrathiafulvalene-oligofluorene-thiophene derivatives (**TTF-F1** and **TTF-F2**) using 1,3-dithiole-2-one derivatives.

Compounds **HU-F1** and **HU-F2** were synthesised using a procedure similar to the Paal-Knorr thiophene reaction (Scheme 2-9). The reaction was achieved using phosphorous pentasulfide producing the thiophene unit between the fluorene moieties. Five equivalents of  $\text{NaHCO}_3$  as a base were used in the procedure, however these reaction conditions were too acidic for preserving the trimethylsilyl substituents. As a result, **HU-F1** was desilylated.

The reaction afforded **HU-F1** and **HU-F2** as amorphous solid in 29% and 66% yield, respectively. A homocoupling reaction using freshly distilled P(OEt)<sub>3</sub> afforded **TTF-F1** and **TTF-F2** in yields 56% and 9% respectively. The yields for each system TTF-F<sub>n</sub>-H, where n = 1 or 2; F<sub>n</sub>-CHO, wherein n = 1 or 2 and HU-F<sub>n</sub>, wherein n = 1 or 2 are shown in Table 2-1.

**Table 2-1.** The yields obtained by compounds synthesised for use in the synthetic route for coupling oligofluorenes to VTC.

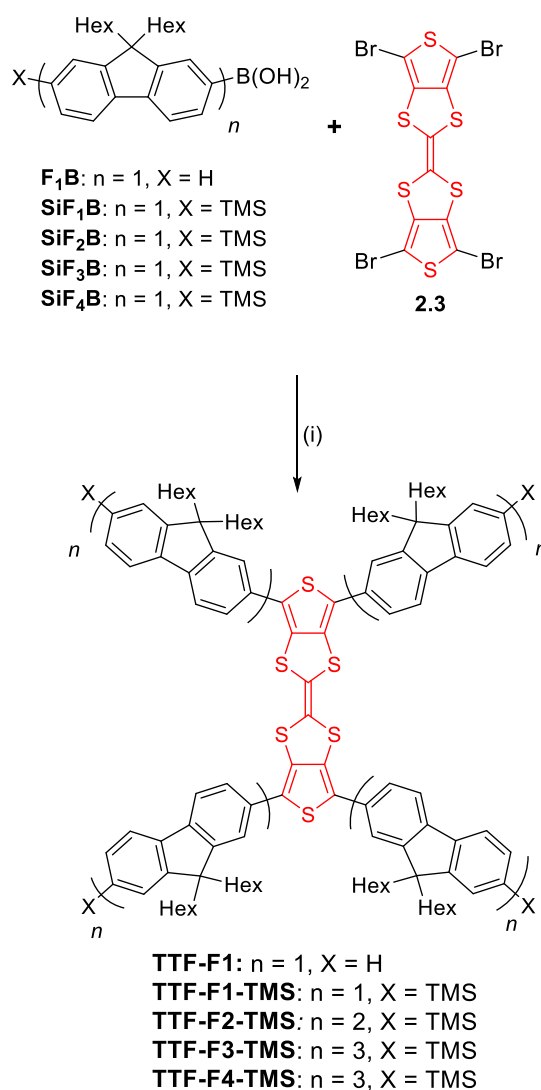
	Number of fluorene monomers ( <i>n</i> )	Yield (%)
<b>F1-CHO</b>	1	64
<b>F2-CHO</b>	2	58
<b>HU-F1</b>	1	29
<b>HU-F2</b>	2	66
<b>TTF-F1</b>	1	56
<b>TTF-F2</b>	2	9

#### **2.4.2 Synthetic strategy 2: perbromo-2,2'-bithieno[3,4-d][1,3]dithiolylidene as a starting material**

The convergent strategy for the synthesis of **TTF-F<sub>n</sub>-X** (n=1-4) series employing the Suzuki coupling protocol is presented in Scheme 2-10. Perbromo-2,2'-bithieno[3,4-*d*][1,3]dithiolylidene **2.3** was used as a starting material.

Microwave-assisted Suzuki polycondensation reactions are known for saving time in multistep synthetic reactions vis-a-vis classical conditions. Furthermore, the reaction

is reported to positively influence the yields of materials while sustaining the physicochemical behaviour of the products.<sup>215</sup> As a result, of the low yields exhibited in strategy 1, wherein fluorene units were built into the 1,3-dithiole-2-one system prior to the formation of TTF, a different strategy was considered. In the following strategy, the oligofluorene units were constructed independently of the 1,3-dithiole-2-one moiety and the TTF moiety. The target system remains identical to the goal system in strategy 1.<sup>198</sup>



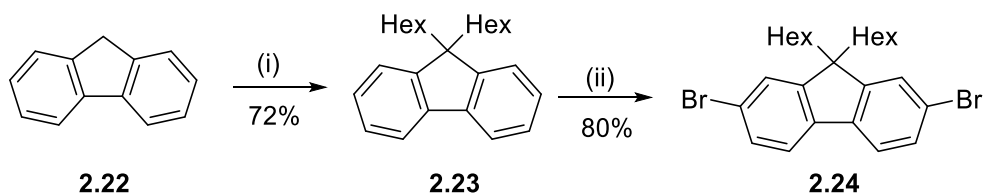
Reaction and conditions: (i)  $Pd(PPh_3)_4$ ,  $Ba(OH)_2 \cdot 8H_2O$ , THF, 140°C, 2h.

**Scheme 2-10.** Formation of the TTF-oligofluorene-thiophene systems **TTF-Fn-X**.

### 2.4.2.1 Synthesis of Oligofluorene Spores

The synthesis of the oligofluorene arms was based on a previous methodology employing the Suzuki coupling.<sup>205</sup> The initial step in the synthetic route was preparation of the 9,9-dihexylfluorene **2.24**. Commercially available reagents fluorene **2.22** and potassium tert-butoxide were used for alkylation reaction as the starting material and a base, respectively. *n*-Butyllithium can be used to deprotonate the C-9 position, however potassium tert-butoxide is sufficient and provides milder conditions. Hexylation was achieved in a solution of tetrahydrofuran (THF) by trapping the carbanion with excess of 1-bromohexane (Scheme 2-11).

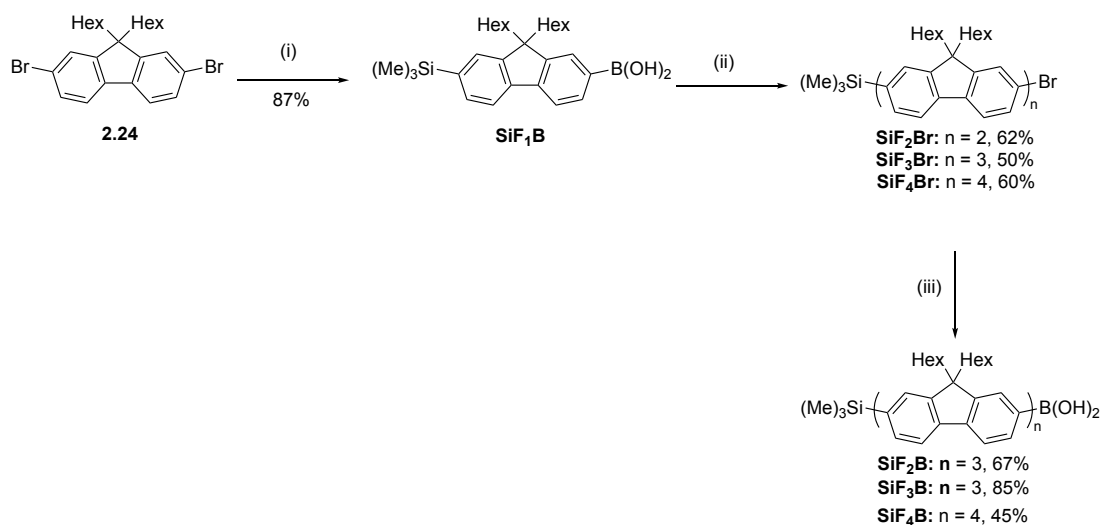
9,9-Dihexylfluorene **2.23** was used as a starting material in the preparation of 9,9-dihexyl-2,7-dibromofluorene **2.24** using 2.5 equivalents of bromine and a catalytic amount of iodine. This light-sensitive reaction proceeded via electrophilic aromatic substitution. The reaction mixture was purified through two sequential recrystallisations before proceeding with bromination. Bromination at both the 2- and 7- positions was strategic in order to provide facile purification of the dibrominated fluorenyl derivative, as the monobrominated derivative affords an oil and requires flash column chromatography for purification.<sup>216</sup> A dibromination as opposed to a monobromination was a strategic decision due to the ease of purification enabled by a dibrominated fluorenyl derivative. The dibrominated derivative **2.24** was successfully isolated, affording colourless crystals in 80% yield.



*Reaction and conditions: (i) KO<sup>t</sup>Bu, C<sub>6</sub>H<sub>13</sub>Br; (ii) Br<sub>2</sub>, rt.*

**Scheme 2-11.** Preparation of 9,9-dihexyl-2,7-dibromofluorene **2.24**.

In the preparation by Suzuki cross-coupling reaction, the 9,9-dihexyl-2,7-dibromofluorene **2.24** was converted to the fluorenyl boronic acid **SiF<sub>1</sub>B** through lithium-halogen exchange using *n*-butyllithium. The 2- position on the bromo-functionalised fluorene **2.24** was substituted for a trimethylsilyl (TMS) as a protective group to prevent polymerisation during the subsequent coupling reaction. The reaction proceeded through two consecutive sequences of lithiation followed by quenching the lithium-organic compound formed with trimethylsilyl chloride in the first sequence and triisopropyl borate in the second sequence.



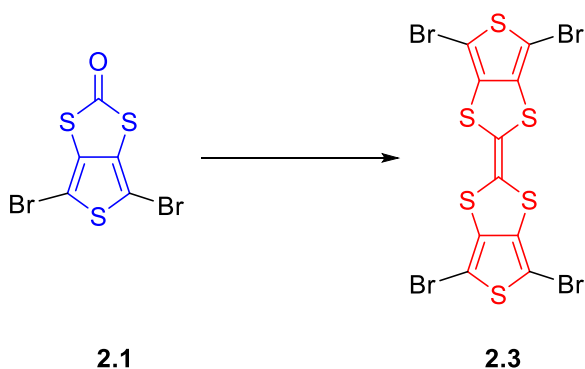
*Reaction and conditions: (i) n-BuLi, Me<sub>3</sub>SiCl, n-BuLi, B(iPrO)<sub>3</sub>, -78, THF, -78°C; (ii) Pd(PPh<sub>3</sub>)<sub>4</sub>,*

*Na<sub>2</sub>CO<sub>3</sub>, toluene, 80°C; (iii) n-BuLi, B(iPrO)<sub>3</sub>, -78°C.*

**Scheme 2-12.** Preparation of oligofluorene arms (n = 1-4) through the Suzuki coupling.

A three-fold excess of 2,7-dibromo-9,9-dihexylfluorene **2.24** was used in the presence of tetrakis(triphenylphosphine)palladium catalyst. The excess was used to inhibit the formation of corresponding trimer during dimer formation. Compound **SiF<sub>2</sub>Br** was isolated affording an amorphous solid in 50% yield. The same reactions were repeated to form the terfluorene **SiF<sub>3</sub>Br** and quaterfluorene **SiF<sub>4</sub>Br** derivatives, exploiting the lithium-halogen exchange achieved by *n*-butyllithium and substituting the bromine substituent for a boronic acid, providing appropriate functionalised reagents for a new coupling wherein the monomer units are extended (Scheme 2-12).

In order to encourage electronic communication between the oligofluorene arms, a thiophene unit was required at the peripherals of the TTF, thereby forming dithiophene-tetrathiafulvalene (DT-TTF) **2.3**. The formation of DT-TTF is possible also through the use of the 1,3-dithiole-2-one building block **2.1** through a facile homocoupling reaction using reagent triethyl phosphite (Scheme 2-13).



**Scheme 2-13.** Formation of starting material perbromo-2,2'-bithieno[3,4-d][1,3]dithiolylylidene **2.3**.<sup>200</sup>

The versatile Suzuki reaction was employed and TTF-F1 was prepared through the coupling of Tetrabromo-TTF **2.3** to fluorenyl boronic acid **F<sub>1</sub>B** in a microwave-assisted reaction. Barium hydroxide was employed in excess as a strong base to encourage an

efficient coupling. The temperature of the reaction was raised step-wise above the boiling point of THF to promote the four-fold coupling of the oligofluorenyl boronic acid.

**Table 2-2.** The yields attained by compounds synthesised through coupling to perbromo-2,2'-bithieno[3,4-d][1,3]dithiolylidene.

	Number of fluorene monomers ( <i>n</i> )	Yield (%)
<b>TTF-F1</b>	1	56
<b>TTF-F2</b>	2	9
<b>TTF-F1-TMS</b>	1	65
<b>TTF-F2-TMS</b>	2	65
<b>TTF-F3-TMS</b>	3	64
<b>TTF-F4-TMS</b>	4	36

The same synthetic approach was used to obtain **TTF-F<sub>n</sub>-TMS** (n=2-4) employing the same reaction conditions and using the corresponding oligofluorenyl boronic acids **SiF<sub>3</sub>B-SiF<sub>3</sub>B** to form these new star-shaped systems. As shown in Table 2-2, the yields for the **TTF-F<sub>n</sub>-X** series using this efficient method are all within 60-65%, with the exception of **TTF-F<sub>4</sub>-TMS** (yield 36%). The loss in yield is attributed to the higher molecular weight of the TTF-oligofluorene system that can inhibit efficient cross-coupling reactions.

## 2.5 Results and discussion

### 2.5.1 Thermal properties

For materials designed with a view in optoelectronic applications, thermal stability is a contributing factor to the life-time of devices. As a result, the thermal properties of these TTF-Fn-X and HU-Fn systems were of interest with respect to their application as PL molecular switches.

Thermogravimetric analysis was performed using the Perkin Elmer Thermogravimetric Analyser TGA7 under a constant flow of argon. Differential scanning calorimetry was conducted on the TA Instruments Q1000 with a RC-90 refrigerated cooling unit attached. The calibration was achieved using indium (melt temperature 156.42 °C,  $\Delta H_f$  28.42 J/g). The procedure used was a standard heat-cool-heat cycle in the range of -50 to 500 °C at a heating rate of 5 or 10 °C/min.

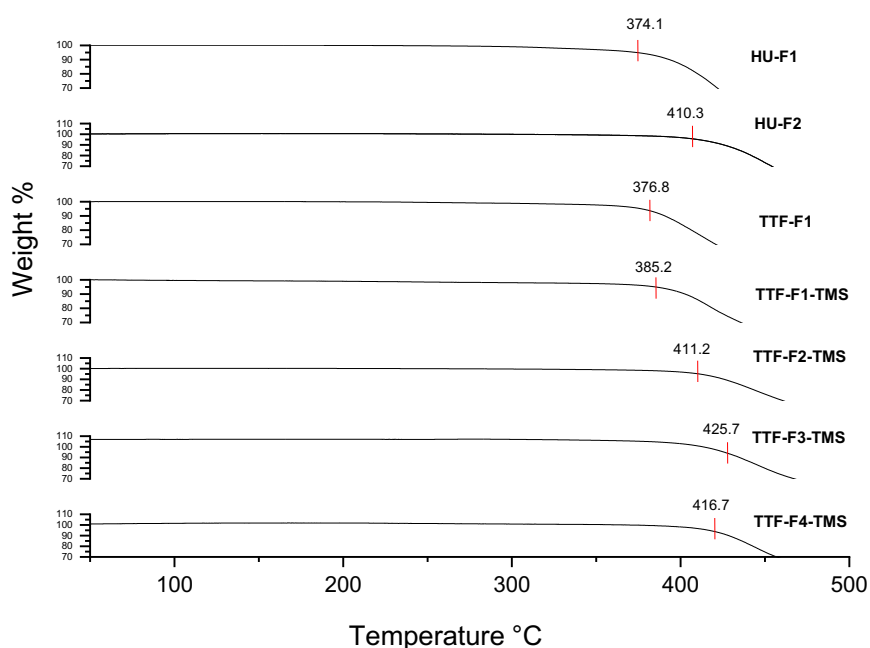


**Figure 2-4.** Thermal gravimetric analysis (TGA) showing decomposition temperature ( $T_d$ , 5% mass loss) of compounds **HU-F1-2** and **TTF-(F1-F4)-X** series.

Thermal gravimetric analysis (TGA) was used to obtain information on the thermal properties of the **TTF-F1** and **TTF-F1-TMS** to **TTF-F4-TMS** systems. In Figure 2-4 we observe thermal stability for each TTF-bearing system with decomposition temperatures ( $T_d$ , 5% mass loss) above 370 °C. Because most optoelectronic devices are not used at such high temperatures, these high decomposition temperatures are accepted and show the high heat-resilience of these materials. The mass loss and glass transition temperatures for the series **TTF-F<sub>n</sub>-X** series and **HU-F<sub>n</sub>** series are shown in Table 2-3. As expected the highest decomposition temperature,  $T_d$ , was observed for the TTF system containing the four terfluorene oligomer arms: **TTF-F3-TMS** at 426 °C and **TTF-F4-TMS**, containing four quaterfluorene oligomer arms, had a similar  $T_d$  of 417 °C. The lowest  $T_d$  was observed for the non-trimethylsilyl substituted monofluorene-TTF system **TTF-F1** ( $T_d$  of 377 °C) and together with **TTF-F1-TMS** showing ( $T_d$  of 385 °C), these two systems were considered the least stable. By comparison, the monofluorene unit containing the 1,3-dithiole-2-one core **HU-F1** had a  $T_d$  of 374 °C similar to **TTF-F1**. The bifluorene half-unit **HU-F2** had a higher  $T_d$  of 410 °C comparable to that of its TTF analogue **TTF-F2-TMS** that showed  $T_d$  of 411 °C.

**Table 2-3.** Thermal properties of compounds **HU-F<sub>n</sub>** (n = 1-2) and **TTF-F<sub>n</sub>-X** series.

	$M_w$ (g mol <sup>-1</sup> )	$T_g$ (°C)	$T_d$ (5% mass loss, °C)
<b>HU-F1</b>	839.31	25	374
<b>HU-F2</b>	1504.37	61	410
<b>TTF-F1</b>	1646.63	65	377
<b>TTF-F1-TMS</b>	1935.35	-	385

	$M_w$ (g mol <sup>-1</sup> )	$T_g$ (°C)	$T_d$ (5% mass loss, °C)
<b>TTF-F2-TMS</b>	3265.48	83	411
<b>TTF-F3-TMS</b>	4595.60	91	425
<b>TTF-F4-TMS</b>	5925.73	96	417

In differential scanning calorimetry (DSC) experiments, a glass transition temperature,  $T_g$ , is observed for all compounds apart from the trimethylsilyl substituted monofluorene–TTF system **TTF-F1-TMS**. All TTF-bearing systems are of an amorphous morphology with glass transition temperatures in the range of 25–96 °C. The amorphous nature of these materials is expected, given the non-planar characteristics of the oligofluorenyl moieties and the 2D architecture of the system which will resist crystallinity.

In addition to the glass transition temperature the bifluorene system comprising the 1,3-dithiole-2-one core **HU-F2** and its TTF analogue **TTF-F2-TMS** possess a crystallisation and melting point. An increased or improved molecular ordering of the system could be the underlying cause as a result of the absence of the TTF core and two oligofluorene spores. The resulting star-shape is suggested to be in a less ordered arrangement. **HU-F1** has the lowest glass transition temperature at 25 °C and the largest system in the series **TTF-F4-TMS** has the highest glass transition at 96 °C. As is shown in Table 2-3, this is in accordance with the trend in molecular weights, wherein the lowest weighing system is **HU-F1** and the highest is **TTF-F4-TMS**. When comparing these results with monodisperse star-shaped oligofluorenes with a central truxene core similar trends have been observed, in which glass transition temperatures increase with higher molecular weight.<sup>69, 205</sup>

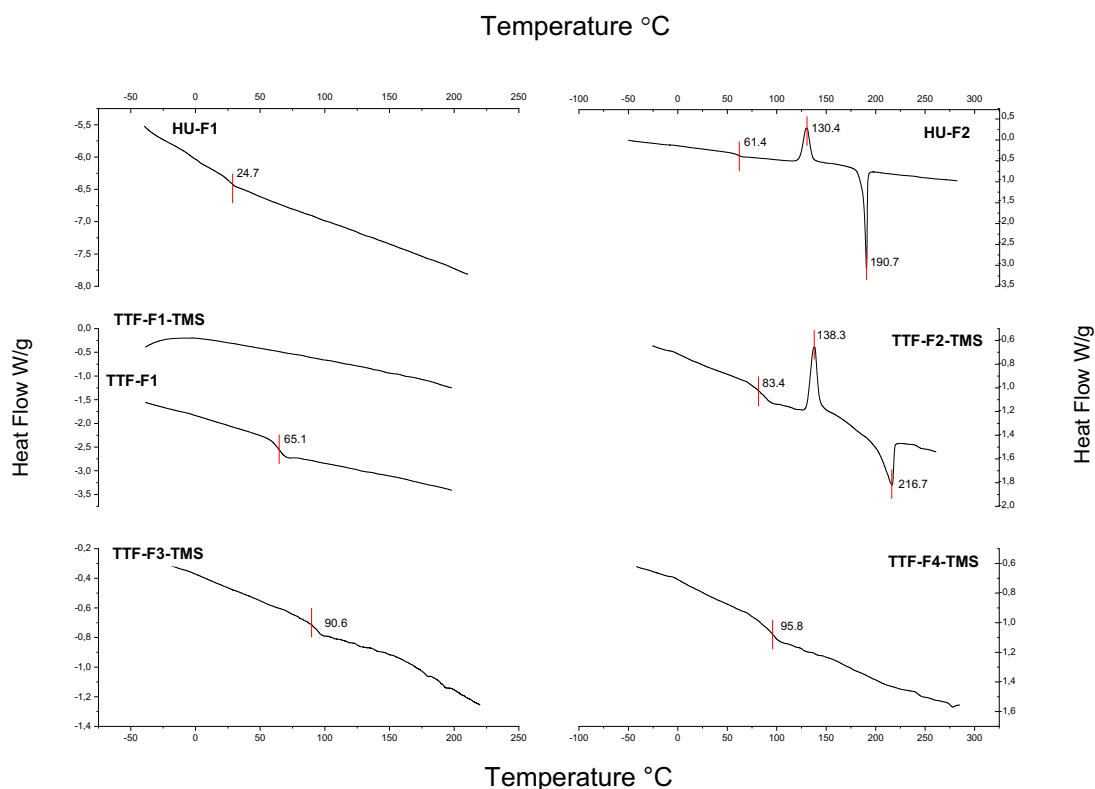


Figure 2-5. DSC of compounds HU-F1-2 and TTF-F(1-4)-X series showing glass transition temperatures ( $T_g$ ).

### 2.5.2 Electrochemical properties

Cyclic voltammetry measurements were obtained using the CH Instruments 660A electrochemical workstation with iR compensation using anhydrous dichloromethane. The scan rate used for all experiments was  $0.1 \text{ V s}^{-1}$ . The electrodes used were glassy carbon, platinum wire and silver wire as the working, counter and reference electrodes, respectively. All solutions were degassed with argon and contained compounds of ca.  $10^{-3} \text{ M}$  and TBAPF<sub>6</sub> (0.1 M) as the supporting electrolyte. All measurements were referenced against  $E_{1/2}$  of the Fc/Fc<sup>+</sup> redox couple.

The electrochemical properties of compounds **HU-F $n$**  and the **TTF-F $n$ -X** series are summarised in Table 2-4. All compounds were run in dichloromethane (DCM) and were not oxidised further than a potential of +2.2 V *versus* Fc/Fc<sup>+</sup> to avoid over-oxidation. The non-trimethyl substituted monofluorene TTF system **TTF-F1** exhibited three quasi-reversible waves upon oxidation at half-wave potentials of +0.30 V, +0.76 V, +1.09 V and one irreversible oxidation wave at +1.28 V. As described previously the first two redox waves are ascribed to the TTF unit<sup>86, 217</sup> and the last two are contributed to the oxidation of conjugated segments in the system, which contain fluorene units attached to the 2- and 5-positions of the peripheral thiophenes. In contrast, the TMS substituted monofluorene TTF system **TTF-F1-TMS** exhibited three quasi-reversible at half-wave potentials of +0.34 V, +0.81 V, +1.13 V and three irreversible oxidation waves with anodic peaks at +1.27 V, +1.36 V and +1.47 V. The formation of the radical cation and dication occurs at potentials similar to those for **TTF-F1** and are consistent with the electrochemical properties of TTF. The TMS substituent allows for additional oxidation waves to be observed, albeit, the lack of reversibility exhibited by these additional waves shows the system struggles to support multi-charged states due to columbic repulsions in the small molecule. Similar properties have been observed in small TTF-bearing molecules previously.

**Table 2-4.** Electrochemical properties of compounds HU-Fn and TTF-Fn-X series, alongside the optical HOMO-LUMO energy gaps,  $E_g^{opt}$ , extracted from the corresponding absorption spectra.

	$E_{ox}^p$ (V) <sup>a</sup>	HOMO (eV) <sup>b</sup>	$E_{red}^p$ (V)	LUMO (eV) <sup>b</sup>	$E_g^{EC}$ (eV)	$E_g^{opt}$ (eV) <sup>c</sup> [ $\lambda_{onset}$ (nm)]
<b>HU-F1</b>	+0.78/+0.52, +1.11, +1.89	-5.45	-	-2.48	2.97	2.88 (430)
<b>HU-F2</b>	+0.77/+0.72, +0.93/+0.88, +1.19/+1.12, +1.48/1.34	-5.55	-2.35	-2.58	2.97	2.66 (466)
<b>TTF-F1</b>	+0.39/+0.21, +0.82/+0.69, +1.14/+1.04, +1.28	-5.1	-2.48	-2.33	2.77	2.84 (436)
<b>TTF-F1-TMS</b>	+0.44/+0.24, +0.89/+0.74, +1.18/+1.08, +1.27, +1.36, +1.47	-5.14	-	-2.42	2.72	2.81 (442)
<b>TTF-F2-TMS</b>	+0.41/+0.23, +0.87/+0.80, +1.19/+1.02, +1.36/+1.21	-5.12	-	-2.53	2.59	2.72 (455)
<b>TTF-F3-TMS</b>	+0.57/+0.35, +0.93/+0.85, +1.17/+1.07, +1.54/+1.43, +1.64/1.55	-5.26	-	-2.57	2.69	2.72 (456)
<b>TTF-F4-TMS</b>	+0.61/+0.28, +0.84/+0.77, +0.99/+0.92, +1.31/+1.17, +1.49/+1.36, +1.59/+1.43	-5.25	-	-2.59	2.66	2.71 (457)

*<sup>a</sup>The positions of peaks on the forward/reverse scan vs. the Fc/Fc<sup>+</sup> redox couple are given for reversible or quasi-reversible waves; for irreversible processes the peaks on a forward scan are presented. <sup>b</sup>The electrochemical HOMO (LUMO) level was calculated using the half-wave potential of the first oxidation wave or the onset of the first irreversible reduction wave, taking into account that the HOMO of Fc is 4.8 eV. <sup>c</sup>The optical HOMO–LUMO gap ( $E_g$ ) has been estimated using the formula  $E_g = 1239.84/\lambda_{\text{onset}}$  from absorption onset ( $\lambda_{\text{onset}}$ ) shown in brackets (in nm). <sup>d</sup>The electrochemical HOMO is estimated from the energy difference between the LUMO and HOMO levels.*

By comparison, the monofluorene system containing 1,3-dithiole-2-one HU-F1 exhibiting one quasi-reversible wave at a half-wave potential of +0.65 V and two irreversible waves with peak potentials at +1.11 V and +1.89 V. The first oxidation appears at a higher onset at around +0.7 V due to the absence of the electroactive TTF core. The bifluorene system bearing a TTF core HU-F2 exhibits three reversible oxidation waves at half-wave potentials of +0.74 V, +0.90 V and +1.15 V and two irreversible waves at –2.35 V and –2.48 V.

The calculated electrochemical HOMO–LUMO gap values for the systems containing the 1,3-dithiol-2-one moiety **HU-F1** and **HU-F2** were found to be 2.97 eV, *ca.* 0.09–0.31 eV higher than the corresponding optical HOMO–LUMO gap. In contrast, the non-substituted monofluorene TTF system TTF-F1 was found to have a HOMO–LUMO gap of 2.77, while the trimethylsilyl-substituted derivative TTF-F1-TMS possessed a similar gap of 2.72. TTF-oligofluorene systems with extended conjugation TTF-F2-TMS, TTF-F3-TMS and TTF-F4-TMS have a slightly lower HOMO–LUMO gaps of 2.59, 2.69 and 2.66, respectively. While there is an increase in conjugation, the HOMO–LUMO gaps have not changed substantially confirming that TTF is responsible for the first oxidation wave in these systems.

From the anodic/cathodic peaks of the oxidation waves, presented in Table 2-4, with the voltammograms shown in Figure 2-6, it was concluded that the length of the arms played a key role in oxidation reversibility and doping stability: with increasing fluorene unit per oligomer arm, more reversible and quasi-reversible oxidation waves were observed, demonstrating an improved stability towards p-doping in the system with longer conjugation paths.

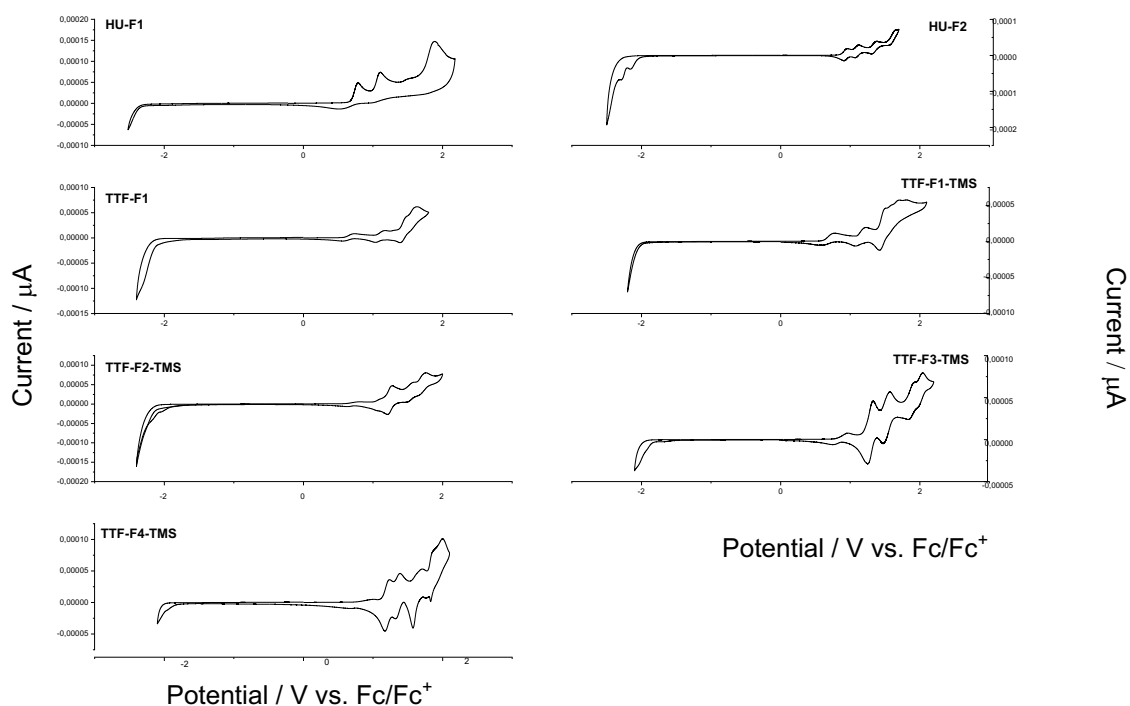


**Figure 2-6.** Cyclic voltammetry of compounds HU-F1 and TTF-(F1-F4)-X in  $\text{CH}_2\text{Cl}_2$ .

Furthermore, a comparison was made of the electrochemical properties of the TTF-cored star-shaped systems against well-defined and discussed monodisperse star-shaped oligofluorenes with a central truxene core (Figure 2-7). Trux-1 to 4 possess an interesting 2D architecture that helps in the arene-arene stacking/self-association which provides overall stability. Interestingly, the estimated band gaps,  $E_g^{opt}$ , of these

oligomers were quite high (reported in the range 3.05 – 3.29 eV) and exceeded the band gap energies found for the TTF-cored systems.

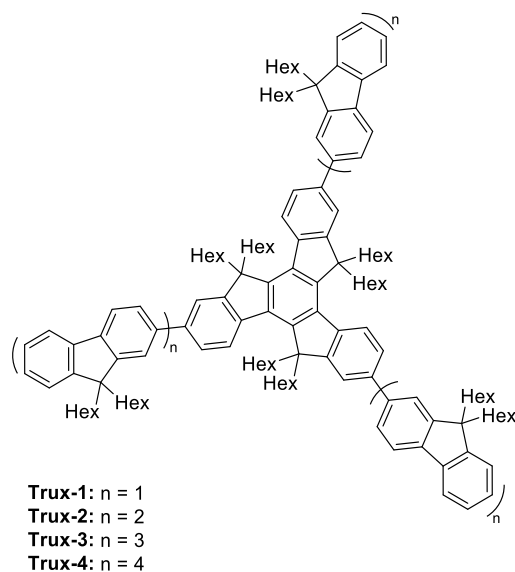


**Figure 2-7.** Structure of star-shaped oligofluorene-truxene derivatives.

The lower estimated band gap energy of the TTF-cored star-shaped systems may partially be attributed to the additional arm present in those systems as compared to the 3-armed oligofluorene-truxene systems. However, the colourless nature of the truxene systems vis-à-vis the yellow colour of the TTF-Fn-X systems, suggests that the band gap of truxene is wider.

### 2.5.3 Optical properties

Emission spectra were recorded using the Perkin Elmer L545 or the Jasco FP-6500 fluorescence spectrometer. Both absorption and emission solutions contained compounds of ca.  $10^{-6}$  M. Photoluminescence quantum yields were measured with the Quantaaurus Plus from Hamamatsu Photonics. The sample (fused silica solution cuvette or thin film sample placed in fused silica petri dish) was placed inside a spectralon coated integrating sphere and fibre coupled excitation is provided with a high-power xenon lamp, filtered for 50 nm bandwidth around the stated wavelength. Detection was made with a baffle protected fibre output port on the sphere, with light coupled into a backthinned multichannel CCD, recording both the excitation and emission spectrum. Measurements were performed by first measuring a blank to capture the power of the excitation, then with the sample to determine the amount of light absorbed and emitted. Software integration of the areas under the peaks, and correction for photometric responses of the sphere, fibres etc., all lead to a final value of the PLQY that is automatically calculated in the Hamamatsu supplied software. UV-Vis absorption spectra were recorded using the UNICAM UV 300, the Jasco V-660 or the Shimadzu UV-2600. The baseline of solvents were measured prior to analysis and the solution spectra recorded in 1 cm or 1 mm path length quartz cells between 190-900 nm.

The absorption and emission properties of compounds **HU-F $n$**  and the **TTF-F $n$ -X** series in DCM were investigated.

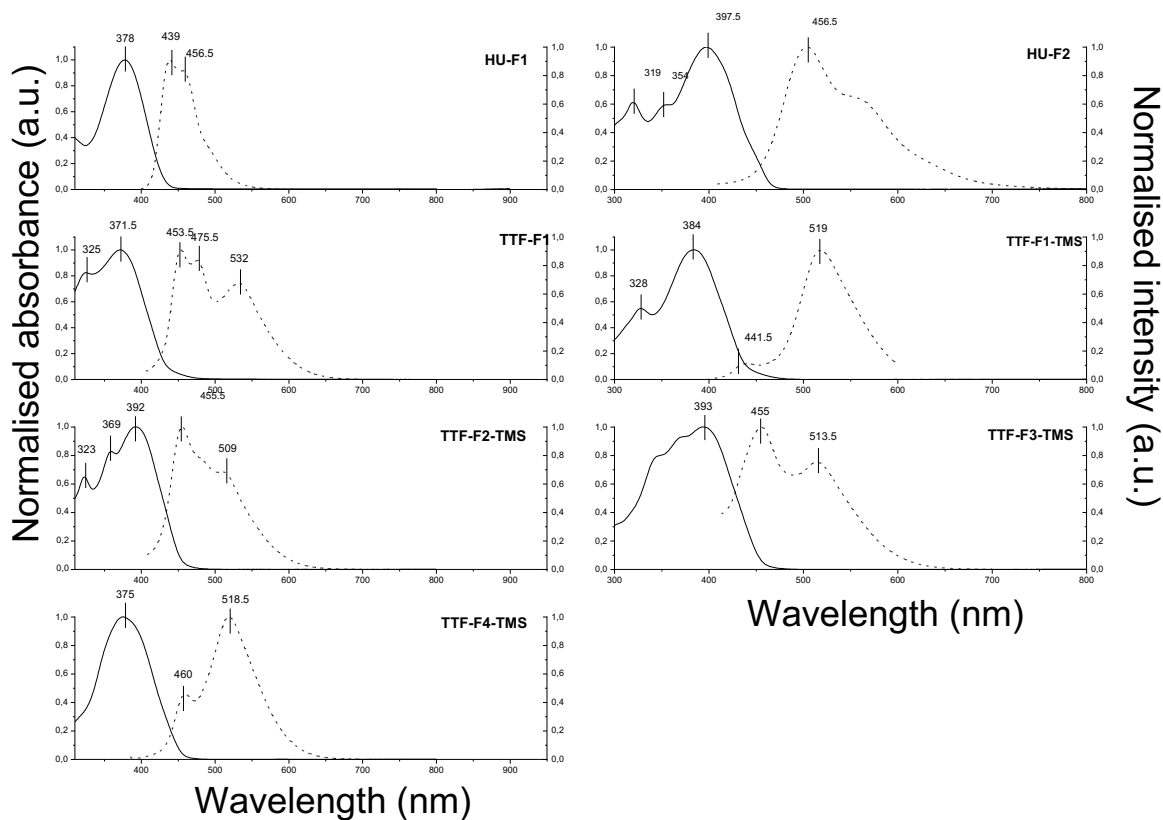


**Figure 2-8.** Normalised absorption and PL spectra of compounds **HU-F1**, **HU-F2** and **TTF-F $n$ -X** in dichloromethane.  $\lambda_{\text{ex}}$  (**HU-F1**) = 378 nm,  $\lambda_{\text{ex}}$  (**HU-F2**) = 399 nm,  $\lambda_{\text{ex}}$  (**TTF-F1**) = 372 nm,  $\lambda_{\text{ex}}$  (**TTF-F1-TMS**) = 384 nm,  $\lambda_{\text{ex}}$  (**TTF-F2-TMS**) = 392 nm,  $\lambda_{\text{ex}}$  (**TTF-F3-TMS**) = 396 nm,  $\lambda_{\text{ex}}$  (**TTF-F4-TMS**) = 378 nm. Concentrations for the emission spectra:  $1.3 \times 10^{-5}$  M (**HU-F1**);  $1.3 \times 10^{-7}$  M (**HU-F2**);  $1.0 \times 10^{-6}$  M (**TTF-F1**);  $3.1 \times 10^{-6}$  M (**TTF-F1-TMS**);  $1.0 \times 10^{-6}$  M (**TTF-F2-TMS**);  $1.0 \times 10^{-6}$  M (**TTF-F3-TMS**);  $1.0 \times 10^{-6}$  M (**TTF-F4-TMS**).

Table 2-5 shows the absorption and emission characteristics of **HU-F $n$**  and **TTF-F $n$ -X** compounds in DCM. Compounds **TTF-F1** and **TTF-F1-TMS** reveal an absorption band at peak maxima at 372 nm and 384 nm, respectively (Figure 2-8). These intense absorption peaks are attributed to the  $\pi$ - $\pi^*$  transition occurring from the HOMO-1 located on the fluorene–thiophene–fluorene units. Compound **TTF-F1-TMS** reveals an additional band in the short-wave region at 328 nm which is attributed to the absorption of the 2,2'-bithieno[3,4-d][1,3]dithiolylydene (DT-TTF) core. This short-

wave region band is more resolved than observed in **TTF-F1** due to the increased electron density on the fluorenyl units afforded by the TMS substituent. Compounds **TTF-F2-TMS** and **TTF-F3-TMS** reveal peak maxima at 392 nm and 394 nm, respectively. Compound **TTF-F2-TMS** reveals additional short-wave region bands at 323 nm and 360 nm. The long-wave band at 392 nm is attributed to the  $\pi$ - $\pi^*$  transition occurring from the HOMO of the core extending to both bifluorene arms. The band at 323 nm is assigned to the absorption within the DT-TTF core, while the band with a peak at 360 nm is related to the absorption of one bifluorene unit. The 2,2'-bithieno[3,4-*d*][1,3]dithiolylydene (DT-TTF) core may play a key role here as its absorption could contribute to the higher energy features around 320 nm in the absorption spectra of **TTF-F1** and **TTF-F $n$ -TMS** ( $n = 1-2$ ).<sup>218</sup>

The extent of the HOMO situated on the core is limited to two bifluorene units on either side and as the oligofluorene chain increases past this limit, the terfluorene unit begins to dominate the absorbance. This can be observed by the broadening of the absorption band and the overlapping of peaks in **TTF-F3-TMS** spectrum. Compound **TTF-F4-TMS** reveals a featureless absorption band at 375 nm. The hypsochromic shift of the peak maximum confirms that as the oligofluorene chain-length increases further, the fluorenyl units dominate absorption, as the position of the peak is similar to the absorption spectrum of quaterfluorene in dichloromethane. The position of the peak maximum is similar to that observed in the absorption spectrum of quaterfluorene molecules in DCM.<sup>219, 220</sup>

By comparison, the monofluorene system containing the 1,3-dithiol-2-one unit **HU-F1** reveals peak maximum at 378 nm, similar to its **TTF-F1** analogue and consistent with absorption of the thieno[3,4-*d*][1,3]dithiol-2-one core extending over the fluorenyl arms. The bifluorene analogue **HU-F2** reveals a peak maximum red-shifted by 20 nm ( $\lambda_{\text{max}} = 398$  nm), when compared to **HU-F1** denoting the effects of extended conjugation. Compounds **HU-F2** and **TTF-F2-TMS** have similar absorption profiles, with the positions of the bands not changing significantly.

**Table 2-5.** UV-Vis absorption data for for **HU-F $n$**  and the **TTF-F $n$ -X** series in CH<sub>2</sub>Cl<sub>2</sub>.

	Peak maximum (nm) [log $\epsilon$ ]/absorption onset (nm)
	CH <sub>2</sub> Cl <sub>2</sub>
<b>HU-F1</b>	378 (4.98)/430
<b>HU-F2</b>	319 (4.99), 354 (4.98), 398 (5.21)/466
<b>TTF-F1</b>	325 (5.19), 372 (5.27)/436
<b>TTF-F1-TMS</b>	328 (5.17), 384 (5.43)/442
<b>TTF-F2-TMS</b>	323 (5.54), 360 (5.65), 392 (5.73)/455
<b>TTF-F3-TMS</b>	394 (5.90)/456
<b>TTF-F4-TMS</b>	375 (5.79)/457

The extinction coefficients for the **HU-F $n$**  and **TTF-F $n$ -X** compounds are shown in Figure 2-9 and shows that the **HU-F1** and **HU-F2** systems exhibit a maximum at the 378 and the 398 wavelength and the **TTF-F $n$ -X** series exhibit a maximum in the range of 372 - 393 nm.

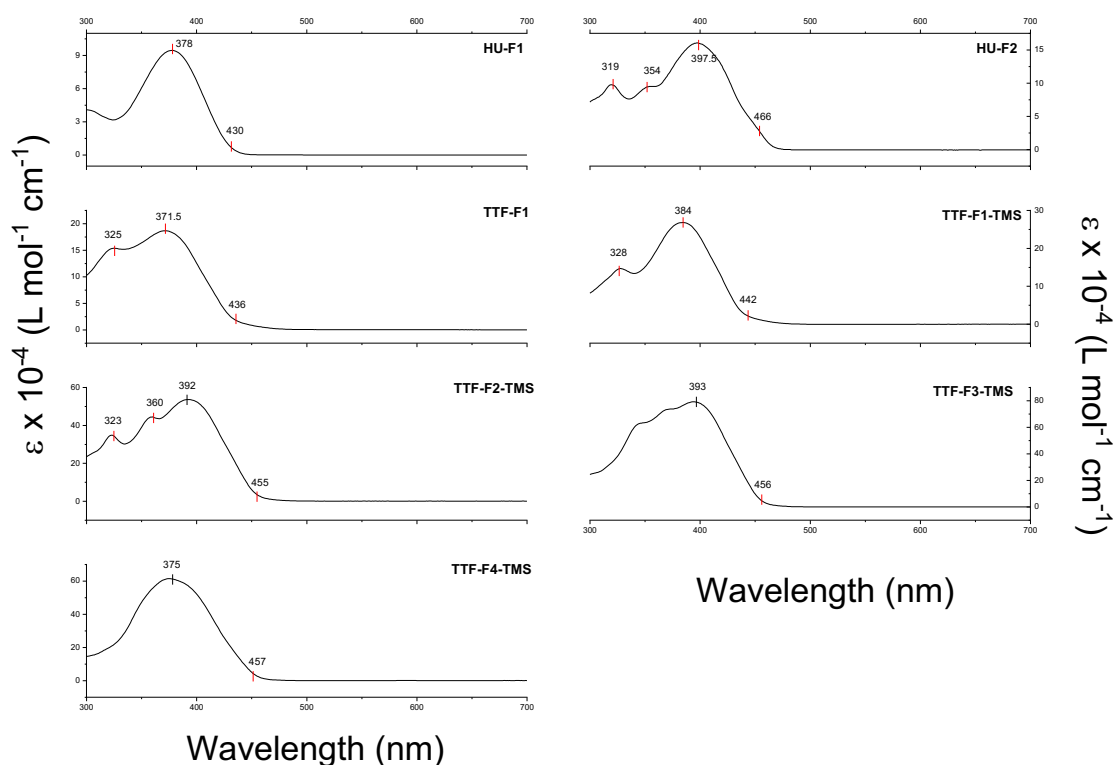


**Figure 2-9.** The spectra of compounds **HU-(F1-F2)** and **TTF-(F1-F4)-X** (extinction coefficient versus wavelength) in dichloromethane. The onsets and positions of peaks are marked.

The fluorescence spectra for compounds **HU-F<sub>n</sub>** and **TTF-F<sub>n</sub>-X** in dichloromethane are shown in Figure 2-8. Compound **TTF-F1** has three emission bands at 454 nm, 476 nm and 532 nm. The short-wave band at position 454 nm is attributed to the emission of the monofluorene segments, while the band at position 532 nm originates from the **TTF-F1** aggregated state. Similarly compounds **TTF-F<sub>n</sub>-TMS** ( $n=1-4$ ) all reveal two emission bands at regions 442-460 nm and 509-519 nm. The relative intensity of these emission bands in all TTF-bearing compounds **TTF-F1** and **TTF-F<sub>n</sub>-TMS** ( $n=1-4$ ) was found to depend on the concentration of solutions (Table 2-9). Interestingly, the aggregation occurrence was revealed through changes in the photoluminescence (PL) spectra (Figure 2-10). The observation of aggregation by PL has also been reported for tetraphenylethene (TPE)–oligofluorene star-shaped systems.<sup>221</sup>

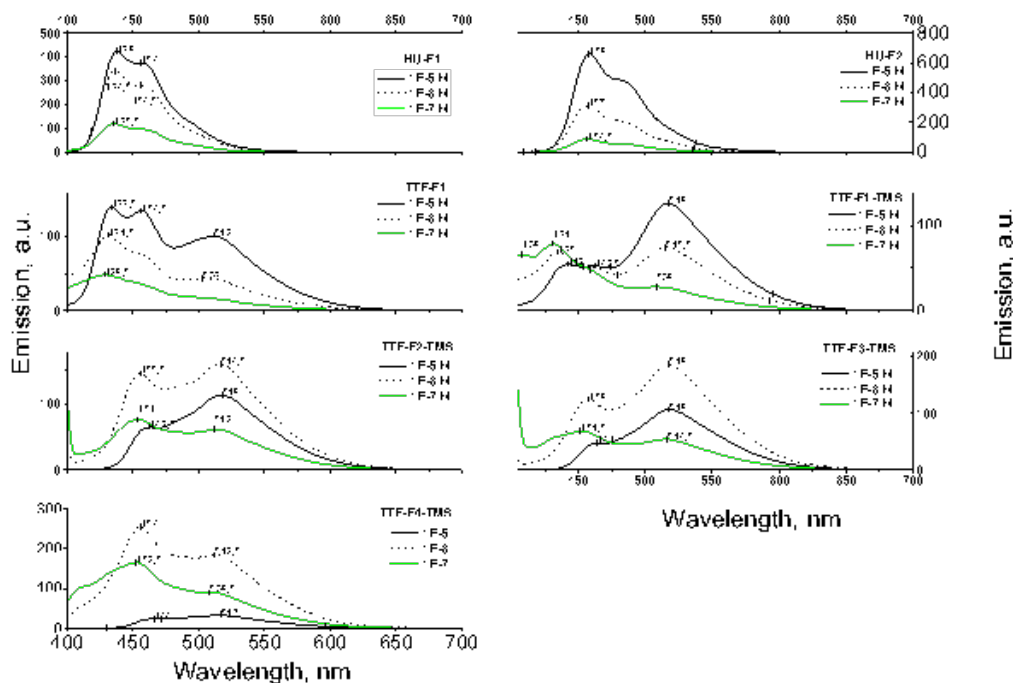


**Figure 2-10.** PL spectra of compounds **HU-F1-2** and **TTF-(F1-F4)-X** in DCM at different concentrations ( $1 \cdot 10^{-5}$  -  $1 \cdot 10^{-7}$  M).  $\lambda_{\text{ex}}$  (**12**) = 378 nm,  $\lambda_{\text{ex}}$  (**13**) = 399 nm,  $\lambda_{\text{ex}}$  (**TTF-F1**) = 372 nm,  $\lambda_{\text{ex}}$  (**TTF-F1-TMS**) = 384 nm,  $\lambda_{\text{ex}}$  (**TTF-F2-TMS**) = 392 nm,  $\lambda_{\text{ex}}$  (**TTF-F3-TMS**) = 396 nm,  $\lambda_{\text{ex}}$  (**TTF-F4-TMS**) = 378 nm. The peak positions are marked.

In solutions of these compounds at a low concentration of  $10^{-7}$  M, the shorter wavelength band is found to dominate the emission spectra. At higher concentrations ( $10^{-5}$  M) the longer wave band becomes dominant. This is a result of the aggregating ability of TTF which at high concentrations results in red-shifted emission. Self-absorption might also contribute to a decrease in the intensity of the short-wave band at higher concentrations. In contrast to TTF-cored oligofluorenes, compounds **HU-Fn** didn't reveal any change in the shape of an emission profile in the range of concentrations  $10^{-7}$  -  $10^{-5}$  M.

The absorption and emission properties of compounds **HU-Fn** and **TTF-Fn-X** in films drop-cast from  $3 \text{ mg}\cdot\text{ml}^{-1}$  solutions in toluene are shown in Figure 2-11. The absorption

spectra of the materials all reveal unresolved bands due to band broadening which arise as a result of the higher degree of aggregation occurring in the solid state. The positions of the absorption peaks do not change significantly, however the absorption onset of these films reveals a bathochromic shift as a result of the more rigid molecular structure in the solid-state.

The emission spectra of TTF-cored star-shaped oligofluorenes **TTF-Fn-X** reveal band broadening and a hypsochromic shift of emission. In the solid-state, emission occurs from the conductance band to the valence band, leading to a broader band being observed. The hypsochromic shift is attributed to the confinement of molecules in the solid state, leading to a hindered structural relaxation within the excited state. In contrast, the emission spectra of compounds **HU-Fn** in films reveal a featureless emission band with a bathochromic shift compared to the emission in solution.

The electrochemical HOMO-LUMO gap values estimated for compounds bearing a TTF core **TTF-F1** and **TTF-Fn-TMS** ( $n=1-4$ ) are in the range of 2.66 - 2.77 eV, showing that the gap is not significantly affected by extending the conjugation through additional fluorene units and that the TTF core is responsible for the initial oxidation of the materials. The oligofluorenes **HU-F1** and **HU-F2**, both show an electrochemical HOMO-LUMO gap of 2.97 eV, respectively. These values are higher than those observed for **TTF-F1-TMS** and **TTF-F2-TMS**, showing the influence of TTF in decreasing the oxidation potential of these species.

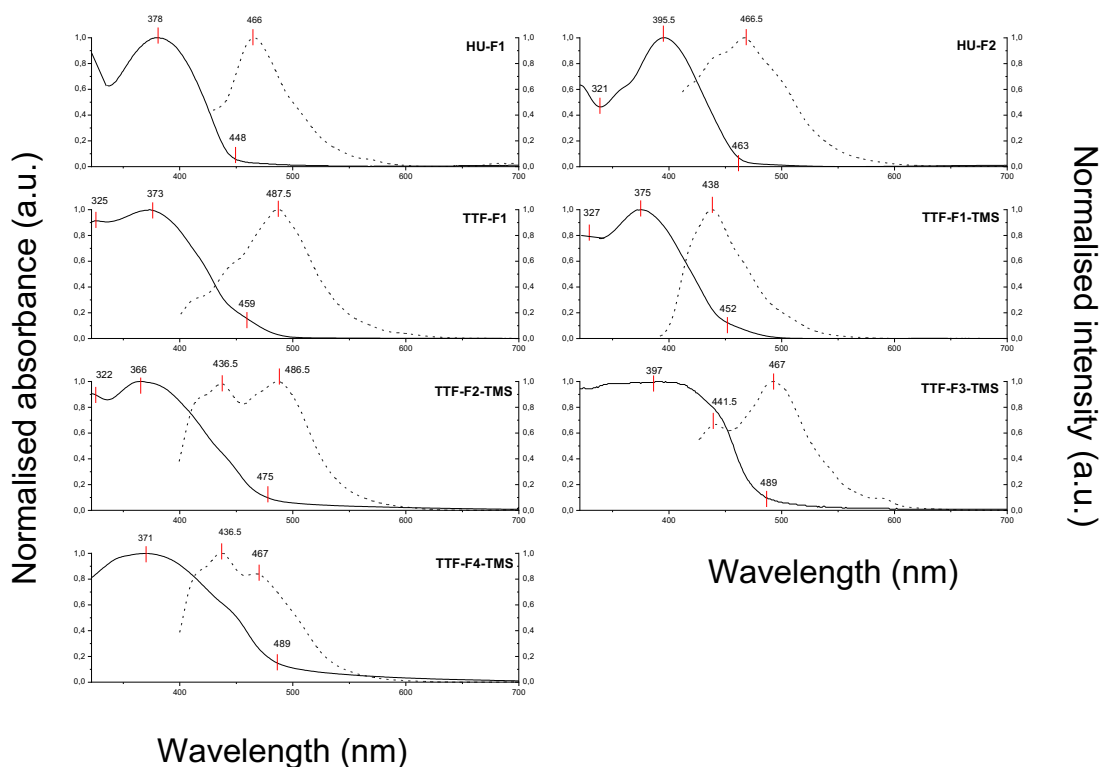


**Figure 2-11.** Normalised absorption and PL spectra of compounds **HU-F1**, **HU-F2** and **TTF-Fn-X** in the solid state as films drop-cast from toluene at  $3 \text{ mg ml}^{-1}$ .  $\lambda_{\text{ex}}$  (**HU-F1**) = 389 nm,  $\lambda_{\text{ex}}$  (**HU-F2**) = 395 nm,  $\lambda_{\text{ex}}$  (**TTF-F1**) = 373 nm,  $\lambda_{\text{ex}}$  (**TTF-F1-TMS**) = 377 nm,  $\lambda_{\text{ex}}$  (**TTF-F2-TMS**) = 367 nm,  $\lambda_{\text{ex}}$  (**TTF-F3-TMS**) = 389 nm,  $\lambda_{\text{ex}}$  (**TTF-F4-TMS**) = 370 nm. The onsets of the absorption are marked, as well as the absorption and emission peak positions.

**Table 2-6.** Photoluminescence (PL) data and quantum yields (PLQY) for **HU-Fn** and the **TTF-Fn-X** series in  $\text{CH}_2\text{Cl}_2$  solution and in the film.

	Peak maximum (nm) [PLQY]	
	$\text{CH}_2\text{Cl}_2$	Film
<b>HU-F1</b>	439, 457 (<2%)	466 (<1%)
<b>HU-F2</b>	457 (25.9%)	467 (<1%)
<b>TTF-F1</b>	454, 476, 532 (<1%)	488 (<1%)
<b>TTF-F1-TMS</b>	442, 519 (<1%)	438 (<1%)

	Peak maximum (nm) [PLQY]	
	CH <sub>2</sub> Cl <sub>2</sub>	Film
<b>TTF-F2-TMS</b>	455, 509 (<1%)	437, 487 (<1%)
<b>TTF-F3-TMS</b>	455, 514 (1%)	442, 493 (<1%)
<b>TTF-F4-TMS</b>	460, 519 (1.2–1.4%)	437, 467 (<1%)

The optical HOMO-LUMO gaps for the TTF-bearing materials (**TTF-F1** and **TTF-Fn-TMS**) are larger than the value calculated through the electrochemical method. In the determination of the HOMO-LUMO gap through electrochemical methods, the HOMO located on the TTF is not involved in the lowest  $\pi$ - $\pi^*$  transition. It has previously been suggested that as a consequence of low oscillator strength, the optical transition in the material could occur from the HOMO-1 orbital as opposed to the HOMO.<sup>201</sup> Compounds **HU-Fn**, in which the TTF core is absent have a lower optical HOMO-LUMO gap, than the value obtained from electrochemical methods. This difference in value is attributed to the energy required to overcome the electron-hole pair binding energy.<sup>19</sup>

The photoluminescence quantum yields (PLQYs) were determined from solution and films of the materials **HU-Fn** and the **TTF-Fn-X** series and were found to be below 1 % for all compounds (Table 2-6). As shown in Figure 2-10, the TTF-Fn-X systems show a propensity to aggregate in the solution state and hence, the low PLQYs have been attributed to the presence of the TTF core.<sup>222</sup>

## 2.6 Conclusions and further work

In conclusion, a novel series of five star-shaped fluorene-based conjugated systems have been developed that incorporate a TTF redox active centre (**TTF-F $n$ -X** series). Furthermore, two novel one-dimensional oligofluorene systems (**HU-F1**, **HU-F2**) have been synthesised, incorporating a 1,3-dithiole-2-one core. The one-dimensional oligofluorene systems **HU-F1** and **HU-F2** thereof, being electroactive and acting as a precursor to the formation of novel TTF-oligofluorene systems. Electronic communication between the oligofluorene arms of varying length (1 to 4) was extended through thiophene, which was fused to the peripherals of the core in each system.

Two convergent synthetic routes to the synthesis of these systems have been demonstrated, showing the most reliable and efficient route. This optimized strategy uses perbromo-2-2'-bithieno[3,4-*d*][1,3]dithiolylidene as a starting material and has proven itself to be a more efficient strategy. This synthetic pathway comprises fewer synthetic steps and yields for the **TTF-F $n$ -X** series are all within 60-65%, with the exception of **TTF-F4-TMS** (yield 36%). The loss in yield is attributed to the higher molecular weight of the TTF-oligofluorene system that can inhibit unwanted, efficient cross-coupling reactions.

The thermal, electrochemical and optical properties of each system have been investigated. In terms of thermal stability, these amorphous fluorene-based conjugated systems expressed high heat-resilience upon observing high decomposition temperatures, making them suitable in most environment applications as optoelectronic devices.

Second, extended electrochemical research has shown that the length of the arms played a key role in oxidation reversibility and doping stability: with increasing fluorene unit per oligomer arm, more reversible and quasi-reversible oxidation waves were observed, demonstrating an improved stability towards p-doping in the system with longer conjugation paths.

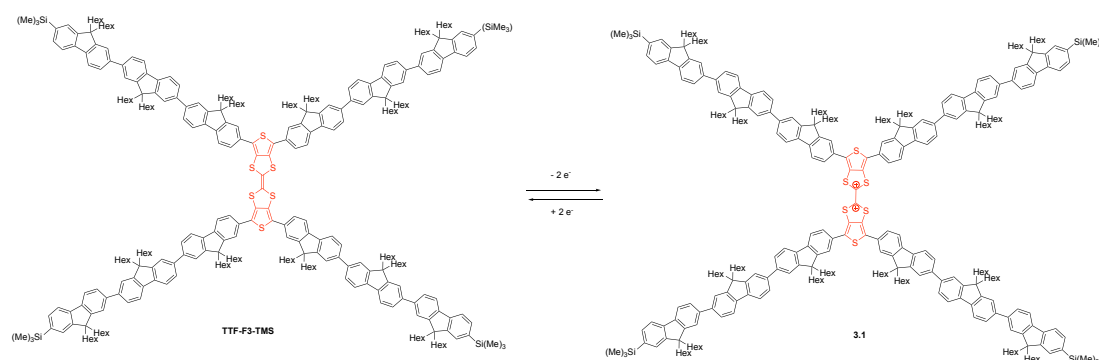
As expected, the fluorescent properties of the novel materials are poor both in solution and film. The TTF-cored star-shaped oligofluorenes were found to strongly aggregate in solution, which has been further demonstrated by the concentration dependence on emission in the solution state.

### **3 Application of hybrid star-shaped tetrathiafulvalene- oligofluorene-thiophene derivatives as a photoluminescence switch**

### 3.1 Abstract

TTFs ability to provide organic systems with increased dimensionality and reliable redox properties, makes it an excellent building block to new OSC materials. Most particularly, in this chapter the oxidizable character of properties of TTF are probed for application as photonic materials in moisture indicators, wherein the TTF acts as a molecular switch for affording emission in the conjugated oligofluorene spores.

Following the synthesis of novel star-shaped tetrathiafulvalene-oligofluorene-thiophene systems and their assessment as poor emitters in solution and solid-state and those properties being attributed to the incorporated TTF core, the proposed step forward was to probe whether oxidation of the TTF core would enable increased rotation of each half of the system (Scheme 3-1), thereby increasing the dimensions of the systems and inhibiting the quenching of emission.



**Scheme 3-1.** Proposed scheme for using TTF as a molecular switch to enhance fluorescence.

In this chapter, the discovery of new spiro-oligofluorene-thiophene systems, spiro-Fn, are discussed. Each **spiro-Fn** system has a different length of oligofluorene arms, mono-, bi- and ter-. The original TTF core in the TTF-Fn-X systems acts as

precursor to the new and exciting **spiro-Fn** systems. All data obtained from these exciting **spiro-Fn** systems are herein discussed.

Some results described herein have already been published as:

Tetrathiafulvalene-oligofluorene star-shaped systems: new semiconductor materials for fluorescent moisture indicators, K. Scanlan, A. L. Kanibolotsky, B. Breig, G. J. Hedley and P. J. Skabara, *Journal of Materials Chemistry C*, 2019, **7**, 6582-6591.

## 3.2 Introduction

Conjugated materials can be designed to allow external stimuli to control their physical properties. Molecular switches are functional materials that exhibit reversible changes in magnetic, optical, electronic or mechanical properties upon exposure to external stimuli.<sup>223-225</sup>

Stimuli responsive photoluminescence refer to a change of photophysical properties of a fluorophore based on the detection of an analyte. The induced change in photophysical properties can occur for example as a change in intensity, lifetime or quantum yield. The impact on the photophysical properties of the fluorophore can occur on exposure to external stimuli such as temperature, pH and redox reagents. Stimuli responsive luminescent materials have been used in applications such as smart switches and sensing devices.<sup>226-228</sup>

In order to exploit the sensitive signalling afforded by photoluminescence switches for practical applications, properties such as fast-response time, high visualisation contrast

and stability are desired. Luminescent films have proven advantageous due to their flexibility, although challenges remain due to luminescent materials tendency to aggregate in the solid-state, thereby reducing their photoluminescence efficiency.<sup>229</sup>

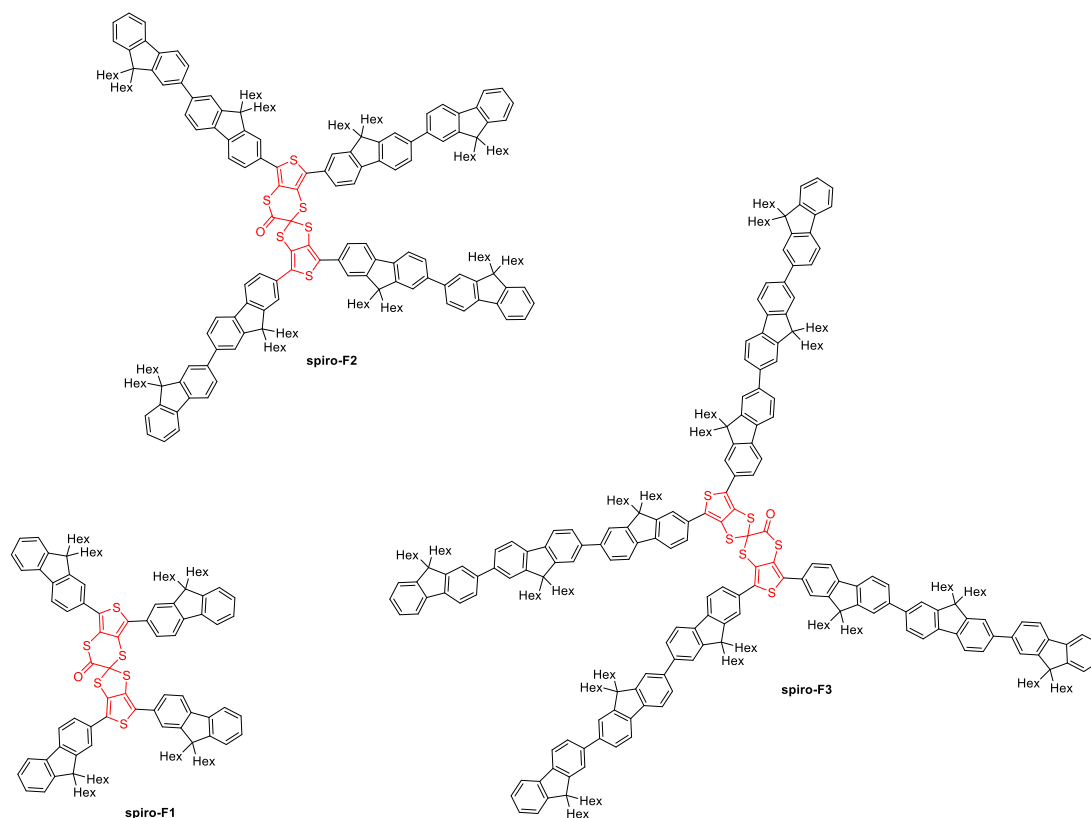


**Figure 3-1.** Structures for new spiro oligofluorene-thiophene **Spiro-F<sub>n</sub>** systems.

As shown in Chapter 2, **TTF-F<sub>n</sub>-X** systems have demonstrated inhibited emission in the solution and solid-state due to their strong tendency to aggregate. It was proposed that the four oligofluorene spores would demonstrate their inherent emissive properties if the planarity afforded by the TTF system was diminished. Taking this factor into consideration, strategic consideration of how to increase conformational flexibility of the TTF system was undertaken. In prior chapters the symmetry of TTF changing upon oxidation has been discussed. It is known that in the neutral state TTF possess  $C_{2v}$  symmetry and after oxidation of the neutral TTF centre, the system possesses  $D_{2h}$

symmetry. A second oxidation of TTF in its cation state provides D<sub>2</sub> symmetry. In view of this, it was considered that the two-time sequential oxidation of TTF followed by methylation would provide a new system wherein emission would be un-inhibited.

As is with chemistry, what was proposed was not what was observed. Surprisingly, what was exhibited by the **TTF-Fn-X** systems, was a rearrangement affording new spiro-systems, **spiro-Fn** (Figure 3-1) with different photophysical properties attributed to the new oxidation state of the ditholium systems. The applicability of these systems as photoluminescence switches is herein discussed.

### 3.3 Experimental

With a view of enhancing the intensity of emission in the TTF-Fn-X systems, it was proposed to oxidise the TTF core, thereby essentially removing the planar characteristics of TTF which are aggregation-inducing. In order to investigate this and achieve at least a proof of concept, the star-shaped oligofluorene systems TTF-Fn-X in their solution state, DCM were used to investigate the possibility of tuning the emissive properties of the systems.

#### 3.3.1 Adjusting the conformational flexibility of TTF-oligofluorene-thiophene systems

The TTF-based systems **TTF-Fn-TMS** were used in their solution-state for these studies. It was necessary to use a TTF-oligofluorene-thiophene system with a larger degree of extended conjugation in order to visibly observe any changes in emission. As **TTF-F3-TMS** fitted this criterion and was the material most abundant at that point

in time, it was used for the investigation of potential emission enhancement. In order to oxidise the TTF core to its dication state, nitrosonium hexafluorophosphate was used. In order to form the dication state of TTF, two equivalents were used. Two equivalents of the oxidising agent were added to compound **TTF-F3-TMS** in  $\text{CH}_3\text{CN}$  at a concentration of  $1 \times 10^{-6}$  M. Compound **TTF-F3-TMS** was excited at 396 nm in accordance with the maximum absorption exhibited in UV-Vis Spectroscopy measurements. The PL spectra were measured at regular intervals in a fluorimeter to gauge any change in emission occurring.

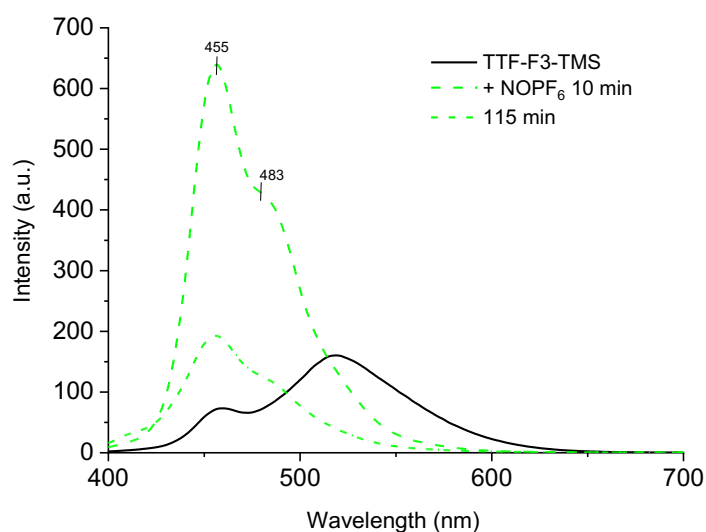
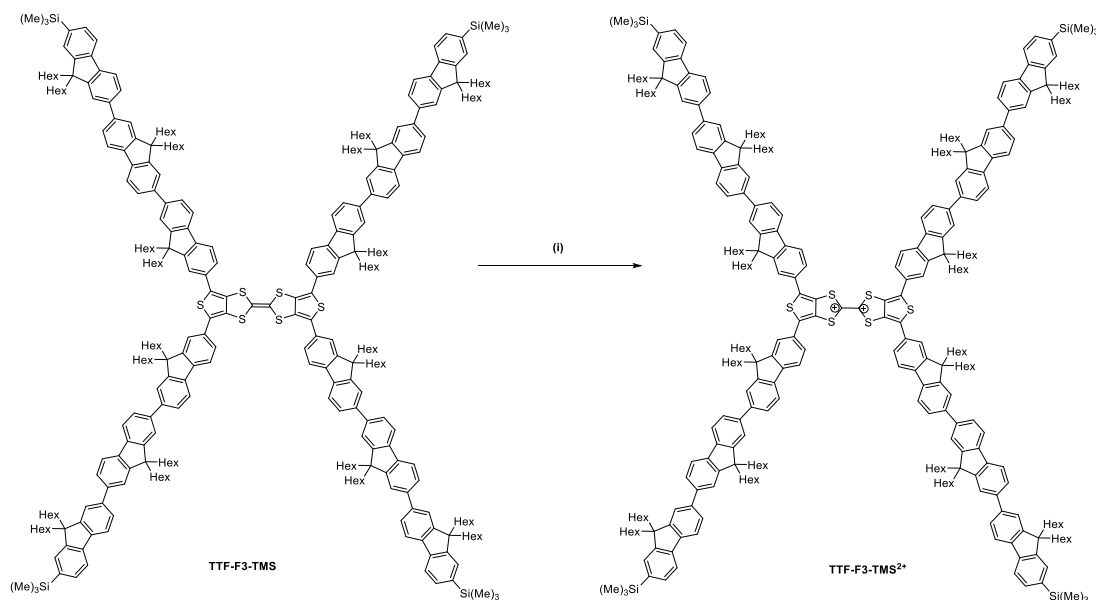


**Figure 3-2.** Photoluminescence spectra showing the enhancement in emission of doped **TTF-F3-TMS** in  $\text{CH}_2\text{Cl}_2$  ( $1.0 \times 10^{-6}$  M) in the presence of water. Dopant used was  $\text{NOPF}_6$  in  $\text{CH}_3\text{CN}$  (2 equiv.);  $\lambda_{\text{ex}} = 396$  nm.

As shown in Figure 3-2, a time-sensitive change in emission intensity was observed. Surprisingly, a change in the emission profile of the **TTF-F3-TMS** systems also occurred. Figure 3-2 shows that neutral **TTF-F3-TMS** exhibits two bands at 455 nm and 514 nm. However, within 10 minutes of the addition of nitrosonium hexafluorophosphate, the long-wavelength band disappeared while a shoulder at ~480

nm compensated for the loss with a rising intensity. The intensity of the band at 455 nm continued to increase resulting in a time-dependent enhancement of emission. The proposed scheme for the enhancement in emission is shown in Scheme 3-2, which demonstrates the two-fold sequential oxidation of the **TTF-F3-TMS** system.



*Reaction and conditions: (i) NOPF<sub>6</sub>/CH<sub>3</sub>CN, CH<sub>2</sub>Cl<sub>2</sub>, rt.*

**Scheme 3-2.** Proposed scheme for oxidation of **TTF-F3-TMS**.

On observing the change in intensity of emission, it was assumed that the emission characteristics were reversible and that upon addition of a reducing agent that the TTF core would be reformed, thereby reverting the emission characteristics back to that of the former **TTF-F3-TMS** system. Commercially available hydrazine monohydrate was employed as a reducing agent. Hydrazine monohydrate is commonly used in the preparation of heterocycles like pyrazoles and pyridazines and is known for its reliable reducing properties. As only two equivalents of nitrosonium hexafluorophosphate were used, which was the necessary amount for a two-time sequential oxidation of neutral

TTF, hydrazine monohydrate was used in excess, as there were no further reactive sites on the **TTF-F3-TMS** system for reduction.

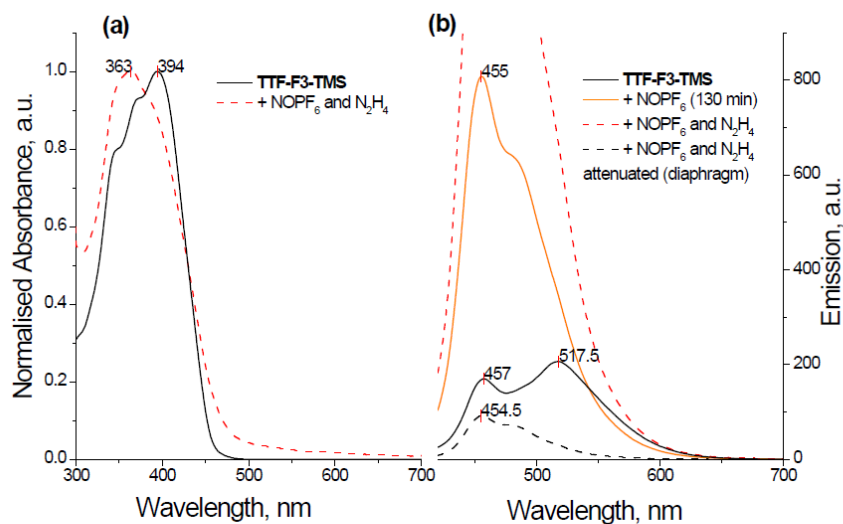
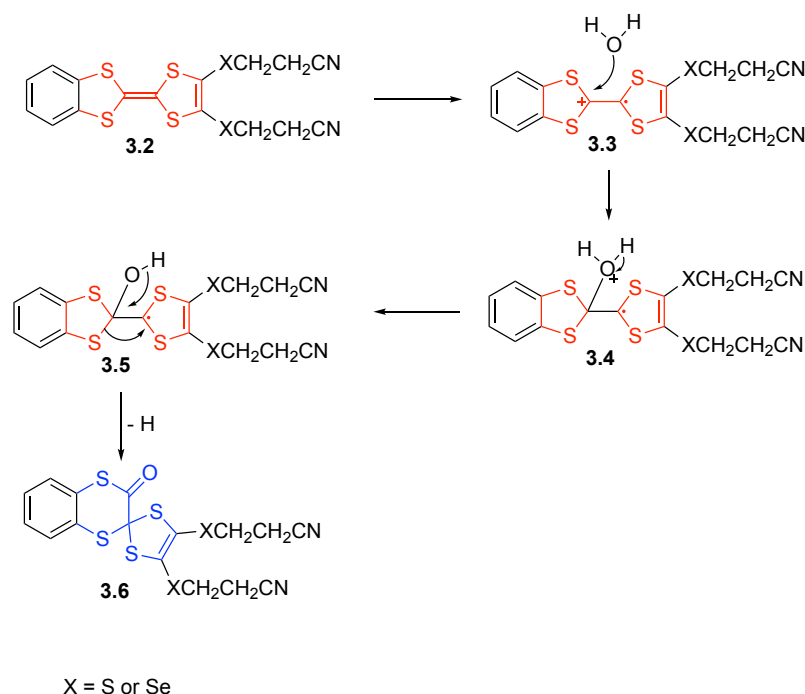


**Figure 3-3.** Absorption spectra of **TTF-F3-TMS** ( $10^{-6}$  M) before and after oxidation with  $\text{NOPF}_6$  followed by treatment with  $\text{N}_2\text{H}_4 \cdot \text{H}_2\text{O}$  (1 drop); (b) PL spectra of **TTF-F3-TMS** in neutral state, after oxidation with  $\text{NOPF}_6$  ( $t=130$  min) and after additional treatment with  $\text{N}_2\text{H}_4 \cdot \text{H}_2\text{O}$  (1 drop).

As shown in Figure 3-3, an enhancement in the PL intensity was observed after the addition of hydrazine monohydrate. The fluorescence spectra show that the short wavelength emission increased beyond the fluorimeter sensitivity range, thereby it was not possible to quantitatively determine exactly how high the intensity reached. It is suggested that the irreversible increase in fluorescence of oxidised **TTF-F3-TMS** with time is a consequence of the strong electrophilic nature of the dication formed upon oxidation, which is susceptible to a reaction with traces of water or  $\text{N}_2\text{H}_4$ .

It has been previously reported that a rearrangement can occur wherein a TTF cation can react with water (Scheme 3-3)<sup>230, 231</sup>. In the reported reaction, the proposed mechanism describes a single electron oxidation of the TTF-cored derivative **3.2** forming the TTF in its cation state **3.3**. The TTF in its cation state **3.3** then reacts with

water, resulting in the formation of a hydroxylic functionality upon the TTF centre **3.4**. An additional single electron oxidation forming TTF in its dication state **3.5** provides a pinacol-type rearrangement wherein a 1,2-sulfenyl shift results in a ring expansion and results in the formation of a spiro-centre and, after the loss of one proton, a carbonyl unit, forming compound **3.6** with a spiro-centre.



**Scheme 3-3.** Previously reported proposed scheme for the rearrangement to form spiro systems from TTF.

The reaction was carried out in ambient conditions for the oxidation of the **TTF-Fn-X** systems. Prior to the oxidation reaction, the **TTF-F3-TMS** system was desilylated in order to ensure there was no interactions with the TMS substituents and hence, encouraging a higher yield of the spiro-terfluorene system (Figure 3-4) for further investigations.

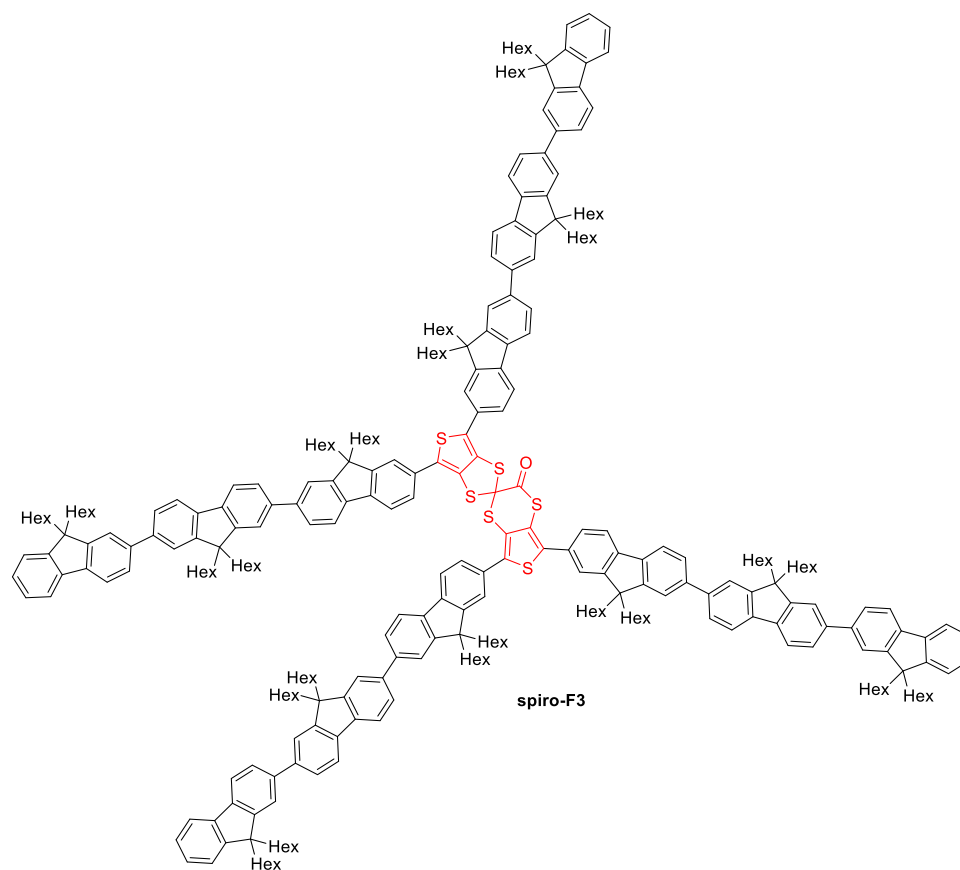


**Figure 3-4.** Proposed rearrangement product of TTF-F3.

The **spiro-F3** system was successfully isolated and characterised using proton nuclear magnetic resonance (NMR) and additionally using matrix-assisted laser desorption/ionisation. The yield of the system was low, with **spiro-F3** being isolated on silica gel with hexane and being precipitated from methanol as an amorphous solid with a yield of 17%. The **TTF-F1-TMS** and **TTF-F2-TMS** systems were also desilylated and oxidised under ambient conditions to form monofluorene and bifluorene spiro-analogues, **spiro-F1** and **spiro-F2**, respectively. **Spiro-F1** and **spiro-F2** were isolated in yields 60% and 45%. The yields appeared to increase with respect to shorter oligomer arm length (Table 3-1).

**Table 3-1.** Spiro-Fn yields vis-à-vis the number of fluorene monomers.

	Number of fluorene monomers ( <i>n</i> )	Yield (%)
<b>spiro-F1</b>	1	60
<b>spiro-F2</b>	2	45
<b>spiro-F3</b>	3	17

### 3.3.2 Perbromo-2,2'-bithieno[3,4,d][1,3]dithiolylidene oligofluorene-thiophene as a PL sensor

The characterisation of the spiro-Fn systems led to the question of the **TTF-Fn-X** systems suitability as fluorescent moisture indicators for use in sensing technologies such as food packaging, wherein an indication of moisture is required for an indication of the lifetime of perishable foods.

As a proof of concept, the trimethylsilyl-substituted terfluorene-TTF derivative, **TTF-F3-TMS** system was incorporated into a photocurable matrix in inert conditions within a glovebox, to ensure no contact with moisture present in ambient conditions. The experiment was designed to ensure that the **TTF-F3-TMS** compound is encapsulated within a photoresist, thereby ensuring that there is no unintentional exposure to air.

The photocurable matrix was based on a previously developed negative photoresist that used a cross-linking system 1,4-cyclohexyldimethanol divinyl ether (CHDV) combined with a photoacid generator (PAG), 4-octyloxydiphenyliodonium hexafluoroantimonate (Figure 3-5).<sup>232</sup>

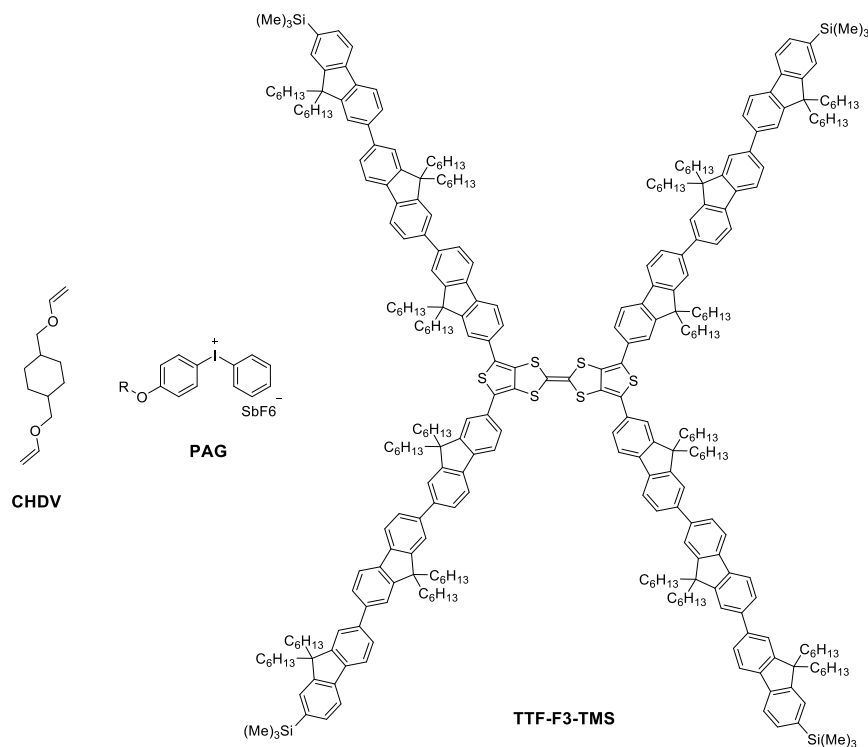
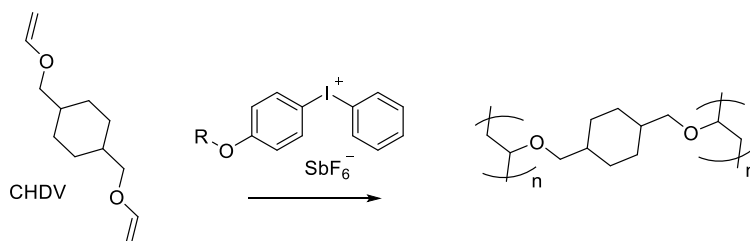


**Figure 3-5.** Components of the photoresist, comprising CHDV, PAG and **TTF-F3-TMS**.

The choice of matrix was strategic in that it is desirable for a matrix to have no interference with the optical properties of the active system, which was in this case **TTF-F3-TMS**. Additionally, CHDV has no present aromatic groups which improves the transparency of the system to UV radiation and decreases the chances of solvatochromic shifts. Increasing the transparency of the photocurable matrix allows maximum photoexcitation of the oligofluorene-thiophene spores. Furthermore, by reducing the chances of solvatochromic shifts, the spectral properties of the active system **TTF-F3-TMS** remain unchanged. The transparency of the photocurable system is beneficial in maximising the photoexcitation of the TTF–oligofluorene system (Figure 2-11). Additionally, reducing the chances of solvatochromic shifts ensures the spectral properties of **TTF-F3-TMS** are sustained. The choice of PAG, 4-octyloxydiphenyliodonium hexafluoroantimonate was desirable for its solubilising properties due to the presence of its alkyl chains. The use of both PAG and CHDV

requires deep UV-radiation to induce photocuring (Scheme 3-4) resulting in a photoresist system which has over 90% transparency at 250 nm.<sup>232</sup>



**Scheme 3-4.** Cross-linking of the monomer CHDV by UV irradiation in the presence of a photoacid generator (PAG).

The CHDV photocurable matrix comprising TTF-F3-TMS was developed using 0.1 wt% PAG and 0.1 wt% TTF-F3-TMS. A larger weight percentage of PAG was initially used but was found to cause an uncontrollable polymerisation without the assistance of UV radiation. The PAG, 4-octyloxydiphenyliodonium hexafluoroantimonate was dissolved in a mixture of dichloromethane:toluene in a ratio of 1:1, which provided improved solubility of the photoinitiator in TTF-F3-TMS/CHDV solution. As a result of the low viscosity of CHDV (4 cP), the fabrication method of drop-casting was used to prepare films onto a fused silica substrate.<sup>51</sup> The matrix was cured using wavelength UV irradiation at 254 nm.

After photocuring the CHDV/TTF-F3-TMS matrix, the matrix was removed from the glovebox and exposed to water as an external stimulus. As shown in Figure 3-6 wherein the matrix to the left of the figure represents the blank CHDV film without the active material TTF-F3-TMS. The matrix in the middle of the figure represents the CHDV/TTF-F3-TMS matrix without exposure to any external stimulus and retained under the inert glovebox conditions. The photocured CHDV/TTF-F3-TMS

to the right of the figure shows the CHDV/**TTF-F3-TMS** matrix after exposure to water. The figure demonstrates that **TTF-F3-TMS** is applicable as a fluorescent moisture indicator.

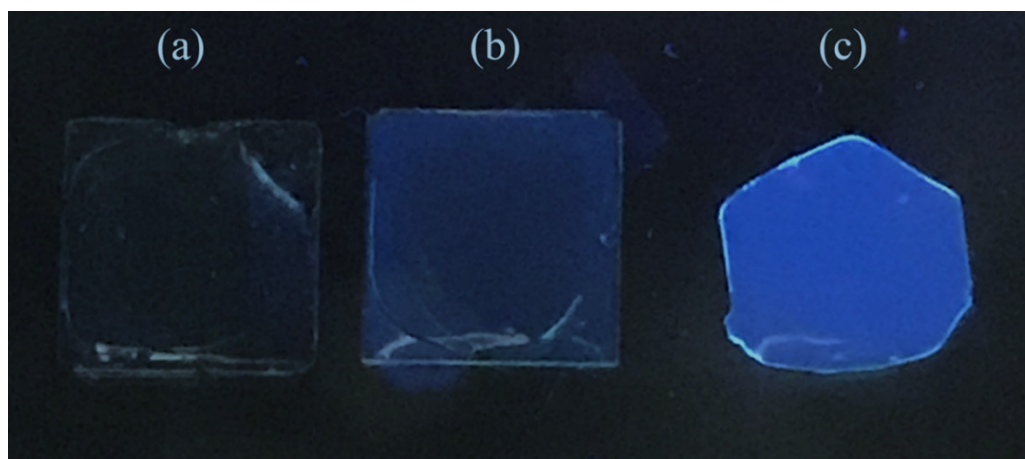


**Figure 3-6.** Photographs of the cured films prepared from blends: CHDV with 0.1% of PAG (left); CHDV with 0.1% of **TTF-F3-TMS** and 0.1% of PAG before (middle) and after exposure to water (right).

The PL spectra for the CHDV/**TTF-F3-TMS** films are shown in Figure 3-7. As can be seen, for the CHDV film with no active material, **TTF-F3-TMS** present, there is a lack of any absorption or emission peaks. For the CHDV/**TTF-F3-TMS** matrix without exposure to ambient conditions, there is a broad absorption peak at 393 nm which demonstrates a hypsochromic shift when compared to the drop-cast film of **TTF-F3-TMS** as described in chapter 2. Upon exposure to water, the CHDV/**TTF-F3-TMS** matrix shows the appearance of a more resolved short-wavelength band, with two peaks emerging at 341 nm and 386 nm.

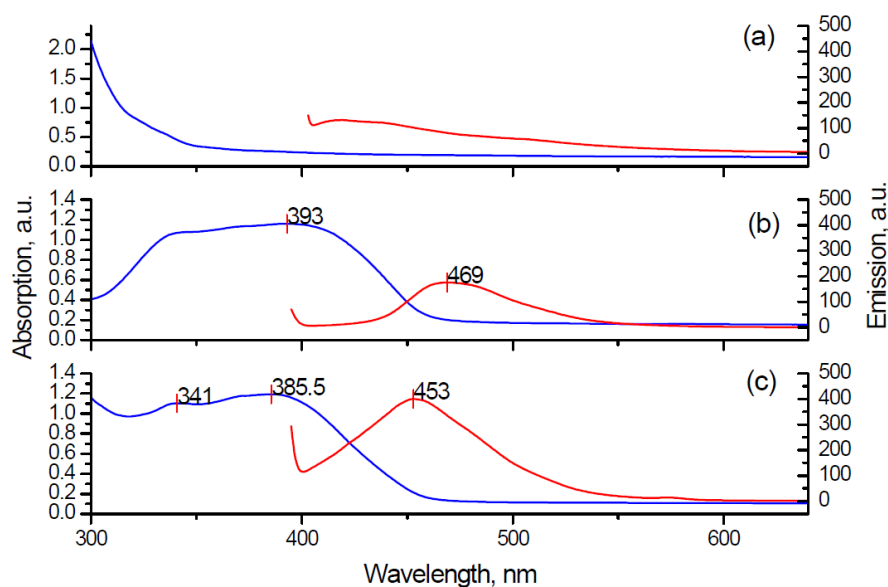


**Figure 3-7.** Absorption/emission spectra of UV cured film drop cast from blends: CHDV with 0.1 % of PAG (a); CHDV with 0.1 % of **TTF-F3-TMS** and 0.1 % of PAG before (b) and after exposure to water (c).

PLQY measurements (Table 3-2) were carried out and show an enhancement in fluorescence attributed to the presence of water. As water has been demonstrated to react with the TTF-oligofluorene derivative, **TTF-F3-TMS** in the matrix, it is proposed that the PAG molecule is responsible for the protonation or oxidation of the TTF core to create an electrophilic intermediate that is then available to react with water.

**Table 3-2.** PLQY measurements of the cured blends.

	<b>Blend composition</b>	<b>PLQY, %</b>
<b>a</b>	CHDV with 0.1% of PAG	<1%
<b>b</b>	CHDV with 0.1% of PAG and 0.1% of <b>TTF-F3-TMS</b> before exposure to water	0.8 – 1.2

	Blend composition	PLQY, %
c	CHDV with 0.1% of PAG and 0.1% of TTF-F3-TMS after exposure to water	2.6 - 2.9

### 3.4 Conclusions and further work

In conclusion, a novel series of TTF–fluorene star-shaped conjugated systems **TTF-Fn-X** was designed and synthesised. Furthermore, a new multi-dimensional spiro-oligofluorene-thiophene systems **Spiro-Fn** have been isolated. In contrast to other star-shaped oligofluorene systems, where we used the core unit for tuning the emission of the materials, the star-shaped oligomers described in this paper contain a TTF unit as the core structure. As expected, the fluorescent properties of the novel materials are poor both in solution and film. The TTF-cored star-shaped oligofluorenes were found to strongly aggregate in solution. While oxidised, the TTF core becomes extremely electrophilic and can react irreversibly with water to increase the PL emission of the oligofluorene arms, allowing for the newly designed star-shaped materials to be considered attractive for applications in fluorescent moisture indicators.

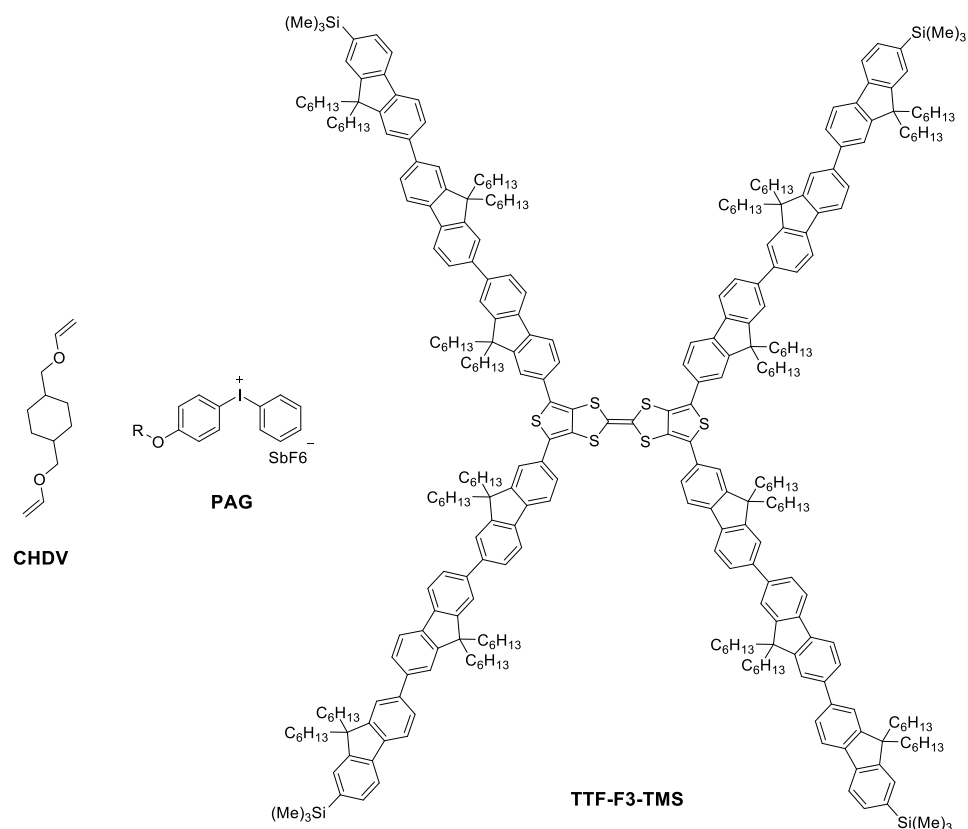
An area of future work would be to scale up the reactions for all spiro-complexes and perform optical, electrochemical and thermal characterisation on the entire series to better gauge the properties of these exciting systems. Furthermore, it would be of interest to investigate the charge-carrier mobilities of **TTF-Fn-X** systems.

Further work on the **spiro-Fn** systems include investigating how to improve the response of the sensor towards the presence of water. In order to achieve this, a better control of the TTF–oligofluorene doping within the matrix is required. Furthermore, a

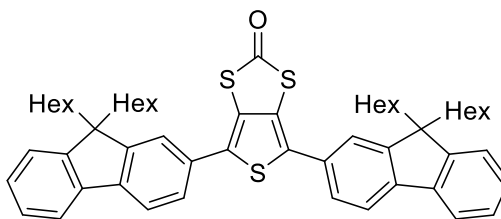
matrix is required which provides improved permeability to water molecules, thereby allowing the TTF-F3-TMS to undergo the spiro-transformation quicker.

## 4 Experimental

Unless otherwise stated, all reagents and solvents were purchased from Sigma Aldrich or Alfa Aesar with no further purification. Dry solvents (dichloromethane, tetrahydrofuran, toluene) were obtained from a solvent purification system (SPS 400, innovative technologies) using alumina as the drying agent. Any additional dry solvents were purchased from Sigma Aldrich.  $^1\text{H}$  and  $^{13}\text{C}$  NMR spectra were recorded on a Bruker Advance DPX400 at 400.13 and 100.61 MHz or a Bruker Advance DRX500 at 500 and 125.75 MHz. Proton and carbon NMR chemical shifts are reported as  $\delta$  values in ppm. The chemical shifts are calibrated to residual solvent signals. For  $^1\text{H}$  NMR chemical shifts are calibrated to 7.26 ( $\text{CDCl}_3$ ) and for  $^{13}\text{C}$  chemical shifts are calibrated to 77.16 ( $\text{CDCl}_3$ ). NMR data are presented as follows: chemical shift, number of nuclei based on integration, multiplicity (s = singlet, d = doublet, dd = doublet of doublets, t = triplet, m = multiplet) and coupling constant(s) ( $J$ ) are in Hz. Multiplets are reported over the range (in ppm) in which they appear. MS MALDI-TOF spectra were recorded on a Shimadzu Axima-CFR spectrometer (mass range 1-150,000 Da) and retinoic acid or dithranol was used as a matrix.

CHDV/TTF-F3-TMS and PAG matrix

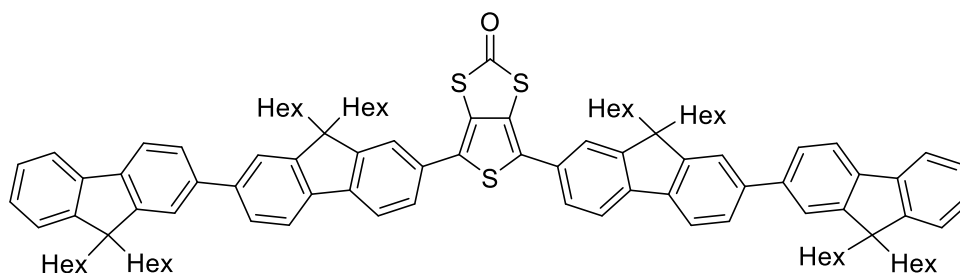
The CHDV photocurable matrix comprising TTF-F3-TMS was developed using 0.1 wt% PAG and 0.1 wt% TTF-F3-TMS. An amount of 0.1 wt% photoacid generator, 4-octyloxydiphenyliodonium hexafluoroantimonate was dissolved in a mixture of dichloromethane:toluene in a ratio of 1:1. The solution of photoacid generator was added to 0.1 wt% TTF-F3-TMS in dichloromethane with rapid stirring. The mixture was drop-casting on fused silica substrate and cured at 254 nm, providing light blue films.

4,6-Bis(9,9-dihexyl-9H-fluoren-2-yl)thieno[3,4-d][1,3]dithiol-2-one (HU-F1)

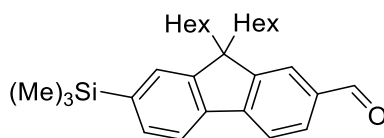
Under N<sub>2</sub>, (2-oxo-1,3-dithiole-4,5-diyl)bis((9,9-dihexyl-9H-fluoren-2-yl)methanone) (0.50 g, 0.83 mmol, 1 equiv), NaHCO<sub>3</sub> (0.37 g, 4.15 mmol, 5 equiv) and 1,4-dioxane (10.5 mL) were stirred. The mixture was heated between 60-90°C for 30 min. The mixture was further heated for 3 hr at 90°C and then allowed to cool to room temperature. Water (2 mL x 10) was added (caution – H<sub>2</sub>S and CO<sub>2</sub> evolution) and the mixture was refluxed for 1 hr and then cooled to room temperature. A brown sticky solid was produced and dissolved in a minimum amount of CH<sub>2</sub>Cl<sub>2</sub>. This mixture was washed with water and extracted with CH<sub>2</sub>Cl<sub>2</sub> (15 mL x 3). The combined organic layers were dried over MgSO<sub>4</sub> and solvent evaporated under reduced pressure. The product was isolated on silica eluting with a mixture of 9:1 hexane/toluene, affording a yellow amorphous solid (0.20 g, 29%).

<sup>1</sup>H NMR (CDCl<sub>3</sub>): 7.78 (d, 7.8 Hz, 1H, Ar-H), 7.74-7.72 (m, 1H, Ar-H), 7.59-5.56 (m, 2H, Ar-H), 7.38-7.32 (m, 3H, Ar-H), 2.03-1.99 (m, 4H, CH<sub>2</sub>), 1.15-1.03 (m, 12H, CH<sub>2</sub>), 0.77 (t, 6.8 Hz, 6H, CH<sub>3</sub>), 0.71-0.64 (m, 4H, CH<sub>2</sub>). <sup>13</sup>C NMR (CDCl<sub>3</sub>): 193.4, 152.1, 151.2, 141.8, 140.3, 133.9, 131.3, 127.8, 127.1, 125.8, 124.6, 123.1, 121.0, 120.6, 120.2, 55.5, 40.5, 31.6, 29.8, 23.9, 22.7, 14.1. Mp: 270°C; MS: MALDI m/z 839.06 (M+H)<sup>+</sup>. Anal. Calcd for C<sub>55</sub>H<sub>66</sub>OS<sub>3</sub>: C, 78.71; H, 7.93; N, 0.00. Found: C, 78.85; H, 8.14; N, 0.00.

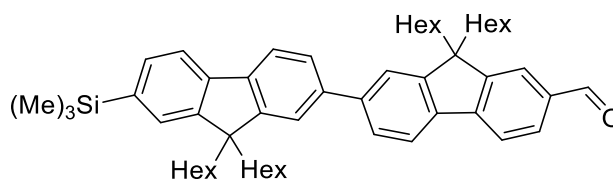
4,6-bis(9,9,9',9'-Tetrahexyl-9H,9'H-[2,2'-bifluoren]-7-yl)thieno[3,4-d][1,3]dithiol-2-one (HU-F2)



Under  $N_2$ , (2-Oxo-1,3-dithiole-4,5-diyl)bis((9,9,9',9'-tetrahexyl-9H,9'H-[2,2'-bifluoren]-7-yl)methanone) (0.369 g, 0.25 mmol, 1 equiv),  $P_4S_{10}$  (0.27 g, 0.61 mmol, 2.49 equiv) and  $NaHCO_3$  (0.11 g, 1.25 mmol, 5 equiv) were stirred in 1,4-dioxane (5 mL). The reaction was heated between 60-90°C for 30 min and then heated at 90°C for 3 hours. The mixture was cooled to room temperature and water (3 x 4 mL) added and refluxed for 1 hour. The reaction mixture was allowed to reach room temperature and then poured onto water (10 mL) and extracted with  $CH_2Cl_2$  (3 x 30 mL). The combined organic layers were washed with water (15 mL), dried over  $MgSO_4$  and solvent removed under reduced pressure. The product was purified on silica using an eluent mixture of hexane/toluene 9:1 increasing to 7:3 to give the product as a yellow amorphous solid (0.25 g, 66%).  $^1H$  NMR ( $CDCl_3$ ): 7.84-7.79 (m, 3H, Ar-H), 7.76-7.74 (m, 1H, Ar-H), 7.70-7.61 (m, 6H, Ar-H), 7.39-7.30 (m, 3H, Ar-H), 2.12-2.02 (m, 8H,  $CH_2$ ), 1.18-1.09 (m, 25H,  $CH_2$ ), 0.81-0.72 (m, 20H,  $CH_3$ ).  $^{13}C$  NMR ( $CDCl_3$ ): 199.3, 152.3, 152.0, 151.6, 151.1, 141.5, 141.4, 140.8, 140.6, 140.4, 139.4, 133.9, 131.2, 127.3, 126.9, 126.5, 126.2, 125.9, 124.6, 123.1, 121.6, 121.5, 121.1, 120.6, 120.4, 120.0, 119.9, 55.6, 55.3, 40.5, 40.4, 31.6, 29.8, 29.77, 24.0, 23.9, 22.7, 22.6, 14.1. Mp: 186-188 °C; MS: MALDI 1475.35 ( $[M - 26]^+$ ). Anal. Calcd for  $C_{105}H_{130}OS_3$ : C, 83.83; H, 8.71; N, 0.00. Found: C, 83.61; H, 8.68; N, 0.00.

9,9-Dihexyl-7-(trimethylsilyl)-9H-fluorene-2-carbaldehyde (F1-CHO)

Under N<sub>2</sub>, 2,7-dibromo-9,9-dihexyl-9H-fluorene (6 g, 12.19 mmol, 1 equiv) was dissolved in dry THF (105 mL). The temperature of the solution was brought to -78°C and 1.58 M *n*-Buli (7.7 mL, 12.20 mmol, 1 equiv) was added dropwise. The mixture was then cooled further to -100°C and chlorotrimethylsilane (1.7 mL, 13.41 mmol, 1.1 equiv) added. The mixture was allowed to reach room temperature with stirring. The mixture was cooled to -78°C and a second portion of 1.58 M *n*-Buli (8.5 mL, 13.41 mmol, 1.1 equiv) added slowly. The temperature was further reduced to -100°C and dimethylformamide (1.2 mL, 15.6 mmol, 1.28 equiv) added. The mixture was allowed to reach room temperature and stirred overnight. The mixture was poured onto cold water (200 mL) and the organic layer extracted with diethyl ether (3 x 150 mL). The combined organic layers were washed with water (300 mL), dried over MgSO<sub>4</sub> and solvent evaporated under reduced pressure. The product was isolated on silica gel, eluting with a gradient of hexane: dichloromethane 9.9: 0.1 increasing to 6:4 (v/v). A colourless oil was afforded (3.4 g, 63.8%). <sup>1</sup>H NMR (CDCl<sub>3</sub>): 10.05 (s, 1H, CHO), 7.87-7.84 (m, 3H, Ar-H), 7.75 (dd, *J* = 6.92, 0.52 Hz, 1H, Ar-H), 7.53 (dd, *J* = 7.52, 0.88 Hz, 1H, Ar-H), 7.50 (s, 1H, Ar-H), 2.03-1.94 (m, 4H, CH<sub>2</sub>), 1.11-0.99 (m, 12H, CH<sub>2</sub>), 0.75 (t, *J* = 6.8 Hz, 6H, CH<sub>3</sub>), 0.64-0.56 (m, 4H, CH<sub>2</sub>), 0.32 (s, 9H, CH<sub>3</sub>). <sup>13</sup>C NMR (CDCl<sub>3</sub>): 192.5, 151.8, 151.4, 147.7, 141.7, 140.2, 135.6, 132.2, 130.6, 127.9, 123.3, 120.3, 120.2, 55.3, 40.1, 31.5, 29.6, 23.8, 22.6, 14.1, -0.80. MALDI MS: *m/z* 435.4400 (M + H)<sup>+</sup>. HRMS (ASAP<sup>+</sup>) calc. for C<sub>29</sub>H<sub>43</sub>OSi theoretical mass: 435.30, found mass: 435.3082.

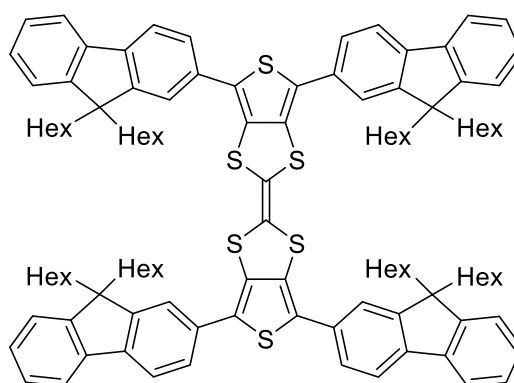
9,9,9',9'-Tetrahexyl-9H,9'H-[2,2'-bifluorene]-7-carbaldehyde (F2-CHO)

Under nitrogen, 7-Bromo-9,9,9',9'-tetrahexyl-9H,9'H-2,2'-bifluorene (4 g, 5.36 mmol, 1 equiv) was dissolved in 55 mL of dry tetrahydrofuran. The temperature was reduced to  $-78^{\circ}\text{C}$  and *n*-BuLi (2.3 mL, 5.79 mmol, 1.08 equiv) added drop-wise over 15 min. The mixture was allowed to stir for 5 min and then the temperature reduced to  $-90^{\circ}\text{C}$ . Dimethylformamide (0.5 mL, 6.86 mmol, 1.28 equiv) was slowly added and the reaction was allowed to reach room temperature. Stirring continued overnight. The mixture was washed with water with water and extracted with 3 x 75 mL diethyl ether. The organic layers were combined washed with water and dried over magnesium sulphate. The solvent was evaporated under reduced pressure. The product was purified using silica gel chromatography, eluting with 99:1 mixture of hexane/ethyl acetate. The product was isolated as a yellow gum solid (2.14 g, 58%).

$^1\text{H}$  NMR ( $\text{CDCl}_3$ ): 10.08 (s, 1H, Ar-CHO), 7.90 (d,  $J = 0.8$  Hz, 1H, Ar-H), 7.87 (d,  $J = 1.2$  Hz, 1H, Ar-H), 7.86 (d,  $J = 8.0$  Hz, 2H, Ar-H), 7.79 (d,  $J = 7.8$  Hz, 1H, Ar-H), 7.76-7.73 (m, 1H, Ar-H), 7.69 (dd,  $J = 6.3, 1.6$  Hz, 1H, Ar-H), 7.66-7.63 (m, 2H, Ar-H), 7.61 (d,  $J = 1.2$  Hz, 1H, Ar-H), 7.38-7.30 (m, 3H, Ar-H), 2.10-2.0 (m, 8H,  $\text{CH}_2$ ), 1.15-1.02 (m, 25H,  $\text{CH}_2$ ), 0.78-0.63 (m, 20H,  $\text{CH}_3$ ).  $^{13}\text{C}$  NMR ( $\text{CDCl}_3$ ): 192.5, 153.1, 151.9, 151.7, 151.1, 147.5, 142.5, 140.9, 140.8, 140.1, 138.8, 135.4, 130.8, 127.3, 127.0, 126.6, 126.3, 123.2, 123.1, 121.7, 121.6, 121.4, 120.1, 119.9, 55.5, 55.3, 40.5,

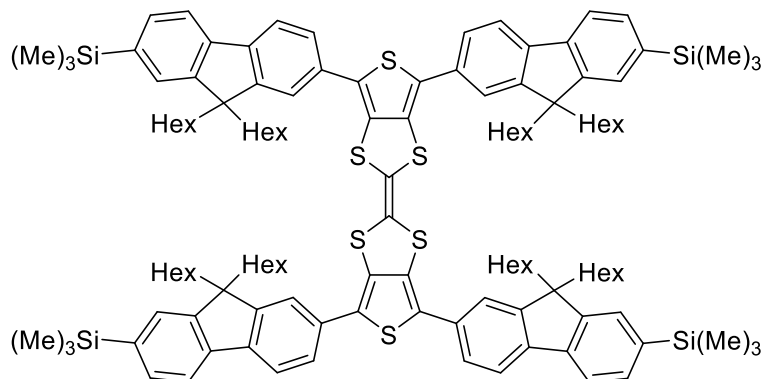
40.3, 31.6, 29.8, 29.7, 23.9, 22.7, 22.73, 22.7, 22.66, 14.11, 14.1; MS: MALDI 695.18 ( $[M + H]^+$ ); HR-MS: 695.5183 ( $[M + H]^+$ ).

4,4',6,6'-Tetrakis(9,9-dihexyl-9H-fluoren-2-yl)-2,2'-bithieno[3,4-d][1,3]dithiolylidene (TTF-F1)



Freshly distilled  $P(OEt)_3$  (12 mL) was added to 4,6-bis(9,9-dihexyl-9H-fluoren-2-yl)thieno[3,4-d][1,3]dithiol-2-one (**HU-F1**) (200 mg, 0.238 mmol, 1 equiv) and stirred under  $N_2$  at 125 C for 3 days. The mixture was cooled to room r/t and the precipitate dissolved in  $CH_2Cl_2$  and solvent removed under reduced pressure. The product was isolated on silica eluting with hexane/toluene (8:2 v/v) and additionally reprecipitated from methanol, affording a yellow amorphous solid (0.22 g, 56 %).  $^1H$  NMR ( $CDCl_3$ ): 7.78-7.72 (m, 2H, Ar-H), 7.61-7.56 (m, 2H, Ar-H), 7.39-7.33 (m, 3H, Ar-H), 2.10-1.98 (m, 4H,  $CH_2$ ), 1.15-1.02 (m, 12H,  $CH_2$ ), 0.77-0.69 (m, 10H,  $CH_3$ ).  $^{13}C$  NMR ( $CDCl_3$ ): 151.3, 150.6, 140.5, 139.9, 131.1, 127.0, 126.4, 124.5, 122.4, 120.2, 119.7, 119.4, 54.8, 39.9, 30.99, 30.95, 29.2, 23.3, 22.1, 13.5. MS: MALDI 1645.59 ( $[M + H]^+$ ).

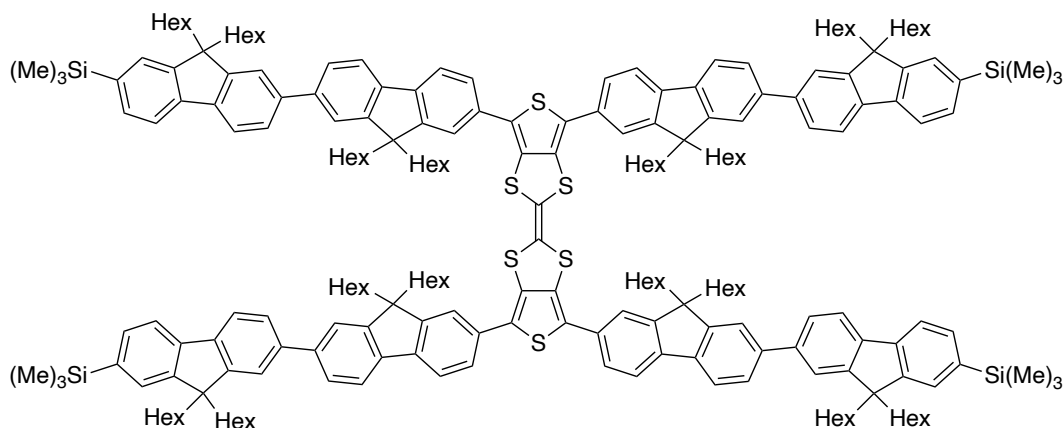
4,4',6,6'-Tetrakis(9,9-dihexyl-7-(trimethylsilyl)-9H-fluoren-2-yl)-2,2'-bithieno[3,4-d][1,3]dithiolylidene (TTF-F1-TMS)



In a microwave-assisted reaction, Pd(PPh<sub>3</sub>)<sub>4</sub> (0.04 g, 0.03 mmol, 0.2 equiv), (9,9-dihexyl-7-(trimethylsilyl)-9H-fluoren-2-yl)boronic acid (0.36 g, 0.79 mmol, 5 equiv) and Ba(OH)<sub>2</sub>·8H<sub>2</sub>O (0.40 g, 1.26 mmol, 8 equiv) were added to perbromo-2,2'-bithieno[3,4-*d*][1,3]dithiolylidene (0.10 g, 0.16 mmol, 1 equiv), under N<sub>2</sub>. Dry THF (4 mL) and degassed water (1 mL) were added. The reaction proceeded at 100°C (5 min), 120°C (5 min) and 140°C for 2 hours. The mixture was added to water (15 mL), extracted with CH<sub>2</sub>Cl<sub>2</sub> (3 x 25 mL) and the combined organic layers washed with water (40 mL). The organic mixture was dried over MgSO<sub>4</sub> and solvent evaporated under reduced pressure. The product was isolated on silica gel eluting with a gradient mixture of hexane: dichloromethane 9.9:0.1 increasing to 9.6:0.4 (v/v). The product was additionally reprecipitated from methanol, affording a yellow amorphous solid (0.20 g, 65%). <sup>1</sup>H NMR (CDCl<sub>3</sub>): 7.78 (d, J = 7.92 Hz, 1H, Ar-H), 7.71 (dd, J = 7.2, 0.32 Hz, 1H, Ar-H), 7.61-7.56 (m, 2H, Ar-H), 7.53-7.50 (m, 2H, Ar-H), 2.07-2.02 (m, 4H, CH<sub>2</sub>), 1.15-1.08 (m, 12H, CH<sub>2</sub>), 0.78-0.68 (m, 10H, CH<sub>3</sub>), 0.34 (s, 9H, CH<sub>3</sub>). <sup>13</sup>C NMR (CDCl<sub>3</sub>): 152.2, 150.4, 141.1, 139.8, 132.1, 131.9, 131.8, 129.5, 127.8, 125.2,

121.0, 120.5, 119.3, 119.0, 55.4, 40.3, 31.5, 29.7, 23.9, 22.7, 14.2, -0.7. MALDI MS:  $m/z$  1934.22 ( $M + H$ )<sup>+</sup>. Anal. Calcd for C<sub>122</sub>H<sub>164</sub>S<sub>6</sub>Si<sub>4</sub>: C, 75.71; H, 8.54 %. Found: C, 75.68; H, 8.43%. Mp: 122°C.

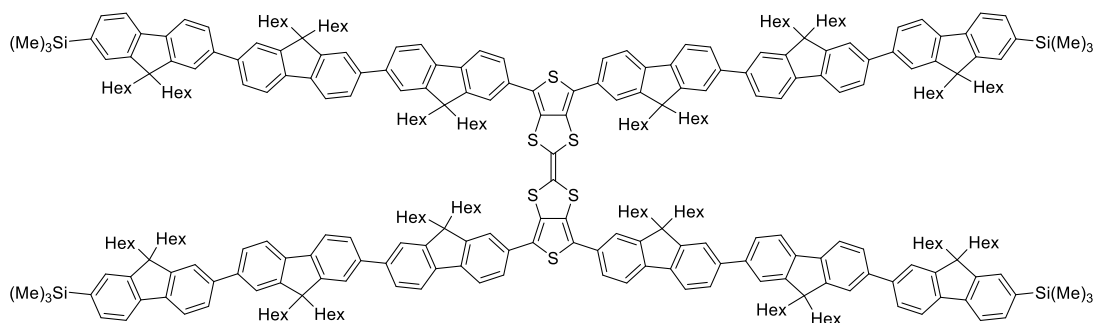
4,4',6,6'-Tetrakis(9,9,9',9'-tetrahexyl-7'-(trimethylsilyl)-9H,9'H-[2,2'-bifluoren]-7-yl)-2,2'-bithieno[3,4-d][1,3]dithiolylidene (TTF-F2-TMS)



In a microwave-assisted reaction, Pd(PPh<sub>3</sub>)<sub>4</sub> (0.02 g, 0.02 mmol, 0.2 equiv), (9,9,9',9'-tetrahexyl-7'-(trimethylsilyl)-9H,9'H-[2,2'-bifluoren]-7-yl)boronic acid (0.37 g, 0.47 mmol, 5 equiv) and Ba(OH)<sub>2</sub>·8H<sub>2</sub>O (0.24 g, 0.76 mmol, 8 equiv) were added to perbromo-2,2'-bithieno[3,4-*d*][1,3]dithiolylidene (0.06 g, 0.095 mmol, 1 equiv), under N<sub>2</sub>. Dry THF (2.5 mL) was added, followed by degassed water (0.5 mL). The reaction proceeded at 100°C for 5 min, 120°C for 5 min followed by 140°C for 2 hours. The mixture was added to water (10 mL) and extracted using CH<sub>2</sub>Cl<sub>2</sub> (3 x 15 mL). The combined organic layers were dried on MgSO<sub>4</sub> and solvent evaporated under reduced pressure. The product was isolated on silica gel eluting with a mixture of hexane:toluene 9.9:0.1 increasing to 9:1 (v/v). The isolated compound was additionally reprecipitated from methanol affording a yellow amorphous solid (0.20 g, 64.5%). <sup>1</sup>H

NMR (CDCl<sub>3</sub>): 7.84-7.79 (m, 3H, Ar-H), 7.74 (d, J = 7.36 Hz, 1H, Ar-H), 7.70-7.61 (m, 6H, Ar-H), 7.54-7.51 (m, 2H, Ar-H), 2.16-2.03 (m, 8H, CH<sub>2</sub>), 1.19-1.11 (m, 24H, CH<sub>2</sub>), 0.80-0.74 (m, 20H, CH<sub>3</sub>), 0.35-0.33 (m, 9H, CH<sub>3</sub>). <sup>13</sup>C NMR (CDCl<sub>3</sub>): 152.3, 152.0, 151.9, 150.3, 141.5, 141.2, 141.0, 140.62, 140.6, 139.7, 139.2, 132.0, 131.9, 131.7, 129.5, 127.8, 126.5, 126.2, 125.3, 121.7, 121.0, 120.4, 120.3, 120.2, 119.2, 55.6, 55.3, 40.6, 40.3, 31.6, 31.5, 29.9, 29.7, 24.0, 23.9, 22.7, 22.6, 14.2, 14.1, -0.7. : MALDI MS: *m/z* 3265 (M<sup>+</sup>). Anal. Calcd for C<sub>222</sub>H<sub>292</sub>S<sub>6</sub>Si<sub>4</sub>: C, 81.66; H, 9.01 %. Found: C, 81.55; H, 8.91 %. Mp: 209-210°C. TGA analysis at a heating rate of 10°C/min (measured at 5% mass loss) showed decomposition at 410.9°C.

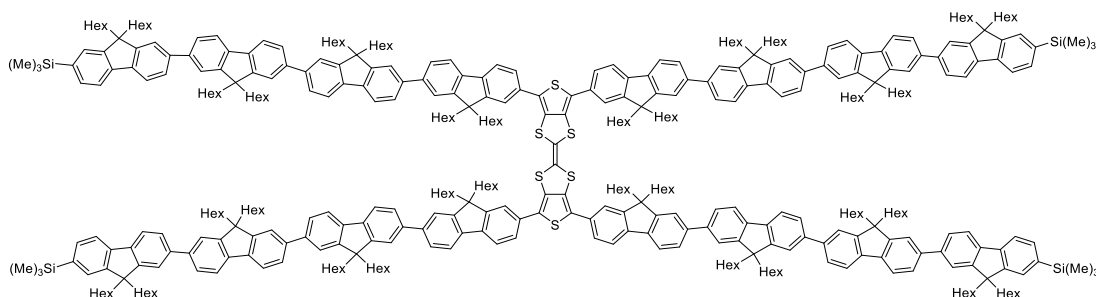
4,4',6,6'-Tetrakis(9,9,9',9',9'',9''-hexahexyl-7''-(trimethylsilyl)-9H,9'H,9''H-[2,2':7',2''-terfluoren]-7-yl)-2,2'-bithieno[3,4-d][1,3]dithiolylidene (TTF-F3-TMS)



In a microwave-assisted reaction, Pd(PPh<sub>3</sub>)<sub>4</sub> (0.02 g, 0.02 mmol, 0.2 equiv), (9,9,9',9',9'',9''-hexahexyl-7''-(trimethylsilyl)-9H,9'H,9''H-[2,2':7',2''-terfluoren]-7-yl)boronic acid (0.53 g, 0.48 mmol, 5 equiv) and Ba(OH)<sub>2</sub>·8H<sub>2</sub>O (0.24 g, 0.76 mmol, 8 equiv) were added to perbromo-2,2'-bithieno[3,4-d][1,3]dithiolylidene (0.06 g, 0.10 mmol, 1 equiv) under N<sub>2</sub>. Dry THF (2.5 mL) and degassed water (0.5 mL) were added and reaction was heated to 100°C for 5 min, 120°C for 5 min and 140°C for 2 h. The

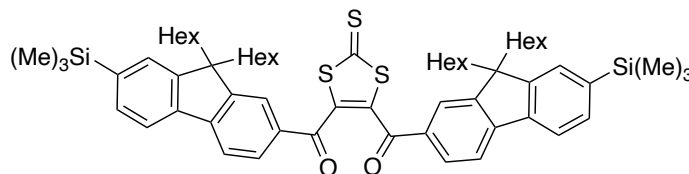
mixture was added to water (20 mL) and extracted with CH<sub>2</sub>Cl<sub>2</sub> (3 x 30 mL). The combined organic layers were washed with water (30 mL) and dried over MgSO<sub>4</sub>. The solvent was removed under reduced pressure and isolated on silica gel eluting with a gradient of hexane: toluene 99.9: 0.1 increasing to 9.5: 0.5 (v/v). The product was additionally reprecipitated from methanol affording a yellow amorphous solid (0.28 g, 64 %). <sup>1</sup>H NMR (CDCl<sub>3</sub>): 7.86-7.79 (m, 5H, Ar-H), 7.74-7.63 (m, 11H, Ar-H), 7.53-7.51 (m, 2H, Ar-H), 2.14-2.03 (m, 12H, CH<sub>2</sub>), 1.20-1.11 (m, 37 H, CH<sub>2</sub>), 0.84-0.77 (m, 31H, CH<sub>3</sub>), 0.34 (s, 9H, CH<sub>3</sub>). <sup>13</sup>C NMR (CDCl<sub>3</sub>): 152.3, 152.0, 151.99, 151.9, 151.86, 150.3, 141.6, 141.2, 140.9, 140.8, 140.5, 140.3, 140.1, 139.7, 139.1, 132.0, 131.9, 131.8, 129.6, 127.8, 126.3, 126.2, 121.7, 120.2, 119.2, 55.7, 55.5, 55.3, 40.5, 40.3, 31.7, 31.6, 31.5, 29.9, 29.8, 29.7, 24.0, 23.9, 22.7, 22.70, 22.6, 14.2, 14.15, -0.7. MALDI: *m/z* 4595 (M<sup>+</sup>). Anal. Calcd for C<sub>322</sub>H<sub>420</sub>S<sub>6</sub>Si<sub>4</sub>: C, 84.16; H, 9.21 %. Found: C, 84.13; H, 9.25 %. Mp: 178°C.

4,4',6,6'-Tetrakis(9,9,9',9',9'',9''',9''''-octahexyl-7''''-(trimethylsilyl) 9H,9'H,9''H,9''''H-[2,2':7',2'':7'',2'''-quaterfluoren]-7-yl)-2,2'-bithieno[3,4-d][1,3]dithiolylidene (TTF-F4-TMS)



In a microwave-assisted reaction, Pd(PPh<sub>3</sub>)<sub>4</sub> (0.02 g, 0.02 mmol, 0.2 equiv), (9,9,9',9',9'',9''',9''',9''''-octahexyl-7'''-(trimethylsilyl)-9*H*,9'*H*,9''*H*,9'''*H*-[2,2':7',2'':7'',2'''-quaterfluoren]-7-yl)boronic acid (0.58 g, 0.4 mmol, 4 equiv) and Ba(OH)<sub>2</sub>·8H<sub>2</sub>O (0.20 g, 0.64 mmol, 8 equiv) were added to perbromo-2,2'-bithieno[3,4-*d*][1,3]dithiolylidene (0.05 g, 0.08 mmol, 1 equiv) under N<sub>2</sub>. Dry THF (2.1 mL) and degassed water (0.4 mL) were added. The reaction proceeded at 100°C (5 min), 120°C (5 min) and 140°C for 2 hours. The mixture was added to water (20 mL) and extracted with CH<sub>2</sub>Cl<sub>2</sub> (3 x 40 mL). The combined organic layers were washed with water (60 mL) and dried over MgSO<sub>4</sub>. The solvent was evaporated under reduced pressure. The product was isolated on silica gel eluting with a gradient mixture of hexane: toluene 9:1 increasing to 7:3 (v/v). The product was additionally reprecipitated from methanol, affording a yellow amorphous solid (0.17 g, 36.2%). <sup>1</sup>H NMR (CDCl<sub>3</sub>): 7.86-7.79 (m, 7H, Ar-H), 7.74-7.63 (m, 15H, Ar-H), 7.53-7.50 (m, 2H, Ar-H), 2.14-2.02(m, 16H, CH<sub>2</sub>), 1.18-1.10 (m, 50H, CH<sub>2</sub>), 0.84-0.76 (m, 41H, CH<sub>3</sub>), 0.33 (s, 9H, CH<sub>3</sub>). <sup>13</sup>C NMR (CDCl<sub>3</sub>): 152.3, 152.1, 152.0, 151.97, 151.93, 151.9, 150.3, 141.6, 141.2, 141.0, 140.8, 140.7, 140.5, 140.46, 140.3, 140.2, 140.1, 139.7, 139.1, 132.0, 131.9, 131.8, 127.8, 126.3, 126.2, 121.7, 120.2, 120.1, 119.2, 55.7, 55.5, 55.48, 55.3, 40.5 40.3, 31.7, 31.6, 31.5, 29.9, 29.8, 29.7, 24.0, 23.9, 22.8, 22.75, 22.7, 22.6, 22.59, 14.2, 14.16, -0.7. MS: MALDI 5926.85 ([M + H]<sup>+</sup>). Anal. Calcd for C<sub>422</sub>H<sub>548</sub>S<sub>6</sub>Si<sub>4</sub>: C, 85.54; H, 9.32 %. Found: C, 85.32; H, 9.28 %. Mp: 166°C

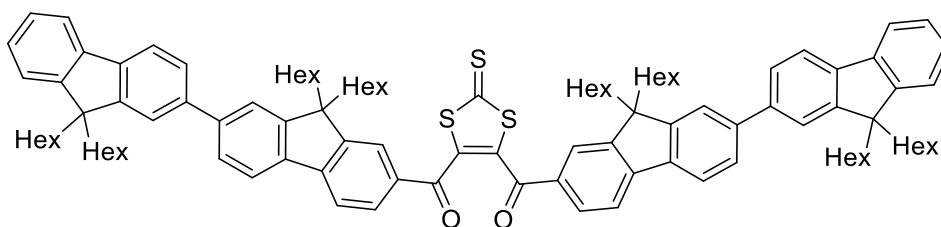
(2-Thioxo-1,3-dithiole-4,5-diyl)bis((9,9-dihexyl-7-(trimethylsilyl)-9H-fluoren-2-yl)methanone) (2.14)



Under N<sub>2</sub>, VTC (1.36 g, 10.07 mmol, 1 equiv) was dissolved in THF (46 mL). The temperature was brought to -70°C and 1.62 M LDA.THF (7.4 mL, 11.98 mmol, 1.19 equiv) was added dropwise. The mixture stirred at -55°C for 30 min and 0.2 M solution of 9,9-dihexyl-7-(trimethylsilyl)-9H-fluorene-2-carbaldehyde in THF (50 mL) was added dropwise. The mixture allowed to stir for a further 30 min. The second portion of 1.62 M LDA.THF (7.4 mL, 11.98 mmol, 1.19 equiv) was added at -55°C and the mixture stirred for 15 min. The temperature was reduced to -80°C and a 0.2 M solution of 9,9-dihexyl-7-(trimethylsilyl)-9H-fluorene-2-carbaldehyde in THF (50 mL) was added slowly and the reaction was allowed to reach room temperature. The mixture was poured onto saturated NaHCO<sub>3</sub> solution (400 mL) to which KBr (40 g) was added. The mixture was then extracted using ethyl acetate (3 x 100 mL) and washed with water (200 mL). The mixture was dried on MgSO<sub>4</sub> and solvent evaporated under reduced pressure. The mixture was dissolved in CH<sub>2</sub>Cl<sub>2</sub> (100 mL) and a 10-fold excess of MnO<sub>2</sub> (w/w) added. The mixture was stirred for 2 min and immediately filtered through a plug of silica. The solvent was evaporated under reduced pressure and the product isolated on silica gel, eluting with a mixture of hexane: toluene 7:3 (v/v). A yellow amorphous solid was afforded (5.1 g, 51.1%). <sup>1</sup>H NMR (CDCl<sub>3</sub>): 7.65-7.58 (m, 3H, Ar-H), 7.55 (d, *J* = 7.8 Hz, 1H, Ar-H), 7.49 (dd, *J*

= 6.8, 0.8 Hz, 1H, Ar-H), 7.46 (s, 1H, Ar-H), 1.97-1.82 (m, 4H, CH<sub>2</sub>), 1.12-0.99 (m, 12H, CH<sub>2</sub>), 0.76 (t, *J* = 6.84 Hz, 6H, CH<sub>3</sub>), 0.53-0.50 (m, 4H, CH<sub>2</sub>), 0.30 (s, 9H, CH<sub>3</sub>).  
<sup>13</sup>C NMR (CDCl<sub>3</sub>): 184.4, 151.7, 151.4, 147.9, 145.5, 142.2, 139.7, 134.6, 132.2, 129.4, 129.2, 128.4, 128.0, 125.4, 124.0, 120.5, 120.0, 55.4, 39.8, 31.5, 30.0, 23.7, 22.6. MALDI MS: *m/z* 999.63 (M<sup>+</sup>). Anal. Calcd for C<sub>61</sub>H<sub>82</sub>O<sub>2</sub>S<sub>3</sub>Si<sub>2</sub>: C, 73.29; H, 8.27%. Found: C, 73.16; H, 8.15%.

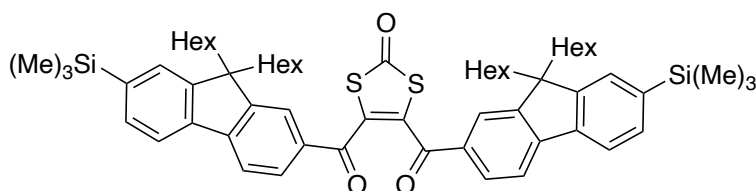
(2-thioxo-1,3-dithiole-4,5-diyl)bis((9,9,9',9'-tetrahexyl-9H,9'H-[2,2'-bifluorene]-7-yl)methanone) (2.19)



Under N<sub>2</sub>, vinylene trithiocarbonate (0.18 g, 1.35 mmol, 1 equiv) was dissolved in dry THF (6 mL). The temperature was reduced to -70°C and LDA.THF (0.76 mL, 1.61 mmol, 1.19 equiv) was added drop-wise. The mixture was stirred at -55°C for 30 min, followed by the drop-wise addition of 9,9,9',9'-tetrahexyl-9H,9'H-[2,2'-bifluorene]-7-carbaldehyde (1.04 g, 1.49 mmol, 1.10 equiv) in dry tetrahydrofuran (7.25 mL). The mixture was allowed to stir for another 30 min. A second equivalent of LDA.THF (0.76 mL, 1.61 mmol, 1.19 equiv) was added and the mixture stirred for 15 min. The temperature of the mixture was reduced to -80°C and a second portion of 9,9,9',9'-tetrahexyl-9H,9'H-[2,2'-bifluorene]-7-carbaldehyde (1.04 g, 1.49 mmol, 1.10 equiv) in dry tetrahydrofuran (7.25 mL) was added slowly. The reaction was allowed to reach room temperature and stirring continued overnight. The mixture was poured onto

saturated NaHCO<sub>3</sub> solution (55 mL) to which KBr (6g) was added. The mixture was extracted using ethyl acetate (3 x 75 mL) and the combined organic layers washed with water. The organic layers were dried on MgSO<sub>4</sub> and solvent evaporated under reduced pressure. The mixture was dissolved in CH<sub>2</sub>Cl<sub>2</sub> and a 10-fold excess (w/w) of MnO<sub>2</sub> added. The mixture was stirred for 1 min and filtered through silica, eluting with CH<sub>2</sub>Cl<sub>2</sub>. The solvent was evaporated under reduced pressure and purified on silica eluting with a mixture of 7:3 hexane: toluene, increasing to 1:1. The product was isolated as a yellow amorphous solid (0.53 g, 26%). <sup>1</sup>H NMR (CDCl<sub>3</sub>): 7.79-7.73 (m, 3H, Ar-H), 7.67 (s, 2H, Ar-H), 7.65 (d, *J* = 1.56 Hz, Ar-H), 7.63-7.60 (m, 3H, Ar-H), 7.58 (d, *J* = 1.16 Hz, Ar-H), 7.38-7.30 (m, 3H, Ar-H), 2.06-1.92 (m, 8H, CH<sub>2</sub>), 1.16-1.06 (m, 24H, CH<sub>2</sub>), 0.78-0.60 (m, 20H, CH<sub>3</sub>). <sup>13</sup>C NMR (CDCl<sub>3</sub>): 208.8, 184.4, 153.2, 151.82, 151.8, 151.7, 151.1, 147.6, 145.4, 142.9, 141.0, 140.7, 140.0, 138.3, 134.4, 134.3, 129.6, 127.3, 127.0, 126.7, 126.3, 123.9, 123.1, 121.8, 121.6, 120.1, 120.0, 119.9, 55.6, 55.3, 40.5, 40.0, 31.63, 31.6, 29.8, 29.7, 23.9, 22.74, 22.7, 14.17, 14.13, 14.1. MS: MALDI 1519.66 ([M + H]<sup>+</sup>). Mp: 88-90°C.

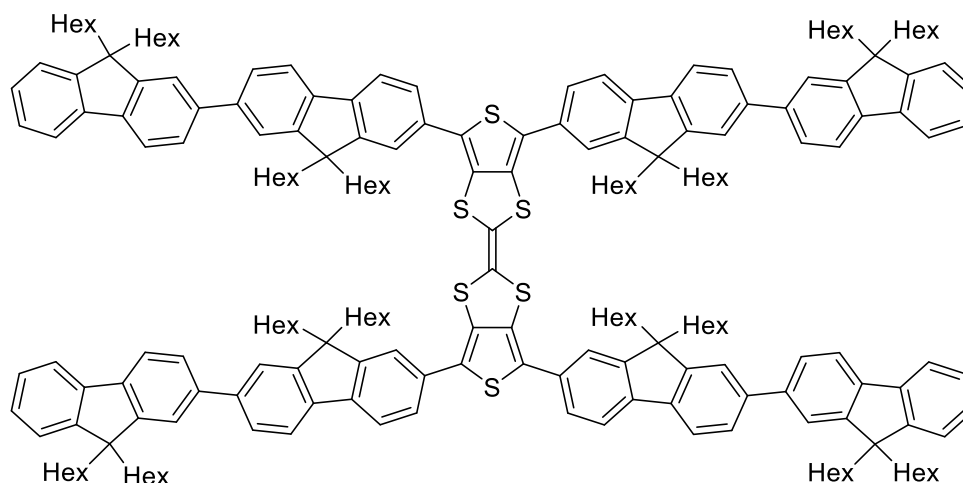
(2-Oxo-1,3-dithiole-4,5-diyl)bis((9,9-dihexyl-7-(trimethylsilyl)-9H-fluoren-2-yl)methanone) (2.20)



(2-Thioxo-1,3-dithiole-4,5-diyl)bis((9,9-dihexyl-7-(trimethylsilyl)-9H-fluoren-2-yl)methanone) (5.15 g, 5.14 mmol, 1 equiv) was dissolved in CH<sub>2</sub>Cl<sub>2</sub>/CH<sub>3</sub>COOH (3:1 v/v). Hg(OAc)<sub>2</sub> was added and the mixture stirred overnight and mixture was filtered

through celite with  $\text{CH}_2\text{Cl}_2$ . The mixture was washed with water (200 mL), washed with  $\text{NaHCO}_3$  (3 x 200 mL) and dried over  $\text{MgSO}_4$  and solvent evaporated under reduced pressure. The product was purified by reprecipitated from methanol, affording a yellow amorphous solid (4.7 g, 65%).  $^1\text{H}$  NMR ( $\text{CDCl}_3$ ): 7.66-7.63 (4H, m, Ar-H), 7.60 (2H, dd,  $J = 6.56, 1.4$  Hz, Ar-H), 7.55 (2H, d,  $J = 7.96$  Hz, Ar-H), 7.50-7.48 (4H, m, Ar-H), 1.99-1.84 (8H, m,  $\text{CH}_2$ ), 1.13-1.03 (24H, m,  $\text{CH}_2$ ), 0.77 (12H, t,  $J 6.84$  Hz,  $\text{CH}_3$ ), 0.54-0.46 (8H, m,  $\text{CH}_2$ ), 0.54-0.16 (18H, m,  $\text{CH}_3$ ).  $^{13}\text{C}$  NMR ( $\text{CDCl}_3$ ): 187.9, 185.9, 151.6, 151.4, 147.6, 142.0, 139.8, 136.6, 134.9, 132.2, 129.3, 128.0, 124.0, 120.4, 120.0, 55.4, 39.8, 31.5, 29.6, 23.7, 22.6, 14.1, -0.8. MS: MALDI 983.58 ( $[\text{M} + \text{H}]^+$ ).

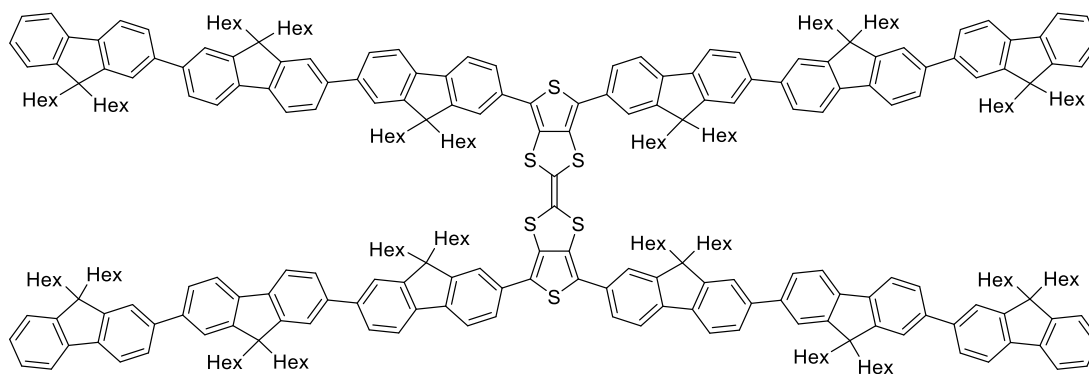
4,4',6,6'-Tetrakis(9,9,9',9'-tetrahexyl-9*H*,9'*H*-[2,2'-bifluoren]-7-yl)-2,2'-bithieno[3,4-*d*][1,3]dithiolylidene (TTF-F2)



4,4',6,6'-Tetrakis(9,9,9',9'-tetrahexyl-7'-(trimethylsilyl)-9*H*,9'*H*-[2,2'-bifluoren]-7-yl)-2,2'-bithieno[3,4-*d*][1,3]dithiolylidene (TTF-F2-TMS) (140 mg, 0.04 mmol, 1 equiv) was dissolved in  $\text{CH}_2\text{Cl}_2$  (28 mL) and  $\text{CF}_3\text{CO}_2\text{H}$  (3 mL) added. The mixture was stirred overnight at room temperature and the mixture was added to water (10 mL), extracted

using  $\text{CH}_2\text{Cl}_2$  (3 x 20 mL) and washed with water (20 mL). The mixture was dried over  $\text{MgSO}_4$  and solvent removed under reduced pressure. Recrystallization from MeOH afforded a yellow amorphous solid (134 mg, 98%).  $^1\text{H}$  NMR ( $\text{CDCl}_3$ ): 7.84-7.74 (m, 4H, Ar-H), 7.70-7.61 (m, 6H, Ar-H), 7.39-7.30 (m, 3H, Ar-H), 2.15-2.02 (m, 8H,  $\text{CH}_2$ ), 1.19-1.08 (m, 24H,  $\text{CH}_2$ ), 0.79-0.72 (m, 20H,  $\text{CH}_3$ ).  $^{13}\text{C}$  NMR ( $\text{CDCl}_3$ ): 152.3, 152.0, 151.7, 151.2, 141.2, 140.9, 140.6, 140.5, 139.7, 131.8, 131.7, 129.5, 127.2, 127.0, 126.5, 126.2, 125.3, 123.1, 121.6, 121.59, 121.0, 120.4, 120.3, 120.0, 119.9, 119.0, 55.6, 55.3, 40.5, 31.6, 29.8, 24.0, 23.9, 22.7, 14.2, 14.15. (MALDI/TOF,  $m/z$ ): 2974.50 ( $\text{M}^+$ ). Anal. Calcd for  $\text{C}_{210}\text{H}_{260}\text{S}_6$ : C, 84.73; H, 8.80%. Found: C, 84.49; H, 8.55%. Mp: 174-176 °C.

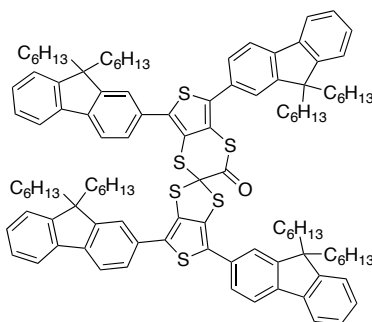
4,4',6,6'-Tetrakis(9,9,9',9',9'',9''-hexahexyl-9*H*,9'*H*,9''*H*-[2,2':7',2''-terfluoren]-7-yl)-2,2'-bithieno[3,4-*d*][1,3]dithiolylidene (**TTF-F3**)



4,4',6,6'-Tetrakis(9,9,9',9',9'',9''-hexahexyl-7''-(trimethylsilyl)-9*H*,9'*H*,9''*H*-[2,2':7',2''-terfluoren]-7-yl)-2,2'-bithieno[3,4-*d*][1,3]dithiolylidene (**TTF-F3-TMS**) (150 mg, 0.02 mmol, 1 equiv) was dissolved in  $\text{CH}_2\text{Cl}_2$  (18 mL) and  $\text{CF}_3\text{CO}_2\text{H}$  (2 mL) added. The mixture was stirred overnight at room temperature and the mixture was added to

water (10 mL), extracted using  $\text{CH}_2\text{Cl}_2$  (3 x 20 mL) and washed with water (20 mL). The mixture was dried over  $\text{MgSO}_4$  and solvent removed under reduced pressure. Reprecipitation from MeOH afforded a yellow amorphous solid (102 mg, 99%).  $^1\text{H}$  NMR ( $\text{CDCl}_3$ ): 7.85-7.62 (m, 16H, Ar-H), 7.38-7.30 (m, 3H, Ar-H), 2.12-2.05 (m, 12H,  $\text{CH}_2$ ), 1.18-1.09 (m, 37H,  $\text{CH}_2$ ), 0.83-0.68 (m, 31H,  $\text{CH}_3$ ).  $^{13}\text{C}$  NMR ( $\text{CDCl}_3$ ): 151.9, 151.6, 151.5, 151.2, 142.0, 141.3, 140.9, 140.7, 140.6, 140.5, 140.3, 140.1, 139.7, 127.1, 126.9, 126.3, 126.2, 123.1, 121.7, 121.6, 120.1, 120.0, 119.86, 55.5, 55.3, 40.5, 31.7, 31.6, 31.58, 29.8, 29.79, 23.97, 23.93, 22.74, 22.7, 22.6, 14.3, 14.2, 14.18, 14.14, 14.1. (MALDI/TOF,  $m/z$ ): 4303.81  $[(\text{M} + \text{H})^+]$ . Mp: 120 °C.

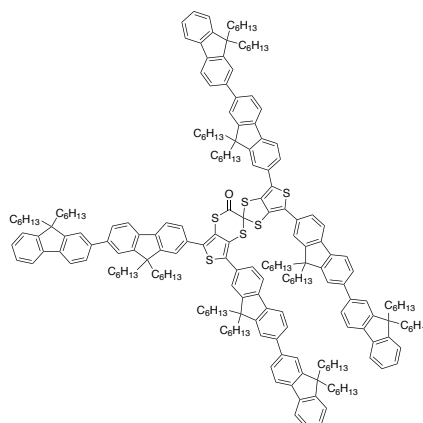
4',5,6',7-Tetrakis(9,9-dihexyl-9H-fluoren-2-yl)-3H-spiro[thieno[3,4-b][1,4]dithiine-2,2'-thieno[3,4-d][1,3]dithiol]-3-one (Spiro-F1)



**TTF-F1** (80 mg, 0.05 mmol, 1 equiv) was dissolved in  $\text{CH}_2\text{Cl}_2$  (20 mL). A solution of oxidising agent  $\text{PhI}(\text{OAc})_2$  ( $5 \times 10^{-3}$  M) and  $\text{CF}_3\text{SO}_3\text{H}$  ( $4 \times 10^{-3}$  M) in acetonitrile (30 mL) was added in 5 mL portions. The addition of 2 portions of the oxidising solution led to the formation of the cation radicals, after which water (0.2 mL) was added. An additional 4 portions led to the formation of the dication species using 50% excess. The mixture was stirred overnight and water (15 mL) added and the organic layers extracted using  $\text{CH}_2\text{Cl}_2$  (3 x 20 mL). The combined organic layers were washed with water (30 mL) and dried over  $\text{MgSO}_4$ . The solvent was removed under reduced

pressure and purified on silica gel eluting with hexane: CH<sub>2</sub>Cl<sub>2</sub> 9:1 (v/v). The product was additionally reprecipitated from methanol affording a yellow amorphous solid (50.5 mg, 60.7 %). <sup>1</sup>H NMR (CDCl<sub>3</sub>): 7.83 (d, *J* = 7.88 Hz, 1H, Ar-H), 7.78-7.75 (m, 1H, Ar-H), 7.71-7.62 (m, 8H, Ar-H), 7.60-7.57 (m, 5H, Ar-H), 7.42-7.26 (m, 13H, Ar-H), 2.10-2.02 (m, 4H, CH<sub>2</sub>), 2.00-1.92 (m, 8H, CH<sub>2</sub>), 1.87-1.80 (m, 2H, CH<sub>2</sub>), 1.72-1.65 (m, 2H, CH<sub>2</sub>), 1.19-0.42 (m, 90H, CH<sub>2</sub>). <sup>13</sup>C NMR (CDCl<sub>3</sub>): 185.8, 151.9, 151.7, 151.3, 151.2, 151.19, 142.7, 142.2, 142.0, 141.3, 140.4, 140.3, 140.27, 138.5, 132.9, 131.4, 130.7, 130.4, 128.1, 127.9, 127.7, 127.6, 127.5, 127.1, 127.0, 126.9, 125.7, 124.9, 123.2, 123.1, 123.05, 120.6, 120.4, 120.2, 120.0, 88.6, 55.5, 55.4, 55.37, 40.5, 40.4, 40.38, 31.7, 31.65, 31.6, 29.9, 29.85, 29.7, 24.0, 23.95, 23.9, 22.7, 22.69, 22.5, 14.2, 14.13, 14.1. (MALDI/TOF, *m/z*): 1634.47 ([M - 26]<sup>+</sup>). Anal. Calcd for C<sub>110</sub>H<sub>132</sub>OS<sub>6</sub>: C, 79.47; H, 8.00 %. Found: C, 79.43; H, 7.97%. Mp: 84-86 °C.

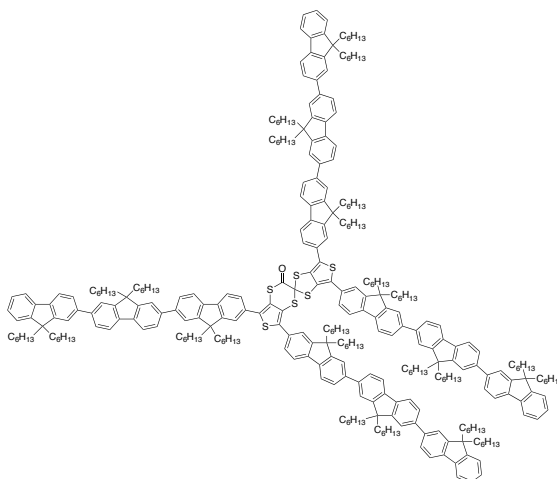
4',5,6',7-Tetrakis(9,9,9'-tetrahexyl-9H,9'H-[2,2'-bifluoren]-7-yl)-3H-spiro[thieno[3,4-b][1,4]dithiine-2,2'-thieno[3,4-d][1,3]dithiol]-3-one (Spiro-F2)



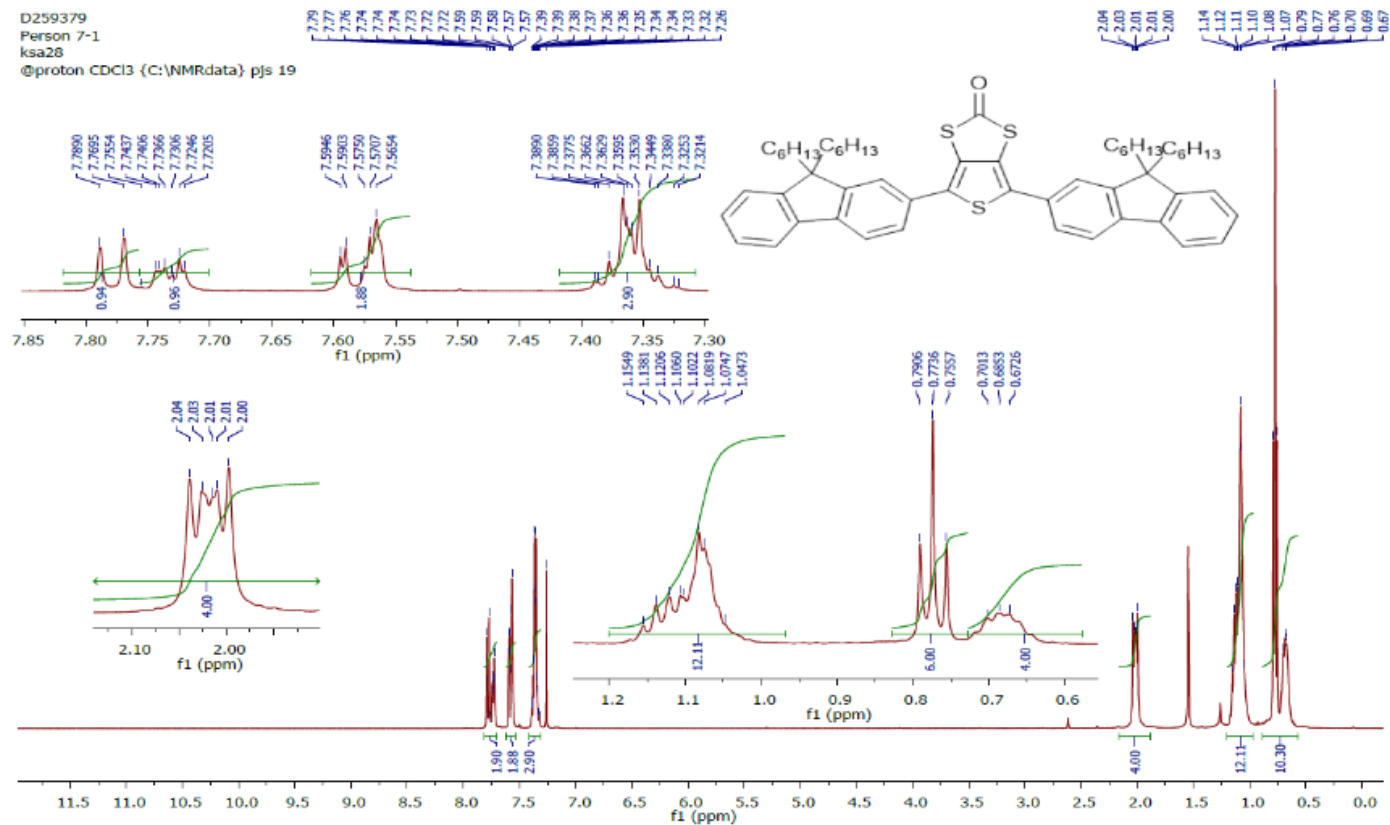
4,4',6,6'-Tetrakis(9,9,9'-tetrahexyl-9H,9'H-[2,2'-bifluoren]-7-yl)-2,2'-bithieno[3,4-*d*][1,3]dithiolylidene (TTF-F2) (54 mg, 0.02 mmol, 1 equiv) was dissolved in CH<sub>2</sub>Cl<sub>2</sub> (7.5 mL). A solution of PhI(OAc)<sub>2</sub> (38 mg, 0.118 mmol, 2.7 equiv) in CH<sub>2</sub>Cl<sub>2</sub>/MeCN (1:6 V/V) (8.42 E<sup>-3</sup> M) was added, followed by the addition of CF<sub>3</sub>SO<sub>3</sub>H (36 mg, 0.24

mmol, 6 equiv) in MeCN (0.88 M). A drop of water was added and the mixture stirred overnight. The mixture was stirred overnight and water (15 mL) added and the organic layers extracted using CH<sub>2</sub>Cl<sub>2</sub> (3 x 20 mL). The combined organic layers were washed with water (30 mL) and dried over MgSO<sub>4</sub>. The solvent was removed under reduced pressure and purified on silica gel eluting with hexane: toluene 9:1 (v/v) increasing to 8:2. The product was additionally reprecipitated from methanol affording a yellow amorphous solid (53.6 mg, 44.8 %). <sup>1</sup>H NMR (CDCl<sub>3</sub>): 7.88-7.56 (m, 10H, Ar-H), 7.38-7.30 (m, 3H, Ar-H), 2.16-1.75 (m, 8H, CH<sub>2</sub>), 1.16-1.04 (m, 22H, CH<sub>2</sub>), 0.92-0.55 (m, 23H, CH<sub>3</sub>). <sup>13</sup>C NMR (CDCl<sub>3</sub>): 185.8, 152.2, 152.04, 152.0, 151.7, 151.6, 151.1, 141.8, 141.5, 141.1, 141.0, 140.9, 140.7, 140.6, 140.5, 139.6, 139.4, 138.5, 132.9, 131.4, 130.8, 130.4, 127.2, 127.0, 126.4, 126.2, 125.8, 125.6, 123.1, 121.6, 121.5, 120.8, 120.5, 120.3, 120.0, 119.9, 55.7, 55.6, 55.56, 55.3, 40.5, 40.4, 31.6, 29.8, 29.7, 24.0, 23.9, 22.7, 22.69, 22.65, 22.6, 14.2, 14.1. (MALDI/TOF, *m/z*): 2992.80 (M<sup>+</sup>).  
Mp: 118-120 °C.

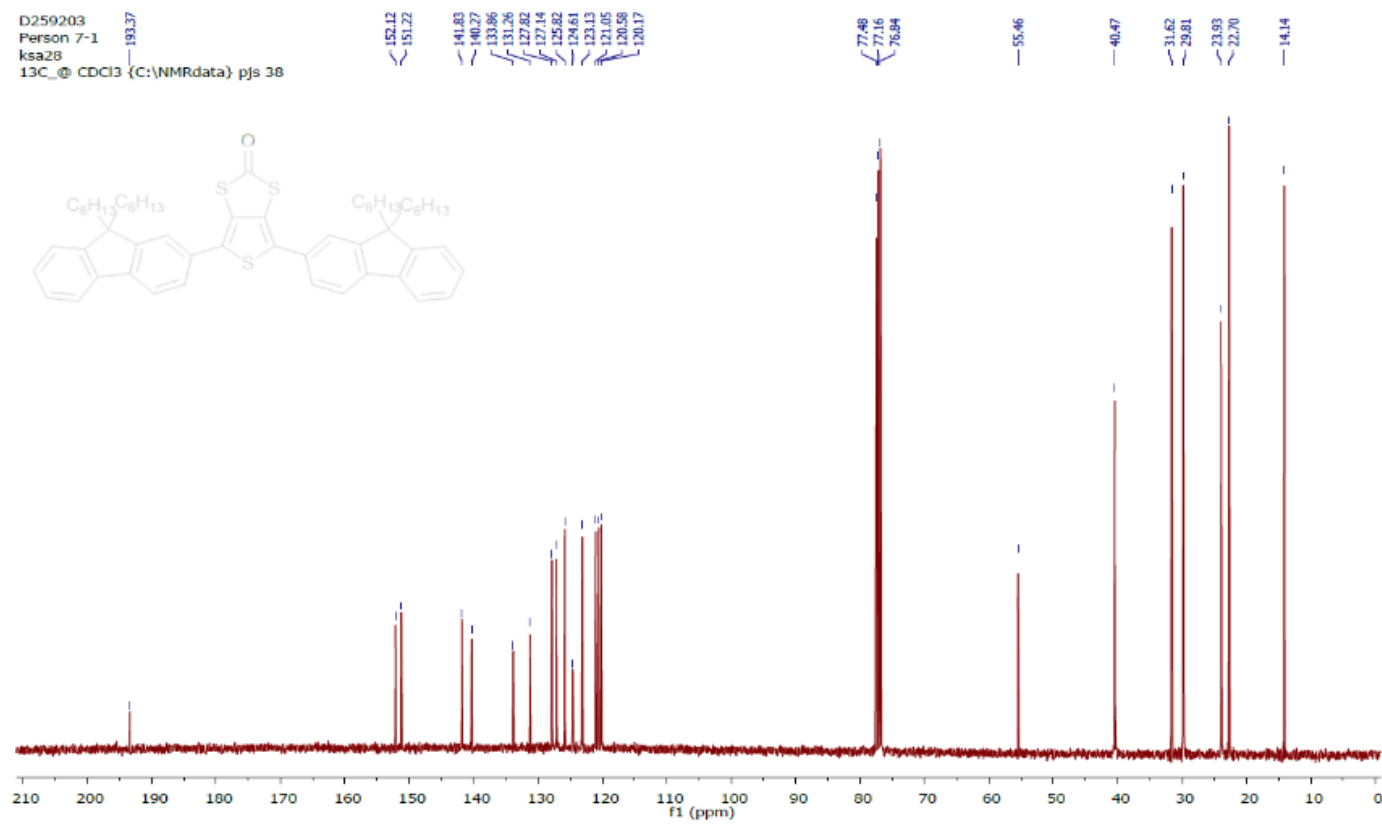
4',5,6',7-Tetrakis(9,9,9',9',9'',9'''-hexahexyl-9H,9''H,9'''H-[2,2':7',2''-terfluoren]-7-yl)-3H-spiro[thieno[3,4-b][1,4]dithiine-2,2'-thieno[3,4-d][1,3]dithiol]-3-one (Spiro-F3)



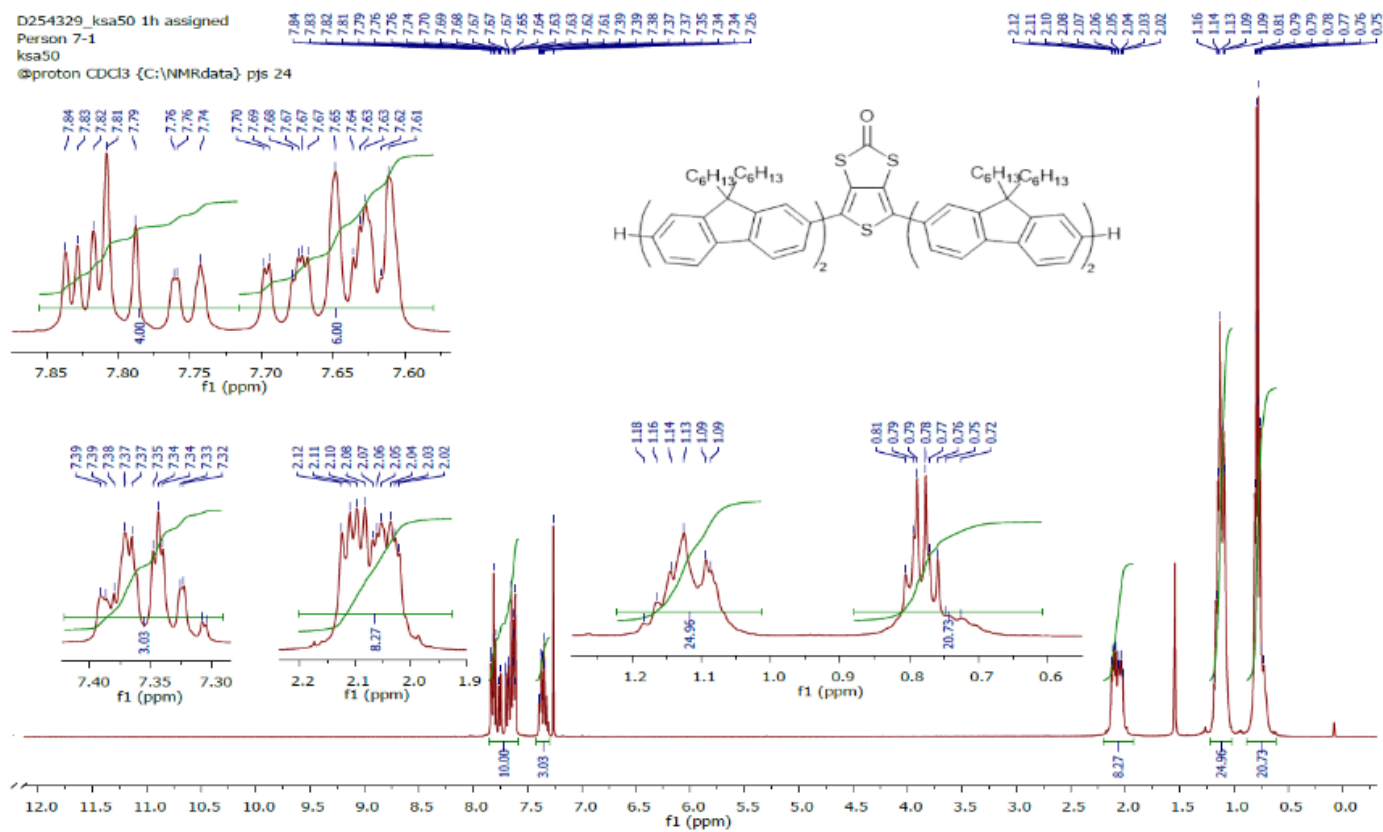
**TTF-F3** (40 mg,  $9.3 \times 10^{-3}$  mmol, 1 equiv) was dissolved in  $\text{CH}_2\text{Cl}_2$  (4 mL). A solution of oxidising agent  $\text{PhI}(\text{OAc})_2$  (7.14 mg,  $5 \times 10^{-3}$  M) and  $\text{CF}_3\text{SOOH}$  (0.01 mL,  $4 \times 10^{-3}$  M) in acetonitrile (4.4 mL) was added in 1.86 mL portions. After the addition of one portion, water (0.1 mL) was added. An additional portion of the  $\text{PhI}(\text{OAc})_2 / \text{CF}_3\text{SOOH}$  solution led to the formation of the dication species. A further 0.68 mL (20% excess) of the oxidant solution was added to ensure the formation of the dication species. The mixture was stirred overnight and water (15 mL) added and the organic layers extracted using  $\text{CH}_2\text{Cl}_2$  (3 x 20 mL). The combined organic layers were washed with water (30 mL) and dried over  $\text{MgSO}_4$ . The solvent was removed under reduced pressure and purified on silica gel eluting with hexane:  $\text{CH}_2\text{Cl}_2$  9:1 (v/v) increasing to 8:2. The product was additionally reprecipitated from methanol affording a yellow amorphous solid (6.8 mg, 17 %).  $^1\text{H}$  NMR ( $\text{CDCl}_3$ ): 7.90-7.47 (m, 16H, Ar-H), 7.38-7.30 (m, 3H, Ar-H), 2.10-1.80 (m, 12H,  $\text{CH}_2$ ), 1.12-1.09 (m, 36H,  $\text{CH}_2$ ), 0.89-0.61 (m, 32H,  $\text{CH}_3$ ). (MALDI/TOF,  $m/z$ ): 4322.39 ( $\text{M}^+$ ).



$^1\text{H}$  spectra of  
 $\text{CDCl}_3$ .



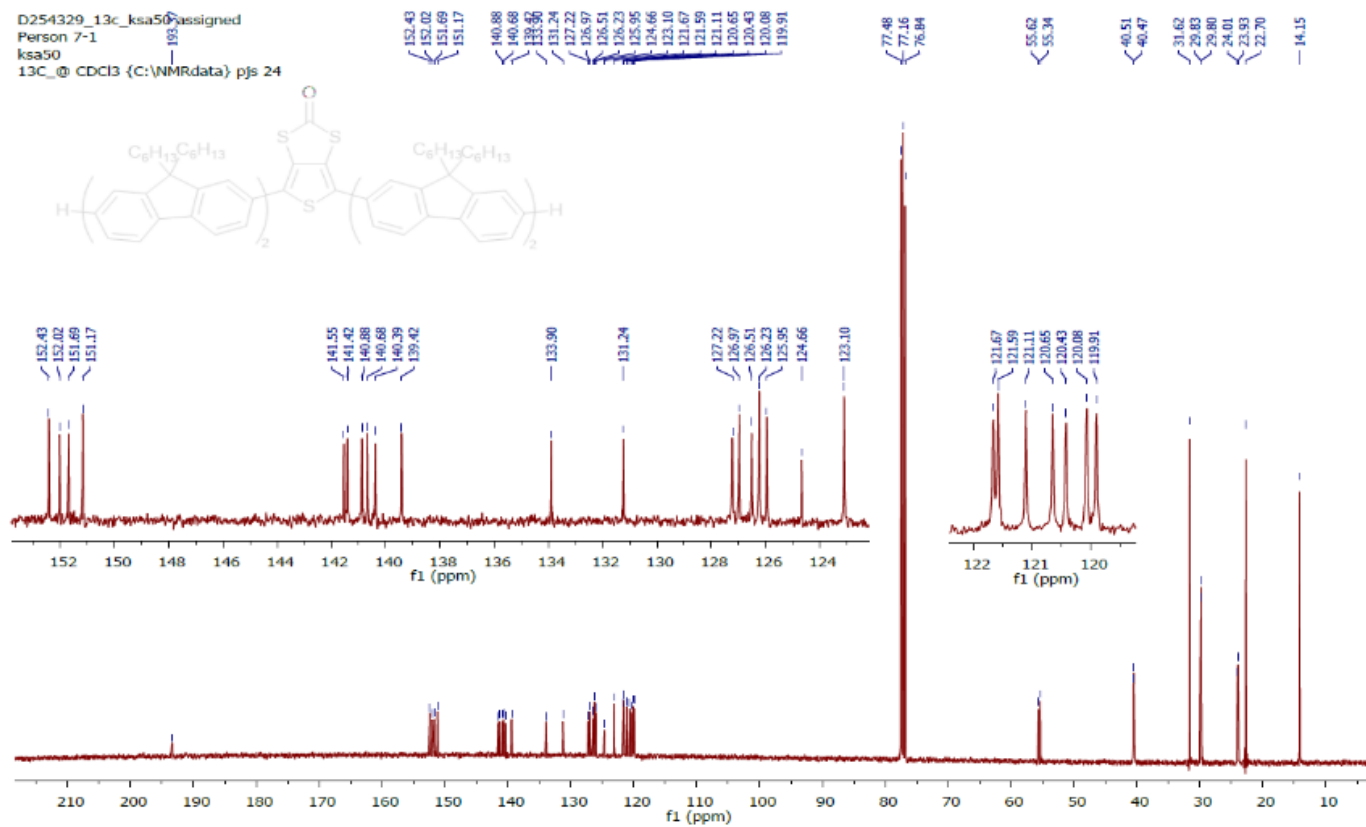
**HU-F1** in



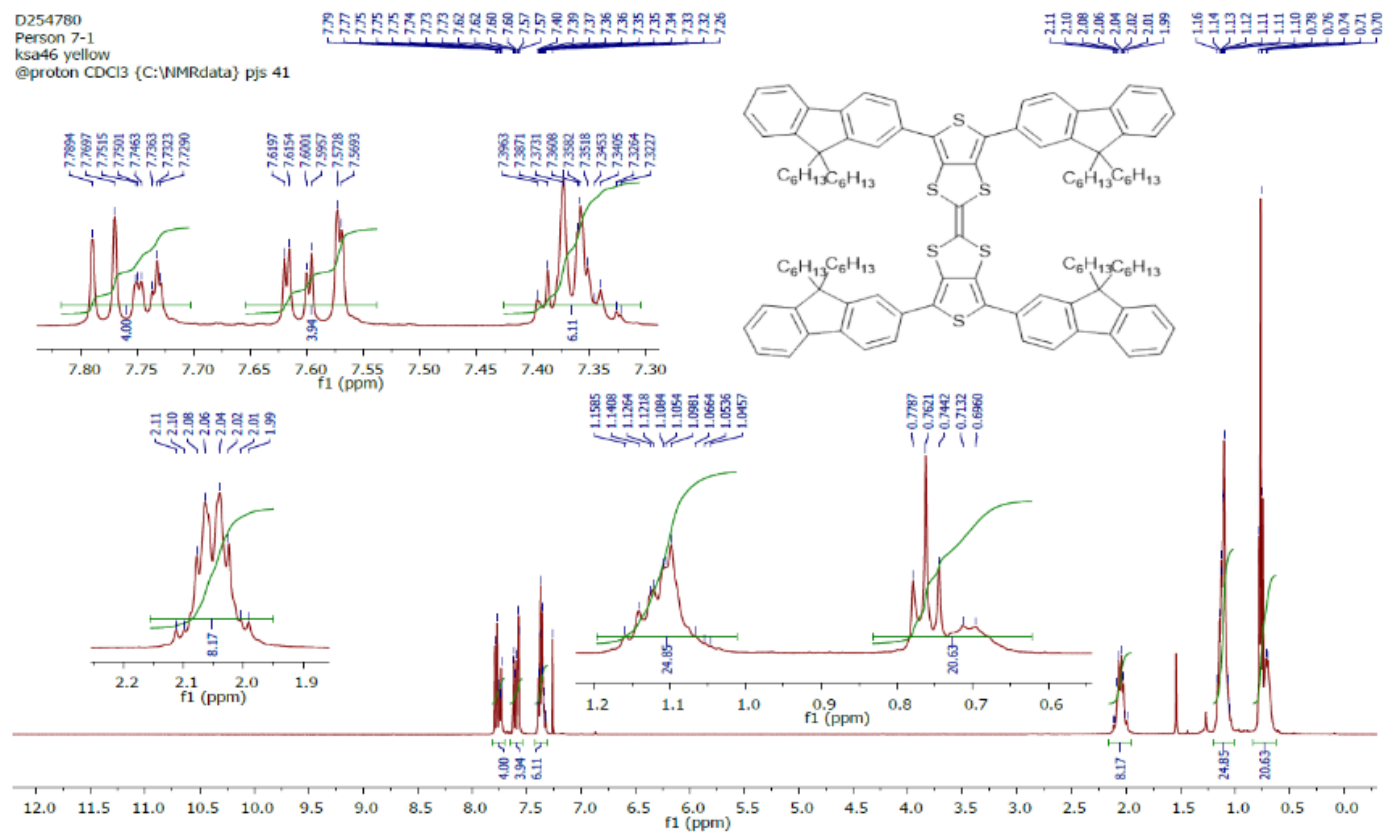
$^{13}\text{C}$  spectra of  
 $\text{CDCl}_3$ .

HU-F1 in

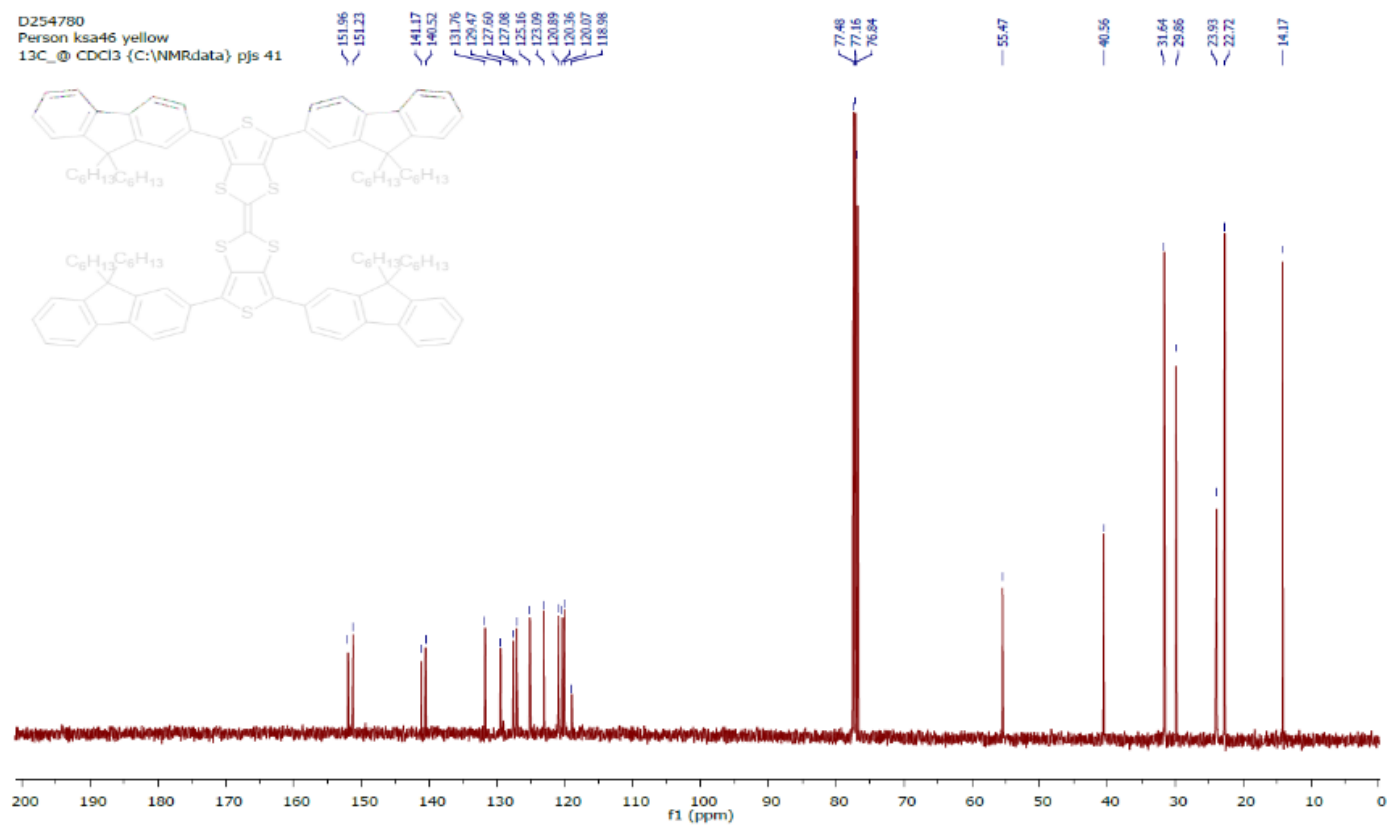
$^1\text{H}$  spectra of HU-F2 in  $\text{CDCl}_3$ .



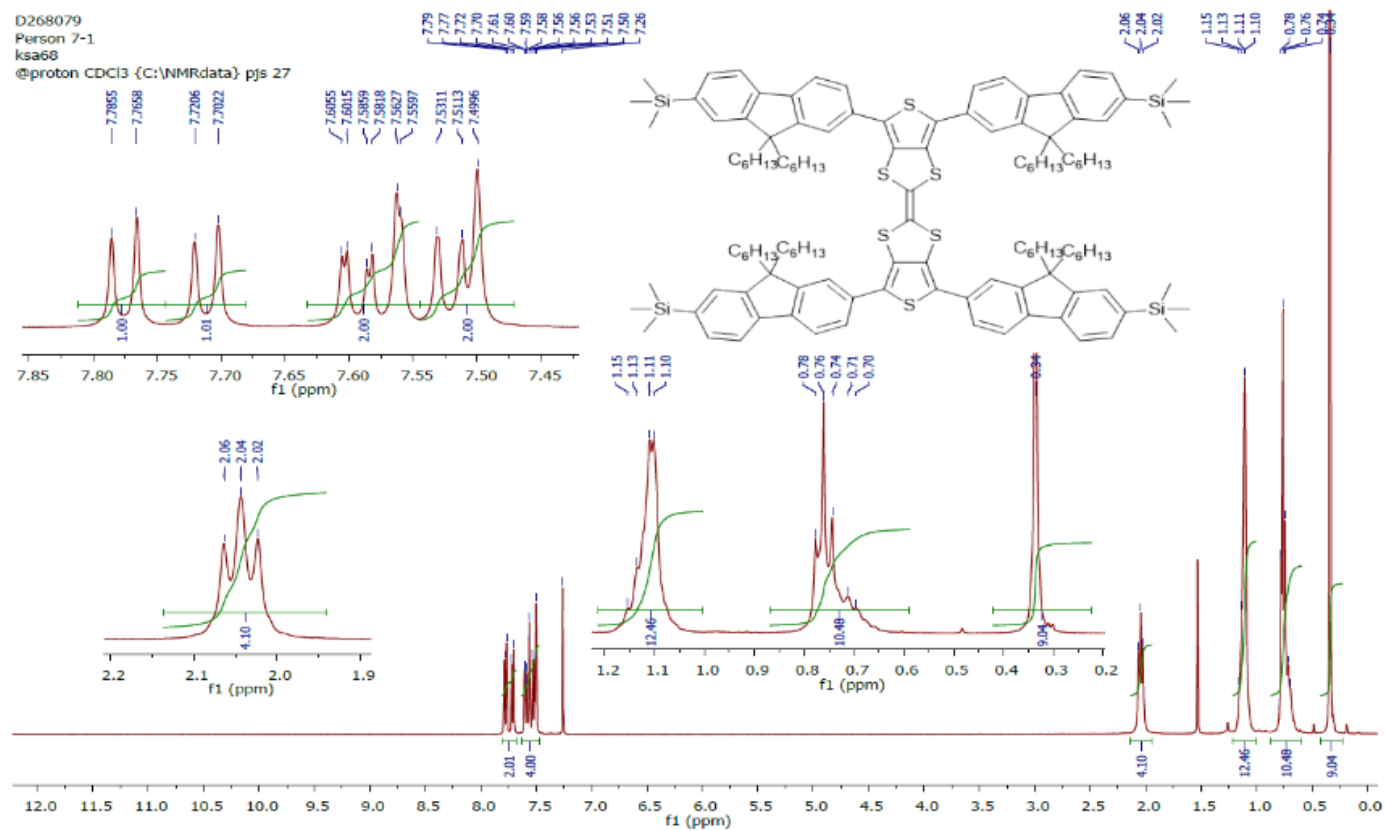
$^{13}\text{C}$  spectra of **HU-F2** in  $\text{CDCl}_3$ .



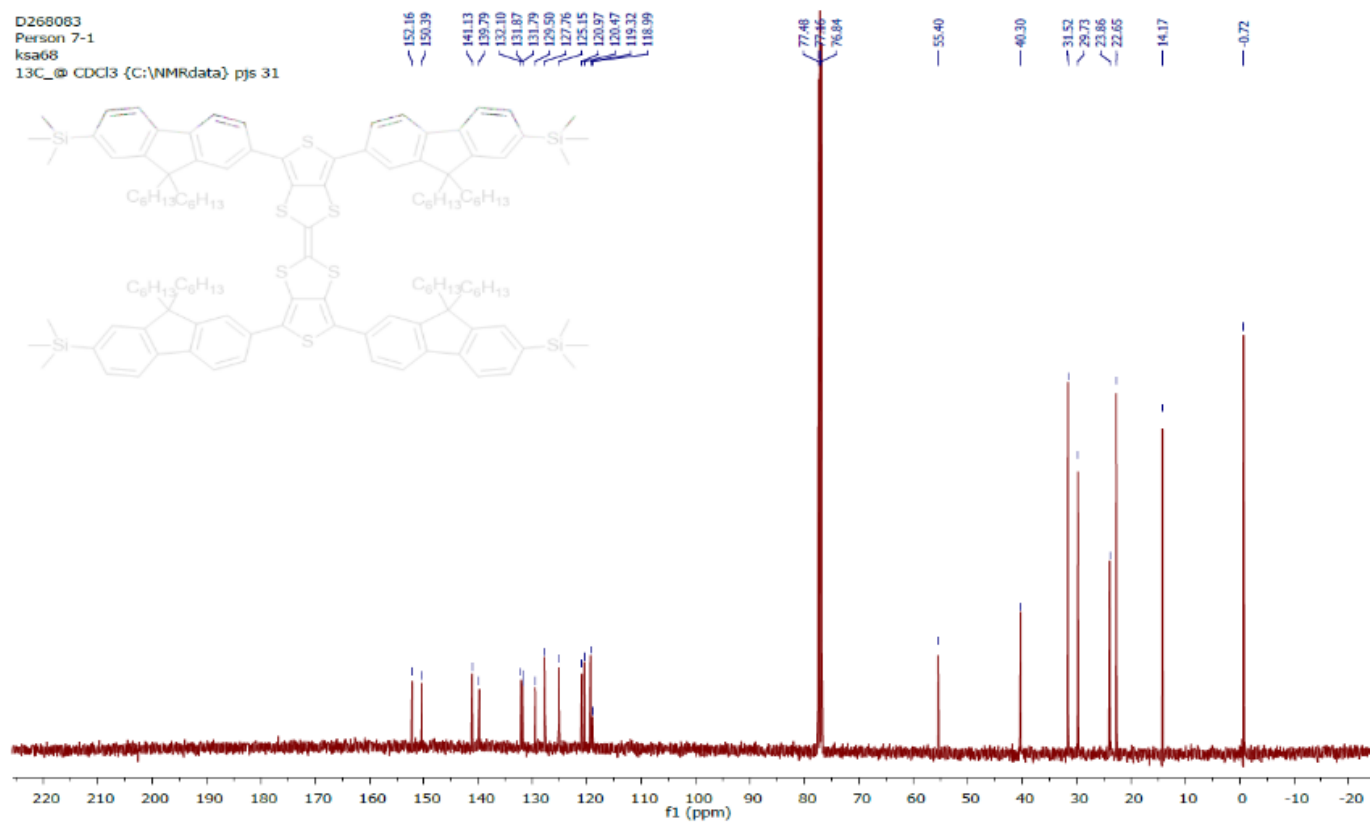
$^1H$  spectra of TTF-F1 in  $CDCl_3$ .



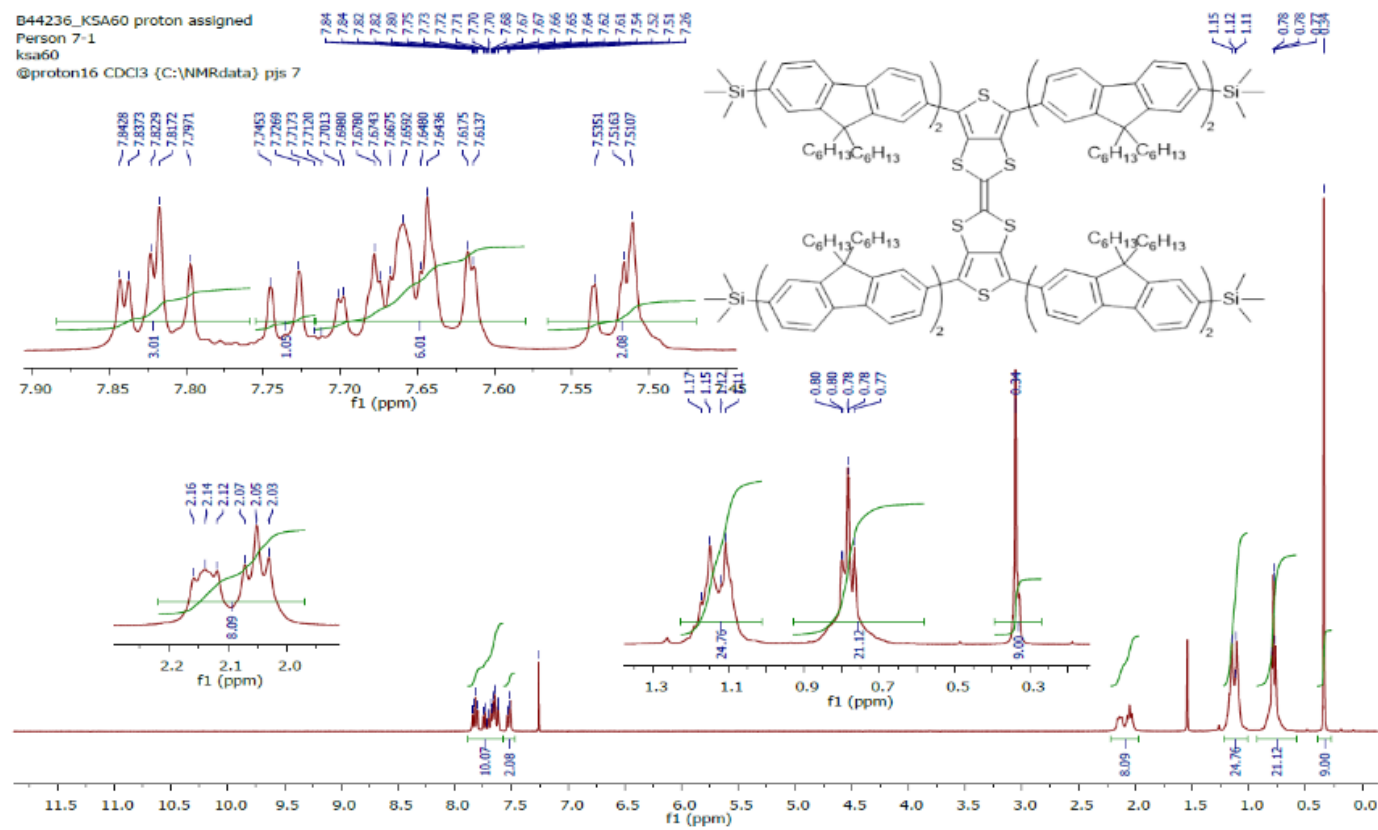
*13*C spectra of **TTF-F1** in CDCl<sub>3</sub>.



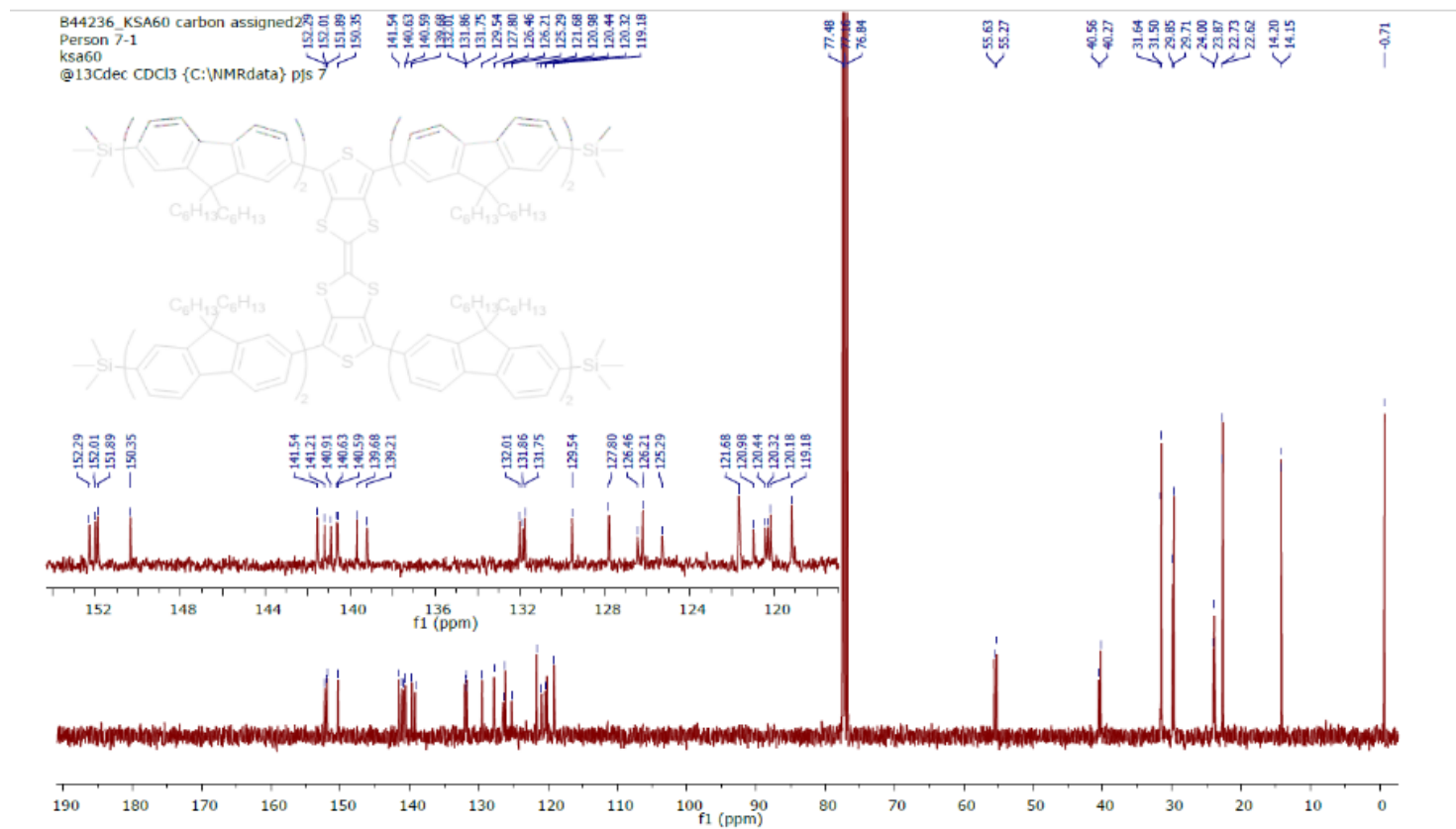
<sup>1</sup>H spectra of TTF-F1-TMS in CDCl<sub>3</sub>.



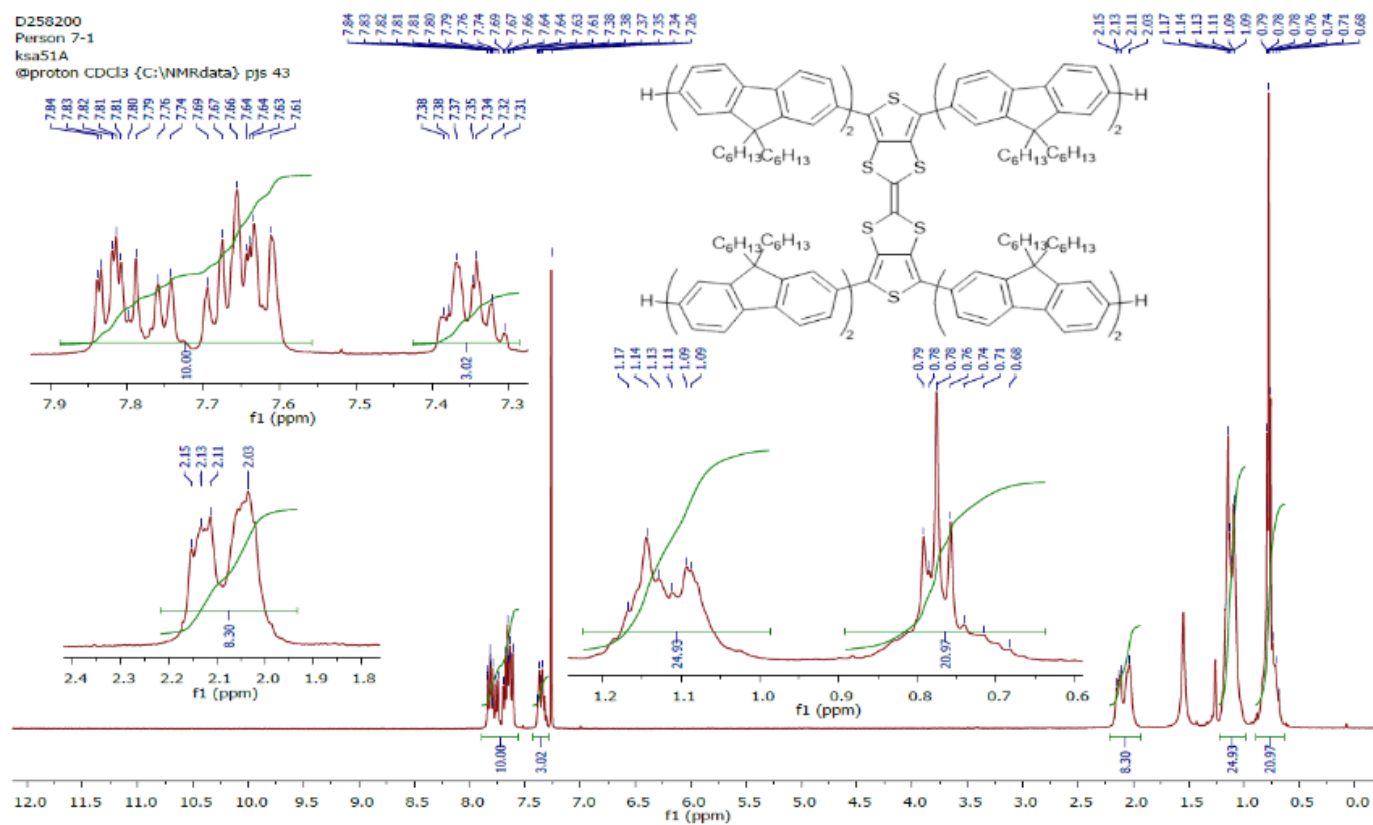
*13*C spectra of TTF-F1-TMS in CDCl<sub>3</sub>.



$^1\text{H}$  spectra of *TTF-F2-TMS* in  $\text{CDCl}_3$ .

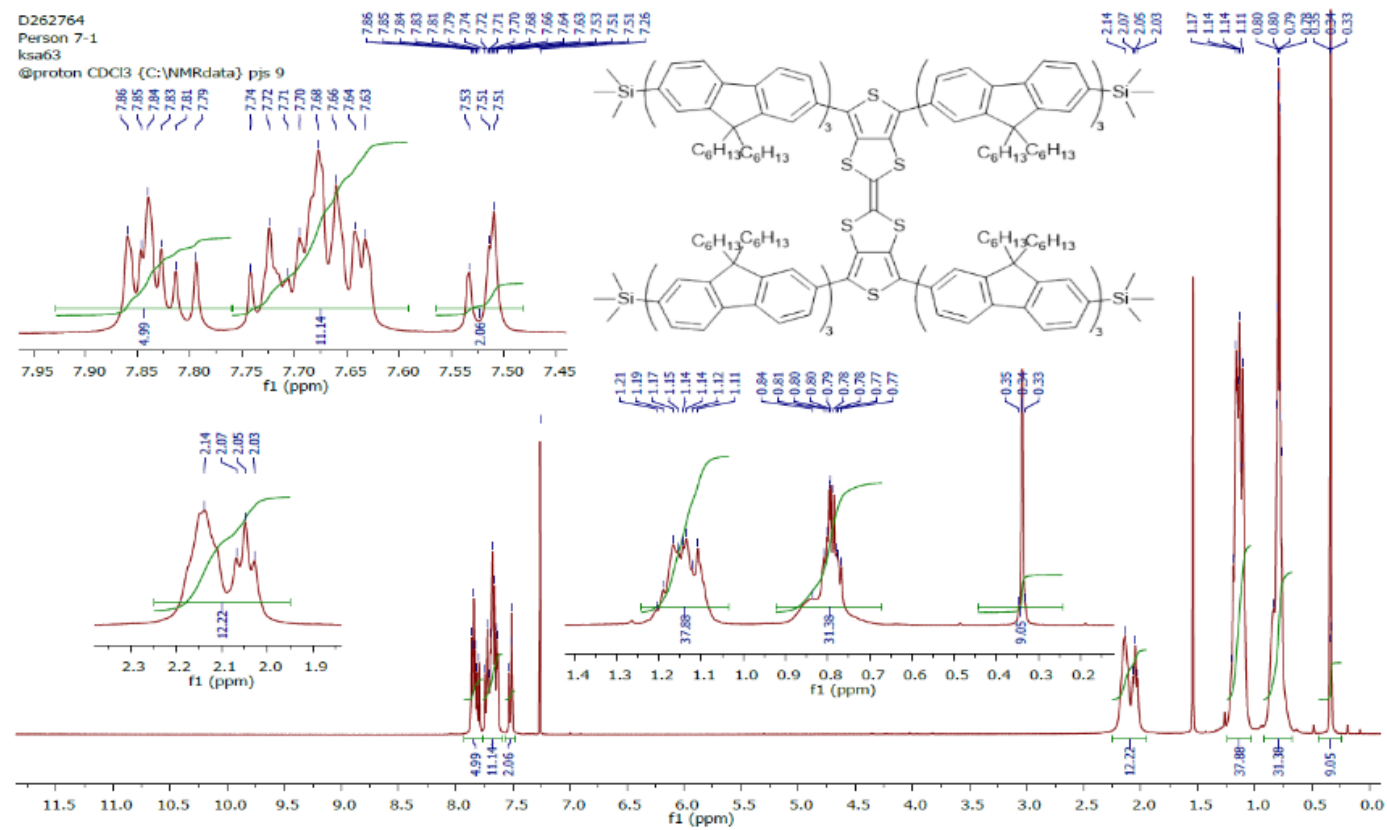


*13*C spectra of TTF-F2-TMS in CDCl<sub>3</sub>.

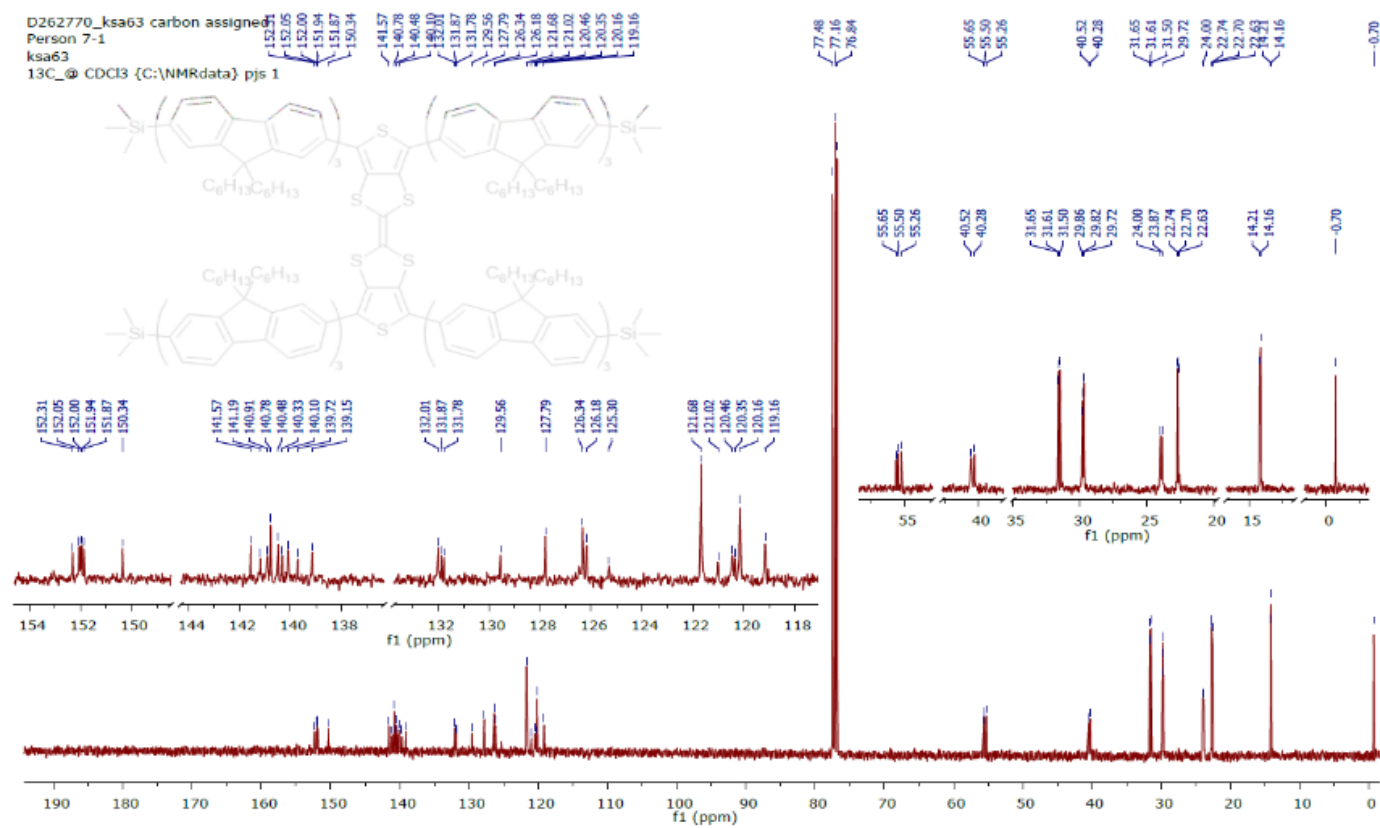


$^1\text{H}$  spectra of **TTF-F2** in  $\text{CDCl}_3$ .

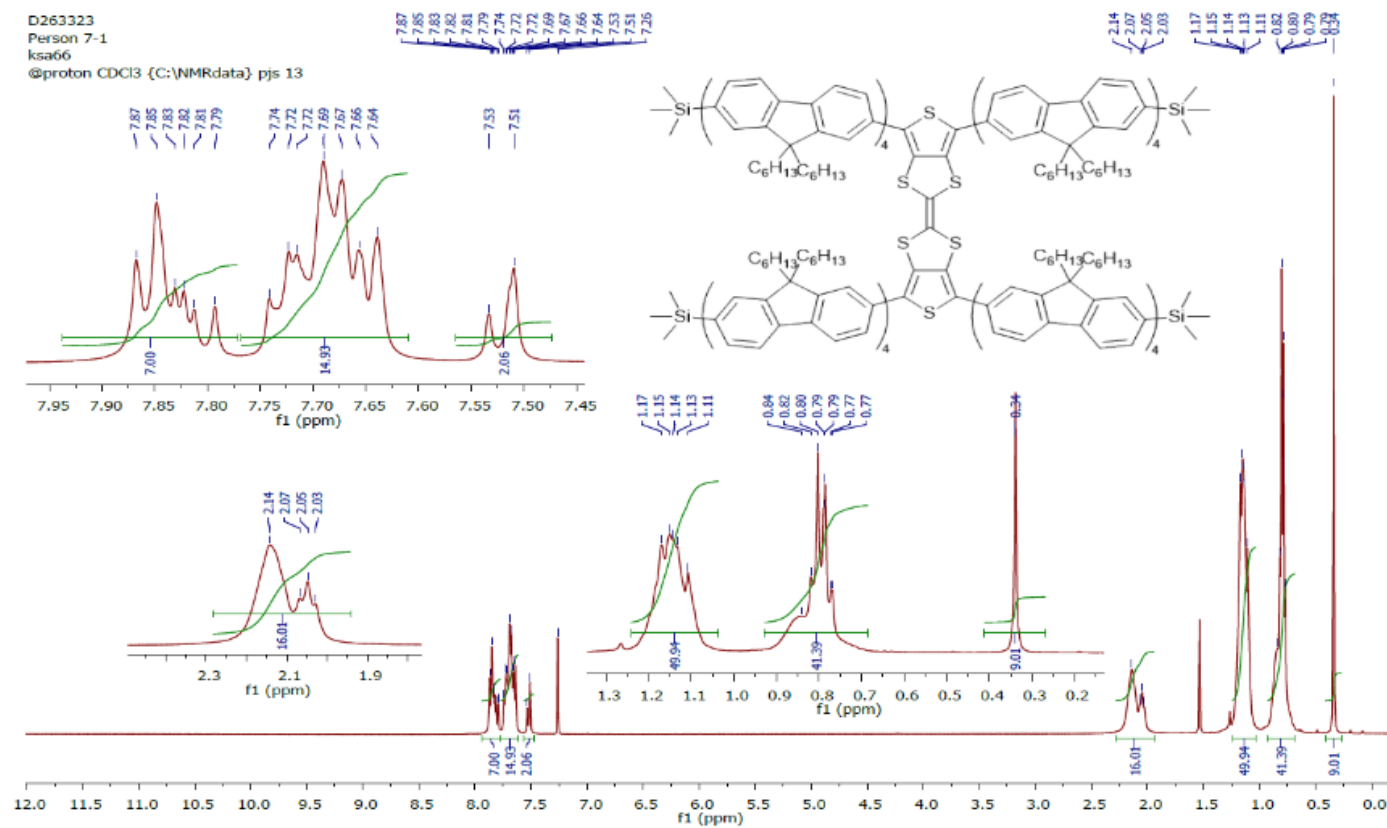




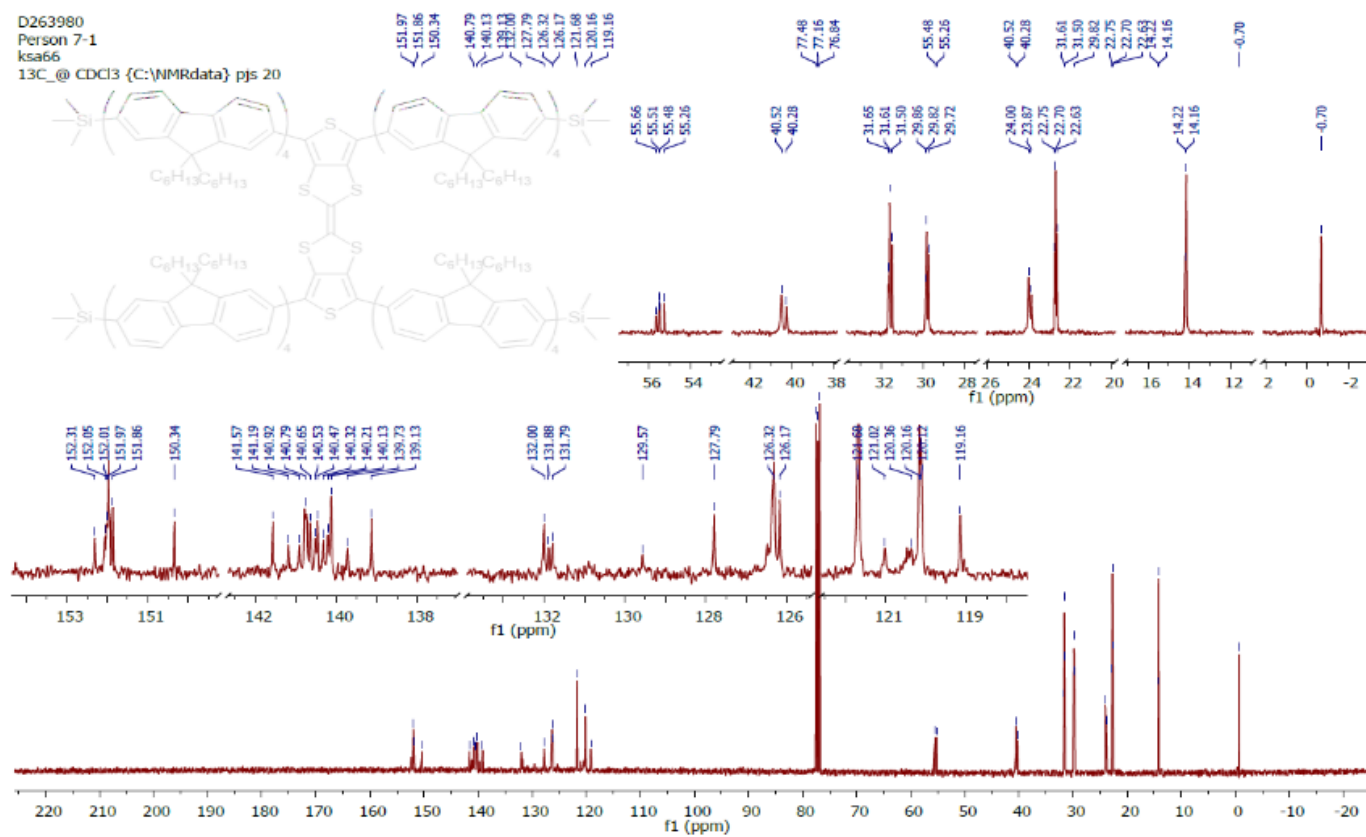
$^1\text{H}$  spectra of *TTF-F3-TMS* in  $\text{CDCl}_3$ .



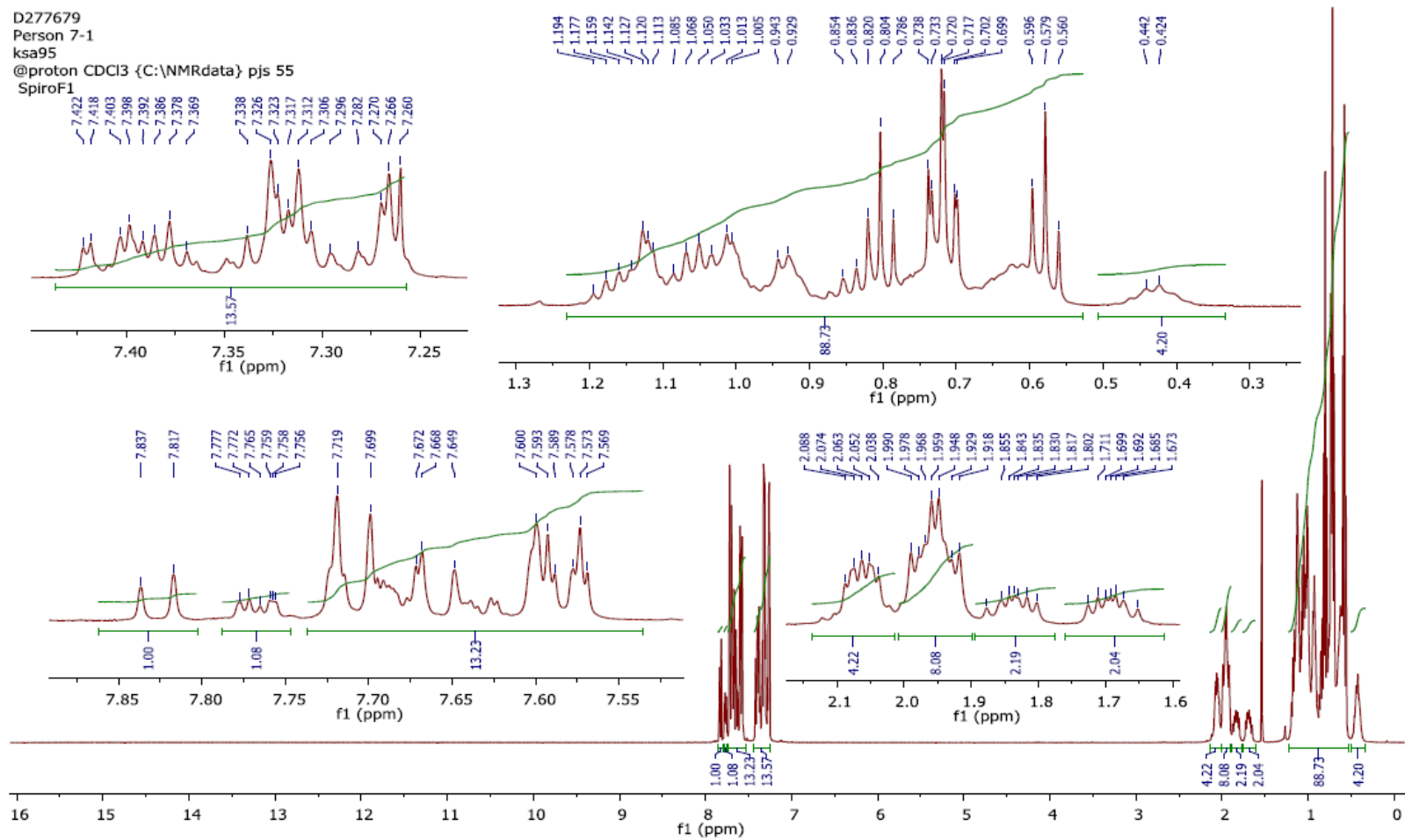
$^{13}\text{C}$  spectra of TTF-F3-TMS in  $\text{CDCl}_3$ .

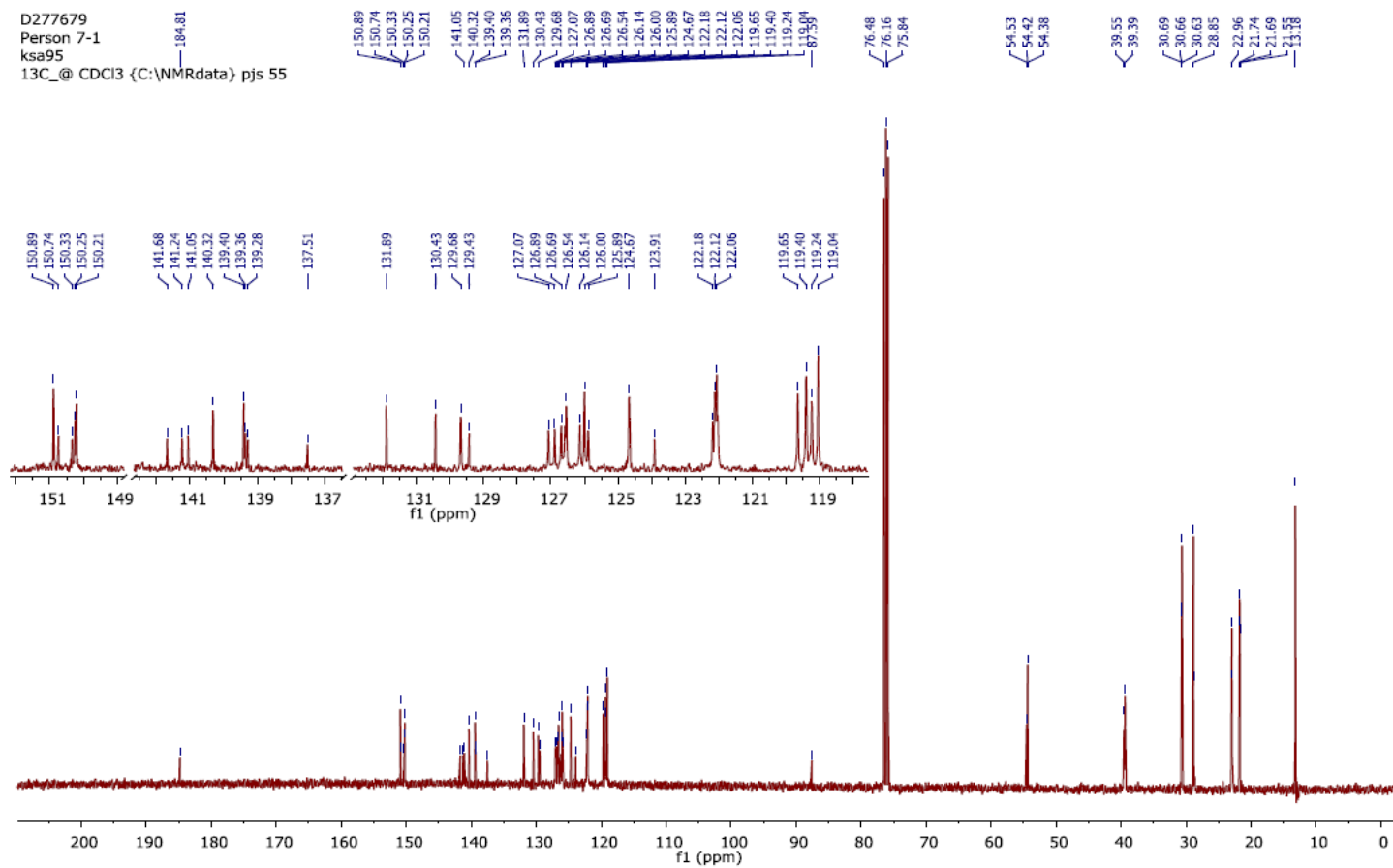


$^1\text{H}$  spectra of TTF-F4-TMS in  $\text{CDCl}_3$ .

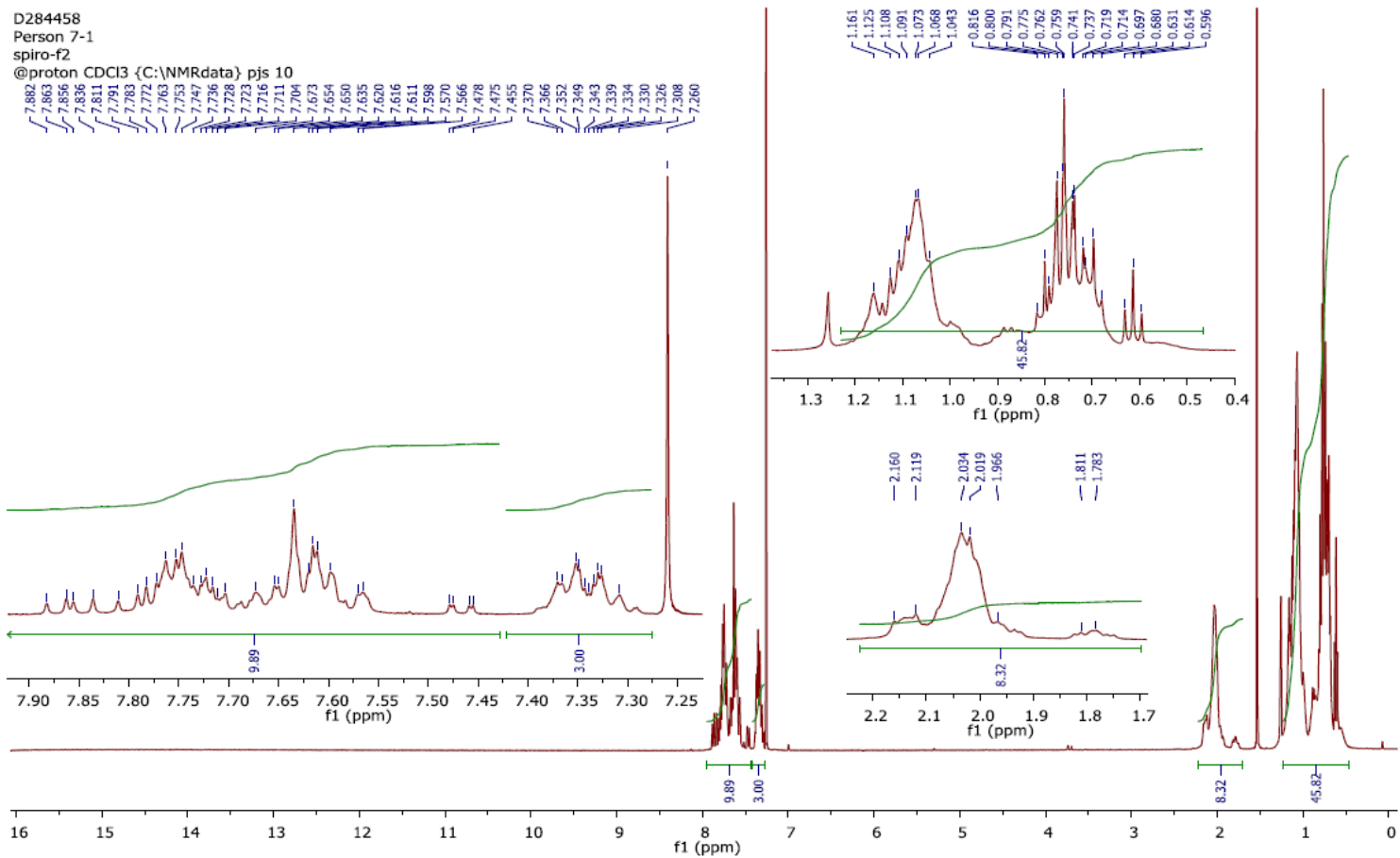


*13C* spectra of TTF-F4-TMS in CDCl<sub>3</sub>.

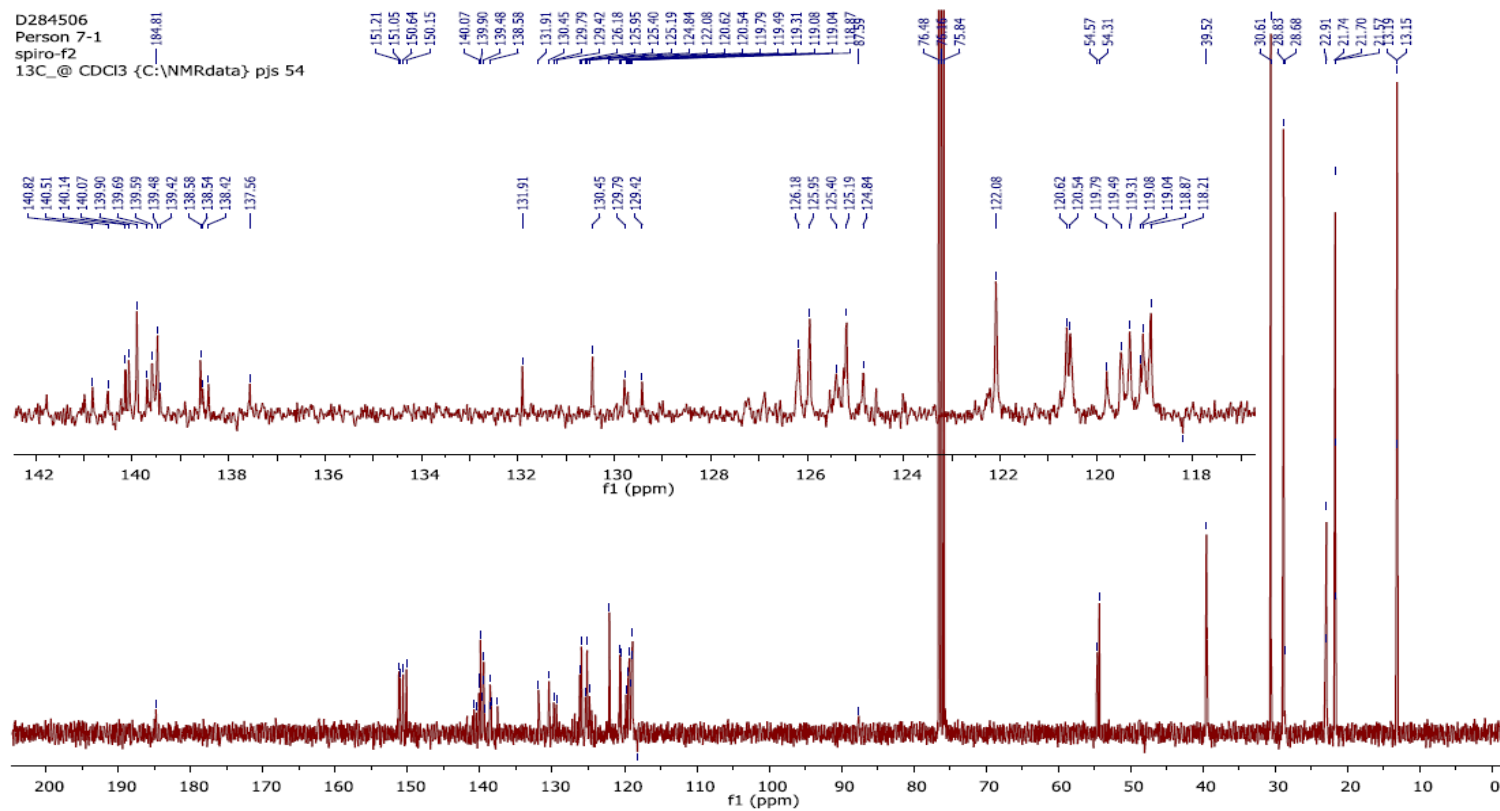
 $^1\text{H}$  spectrum of spiro-F1



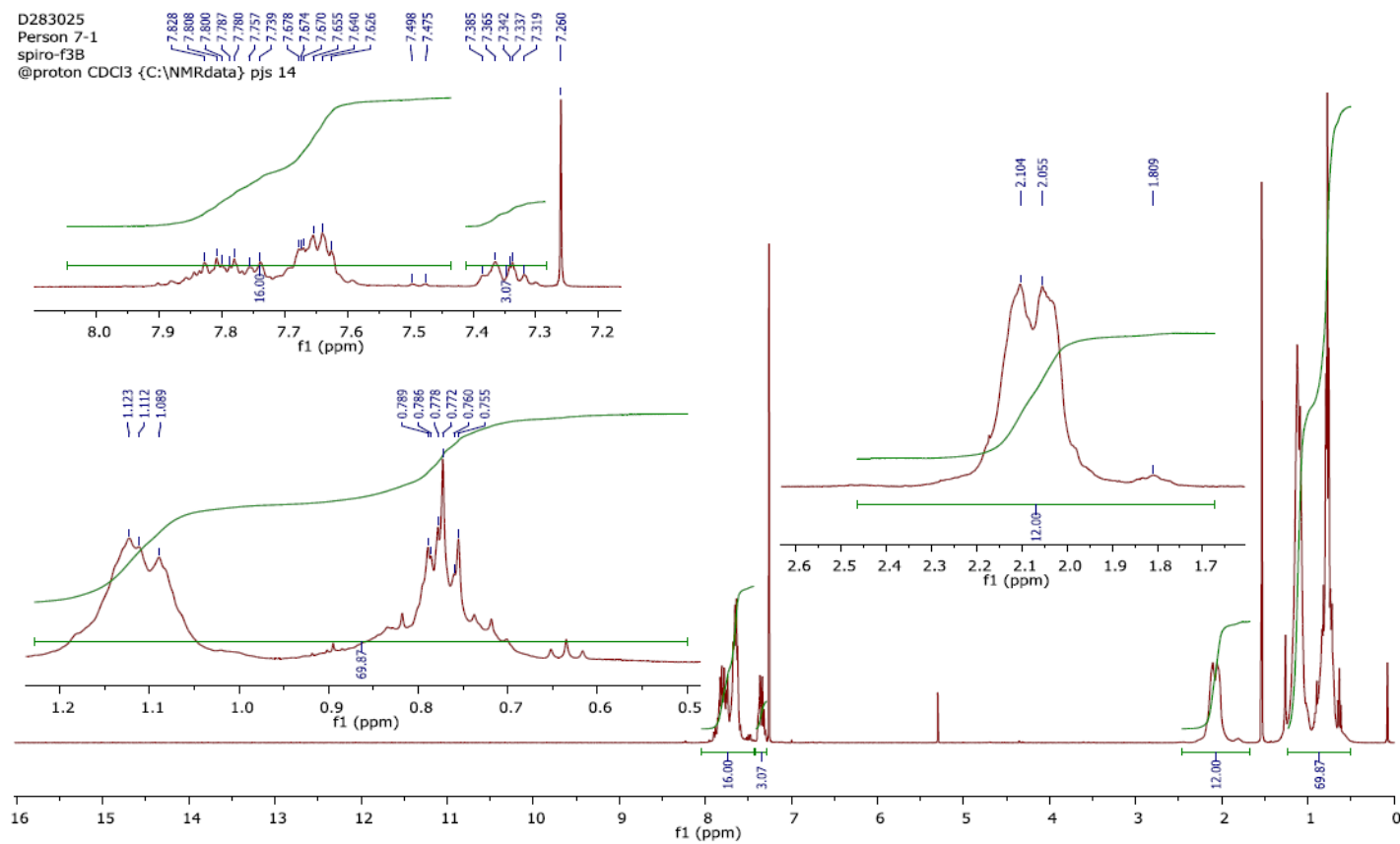
$^{13}\text{C}$  spectrum of spiro-F1



$^1\text{H}$  spectra of spiro-F2



$^{13}\text{C}$  spectrum of spiro-F2



$^1\text{H}$  spectra of spiro-F3

## 5 References

1. H. Shirakawa, *Curr. Appl. Phys.*, 2001, **1**, 281-286.
2. H. Shirakawa, *Rev. Mod. Phys.*, 2001, **73**, 713-718.
3. Y.-J. Cheng, S.-H. Yang and C.-S. Hsu, *Chem. Rev.*, 2009, **109**, 5868-5923.
4. H.-L. Yip and A. K. Y. Jen, *Energy Environ. Sci.*, 2012, **5**, 5994-6011.
5. *US Pat.*, USD682799, 2012.
6. V. Coropceanu, J. Cornil, D. A. da Silva Filho, Y. Olivier, R. Silbey and J.-L. Brédas, *Chem. Rev.*, 2007, **107**, 926-952.
7. M. Hirata and L. Sun, *Sens. Actuators A Phys.*, 1994, **40**, 159-163.
8. J. Reeder, M. Kaltenbrunner, T. Ware, D. Arreaga-Salas, A. Avendano-Bolivar, T. Yokota, Y. Inoue, M. Sekino, W. Voit, T. Sekitani and T. Someya, *Adv. Mater.*, 2014, **26**, 4967-4973.
9. J. Mei, Y. Diao, A. L. Appleton, L. Fang and Z. Bao, *J. Am. Chem. Soc.*, 2013, **135**, 6724-6746.
10. P. Atkins, J. de Paula and J. Keeler, *Physical Chemistry*, University of Oxford, Oxford, 11th edn., 2018.
11. J. Clayden and N. Greeves, *Organic Chemistry*, Oxford University Press, Oxford, 2nd edn., 2012.
12. P. Atkins and J. de Paula, in *Atkins' Physical Chemistry*, Oxford University Press, Oxford, 10 edn., 2014, vol 1, ch. 18, pp. 764-767.
13. J. Singleton, *Band theory and electronic properties of solids*, Oxford, New York, 7th edn., 2001.
14. C. Tong, *Introduction to Materials for Advanced Energy Systems*, Springer International Publishing, Cham, 1st edn., 2019.
15. A. J. Heeger, S. Kivelson, J. R. Schrieffer and W. P. Su, *Rev. Mod. Phys.*, 1988, **60**, 781-850.

16. I. Kulszewicz-Bajer, A. Proń, J. Abramowicz, C. Jeandey, J.-L. Oddou and J. W. Sobczak, *Chem. Mater.*, 1999, **11**, 552-556.
17. C. Wang, K. Sun, J. Fu, R. Chen, M. Li, Z. Zang, X. Liu, B. Li, H. Gong and J. Ouyang, *Adv. Sustain. Syst.*, 2018, **2**, 1800085.
18. I. E. Jacobs and A. J. Moulé, *Adv. Mater.*, 2017, **29**, 1703063.
19. J.-L. Bredas, *Mater. Hor.*, 2014, **1**, 17-19.
20. A. R. West, *Solid State Chemistry and its Applications*, John Wiley & Sons, Sheffield, 2nd edn., 2014.
21. T. Okuyama and H. Maskill, *Organic Chemistry: A Mechanistic Approach*, OUP Oxford, Oxford, 1st edn., 2013.
22. J. Clayden, N. Greeves and S. Warren, *Organic Chemistry*, Oxford University Press, New York, 2nd edn., 2001.
23. R. L. Madan, *Organic Chemistry*, McGraw Hill, New York, 1st edn., 2013.
24. C. M. Hussain, *Handbook of Nanomaterials for Industrial Applications*, Elsevier, New Jersey, 1st edn., 2018.
25. S. A. Duraj, *J. Am. Chem. Soc.*, 1999, **121**, 12216-12216.
26. P. Bäuerle, *Adv. Mater.*, 1992, **4**, 102-107.
27. M. Mas-Torrent and C. Rovira, *Chem. Rev.*, 2011, **111**, 4833-4856.
28. H. Dong, C. Wang and W. Hu, *Chem. Commun.*, 2010, **46**, 5211-5222.
29. B. Lüssem, M. Riede and K. Leo, *Phys. status solidi A*, 2013, **210**, 9-43.
30. K. Amundson, J. Ewing, P. Kazlas, R. McCarthy, J. D. Albert, R. Zehner, P. Drzaic, J. Rogers, Z. Bao and K. Baldwin, *Dig. Tech. Pap.*, 2001, **32**, 160-163.
31. S. H. Lee, H. Park, S. Kim, W. Son, I. W. Cheong and J. H. Kim, *J. Mater. Chem. A*, 2014, **2**, 7288-7294.

32. K. Fukuda, Y. Takeda, M. Mizukami, D. Kumaki and S. Tokito, *Sci. Rep.*, 2014, **4**, 3947.
33. I. Salzmann, G. Heibel, M. Oehzelt, S. Winkler and N. Koch, *Acc. Chem. Res.*, 2016, **49**, 370-378.
34. S. T. Bromley, M. Mas-Torrent, P. Hadley and C. Rovira, *J. Am. Chem. Soc.*, 2004, **126**, 6544-6545.
35. P. Friederich, A. Fediai, S. Kaiser, M. Konrad, N. Jung and W. Wenzel, *Adv. Mater.*, 2019, **31**, 1808256.
36. F. Garnier, A. Yassar, R. Hajlaoui, G. Horowitz, F. Deloffre, B. Servet, S. Ries and P. Alnot, *J. Am. Chem. Soc.*, 1993, **115**, 8716-8721.
37. C. J. Brabec, M. Heeney, I. McCulloch and J. Nelson, *Chem. Soc. Rev.*, 2011, **40**, 1185-1199.
38. C. D. Dimitrakopoulos and P. R. L. Malenfant, *Adv. Mater.*, 2002, **14**, 99-117.
39. F. Garnier, *Acc. Chem. Res.*, 1999, **32**, 209-215.
40. H. Bronstein, C. B. Nielsen, B. C. Schroeder and I. McCulloch, *Nat. Rev. Chem.*, 2020, **4**, 66-77.
41. J. Roncali, *Chem. Rev.*, 1997, **97**, 173-206.
42. M. Kertesz and Y. S. Lee, *J. Phys. Chem.*, 1987, **91**, 2690-2692.
43. J. R. Reynolds, B. C. Thompson and T. A. Skotheim, *Handbook of Conducting Polymers*, CRC Press, London, 4th edn., 2019.
44. J. Roncali, *Macromol. Rapid Commun.*, 2007, **28**, 1761-1775.
45. H. Peng, X. Sun, W. Weng and X. Fang, *Polymer Materials for Energy and Electronic Applications*, Academic Press, Amsterdam, 1st edn., 2016.
46. F. Wudl, M. Kobayashi and A. J. Heeger, *J. Org. Chem.*, 1984, **49**, 3382-3384.

47. N. E. Carpenter, *Chemistry of Sustainable Energy*, CRC Press, New York, 1st edn., 2014.
48. N. Koch, *Supramolecular Materials for Opto-Electronics*, Royal Society of Chemistry, Cambridge, 1st edn., 2014.
49. B. Rybakov, *Scintillation Method in Radiometry*, U.S. Atomic Energy Commission, Division of Technical Information, New York, 1st edn., 1962.
50. F. Grein, *J. Mol. Struct.:Theochem*, 2003, **624**, 23-28.
51. A. Pross, L. Radom and R. W. Taft, *J. Org. Chem.*, 1980, **45**, 818-826.
52. P. Sakellariou, M. H. Abraham and G. S. Whiting, *Colloid Polym. Sci.*, 1994, **272**, 872-875.
53. H.-J. Jhuo, P.-N. Yeh, S.-H. Liao, Y.-L. Li, Y.-S. Cheng and S.-A. Chen, *J. Chin. Chem. Soc.*, 2014, **61**, 115-126.
54. T. Xu and L. Yu, *Mater. Today*, 2014, **17**, 11-15.
55. P. Cheng and Y. Yang, *Acc. Chem. Res.*, 2020, **53**, 1218-1228.
56. Y. Don Park, J. A. Lim, H. S. Lee and K. Cho, *Mater. Today*, 2007, **10**, 46-54.
57. D. D. Medina, M. L. Petrus, A. N. Jumabekov, J. T. Margraf, S. Weinberger, J. M. Rotter, T. Clark and T. Bein, *ACS Nano*, 2017, **11**, 2706-2713.
58. R. Noriega, J. Rivnay, K. Vandewal, F. P. V. Koch, N. Stingelin, P. Smith, M. F. Toney and A. Salleo, *Nat. Mater.*, 2013, **12**, 1038-1044.
59. A. Salleo, *Mater. Today*, 2007, **10**, 38-45.
60. E. Verploegen, R. Mondal, C. J. Bettinger, S. Sok, M. F. Toney and Z. Bao, *Adv. Funct. Mater.*, 2010, **20**, 3519-3529.
61. B. S. Ong, Y. Wu, P. Liu and S. Gardner, *J. Am. Chem. Soc.*, 2004, **126**, 3378-3379.
62. G. Zhao, Y. He and Y. Li, *Adv. Mater.*, 2010, **22**, 4355-4358.

63. S. Yu-Wei, L. Yu-Che and W. Kung-Hwa, *J. Mater. Chem. A.*, 2017, **5**, 8684-8692.
64. B. C. Thompson and J. M. J. Fréchet, *Angew. Chem. Int. Ed.*, 2008, **47**, 58-77.
65. O. D. Jurchescu, J. Baas and T. T. M. Palstra, *Appl. Phys. Lett.*, 2004, **84**, 3061-3063.
66. P. Leriche and A. Cravino, *Adv. Mater.*, 2007, **19**, 2045-2060.
67. A. B. Koren, M. D. Curtis, A. H. Francis and J. W. Kampf, *J. Am. Chem. Soc.*, 2003, **125**, 5040-5050.
68. I. Aujard, J.-P. Baltaze, J.-B. Baudin, E. Cogné, F. Ferrage, L. Jullien, É. Perez, V. Prévost, L. M. Qian and O. Ruel, *J. Am. Chem. Soc.*, 2001, **123**, 8177-8188.
69. A. L. Kanibolotsky, I. F. Perepichka and P. J. Skabara, *Chem. Soc. Rev.*, 2010, **39**, 2695-2728.
70. T. Spehr, R. Pudzich, T. Fuhrmann and J. Salbeck, *Org. Electr.*, 2003, **4**, 61-69.
71. D. Kolosov, D. S. English, V. Bulovic, P. F. Barbara, S. R. Forrest and M. E. Thompson, *J. Appl. Phys.*, 2001, **90**, 3242-3247.
72. L. Ke, P. Chen and S. J. Chua, *Appl. Phys. Lett.*, 2002, **80**, 697-699.
73. J. W. Lehmann, D. J. Blair and M. D. Burke, *Nat. Rev. Chem.*, 2018, **2**, 0115.
74. J. H. Gao, R. J. Li, L. Q. Li, Q. Meng, H. Jiang, H. X. Li and W. P. Hu, *Adv. Mater.*, 2007, **19**, 3008-3011.
75. S. Zhang, Y. Guo, Y. Zhang, R. Liu, Q. Li, X. Zhan, Y. Liu and W. Hu, *Chem. Comm.*, 2010, **46**, 2841-2843.
76. D. Fichou, *J. Mater. Chem.*, 2000, **10**, 571-588.
77. K. Schulze, C. Uhrich, R. Schüppel, K. Leo, M. Pfeiffer, E. Brier, E. Reinold and P. Bäuerle, *Adv. Mater.*, 2006, **18**, 2872-2875.

78. I. A. Wright, P. J. Skabara, J. C. Forgie, A. L. Kanibolotsky, B. Gonzalez, S. J. Coles, S. Gambino and I. D. W. Samuel, *J. Mater. Chem.*, 2010, **21**, 1462–1469.
79. L. Zhang, N. S. Colella, B. P. Cherniawski, S. C. B. Mannsfeld and A. L. Briseno, *ACS Appl. Mater.*, 2014, **6**, 5327-5343.
80. J. Li, X. Qiao, Y. Xiong, W. Hong, X. Gao and H. Li, *J. Mater. Chem. C*, 2013, **1**, 5128-5132.
81. T. Nishinaga, *Organic Redox Systems: Synthesis, Properties, and Applications*, John Wiley & Sons, New Jersey, 1st edn., 2015.
82. T. Baumgartner and F. Jaekle, *Main Group Strategies towards Functional Hybrid Materials*, John Wiley & Sons, New Jersey, 1st edn., 2018.
83. N. Rice, F. Magnan, O. Melville, J. Brusso and B. Lessard, *Mater.*, 2017, **11**, 8.
84. J. Zhang, J. S. Moore, Z. Xu and R. A. Aguirre, *J. Am. Chem. Soc.*, 1992, **114**, 2273-2274.
85. P. Bharathi, U. Patel, T. Kawaguchi, D. J. Pesak and J. S. Moore, *Macromolecules*, 1995, **28**, 5955-5963.
86. M. R. Bryce, *J. Mater. Chem.*, 2000, **10**, 589-598.
87. J. Ferraris, D. O. Cowan, V. Walatka and J. H. Perlstein, *J. Am. Chem. Soc.*, 1973, **95**, 948-949.
88. D. Jérôme, *Chem. Rev.*, 2004, **104**, 5565-5592.
89. A. M. Kini, U. Geiser, H. H. Wang, K. D. Carlson, J. M. Williams, W. K. Kwok, K. G. Vandervoort, J. E. Thompson and D. L. Stupka, *Inorg. Chem.*, 1990, **29**, 2555-2557.

90. Y. Morita, S. Maki, M. Ohmoto, H. Kitagawa, T. Okubo, T. Mitani and K. Nakasuji, *Org. Lett.*, 2002, **4**, 2185-2188.
91. T. Murata, Y. Morita, K. Fukui, K. Sato, D. Shiomi, T. Takui, M. Maesato, H. Yamochi, G. Saito and K. Nakasuji, *Angew. Chem. Int. Ed.*, 2004, **43**, 6343-6346.
92. O. Basu and S. K. Das, *J. Chem. Sci.*, 2020, **132**, 46.
93. F. Wudl, G. M. Smith and E. J. Hufnagel, *J. Chem. Soc. Chem. Commun.*, 1970, **21**, 1453-1454.
94. C. Katan, *J. Phys. Chem. A*, 1999, **103**, 1407-1413.
95. M. Bendikov, F. Wudl and D. F. Perepichka, *Chem. Rev.*, 2004, **104**, 4891-4946.
96. E. Demiralp and W. A. Goddard, *J. Phys. Chem. A*, 1997, **101**, 8128-8131.
97. X. Zhou, X. Guo, F. Jian and G. Wei, *ACS Omega*, 2018, **3**, 4418-4422.
98. A. Suzuki, *Angew. Chem. Int. Ed.*, 2011, **50**, 6722-6737.
99. E.-i. Negishi, *Angew. Chem. Int. Ed.*, 2011, **50**, 6738-6764.
100. C. C. C. Johansson Seechurn, M. O. Kitching, T. J. Colacot and V. Snieckus, *Angew. Chem. Int. Ed.*, 2012, **51**, 5062-5085.
101. Z. Wang, in *Comprehensive Organic Name Reactions and Reagents*, John Wiley & Sons, New Jersey, 1st edn., 2010, vol. 72, ch. 6, pp. 2733-2743.
102. A. Iraqi and G. W. Barker, *J. Mater. Chem.*, 1998, **8**, 25-29.
103. G. C. Fu, *Acc. Chem. Res.*, 2008, **41**, 1555-1564.
104. J. A. Joule and K. Mills, *Heterocyclic Chemistry*, John Wiley & Sons, New Jersey, 5th edn., 2013.
105. N. Miyaura, T. Yanagi and A. Suzuki, *Synth. Comm.*, 1981, **11**, 513-519.
106. A. Suzuki, *J. Organomet. Chem.*, 1999, **576**, 147-168.

107. S. Akira, *Pure Appl. Chem.*, 1991, **63**, 419-422.
108. B. H. Ridgway and K. A. Woerpel, *J. Org. Chem.*, 1998, **63**, 458-460.
109. M. B. Thathagar, J. Beckers and G. Rothenberg, *J. Am. Chem. Soc.*, 2002, **124**, 11858-11859.
110. A. J. J. Lennox and G. C. Lloyd-Jones, *Chem. Soc. Rev.*, 2014, **43**, 412-443.
111. M. Bernius, M. Inbasekaran, E. Woo, W. Wu and L. Wujkowski, *J. Mater. Sci.: Mater. Electr.*, 2000, **11**, 111-116.
112. A. C. Grimsdale and K. Müllen, in *Polyfluorenes*, eds. U. Scherf and D. Neher, Springer Berlin Heidelberg, Berlin, 1st edn., 2008, vol. 212, ch. 1, pp. 1-48.
113. D. Morales-Morales, *J. Org. Chem.* 2005, **70**, 9215–9221.
114. P. Espinet and A. M. Echavarren, *Angew. Chem. Int. Ed.*, 2004, **43**, 4704-4734.
115. J. J. Li, in *Progress in Heterocyclic Chemistry*, ed. G. W. Gribble and T. L. Gilchrist, Elsevier, 2000, vol. 12, ch. 1, pp. 37-56.
116. L. Rejc, V. Gómez-Vallejo, J. Alcázar, N. Alonso, J. I. Andrés, A. Arrieta, F. P. Cossío and J. Llop, *Chem. Comm.*, 2018, **54**, 4398-4401.
117. P. Atkins, J. de Paula and J. Keeler, *Physical Chemistry*, Oxford, New York, 11th edn., 2018.
118. C. Karunakaran and M. Balamurugan, in *Spin Resonance Spectroscopy*, ed. C. Karunakaran, Elsevier, Amsterdam, 1st edn., 2018, vol. 4, ch. 3, pp. 169-228.
119. J. R. Lakowicz, *Principles of Fluorescence Spectroscopy*, MA: Springer US, Boston, 1st edn., 2006.
120. G. A. Jones and D. S. Bradshaw, *Front. Phys.*, 2019, **7**.
121. N. J. Turro, *Modern Molecular Photochemistry*, Calif. : University Science Books, Mill Valley, 1st edn., 1991.

122. M. Fakis, D. Anastopoulos, V. Giannetas and P. Persephonis, *J. Phys. Chem. B*, 2006, **110**, 24897-24902.
123. A. Y. Sosorev, O. D. Parashchuk, S. A. Zapunidi, G. S. Kashtanov, I. V. Golovnin, S. Kommanaboyina, I. F. Perepichka and D. Y. Paraschuk, *Phys. Chem.*, 2016, **18**, 4684-4696.
124. A. Mishra and P. Bäuerle, *Angew. Chem. Int. Ed.*, 2012, **51**, 2020-2067.
125. C. Wang and Z. Li, *Mater. Chem. Front.*, 2017, **1**, 2174-2194.
126. A. U. Alam, Y. Qin, S. Nambiar, J. T. W. Yeow, M. M. R. Howlader, N.-X. Hu and M. J. Deen, *Prog. Mater. Sci.*, 2018, **96**, 174-216.
127. H. Yousefi, H.-M. Su, S. M. Imani, K. Alkhaldi, C. D. M. Filipe and T. F. Didar, *ACS Sensors*, 2019, **4**, 808-821.
128. J. Dai, O. Ogbeide, N. Macadam, Q. Sun, W. Yu, Y. Li, B.-L. Su, T. Hasan, X. Huang and W. Huang, *Chem. Soc. Rev.*, 2020, **49**, 1756-1789.
129. M. Wei, Y. Gao, X. Li and M. J. Serpe, *Polym. Chem.*, 2017, **8**, 127-143.
130. A. Hulanicki, S. Glab and F. Ingman, *Pure Appl. Chem.*, 1991, **63**, 1247-1250.
131. S. Navale, A. Mane, M. Chougule, R. D. Sakhare, S. R. Nalage and D. V. Patil, *Synth. Met.*, 2014, **189**, 94-99.
132. P. P. Sengupta, S. Barik and B. Adhikari, *Mater. Manuf. Process*, 2006, **21**, 263-270.
133. R. M. White, *IEEE t. ultrason. ferr.*, 1987, **34**, 124-126.
134. R.-C. Qian and Y.-T. Long, *ChemistryOpen*, 2018, **7**, 118-130.
135. V. C. Gonçalves and D. T. Balogh, *Sens. Actuators B Chem.*, 2012, **162**, 307-312.
136. H. Sahoo, *RSC Adv.*, 2012, **2**, 7017-7029.
137. T. Kálai and K. Hideg, *Tetrahedron*, 2006, **62**, 10352-10360.

138. G. Saroja, B. Ramachandram, S. Saha and A. Samanta, *J. Phys. Chem. B*, 1999, **103**, 2906-2911.
139. H. Szmecinski, in *Principles of Fluorescence Spectroscopy*, ed. J. R. Lakowicz, Springer US, Boston, 1st edn., 2006, vol. 65, ch. 13, pp. 623-673.
140. I. Krzysztof, *Smart Sensors for Industrial Applications*, CRC Press, New-York, 1st edn., 2017.
141. H. H. Qazi, A. B. bin Mohammad and M. Akram, *Sensors (Basel, Switzerland)*, 2012, **12**, 16522-16556.
142. M. J. Almendral Parra and S. S. Paradinas, in *Comprehensive Analytical Chemistry*, eds. M. Valcárcel and Á. I. López-Lorente, Elsevier, Amsterdam, 2014, vol. 66, ch. 2, pp. 477-527.
143. C. Beck and Y. Gong, *Sci. Rep.*, 2019, **9**, 15878.
144. J. A. Mitchell, W. H. Zhang, M. K. Herde, C. Henneberger, H. Janovjak, M. L. O'Mara and C. J. Jackson, *Methods mol. biol.*, 2017, **1596**, 89-99.
145. J. R. Lakowicz, *Principles of Fluorescence Spectroscopy*, Springer Science & Business Media, Berlin, 3rd edn., 2007.
146. T. H. Kim, B. Y. Lee, J. Jaworski, K. Yokoyama, W.-J. Chung, E. Wang, S. Hong, A. Majumdar and S.-W. Lee, *ACS Nano*, 2011, **5**, 2824-2830.
147. Y. Li, X. Liu and D. Wen, *Acta Cryst.*, 2020, **76**, 233-240.
148. T.-F. Wu and J.-D. Hong, *RSC Adv.*, 2016, **6**, 96935-96941.
149. J.-C. Chiang and A. G. MacDiarmid, *Synth. Met.*, 1986, **13**, 193-205.
150. Y. H. Lee, M. Jang, M. Y. Lee, O. Y. Kweon and J. H. Oh, *Chem*, 2017, **3**, 724-763.
151. X. Wu, S. Mao, J. Chen and J. Huang, *Adv. Mater.*, 2018, **30**, 1705642.
152. A. Tsumura, H. Koezuka and T. Ando, *Appl. Phys. Lett.*, 1986, **49**, 1210-1212.

153. A. Sou, *Practical Guide to Organic Field Effect Transistor Circuit Design*, Smithers Rapra, Shropshire, 1st edn., 2016.
154. X. Tao and V. Koncar, in *Smart Textiles and their Applications*, ed. V. Koncar, Woodhead Publishing, Oxford, 1st edn., 2016, vol. 2, ch. 1, pp. 569-598.
155. W. Hu, F. Bai, X. Gong, X. Zhan, H. Fu and T. Bjornholm, *Org. Electron.*, 2012, **55**, 718-725.
156. J. Yang, Z. Zhao, S. Wang, Y. Guo and Y. Liu, *Chem*, 2018, **4**, 2748-2785.
157. A. S. M. Tripathi, N. Kumari, S. Nagamatsu, S. Hayase and S. S. Pandey, *Org. Electron.*, 2019, **65**, 1-7.
158. F. Garnier, G. Horowitz and D. Fichou, *Synth. Metals*, 1989, **28**, 705-714.
159. S. Hotta and T. Yamao, *J. Mater. Chem.*, 2011, **21**, 1295-1304.
160. C. Dimitrakopoulos, S. Purushothaman, J. Kymissis, A. Callegari and J. M. Shaw, *Science*, 1999, **283**, 822-824.
161. G. Horowitz, *Adv. Mater.*, 1998, **10**, 365-377.
162. N. Zhang, J. Chen, Y. Huang, W. Guo, J. Yang, J. Du, X. Fan and C. Tao, *Adv. Mater.*, 2016, **28**, 263-269.
163. C.-Y. Hwang, G.H. Kim, J.-H. Yang, C.-S. Hwang, S.M. Cho, W.-J. Lee, J.-E. Pi, J.H. Choi, K. Choi, H.-O. Kim, S.-Y. Lee, and Y.-H. Kim, *Nanoscale*, 2018, **10**, 21648-21655.
164. C. Amador-Bedolla, R. Olivares-Amaya, J. Hachmann and A. Aspuru-Guzik, *Informatics for Materials Science and Engineering*, Butterworth-Heinemann, Oxford, 1st edn., 2013.
165. C. Toro and J. M. Buriak, *Chem. Mater.*, 2014, **26**, 5181-5182.
166. Q. Liu, Y. Jiang, K. Jin, J. Qin, J. Xu, W. Li, J. Xiong, J. Liu, Z. Xiao, K. Sun, S. Yang, X. Zhang and L. Ding, *Sci. Bull.*, 2020, **65**.

167. N. C. Lewis and D. G. Nocera, *Proc. Natl. Acad. Sci.*, 2007, **104**, 20142.
168. B. Qi and J. Wang, *J. Mater. Chem.*, 2012, **22**, 24315-24325.
169. J. C. Blakesley and D. Neher, *Phys. Rev. B*, 2011, **84**, 075210.
170. B. P. Rand and H. Richter, *Organic Solar Cells: Fundamentals, Devices, and Upscaling*, CRC Press, Boca Raton, 1st edn., 2014.
171. *US Pat.*, US20050110420A1, 2004.
172. S. Prasad, in *Organic Light-Emitting Diodes (OLEDs)*, ed. A. Buckley, Woodhead Publishing, Cambridge, 1st edn., 2013, vol. 1, ch.6, pp. 548-571.
173. P. Samori and V. Palermo, *Flexible Carbon-based Electronics*, John Wiley & Sons, Palermo, 1st edn., 2019.
174. F. So, *Organic Electronics: Materials, Processing, Devices and Applications*, CRC Press, 1st edn., 2009.
175. S. V. Dayneko, M. Rahmati, M. Pahlevani and G. C. Welch, *J. Mater. Chem. C*, 2020, **8**, 2314-2319.
176. Y. S. Negi, P. Mittal and D. B. Kumar, in *New Horizons of Process Chemistry*, eds K. Tomioka, T. Shioiri and H. Sajiki, Springer, Singapore, 1st edn., 2017, vol. 1, ch. 1, pp. 11-27.
177. J. Shinar and R. Shinar, *J. Phys. D: Appl. Phys.*, 2008, **41**, 133001.
178. Y. Li, *Organic Optoelectronic Materials*, Springer International Publishing, New York, 1st edn., 2015.
179. R. J. Young and P. A. Lovell, *Introduction to Polymers*, CRC Press, New York, 1<sup>st</sup> edn., 2011.
180. P. Heinz-Helmut, *UV-VIS Spectroscopy and its Applications*, Springer Science & Business Media, New York, 1st edn., 2013.

181. M. H. Weik, in *Computer Science and Communications Dictionary*, ed. M. H. Weik, Springer US, Boston, 1st edn., 2001, vol. 1, ch. 6, pp. 1284-1284.
182. D. F. Swinehart, *J. Chem. Ed.*, 1962, **39**, 333.
183. R. J. Anderson, D. J. Bendell and P. W. Groundwater, *Organic Spectroscopic Analysis*, Royal Society of Chemistry, London, 1st edn., 2004.
184. W. R. Browne, *Electrochemistry*, Oxford University Press, Oxford, 1st edn., 2018.
185. G. Day and A. Rose, *Faraday Effect Sensors: The State Of The Art*, SPIE, Bellingham, 1st edn., 1989.
186. D. L. Reger, S. R. Goode and D. W. Ball, *Chemistry: Principles and Practice*, Cengage Learning, Bedford, 3rd edn., 2009.
187. A. S. Feiner and A. J. McEvoy, *J. Chem. Ed.*, 1994, **71**, 493.
188. F. J. Vidal-Iglesias, J. Solla-Gullón, A. Rodes, E. Herrero and A. Aldaz, *J. Chem. Ed.*, 2012, **89**, 936-939.
189. S. A. Ashter, in *Thermoforming of Single and Multilayer Laminates*, ed. S. A. Ashter, William Andrew Publishing, Oxford, 2014, vol. 1, ch. 6, pp. 123-145.
190. Pandey, *Handbook of Semiconductor Electrodeposition*, CRC Press, Boca Raton, 1st edn., 1996.
191. C. G. Zoski, *Handbook of Electrochemistry*, Elsevier, Amsterdam, 1st edn., 2007.
192. P. T. Kissinger and W. R. Heineman, *J. Chem. Ed.*, 1983, **60**, 702.
193. A. Lewandowski, L. Waligora and M. Galinski, *Electroanalysis*, 2009, **21**, 2221-2227.
194. L. Leonat, S. Beatrice Gabriela and I. V. Brañzoi, *Sci. Bull. B Chem. Mater. Sci. UPB*, 2013, **75**, 111-118.

195. F. R. Simões and M. G. Xavier, in *Nanoscience and its Applications*, eds. A. L. Da Róz, M. Ferreira, F. de Lima Leite and O. N. Oliveira, William Andrew Publishing, 2017, vol. 1, ch. 6, pp. 155-178.
196. L. Ramaley and M. S. Krause, *Anal. Chem.*, 1969, **41**, 1362-1365.
197. P. J. Skabara and M. Sallé, *Beilstein J. Org. Chem.*, 2015, **11**, 1528-1529.
198. P. J. Skabara, R. Berridge, E. J. L. McInnes, D. P. West, S. J. Coles, M. B. Hursthouse and K. Müllen, *J. Mater. Chem.*, 2004, **14**, 1964-1969.
199. I. A. Wright, A. L. Kanibolotsky, J. Cameron, T. Tuttle, P. J. Skabara, S. J. Coles, C. T. Howells, S. A. J. Thomson, S. Gambino and I. D. W. Samuel, *Angew. Chem. Int. Ed.*, 2012, **51**, 4562-4567.
200. R. Berridge, P. J. Skabara, C. Pozo-Gonzalo, A. Kanibolotsky, J. Lohr, J. J. W. McDouall, E. J. L. McInnes, J. Wolowska, C. Winder, N. S. Sariciftci, R. W. Harrington and W. Clegg, *J. Phys. Chem. B*, 2006, **110**, 3140-3152.
201. I. A. Wright, N. J. Findlay, S. Arumugam, A. R. Inigo, A. L. Kanibolotsky, P. Zassowski, W. Domagala and P. J. Skabara, *J. Mater. Chem. C*, 2014, **2**, 2674-2683.
202. A. L. Kanibolotsky, N. J. Findlay and P. J. Skabara, *Beilstein J. Org. Chem.*, 2015, **11**, 1749-1766.
203. C. Sutton, C. Risko and J.-L. Brédas, *Chem. Mater.*, 2016, **28**, 3-16.
204. A. W. Grice, D. D. C. Bradley, M. T. Bernius, M. Inbasekaran, W. W. Wu and E. P. Woo, *Appl. Phys. Lett.*, 1998, **73**, 629-631.
205. A. L. Kanibolotsky, R. Berridge, P. J. Skabara, I. F. Perepichka, D. D. C. Bradley and M. Koeberg, *J. Am. Chem. Soc.*, 2004, **126**, 13695-13702.
206. G. Shi, D. Chen, H. Jiang, Y. Zhang and Y. Zhang, *Org. Lett.*, 2016, **18**, 2958-2961.

207. R. P. Kaiser, I. Caivano and M. Kotora, *Tetrahedron*, 2019, **75**, 2981-2992.
208. A. C. Grimsdale and K. Mullen, *Macromol. Rapid Commun.*, 2007, **28**, 1667-1672.
209. S. P. Dudek, M. Pouderoijen, R. Abbel, A. P. H. J. Schenning and E. W. Meijer, *J. Am. Chem. Soc.*, 2005, **127**, 11763-11768.
210. Y. Geng, A. Trajkovska, D. Katsis, J. J. Ou, S. W. Culligan and S. H. Chen, *J. Am. Chem. Soc.*, 2002, **124**, 8337-8347.
211. F. G. Bordwell, G. E. Drucker and H. E. Fried, *J. Org. Chem.*, 1981, **46**, 632-635.
212. H. Jiao, P. v. R. Schleyer, Y. Mo, M. A. McAllister and T. T. Tidwell, *J. Am. Chem. Soc.*, 1997, **119**, 7075-7083.
213. J. U. Wallace and S. H. Chen, in *Polyfluorenes*, eds. U. Scherf and D. Neher, Springer Berlin Heidelberg, Berlin, 1st edn., 2008, vol. 212, ch. 124, pp. 145-186.
214. Y. Geng, S. W. Culligan, A. Trajkovska, J. U. Wallace and S. H. Chen, *Chem. Mater.*, 2003, **15**, 542-549.
215. R. Vázquez Guilló, A. Falco, M. Martínez-Tomé, C. R. Mateo, M. Herrero, E. Vázquez and R. Mallavia, *Polymers*, 2018, **10**, 215.
216. P. K. Tsolakis and J. K. Kallitsis, *Chem. Eur. J.*, 2003, **9**, 936-943.
217. E. Ertas, İ. Demirtas and T. Ozturk, *Beilstein J. Org. Chem.*, 2015, **11**, 403-415.
218. C. Rovira, J. Veciana, N. Santalo, J. Tarres, J. Cirujeda, E. Molins, J. Llorca and E. Espinosa, *J. Org. Chem.*, 1994, **59**, 3307-3313.
219. R. Anémian, J.-C. Mulatier, C. Andraud, O. Stéphan and J.-C. Vial, *Chem. Comm.*, 2002, **15**, 1608-1609.

220. P. Robert, A. Bolduc and W. G. Skene, *J. Phys. Chem. A*, 2012, **116**, 9305-9314.
221. C. Orofino, C. Foucher, F. Farrell, N. J. Findlay, B. Breig, A. L. Kanibolotsky, B. Guilhabert, F. Vilela, N. Laurand, M. D. Dawson and P. J. Skabara, *J. Polym. Sci. Part A: Polym. Chem.*, 2017, **55**, 734-746.
222. F. Pop and N. Avarvari, *Chem. Commun.*, 2016, **52**, 7906-7927.
223. S. Horiuchi, Y. Tokunaga, G. Giovannetti, S. Picozzi, H. Itoh, R. Shimano, R. Kumai and Y. Tokura, *Nature*, 2010, **463**, 789-792.
224. N. K. Nath, M. K. Panda, S. C. Sahoo and P. Naumov, *CrystEngComm*, 2014, **16**, 1850-1858.
225. S. Chorazy, R. Podgajny, W. Nogaś, S. Buda, W. Nitek, J. Mlynarski, M. Rams, M. Koziel, E. Juszyńska Gałązka, V. Vieru, L. F. Chibotaru and B. Sieklucka, *Inorg. Chem.*, 2015, **54**, 5784-5794.
226. S. Kobatake, S. Takami, H. Muto, T. Ishikawa and M. Irie, *Nature*, 2007, **446**, 778-781.
227. Y. Zhou, D. Yan and M. Wei, *J. Mater. Chem.*, 2015, **3**, 10099-10106.
228. W. Yao, Y. Yan, L. Xue, C. Zhang, G. Li, Q. Zheng, Y. S. Zhao, H. Jiang and J. Yao, *Angew. Chem. Int. Ed.*, 2013, **52**, 8713-8717.
229. B. Valeur and M. N. Berberan-Santos, *Molecular Fluorescence: Principles and Applications*, Wiley-VCH Verlag GmbH, Weinheim, 1st edn., 2012.
230. W. R. H. Hurlley and S. Smiles, *J. Chem. Soci.*, 1926, **129**, 2263-2270.
231. L. Boudiba, L. Ouahab and A. Gouasmia, *Tetrahedron Lett.*, 2006, **47**, 3123-3125.

232. A. J. C. Kuehne, D. Elfstrom, A. R. Mackintosh, A. L. Kanibolotsky, B. Guilhabert, E. Gu, I. F. Perepichka, P. J. Skabara, M. D. Dawson and R. A. Pethrick, *Adv. Mater.*, 2009, **21**, 781-785.